Dissertation

submitted to the

Combined Faculty of of Mathematics, Engineering and Natural Sciences

of Heidelberg University, Germany

for the degree of

Doctor of Natural Sciences

Put forward by

Marco Albán

born in: Guayaquil (Ecuador)

Oral examination: 14-10-2025

Mapping ionized gas outflows in and Beyond AGN: A Multi-Wavelength Approach Using SDSS-IV MaNGA

Referees: Prof. Dr. Dominika Wylezalek

Prof. Dr. Jochen Heidt

Abstract

The role of active galactic nuclei (AGN) in regulating galaxy evolution is widely accepted as a feedback process suppressing star formation. However, observational evidence for it remains controversial. This thesis examines ionized gas outflows across and beyond AGN populations, utilizing SDSS-IV MaNGA's spatially resolved spectroscopy together with multi-wavelength AGN selection. We demonstrate that radio and optical diagnostics identify distinct AGN populations. Radio-selected AGN exhibit broader emission lines reaching larger radii, suggesting evolved or longer-lasting feedback. Furthermore, when radio and optical AGN signatures are simultaneously present, feedback appears maximized, hinting at combined radiative and kinetic modes. Since radio signatures appear to hint at long-lasting AGN signatures, we investigate galaxies lacking ongoing AGN. Strikingly, radio-detected galaxies without current AGN exhibit broader emission linewidths than those without radio. These show outflow-like kinematics and share global properties (e.g., radio compactness and redder colors) with radio-detected AGN. This alignment suggests shared physical origins, likely connecting past AGN activity. Pointing to feedback that persists beyond the AGN's observable phase, these systems are strong fossil-outflow candidates. This thesis presents a time-dependent view of AGN feedback, laying the foundation for future studies that connect AGN duty cycles, multiwavelength selection, and spatially resolved diagnostics.

Zusammenfassung

Die Rolle aktiver galaktischer Kerne (AGN) bei der Regulierung der Galaxienentwicklung wird weithin als Feedback-Prozess anerkannt, der die Sternentstehung unterdrückt. Der Beobachtungsnachweis bleibt jedoch umstritten. Diese Arbeit untersucht ionisierte Gaswinde innerhalb und außerhalb von AGN-Populationen mithilfe der räumlich aufgelösten Spektroskopie von SDSS-IV MaNGA in Kombination mit einer multiwellenlängenbasierten AGN-Selektion. Wir zeigen, dass Radio- und optische Diagnostik unterschiedliche AGN-Populationen identifizieren. Radio-identifizierte AGN weisen breitere Emissionslinien auf, die sich bis in größere Radien erstrecken, ein Hinweis auf entwickelteres oder langlebigeres Feedback. Insbesondere wenn Radio- und optische AGN-Signaturen gleichzeitig vorhanden sind, scheint das Feedback maximiert zu sein, was auf eine Kombination aus Strahlungs- und kinetischen Modi hindeutet. Da Radiosignaturen offenbar langanhaltende AGN-Aktivität widerspiegeln, analysieren wir Galaxien ohne aktuell aktiven AGN. Auffällig ist, dass radioerfasste Galaxien ohne optischen AGN breitere Emissionslinien zeigen als solche ohne Radio. Diese weisen ausflussähnliche Kinematik auf und teilen globale Eigenschaften (z.B. kompakte Radiomorphologie, rötere Farben) mit radioerfassten AGN. Dies deutet auf gemeinsame physikalische Ursprünge und vergangene AGN-Aktivität hin. Diese Arbeit präsentiert eine zeitabhängige Ansicht des AGN-Feedback und legt den Grundstein für zukünftige Studien, die AGN-Aktivitätszyklen, Multiwellenlängenauswahl und räumlich aufgelöste Diagnostik miteinander verbinden.

Contents

List of Figures

List of Tables

Chapter 1

Introduction

There is a wound that won't heal at the center of the galaxy.

— *Maarva Carrassi Andor (a fictional character in Star Wars)*

1.1 Motivation

A long time ago, in a galaxy far, far away, vast clouds of cold gas were ready to form stars for many Hubble times. Except, they did not. Today, this galaxy turned red and dead; it went silent and quiescent. Gas, when cold, is the fuel of star formation, but something in this galaxy has kept it hot, preventing it from collapsing. This galaxy does not sit alone in our Universe; many more show the same fate, sometimes even too soon. A consistent paradox reveals that there is enough fuel to sustain star formation for tens of billions of years, and yet, our Universe is quieter than we estimate. Astronomers have long sought an explanation, a suspect. The leading candidate is sometimes caught in the act, sometimes cloaked or obscured by its own appetite, and sometimes suspiciously dormant in a red galaxy. At the heart of the galaxy, a likely suspect waits: a supermassive black hole (SMBH).

Allow me to render this dramatic monologue into a formal narrative. Today's best galaxy evolution and structure formation model involves the Λ Cold Dark Matter (ΛCDM; see Abdalla et al. 2022; Bull et al. 2016, for useful reviews). Large-volume cosmological simulation runs based on this model have been shown to successfully reproduce many observables (e.g., Illustris, EAGLE; Schaye et al. 2015; Vogelsberger et al. 2014), such as the cosmic microwave background (CMB) power spectrum (Planck Collaboration et al. 2014), the accelerated expansion of the Universe and its large-scale structures, the observed abundances of primordial elements (Cyburt et al. 2016), to mention a few. Despite this success, some of their predictions conflict with our observations (see Naab & Ostriker 2017, for a review). A common manifestation

of this problem is that simulations overpredict today's baryon conversion efficiency, resulting in too many stars forming in the most massive halos (see Harrison 2017). This suggests the need for a star-formation regulator with consequences for galaxy evolution. Notably, the existence of scaling relations involving galaxy properties and their central SMBHs (see a summary in Section 13 of D'Onofrio et al. 2021), together with further observables, supports that both SMBHs and their galaxies grow together through cosmic times (Morganti 2017b).

Remarkably, there is strong evidence supporting the existence of an SMBH in most galaxy centers (Graham 2016; Kormendy & Ho 2013). Their simple presence, considering their enormous confirmed mass (Kormendy & Richstone 1995), poses a challenging question: how do these monsters grow, and what is the impact of this growth on their surroundings (i.e., in their host galaxies)? The event of the active growth of a supermassive black hole is modernly known as active galactic nuclei (AGN). No matter what generous calculations one can devise, the implications of a black hole growing that large imply an enormous accretion and energy release that would not go unnoticed (Fabian 2012, 1979). The fact that we observe galaxies with either actively accreting and dormant (inactive) SMBHs also implies, quite obviously, what the literature has largely come to a consensus on, that AGNs are events that are part of the life cycle of galaxies (Alexander et al. 2025; Harrison & Ramos Almeida 2024). Indeed, current observations of the farthest studied galaxies suggest that, even in the early universe, the cores of galaxies were already taken over by an SMBH (e.g., Bañados et al. 2018; Jeon et al. 2025; Juodžbalis et al. 2024).

AGNs are therefore seen as key agents that regulate star formation and tie black hole growth to galaxy evolution. Such a process is referred to as AGN feedback (Fabian 1979), which has a negative effect on star formation, potentially suppressing or regulating it. However, testing this idea is far from straightforward, and the evidence has not reached a consensus in the literature. For example, well-resolved studies of individual galaxies often detect signs of star-formation suppression or outflows driven by AGN activity (e.g., Alatalo et al. 2015; Alonso Herrero et al. 2023; Baron et al. 2018; Feruglio et al. 2010). However, equally detailed examples exist where the presence of an AGN appears to have little to no measurable impact (e.g., Lai et al. 2022; Toba et al. 2017). Trading detail for sample size, large survey studies face a similar puzzle, where evidence is rather ambiguous (e.g., Almaini et al. 2025; Bae et al. 2017; Cicone et al. 2014; Le Fèvre et al. 2019; Yesuf et al. 2017). Ambitious multi-wavelength campaigns have tried to address these tensions (e.g., Baron et al. 2020), but often return inconclusive results (e.g., Fluetsch et al. 2019). This tension naturally fuels controversial discussions in the community about whether AGN feedback (in terms of star formation) is negative, positive, or irrelevant altogether (Combes 2017; Husemann & Harrison 2018; Kormendy & Ho 2013; Wylezalek & Morganti 2018). Yet, observational scaling relations, the cosmic star-formation history and its link to BH accretion history, theoretical models, and clear, powerful gas ejecta ubiquitous in the presence of AGN, just to mention a few of them, insist that AGN must play a

significant role (D'Onofrio et al. 2021).

Bridging this gap between strong theoretical expectations and ambiguous observational evidence remains a major challenge, likely involving a combination of observational limitations, methodological biases, and the complex nature of AGN activity itself.

1.1.1 Towards a novel approach

Part of the conflict has often been attributed to the narrow lens through which AGN are selected, which can lead to biases (Padovani 2017). For example, in the early days of radio astronomy, powerful double-lobed jets significantly influenced our understanding of radio emission in AGN (see Urry & Padovani 1995, for an early review). Today's deeper and more sensitive radio surveys have revealed a more complex reality: an entire population of low-luminosity or compact radio AGN exists, including objects with no obvious jets at all (e.g., Morabito et al. 2025; Padovani 2016; Sabater et al. 2019). Another example comes from optical selection (e.g., Kewley et al. 2001a; Kewley et al. 2006; Veilleux & Osterbrock 1987), which brings its own blind spots (see Singh et al. 2013a). While emission-line diagnostics build large AGN samples (allowing extensive AGN studies; e.g., Kauffmann et al. 2003), they depend on tracing specific ionization states, typically missing weakly accreting or heavily obscured sources (Assef et al. 2018; Best et al. 2005).

Comparing different selection methods directly (as shown in Hickox et al. 2009) highlights how they can yield fundamentally different AGN populations (see Section 1.6), increasing the complexity of looking for evidence of feedback. Another challenge lies in the mismatch of timescales. Our telescopes capture mere moments in the lifetime of a galaxy, while the processes over which galaxies evolve (e.g., star formation processes; Kennicutt et al. 2009) operate over tens to hundreds of millions of years. A further complication is that an AGN episode may be short-lived compared to the star-formation cycle (Netzer 2015), and its imprint, like outflows, might persist long after the AGN has faded away (Zubovas & Maskeliūnas 2023).

Recognizing these challenges, the direction of the research in this thesis adopts a combination of strategies:

- Spatial information. The main dataset used in this thesis involves integral field spectroscopy (IFS; see Section 1.2 for a description of the dataset). While most foundational studies on AGN encompass large samples of galaxies from surveys focusing on spectra from their central regions, ambitious surveys focused on resolving the spectral features of galaxies have taken a prominent place in the literature. We discuss this in further detail in Section 1.3.3.

- Combining and refining selection techniques: Following the refinement of optical diagnostics with IFS (summarized in Section 1.4.1), we compare them against

multi-wavelength methods (see Section 1.6), aiming to trace the physical origins behind any observed differences between galaxy samples.

- Strict control samples: as we explore sources in Chapter 2, matching key host galaxy properties when comparing two populations of galaxies is indispensable. We actively incorporate this into our analysis strategies across our studies, minimizing the likelihood of artificial trends that selection biases can introduce. This is often underestimated (see an example in Smirnova-Pinchukova et al. 2022).

- AGN duty cycle perspective: We refer to AGN duty cycle as its episodic nature across the evolution of its host galaxy. While AGN-driven outflows are broadly documented in AGN, much less has been said about AGN-driven outflows persisting in currently inactive galaxies. To first order, we investigate outflow signatures in galaxies without ongoing AGN activity, searching for kinematic evidence that may trace a previous, now-faded AGN episode.

The structure of this thesis is mainly based on three papers (Albán et al. 2024,Kukreti et al. 2025, and Albán et al submitted) distributed across three chapters (Chapter 2, Chapter 3, and Chapter 4, respectively). We will refer to them as Paper I, Paper II, and Paper III (see Section 1.7).

In the remainder of this chapter, we establish the theoretical foundation. In section 1.2, we start by describing Integral field spectroscopy and the main survey and datasets used. Section 1.3 provides a focused context (relevant to our study) on what is known about AGN and its connection to galaxy evolution. Section 1.4 describes the Optical perspective of AGN through emission-line ratios in combination with integral field spectroscopy. Section 1.5 focuses on describing the local radio Universe, highlighting its potential for AGN studies. Ultimately, Section 1.6 discusses additional selection techniques relevant to our study. Lastly, an overview of this thesis is provided in Section 1.7.

1.2 Integral field spectroscopy

A natural limitation of optical spectroscopy is the longer exposure times required for each target (compared to broadband optical imaging), leading to the development of observatories that target multiple objects, focusing on their central regions with a fixed aperture (Strauss et al. 2002). While broadband optical images provide a broad and spatially resolved insight into the galaxy continuum at a specific filter (e.g., Abazajian et al. 2003; York et al. 2000), optical spectroscopy reveals detailed physical processes, such as the exact spectral shape and absorption and emission processes (a comprehensive review is described in Kewley et al. 2019). This has enabled remarkable statistical studies that have laid the foundations and established the constraints of modern astrophysics and cosmology. However, early observations in single objects, aimed at obtaining spatial spectroscopic information (e.g., using long slit spectroscopy

Durret & Bergeron 1988), already resulted in a somewhat expected landscape, where gradient-behaved processes dominate galaxies' spectral properties (see a review in Sánchez et al. 2018). The techniques that aim to recover a spectroscopic map of galaxies are called integral field spectroscopy (IFS; see Figure 1.1; Westmoquette et al. 2009).

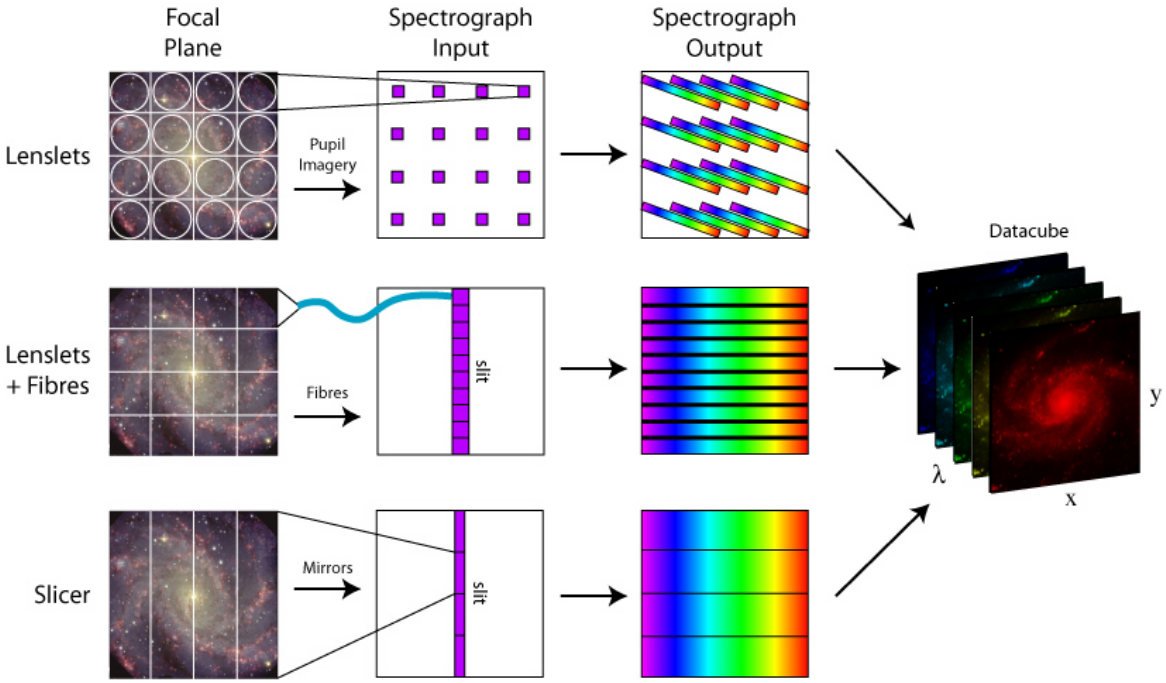

Figure 1.1. The main techniques for achieving integral field spectroscopy. MaNGA's mode uses fibers, as the configuration shown in the second row. Credit and further details on the other techniques are discussed in Westmoquette et al. (2009).

The nuclear origin of AGN-driven processes demands understanding both the galaxy's central region and its surroundings. This requires spatially resolved spectroscopy. Therefore, the integration of IFS in galaxy evolution studies is extremely informative.

1.2.1 Mapping Nearby Galaxies at Apache Point Telescope

Mapping Nearby Galaxies at Apache Point Observatory or MaNGA (MaNGA; Bundy et al. 2015) is part of the SDSS-IV missions and uses the 2.5 m Sloan Telescope (SDSS for Sloan Digital Sky Survey; Gunn et al. 2006). MaNGA is an IFS survey that utilizes an array of fibers on each observed target, serving as the primary data source for this thesis. The survey targets 10 010 galaxies at low redshift ($z < 0.15$), and publicly released its final dataset (DR17) in December 2021. With a spectral resolution of R$\sim$2000, each fiber has a spectral coverage from 3622 Å to 10354 Å. The fibers, each with a size of 2 arcseconds, are arranged in hexagonal fields of view (FoV) ranging from 12 to 32 arcseconds. Given that a configuration of these characteristics has space between the fibers, additional observations are performed for each galaxy after slightly

offsetting the IFU to increase its filling factor.

The sample has been selected from two samples such that the field of view (FoV) of each galaxy covers around 1.5 to 2.5 effective radius (r-band) in the targets. Also, one of the goals in the target choice is to preserve a flat stellar mass distribution above stellar masses of $\sim 10^9\ M\odot$ and a uniform NUV−i color coverage. Specific details on the MaNGA target selection can be found in Wake et al. (2017).

Each spectrum on each galaxy passes through a standard data reduction phase provided by the survey team. This is called the MaNGA Data Reduction Pipeline (DRP; see the details in Law et al. 2016). In summary, the DRP is responsible for extracting the spectra and assigning them to each galaxy, along with their corresponding spatial positions, taking into account spectral dithering. It also calibrates flux and wavelength and subtracts the sky background. The DRP outputs FITS files arranged in either row-stacked spectra or a cube dataset containing a 3D array where two axes correspond to the pixel (spaxel) spatial location of the spectra and the third axis contains the spectral information. The DRP grids back the data, achieving a 0.5 arcsec resolution in each spaxel. This 3D data is the input for several IFS-oriented pipelines. Below, we describe the most relevant pipelines responsible for the data products used in this thesis.

MaNGA Data Analysis Pipeline

The MaNGA Data Analysis Pipeline (DAP) is a software responsible for obtaining properties derived from the spectra of the data products from the DRP. The details are described in Westfall et al. (2019a). The DAP takes care of spatially binning (particularly Voronoi binning; Cappellari & Copin 2003) spectra to increase the reliability of derived properties, some of which need a minimum signal-to-noise (S/N), specifically for continuum features (e.g., spectral indexes). It performs stellar continuum modeling based on the stellar libraries from MILES (Falcón-Barroso et al. 2011; Sánchez-Blázquez et al. 2006). The DAP also characterizes the emission lines (details of this are described in Belfiore et al. 2019) to obtain their moment maps (e.g., flux or line kinematics). The MaNGA DAP provides this information as full-fitted spectra or individual maps for each galaxy, providing a per-spaxel array of properties. The specific properties used in our studies are further detailed in each of the relevant papers (see Paper I, Paper II, Paper III in their corresponding chapters).

Pipe3D

The Pipe3D (Sánchez et al. 2016) is a pipeline designed for fitting cube-like spectroscopic data, based on the FIT3D (Lacerda et al. 2022) method. While Pipe3D has been broadly used in MaNGA, it has also been tested in data from other IFS surveys, such as the Calar Alto Legacy Integral Field Area (CALIFA Sánchez et al. 2012). The details have been described and summarized in numerous published versions of the tool's usage, with one of the broadest found in Sánchez et al. (2022). In sum-

mary, the pipeline models separately the ionized gas emission lines and the stellar light in each rest-frame spectrum. The stellar continuum is modeled by combining dust-attenuated (Cardelli et al. 1989) SSP templates, from which parameters like stellar velocities, stellar velocity dispersion, and stellar extinction are estimated. After this is done, ionized gas emission lines are modeled to derive their fluxes, velocities, and velocity dispersions.

Some notable differences between Pipe3D and the MaNGA DAP are that the former employs a more sophisticated, iterative procedure to fit the emission lines. Furthermore, it uses a continuum segmentation binning that better preserves galaxy morphology. It focuses on providing star formation histories (SFHs) and other stellar population properties beyond the basic kinematics and line fluxes provided by the DAP. We broadly utilize their integrated properties, which are sometimes referred to as the MaNGA Valued-Added Catalog (VAC; Sánchez et al. 2018). Some of these properties are mentioned later in the corresponding papers, when applicable.

MEGACUBES

The MEGACUBES is another pipeline focused on IFS data, particularly for MaNGA (Riffel et al. 2023). The procedure uses the URUTAU code (Dullius Mallmann & Riffel 2023) and performs a spaxel-by-spaxel spectral synthesis following the procedures from the STARLIGHT code (Cid Fernandes et al. 2005). It adopts standard procedures similar to those used in other pipelines to produce stellar continuum fitting, emission line fitting, and derive their fundamental properties. In contrast to Pipe3D's continuum binning or the MaNGA DAP's standard Voronoi binning, MEGACUBES maximizes spatial detail by avoiding binning altogether, making it also an excellent complement and consistency check when comparing results across different pipelines.

A significant feature of the data products from this pipeline is that it provides public catalogs of radial profiles for many properties, not only at different radial steps but also in different units (kpc, arcseconds, and normalized by the galaxy's effective radius). The radial profiles also consider the galaxies' b/a axis ratio. This is not available in the DAP or Pipe3D, although it can be recovered manually. However, many of the properties needed to study spatially are substantially more accessible from the MEGACUBES, which is why we broadly opt for their radial profiles[1]. While such profiles can be reconstructed from the other pipelines, MEGACUBES makes access to this information more straightforward. Notably, the Pipe3D VAC does provide slopes for radial gradients of some properties, which we find to be broadly consistent with MEGACUBES. We further discuss these comparisons in the individual analysis

[1]Initially, in Paper I we focused on ionized gas outflows fitting up to two Gaussian components to the emission lines (not accounted for in the described pipelines; see the last sub section from Section 1.2.1) and therefore, no additional radial profiles were used. However, in the next papers (Paper II and Paper III), we made use of the readily available radial profiles from MEGACUBES. This reduces redundant processing steps by eliminating the need to download large data products (which also translates to huge amounts of gigabytes of storage) and run our own radial annuli code.

chapters (in the individual papers).

A pipeline designed to pursue outflow signatures

The data products described above contain valuable information that is widely used throughout this thesis. However, none of them attempt to trace non-gravitational kinematic components seen in emission lines, usually used as outflow tracers (see Section 1.3.2). A common technique for indicating the presence of outflows involves accounting for double Gaussian components in emission lines. We make a special treatment to tackle this problem and create a code that accounts for such asymmetries in the emission lines of spectra. We specifically use [O III] for this matter in the three papers that make up this work, as it is a strong line both for star-forming galaxies and AGN (see Section 1.4). Considering all MaNGA galaxies and their available spectra, approximately 30 million individual spectra are present, and we required the use of multi-parallel processing environments for the fitting procedure. Our code outputs non-parametric velocity width maps (from [O III]), and we routinely refer to them s W_{80}; see Paper I). Additionally, graphical user interfaces were developed to visualize and explore as many spectra as possible. After visualizing a representative spectrum set, we have ensured that the fits work correctly. This algorithm is one of the pillars of Paper I, which focuses on mapping ionized outflows in AGN (see the paper for the details). The details on how our algorithm decides if an emission line has a second component are based on the reduced chi-square, and the details can be found in Appendix A.2.

The combination of these different pipelines offers several benefits. Not only does it deliver complementary data products, but it also allows for demonstrating a broad consistency across methods. Furthermore, it reinforces the reliability of the derived physical properties. Despite MaNGA's limitations in spatial resolution (typically 1.3 kpc), it offers an extensive spectral wavelength range and is the largest Integral Field Unit (IFU) survey of low-redshift ($z < 0.15$) galaxies. This combination is particularly valuable for investigating the widespread influence of AGN on their host galaxies, extending beyond the central regions. MaNGA serves as an ideal foundational IFU dataset for future generations of galaxy evolution studies.

1.3 Active galactic nuclei

1.3.1 Supermassive black hole growth

Black holes come in many sizes, depending on their mass. Theoretically, a black hole is a very dense object, with a mass (M) enclosed within a region smaller than its Schwarzschild radius ($r_s = 2GM/c^2$; with G as the gravitational constant, and c the speed of light). Observationally, we can broadly set black holes into three categories (see Bambi 2020, for a review). The first ones are stellar-mass black holes (with

typical masses of $5 < M\odot < 100$), which are a result of the gravitational collapse of a dying star. This collapse can occur, for example, after a supernova explosion or in binary star systems, where a companion star draws mass from its neighboring star and exceeds the Chandrasekhar limit (see Heger et al. 2023, for a review). In the second category are the intermediate-mass black holes ($10^2 < log(M\odot) < 10^5$), and one channel to their origin is a result of black hole mergers (see Greene et al. 2020). And lastly, one of the main characters of this thesis is the supermassive black hole. An SMBH resides in the center of its host galaxy and is believed to have done so since the earliest times of that galaxy's existence.

The origin of SMBHs and how they became so massive in the very early Universe is something about which we know very little. We have evidence of their early existence (see Bañados et al. 2018; Jeon et al. 2025; Juodžbalis et al. 2024). Some pose fundamental cosmological challenges, particularly regarding the limited time available for their formation and growth. Classically, theories suggest that supermassive black holes should be a result of intermediate-mass black hole mergers, which are also a consequence of merging stellar-mass black holes (Volonteri 2010). Some studies suggest models that often require sustained accretion at or above the Eddington limit and conditions that may not be present in today's Universe (e.g., Larson et al. 2023). This is driving exciting discoveries in modern astrophysics.

However, in this thesis, we focus on the effect that growing these SMBHs has on the evolution of their host galaxies, particularly when observed at low redshift. SMBHs have to grow at some point in their life to get that massive. This growth is believed to occur during many epochs of galaxy evolution, and its effect manifests as what we know as an active galactic nucleus (AGN).

1.3.2 AGN and their structure

Early astronomical observations pointed to the existence of objects so powerful that they could not be explained by known stellar processes (Lynden-Bell 1969). Soon enough, similar objects were found, proving to be ubiquitous (Shields 1999). It was theorized and shown that the radiation from these objects is consistent with the effect of the growth of an SMBH (Fabian 1979; Rees 1984). Later on, it was found that most massive galaxies have an SMBH in their center, if one looks deep enough (using nearby galaxies; see Kormendy & Richstone 1995). Even in dwarf galaxies, the field is evolving and finding evidence for the presence of SMBHs, as observations become deeper (e.g., Greene & Ho 2004; Pardo et al. 2016).

A galaxy is said to host an active nucleus if its central SMBH is at a phase of non-negligible accretion. Once active, the theoretical or observationally motivated inner structure of an AGN might vary depending on its type. Figure 1.2 illustrates some of these key components, and some of the most relevant to this thesis are shortly described below. While the majority of these structures remain unresolved in our thesis data (with resolutions above the kpc scale), they nevertheless provide vital

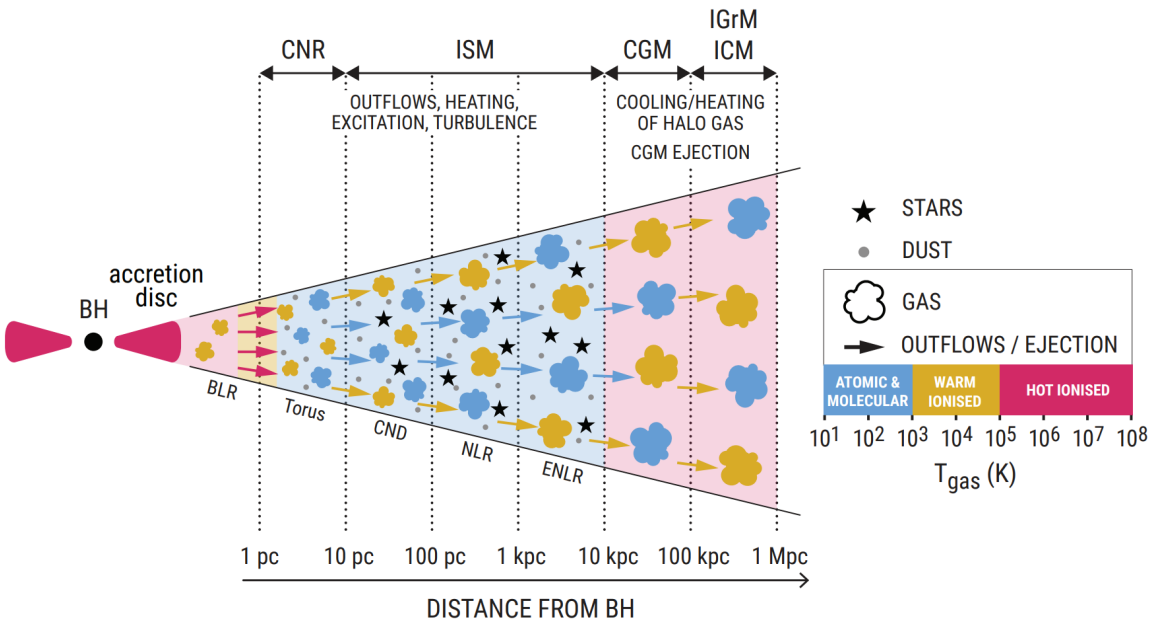

Figure 1.2. The spatial scales of AGN feedback. Taken from Harrison & Ramos Almeida (2024), and adapted caption: A schematic diagram to highlight the orders-of-magnitude range in temperature (colorcoding of gas clouds, intra-clouds medium and outflows) and spatial scales of AGN feedback. Gas in a range of phases, with a huge range in temperatures, can be affected by the energy released by AGN. This can occur from nuclear scales through to galaxy cluster scales. This large range in spatial scales naturally corresponds to an equally large range in temporal scales. Discussion continues in Section 2 of the paper from these authors.

context for understanding how the spectra of AGN behave. Most of the information below has been summarized primarily from Netzer (2015). When referring to density, we use the hydrogen number density.

- Accretion disk: region of high-density ($\sim 10^{15} \mathrm{cm}^{-3}$) gas surrounding and falling into the SMBH's vicinity ($\sim 10^{-3}$pc). Material, either from the surrounding gas or disrupted infalling stars, loses angular momentum (e.g., through gravitational torques; see Section 3 in Alexander et al. 2025), converting gravitational potential energy into thermal energy, fueling intense radiation over the whole electromagnetic spectrum, from X-rays to radio.

- Broad-line region (BLR): this is a very dense ($\sim 10^{10} \mathrm{cm}^{-3}$) region of gas located within a parsec of distance from the SMBH. The strong gravitational pull gives rise to high gas velocities. As a result, collisionally ionized permitted lines originating in this region appear strongly broadened when observed in spectra (with typical velocities of thousands of km s^{-1}). This Doppler broadening gives this region its famous name. The BLR, therefore, is typically traced by broad emission lines (e.g., broadened Balmer lines).

- Dusty torus: gas and dust ($\sim 10^{3-6} \mathrm{cm}^{-3}$) in the inner regions (within tens of

parsecs) that will feed the AGN's SMBH, is also responsible for obscuring the central radiation sources. Such a region absorbs a portion of X-ray and UV radiation from the accretion disk and re-emits at infrared wavelengths. The nature and geometry of this obscuration have been largely discussed in the context of AGN unification models (e.g., Urry & Padovani 1995), motivated by evidence of apparently distinct AGN types depending on inclination angles. As a result, a common model suggests that this gas forms a clumpy (characterized by large density inhomogeneities) and toroidal (donut-shaped) structure (Hickox & Alexander 2018a).

- Narrow-line region: at about a couple of hundred parsecs and beyond, the gas density drops ($\sim 10^4 \mathrm{cm}^{-3}$) while still being ionized by the AGN radiation. Extending beyond the torus allows it to be easily observed in several active galaxies. The low density allows forbidden lines to take place, which are usually used as tracers of this region (e.g., [O III]).

- Jets: while not shown in the Figure 1.2, jets can happen in around ∼10% of AGN (Panessa et al. 2019). They are a result of relativistic particles in the vicinity of the SMBH, which are subject to a strong magnetic field, giving rise to synchrotron emission. Jets have been observed to have a range of sizes, spanning from sub-kiloparsec to several hundred kiloparsecs.

- AGN outflows: Outflows are ejected gas from radiative winds or collimated jets. They exhibit non-gravitational motions, typically detected by velocity shifts in emission lines. They can extend to kpc scales and adopt bi-conical shapes (e.g., Wylezalek et al. 2017) with their center at the heart of the AGN.

The inner structure of the AGN phenomenon has been constructed around the unified model (Antonucci 1993; Netzer 2015; Urry & Padovani 1995). This model assumes that the diversity of signatures and appearances of different AGN can be attributed to geometrical factors. For example, AGN with spectral signatures of a BLR are referred to as type-I AGN, and are attributed to be an observational effect related to orientation. Consequently, not all AGN exhibit a BLR and are often referred to as type-II AGN. Indeed, several studies have shown that type-II AGN can exhibit BLR features in spectropolarimetric studies (e.g., Du et al. 2017; Ramos Almeida et al. 2016). This suggests that the different AGN classes are fundamentally the same physical objects, and the absence of a BLR is due to obscuration effects. However, this assumes the existence of a donut-shaped torus, which has been challenged and replaced by the idea of a clumpy one (Hickox & Alexander 2018b).

The miscellaneous ways to name an AGN are sometimes referred to as the AGN Zoo. Apart from type-I and type-II AGN. Depending on several other properties, AGN can be referred to as many other types. A quasar, for example, normally refers to a powerful AGN, commonly referring to sources at higher redshifts. Another example is a radio-loud AGN, typically when they present radio jets. The AGN exposed in

this work are not the typically powerful (or jetted AGN). Therefore, in this thesis, most AGN-zoo terms will not be relevant (see also Section 1.6), and we will specify a specific type of AGN in the corresponding paper when useful.

Given that the active growth of an SMBH happens in intervals. Therefore, AGN are events in the galaxy evolution cycle. Evidence for galaxies that have suffered multiple AGN through their evolution has been found in several studies (e.g., Das et al. 2021; Rao et al. 2023). Therefore, most of the components described above have a transient nature as well, and may be present or absent during the observation of a galaxy (whether it is currently active or not). Such an event, whether energetic or not, and even if it occurs cumulatively, would play a significant role in the evolution of galaxies. The impact of the growth of SMBHs is known as AGN feedback (Fabian 2012).

A universe with no feedback

In a fictitious universe, our far, far away galaxy would still be producing stars today (at $z \sim 0$), at a surprising rate. In this hypothetical universe, the impact of black hole growth, i.e., AGN, does not exist. Here, other galaxies face a similar fate, unable to quench their star formation. This has been routinely seen in cosmological simulations (see Naab & Ostriker 2017, for a review). Figure 1.3 summarizes some of these aspects, and further details can be found in Alexander et al. (2025).

For example, in the left panel, the top and bottom pairs of images display two sets of galaxies. On the right, we see galaxies from a simulated universe with no AGN feedback recipes, while on the left, we see the same galaxy that has evolved in a universe with AGN feedback. Dubois et al. (2016) show that an AGN-feedbackless universe discourages red ellipticals in massive galaxies with low V/σ (rotational / dispersion velocity) ratios and promotes galaxies with stellar masses above 10^{12} $M\odot$. Therefore, a natural consequence of this is that the stellar to halo mass function, or in other words, the baryon to stars conversion efficiency, is strongly overestimated in a universe without feedback. This is shown in the central panel. The solid line with white shaded regions shows the semi-empirical relation from Behroozi et al. (2019) at $z = 0$. The colored circles represent bins from simulations with no AGN feedback, and the gray circles represent the same for runs including different recipes of AGN feedback.

Lastly, the right panel of Figure 1.3 shows the distribution of the specific star formation rate (sSFR) observed in our Universe at $z = 0$ (gray-shaded histogram) and in different simulation runs at the same redshift. The green empty histograms show models with no BH accretion (AGN) feedback, and the black (solid and dotted) histograms show simulation runs with AGN feedback. Terrazas et al. (2020) shows that simulations without feedback fail to produce a population of quiescent galaxies.

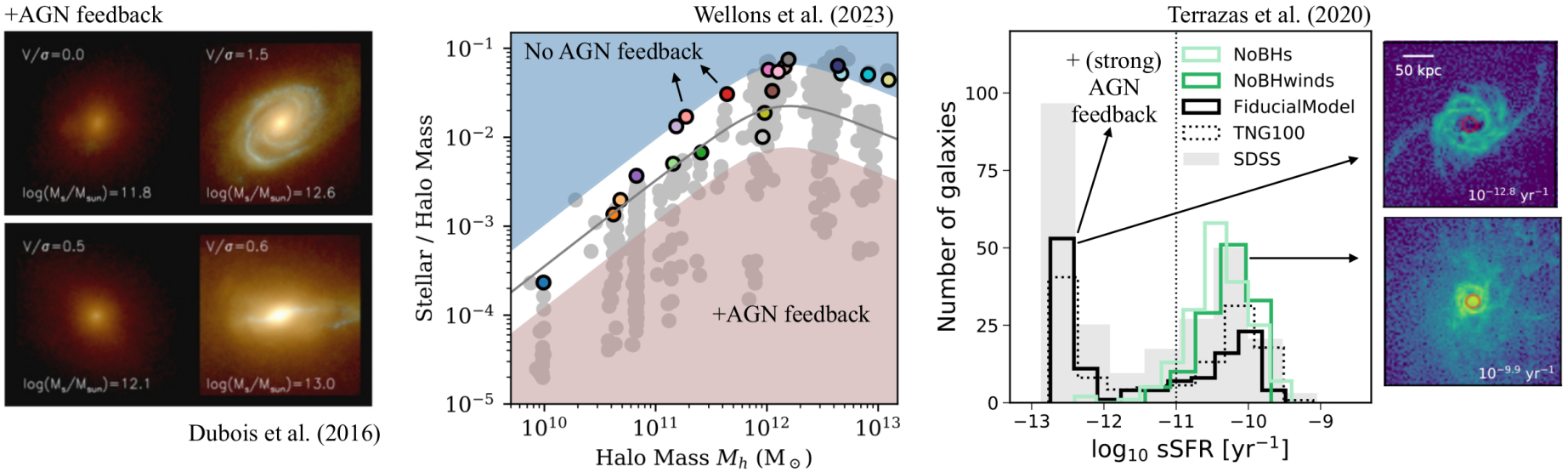

Figure 1.3. The universe with and without feedback. Taken from Alexander et al. (2025): Despite the use of different hydrodynamic solvers, different models for star formation, stellar feedback, interstellar medium, virtually all cosmological models of galaxy evolution must invoke feedback from AGN in order to produce a realistic population of massive galaxies. According to cosmological hydrodynamic simulations, AGN feedback regulates the gas content of massive halos and their central galaxies, modulating morphological transformations (left-hand panel), the stellar-to-halo mass ratio (central panel) and quiescent fraction of massive galaxies (right-hand panel), among a long catalog of other galaxy properties (see text). On the left-hand panel (adapted from Fig. 2 of Dubois et al. 2016), the annotations give the halo mass (at the bottom) and the ratio of rotation to dispersion velocities for the stellar component. The central panel shows results from Wellons et al. (2023) (adapted from their Fig. 2), who compare simulations that do not include AGN feedback (colored points), with simulations including various AGN feedback prescriptions (grey points) and with the semi-empirical relation (solid curve). The right-most plot shows the specific SFR (sSFR) for different runs the IllustrisTNG simulations (empty histograms; adapted from Fig. 1 of Terrazas et al. 2020) and observations (filled histogram). The fiducial simulation (black histogram) includes two modes of AGN feedback, which are required to produce the quiescent (low sSFR) galaxy population. The two smaller panels show example star-forming and quenched galaxies from the simulations (adapted from Fig. 3 of Terrazas et al. 2020).

Without AGN feedback, alternative explanations have been proposed, such as Type Ia supernova explosions and winds from asymptotic giant branch stars, but have not been implemented with significant success (Naab & Ostriker 2017). In summary, without AGN feedback, galaxies are too efficient at forming stars (see also Harrison 2017). Similarly, the morphological dichotomy observed in galaxies is not well reproduced, as it misses many elliptical galaxies, among other key observables that are in conflict (see Alexander et al. 2025, for a review). Indeed, models invoking AGN feedback are the most successful and are a promising candidate for connecting theoretical models with observations.

However, some studies fail to find a clear connection between the presence of an AGN and its impact on host galaxy properties. Part of this tension's origin can be that the timescales of the AGN's activity and the duration of its impact on a galaxy may differ. For example, the effect of an AGN can still be present in a galaxy after the AGN has turned off (e.g., Zubovas & Maskeliūnas 2023). Given that AGN are expected to impact the host galaxy, and several studies do not find convincing evidence (nor contrary) to support this, multiple efforts in the literature have pointed towards a cumulative effect, considering that AGN can be present multiple times in the same galaxy (Harrison & Ramos Almeida 2024). Therefore, our research actively discusses the results in terms of the possibility of having a cumulative AGN effect imprint in galaxies.

This is not only a tension arising from large simulation runs. For example, rich galaxy clusters reveal that their central hot gas is a source of X-ray emission, whose cooling times are significantly shorter than the age of the Universe. Such gas should therefore cool down fast into large amounts of cold gas and form stars. This is, however, not observed (Fabian 1994), and rather, a mechanism regulating this cooling should be in place. Models suggesting star-formation feedback, including supernovae, can't account for the energy needed (Canizares et al. 1987). It was remarkably observed that most, if not all, of these rich clusters host an AGN at their center, which has sufficient power to keep the gas hot (Croton et al. 2006; Hardcastle et al. 2019).

Below, we list more important observationally motivated facts that strongly suggest a connection between SMBH growth and galaxy evolution. Below, we discuss a few of them.

Scaling relations

The sphere of influence over which an SMBH dominates is several orders of magnitude smaller than the scale of galactic structures (e.g., the bulge). Yet, one of the most compelling discoveries in extragalactic astrophysics is the existence of tight correlations between the properties of SMBHs (mainly, their mass) and those of their host galaxies (see Kormendy & Ho 2013, for a review). What is even more surprising is how these relations are very tight for several decades of SMBH masses (see Figure 1.4). The $M_{\rm BH} - \sigma_\star$ relation is one of the most common and perhaps most

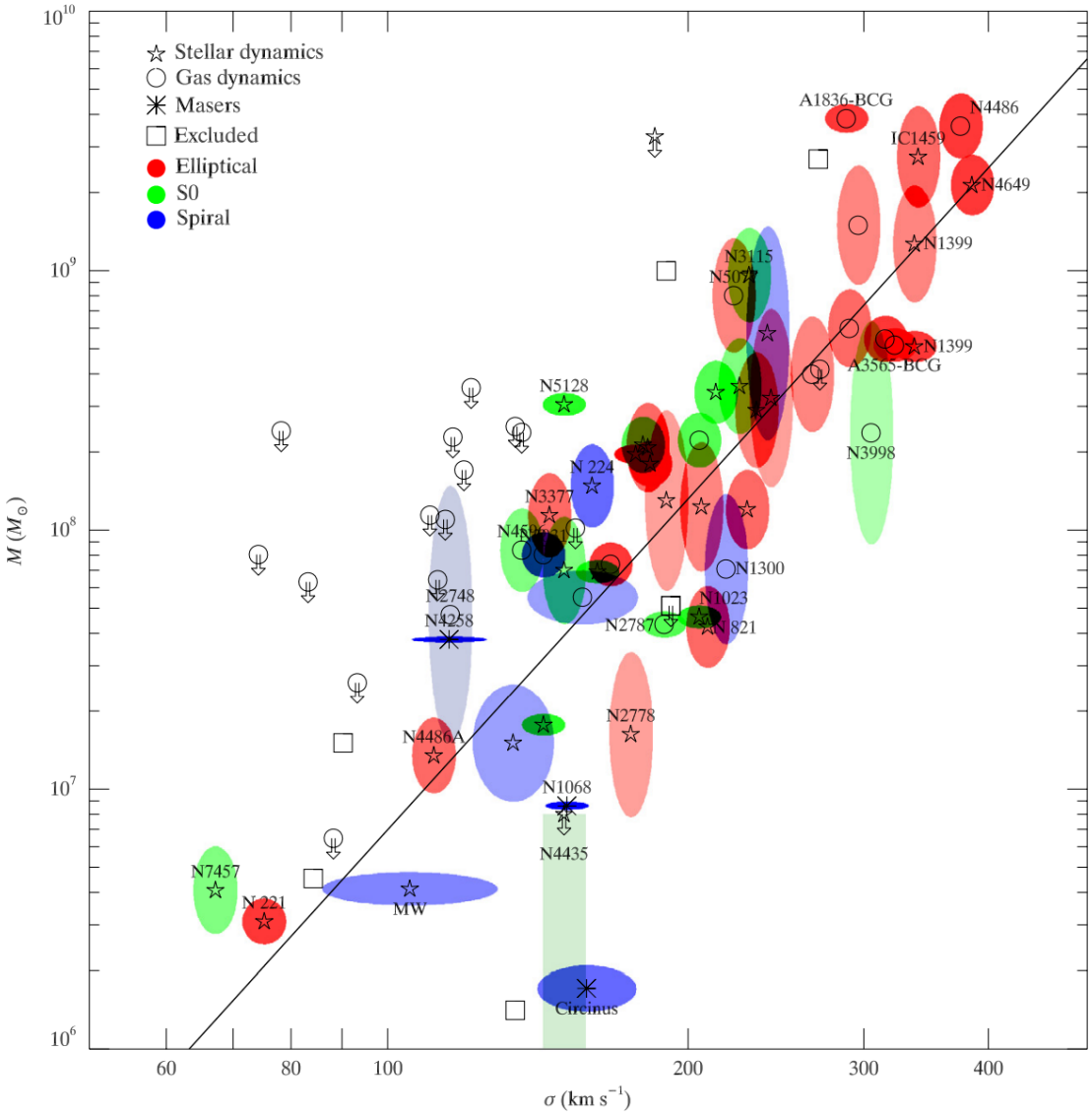

Figure 1.4. The $M\sigma$ relation for galaxies with dynamical measurements. Taken from Gültekin et al. (2009). The symbol indicates the method of BH mass measurement: stellar dynamical (pentagrams), gas dynamical (circles), masers (asterisks). Arrows indicate $3\sigma_{68}$ upper limits to BH mass. If the $3\sigma_{68}$ limit is not available, we plot it at 3 times the $1\sigma_{68}$ or at 1.5 times the $2\sigma_{68}$ limits. For clarity, we only plot error boxes for upper limits that are close to or below the best-fit relation. The color of the error ellipse indicates the Hubble type of the host galaxy: elliptical (red), S0 (green), and spiral (blue). The saturation of the colors in the error ellipses or boxes is inversely proportional to the area of the ellipse or box. Squares are galaxies that we do not include in our fit. The line is the best fit relation to the full sample: $M_{BH} = 10^{8.12}\ M\odot\ (\sigma/200\ \mathrm{km\ s}^1)^{4.24}$. The mass uncertainty for NGC 4258 has been plotted much larger than its actual value so that it will show on this plot. For clarity, we omit labels of some galaxies in crowded regions. Note: σ_{68} is the 68%-confidence level, to distinguish it from velocity dispersion (see Gültekin et al. 2009).

studied ones (Ferrarese & Merritt 2000). It demonstrates how the mass of the black hole is tightly correlated with the stellar velocity dispersion ($\sigma_\star$) of the galactic bulge. The relatively small scatter in this relation suggests a fundamental connection between SMBH growth and the dynamics of galactic bulges. Either both have common growth drivers or share a regulatory mechanism. Other scaling relations include the $M_{\rm BH} - M_{\rm bulge}$ and $M_{\rm BH} - L_{\rm bulge}$ (connecting the mass and luminosity of the galaxy bulge to the mass of its SMBH; Gültekin et al. 2009), although these typically show larger scatter.

These have been interpreted as evidence of coevolution between SMBHs and their host galaxies (see also D'Onofrio et al. 2021, specifically Sections 13 and 14). In a picture of multiple nuclear activity phases, the SMBHs' growth energy release over their lifetime can exceed the binding energy of their host galaxy by several factors (Fabian 2012). This energy injection may be sufficient to establish a regulatory channel linking host galaxy properties to the masses of their SMBHs. Indeed, more evidence is evident when examining the historical BH accretion and SFR densities (see below).

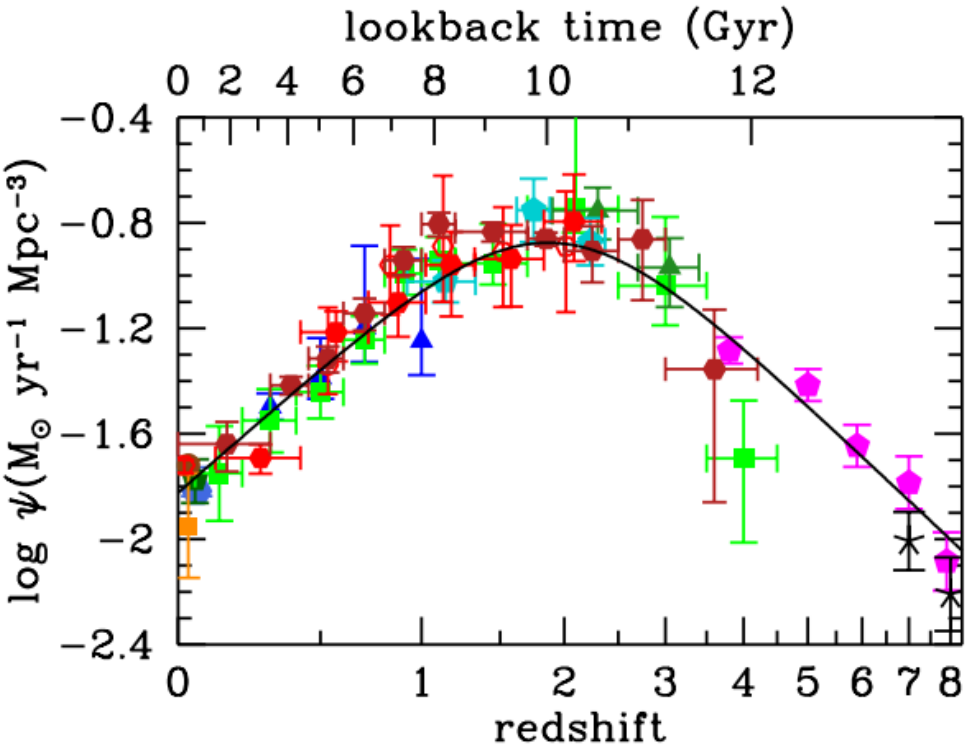

Figure 1.5. The history of cosmic star formation from FUV+IR rest-frame measurements. This plot is taken from Figure 9c of Madau & Dickinson (2014), and its caption has been adapted. Each point corresponds to data from either IR measurements (represented by red, dark red, or orange colors) or from the UV (represented by any other color). The solid curve plots the best-fit of the SFR density. See Madau & Dickinson (2014) for the details.

Cosmic evolution of star formation and AGN activity

More relevant evidence comes from comparing the AGN activity history, as traced by the accretion rate density, with that from star formation. The star formation rate density history of the Universe, e.g., as discussed in Madau & Dickinson (2014), is shown in Figure 1.5. Here, the y-axis represents the star formation rate density, and the x-axis represents the behavior as a function of lookback time. It can be seen that most of the star formation in the universe has occurred at the so-called cosmic noon ($z \sim 2$), where it reaches its peak. Notably, if we trace the AGN accreting power estimated by the SMBH accretion rate density and study this as a function of lookback time, its behavior follows that of star formation. This is shown in Figure 1.6. It follows that SMBHs and galaxies have a similar efficiency history, suggesting that they regulate each other over cosmic time. It remains unknown whether AGN activity regulates star formation or if SMBH growth is itself a product of a process that also triggers starbursts.

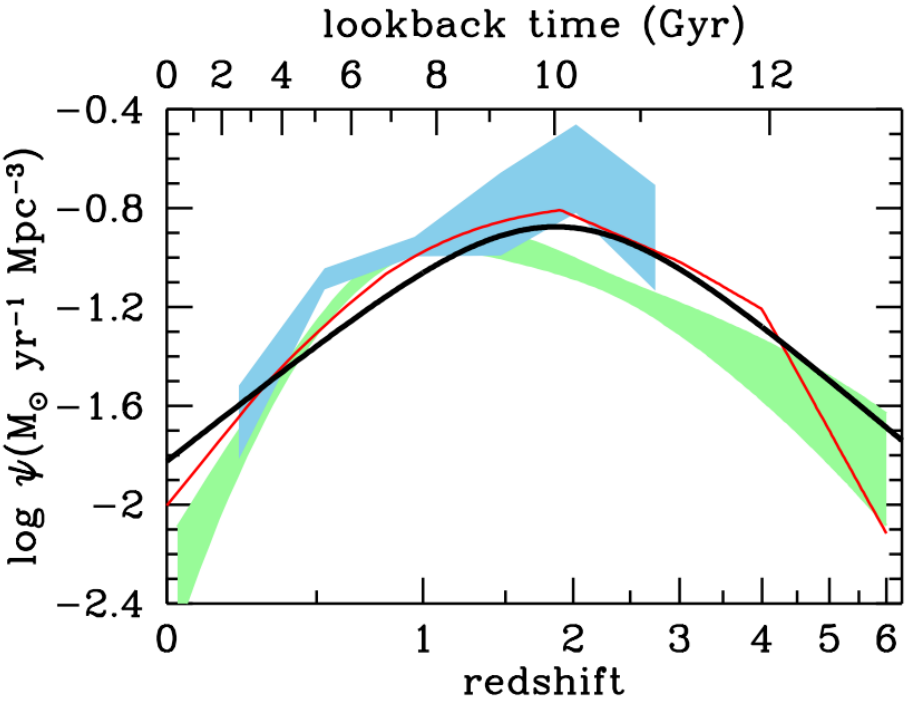

Figure 1.6. Comparison of the best-fit star-formation history with the massive black hole accretion history. Taken from Madau & Dickinson (2014). The black solid curve represents the same best-fit line shown in Figure 1.5. The light blue and light green shaded regions display the black hole accretion rate history estimated from two independent studies using X-rays, and the red line represents the same using infrared observations.

During cosmic noon ($z \sim 2$) and before, fascinating AGN activity is ubiquitous, finding clear kpc-scale gas ejecta or outflows (see several examples in Davies et al. 2024). Today's universe is a much peaceful place, where powerful AGN are not very common. However, outflows in such systems are routinely observed (e.g., Baron &

Netzer 2019; Mullaney et al. 2013; Woo et al. 2016). Moreover, the realization that the outflow properties correlate with the properties of their radio emission (Jarvis et al. 2021, 2019; Molyneux, S. J. et al. 2019), especially in the presence of compact radio sources, has been interpreted as a mechanism of AGN feedback in low-redshift targets (Girdhar et al. 2022). We emphasize that the discussion in this thesis will focus on AGN in the local universe ($z < 0.15$). Our study is inspired by some of the works mentioned above, which find an important connection between outflows and radio emission. We introduce a crucial component to our study: integral field spectroscopy.

1.3.3 Galaxies and AGN in the context of IFS

Non-active galaxies

Galaxies follow tight correlations in fundamental properties (see a review in D'Onofrio et al. 2021). For example, star-forming galaxies typically obey a tight relation in the stellar mass versus star formation rate (SFR) plane, which has been attributed to the result of a balance between gas accretion, star formation, and feedback processes that regulate galaxy growth over cosmic timescales (Lilly et al. 2013). This correlation is typically known as the galaxy's star-forming main sequence (SFMS), and it remarkably holds over several decades of stellar mass and across multiple redshifts (e.g., Daddi et al. 2022; Thorne et al. 2021). Similarly, the so-called mass-metallicity relation (MZR), as observed by Tremonti et al. (2004), establishes a tight correlation between stellar mass and the chemical evolution of galaxies, indicating a connection between star formation, metal loss, and gas recycling from galactic outflows and inflows.

These behaviors have been typically studied, focusing on the central regions of galaxies. Although aperture effects have been accurately addressed in foundational studies, it is expected that such relations hold in a resolved manner. This was recently possible, thanks to the advent of large IFS surveys. Sánchez (2020) tested both the SFMS and the MZR and remarkably showed that these scaling relations hold in resolved counterparts. To achieve this, they used radial profiles averaging properties in annuli normalized by the effective radius of galaxies. We emphasize that this is an active technique that we use across the analysis in the papers.

Active galaxies

Studies with large samples of galaxies with IFS are also now possible for AGN galaxies. A particular interest in this topic is to understand whether the central activity can have an impact on the host galaxy. For example, kpc-scale outflows have been ubiquitously found in galaxies hosting AGN. While this was already known using a limited number of objects (e.g., McElroy et al. 2015) at low-redshift sources, observations of the large-scale effect of an AGN in its host galaxy in a large sample of IFS data have recently become possible. For example, in a pioneering study, Wylezalek et al. (2020) showed

that AGN have higher velocity dispersion warm ionized gas than their non-AGN counterparts, even at off-nuclear distances (see also Deconto-Machado et al. 2022).

In the context of large surveys, the latter has typically been tested in optically selected AGN. A more comprehensive picture, utilizing a multi-wavelength approach to trace AGN signatures (see the discussion in Section 1.1.1), is still required. This is one of the main motivations of the analysis pursued in Paper I. Important insights about feedback using IFS can also be gained by analyzing outflow signatures together with other resolved properties. For example, Lammers et al. (2023) found that AGN can present similar global SFRs as their controls, but centrally suppressed SFRs when looking at their resolved behavior. Therefore, Paper II and Paper III in our work focus on expanding the analysis beyond gas kinematics to galaxy-wide properties, providing a comprehensive picture of the AGN's influence in their host galaxies.

1.4 Galaxies in the context of emission line ratios

Emission lines provide relevant information about the physical conditions of the interstellar medium (ISM) in our Galaxy and extragalactic objects. Typical nebular emission in the Milky Way arises from H II regions or supernova remnants (SNRs). While H II regions are regions of ionized hydrogen gas around young massive stars where ultraviolet radiation ionizes the surrounding material (Shields 1990), SNRs are shells of gas and dust expanding due to a supernova explosion, where shock waves heat, accelerate, and ionize the ISM (Vink 2004). Observational and theoretical studies of these objects provide valuable tools for studying ionization mechanisms, chemical composition, and even kinematic properties of the ISM (e.g., Dopita et al. 2000).

In the context of extragalactic astrophysics, and particularly relevant to this thesis, AGN typically present distinguishable ionization conditions compared to those found in typical star-forming galaxies. For example, Baldwin et al. (1981) showed that emission-line ratios (e.g., [O III]/Hβ) can provide hints of the main excitation mechanism of the observed spectrum. Later, by comparing photoionization models with observations, Veilleux & Osterbrock (1987) showed that these emission line ratios have the potential to identify AGN. Emission line ratios provide the most useful diagnostics in this context. Ratios of specifically close emission lines, such as [O III]/Hβ, [N II]/Hα, [S II]/Hα, [O I]/Hα, are used to avoid aperture corrections, flux calibration issues, and minimize reddening effects (Baldwin et al. 1981).

This line of analysis is often referred to as BPT diagrams and has become a standard method for classifying galaxies based on their dominant ionization source. Kewley et al. (2001a) and Kewley et al. (2006) have combined empirically motivated demarcation lines based on photoionization models to distinguish between star-forming galaxies, AGNs, and a bridging population referred to as composite or transition objects. A substantial fraction of galaxies, however, are found to lie in the region associated with low-ionization nuclear emission-line regions (LINERs Heckman 1980).

While initially thought to be primarily AGN-driven (e.g., Ho 1999), alternative mechanisms, such as shocks (Dopita & Sutherland 1995) or ionization by hot evolved stars (Stasińska et al. 2008), have also been proposed (Singh et al. 2013a). Although careful studies have proposed ways to minimize these selection effects, such as selecting true AGN from LINERs (Cid Fernandes et al. 2011), the degeneracies in optical diagnostics sometimes make it difficult to unambiguously identify the true ionization source based solely on optical diagnostics.

In the Milky Way, we can find a diverse range of ionizing sources. This is also true for nearby galaxies. It is therefore completely natural to note that galaxies can have broad gradients of excitation mechanisms in their ISM. However, most big surveys gathering spectroscopic data, SDSS (II/III), are based on (single) fiber-fed observations that capture only the central few kiloparsecs of a galaxy. While this is useful for capturing the dominant integrated nature of a large number of galaxies, critical details are often missed. As a result, some galaxies with a very optically compact AGN might have their signature washed out by star-forming regions in the integrated spectrum.

Aware of these challenges, the astronomical community has increasingly shifted toward large spatially resolved spectroscopic surveys (see Section 1.2). Motivated by the availability of MaNGA survey data, part of our initial work has investigated the aperture effects on optical classification.

1.4.1 Optical diagnostics in flexible apertures

Here, we provide a summary of our work, as carried out in Albán & Wylezalek (2023). It follows a BPT diagnostic of the 10 000 MaNGA galaxies, and it has a special focus on AGN classification. A key motivation is to investigate how the choice of aperture size influences AGN classification. Thus, the classification employs a novel approach, where instead of selecting a fixed aperture for all galaxies, it attempts to produce a flexible aperture selection for the classification. It provides the emission line ratios of each source as a function of sixty different apertures: 20 kpc steps, 20 effective radius (R_{eff}) steps, and 20 steps in arcseconds. We mainly use the [N II] and the [S II] BPT diagrams together with requiring an Hα equivalent width (EW(Hα)) to be greater than 3. The latter has been motivated by the observation of a reliable sample of Seyfert, where they typically have EW($H\alpha$) $>$ 3.0 Å (Cid Fernandes et al. 2011).

The effect of how aperture size changes the classification of a galaxy using the [N II]-BPT diagram is shown in the bottom-right of Figure 1.7. Note that this is not a radial profile, but a cumulative integrated (at different aperture sizes) emission line ratio. While one galaxy (10218-12703) remains persistently an AGN at all apertures, the two remaining galaxies are observed to cross demarcation lines. The color in each of the symbols marks the increase in the aperture size (from blue to red). This demonstrates that the observed line ratios are not static properties, but scale-dependent. To quantify this effect, we look at how the number of classified AGN changes with in-

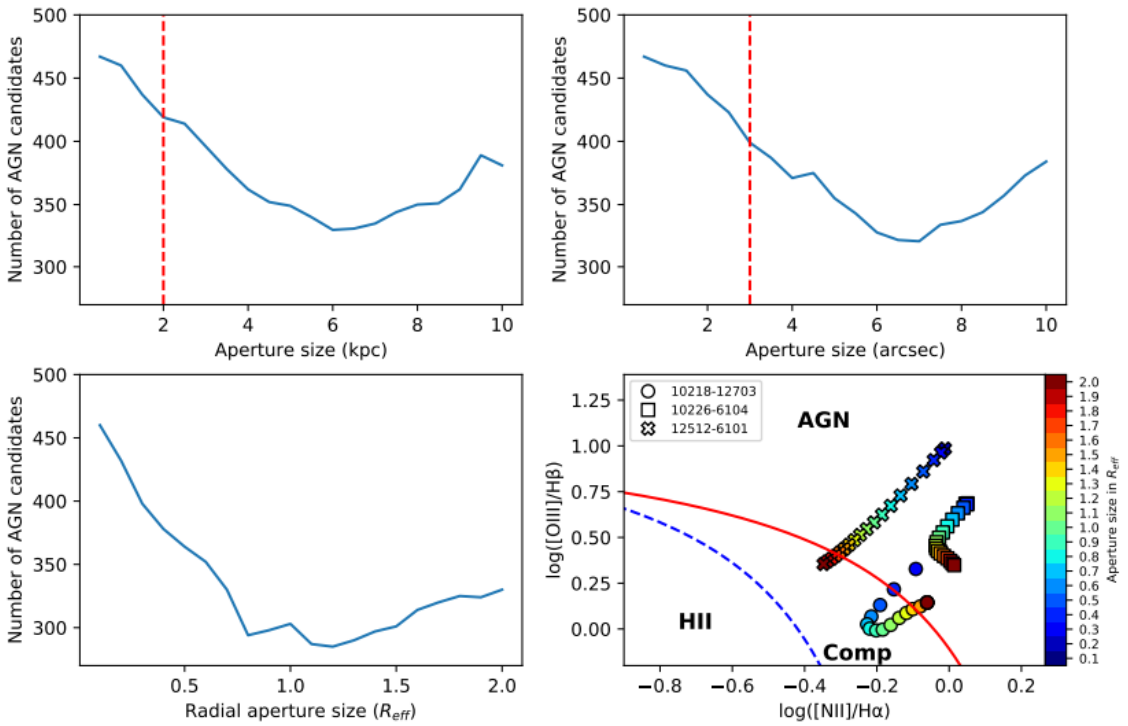

Figure 1.7. Variation in AGN classification with different aperture sizes. The plots taken from Albán & Wylezalek (2023) and we provide a modified caption: The y-axis in the top plots and the bottom left plot shows the number of galaxies classified as AGN (solid blue line) selected based on different aperture sizes and using different units. The selection is made following the BPT selection algorithm described in Section 1.4, excluding the [O I]/Hα BPT diagram. In the top left plot, the kiloparsec aperture increases in steps of 0.5 kpc (in diameter). In the top right plot, the arcsecond aperture increases in steps of 0.5 (in diameter). In the bottom left plot, the effective radius aperture increases in steps of 0.1 R_{eff} (in radius). The red (vertical-dashed) line in the top panels corresponds to the apertures used for the comparisons in Albán & Wylezalek (2023). In the bottom right plot, we show how the flux ratios in one BPT diagram change as a function of the aperture. This is done for three individual galaxies illustrated with different symbols (see the legend for their corresponding MaNGA-IDs). Each symbol is filled with a specific color that corresponds to the size of its aperture. In the bottom right plot, we also include the empirical division lines that will give each target a specific classification (e.g., AGN-like galaxy, composite object, or HII-star forming galaxies): red lines correspond to Kewley et al. (2001a), and the blue dashed line on the left plot corresponds to Kauffmann et al. (2003).

creasing aperture size. Given the central origin of AGN, it is expected that larger apertures, which average larger galactic regions dominated by star-forming processes, would dilute the AGN signatures (even when the galaxy harbors an AGN). We observe this behavior in the inner annuli steps (e.g., 1 R_{eff} <). However, we note that increasing the aperture size beyond this point increases the number of detected AGN (see the behavior in each line-plot panel in Figure 1.7).

Given that diffuse ionized gas (DIG; Haffner et al. 2009) can mimic AGN-like

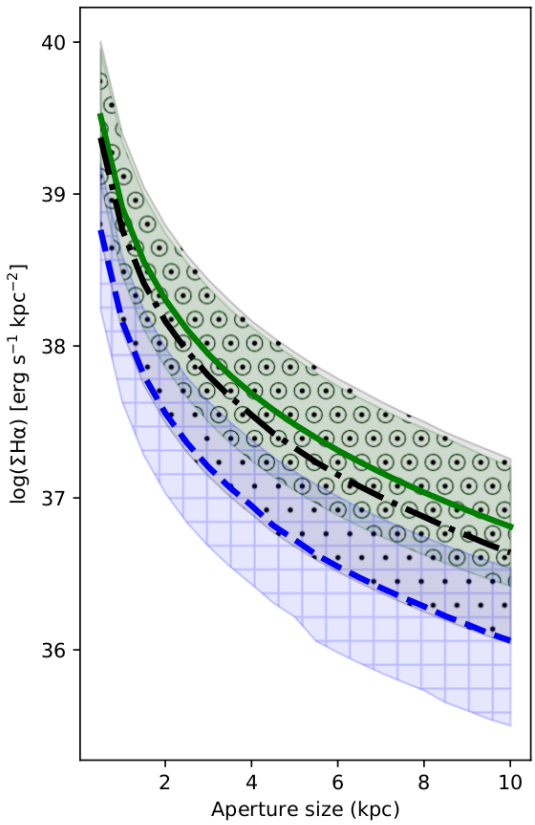

Figure 1.8. Average radial profiles of the Hα surface brightness stacked according to specific AGN candidates. The shaded regions correspond to the 16th and 84th percentiles of each stacked radial profile. The solid green line corresponds to the AGN selected using a 2 kpc circular aperture, and hollow circles hatch its shaded area. The black dash-dot line corresponds to the AGN selected by an aperture of 10 kpc, and dots hatch its shaded area. Finally, the blue dashed line corresponds to the AGNs selected by the 10 kpc aperture but excludes the AGNs selected by the 2 kpc aperture. The last line has a shaded area hatched by hollow squares. Taken from Albán & Wylezalek (2023).

emission line ratios (Zhang et al. 2017) due to their low Hα surface brightness, we study this parameter as a function of kpc aperture size (see Figure 1.8). AGN classified with a 10 kpc aperture (black dash-dotted line) display a comparable but lower surface brightness radial profile than the 2 kpc-classified AGN population (green solid line). If we exclude the AGN classified using the 2 kpc aperture from the ones classified with a 10 kpc (blue dashed line), this new population displays relatively low central surface brightness ($\Sigma_{H\alpha} < 10^{39}$ erg s^{-1}kpc^{-2}). We find that using large apertures beyond a specific aperture radius for classification purposes leads to significant contamination from DIG, resulting in a sharp increase in the number of galaxies falsely identified as LINERs or Seyferts. This contamination is traced through declining Hα surface brightness profiles, confirming that large apertures incorporate emission from extended, non-nuclear regions that mimic AGN-like signatures.

While the EW(Hα)>3.0 Å criterion alleviates part of the BPT classification caveats,

we note that this strict cut can exclude low accreting SMBH (i.e., low luminous AGN). Therefore, optical AGN selection techniques can be refined and obtain a more coherent picture by complementing it with multiwavelength observations (see Section 1.6). Lastly, IFS studies have broadened the research status of optical AGN classification. For example, using a per-spaxel classification in ∼2700 MaNGA galaxies, Wylezalek et al. (2018) found a population of off-central AGN-like signatures that would not have been picked up by studies using single fiber spectroscopy. Such a population could be explained by a centrally obscured AGN with its ionization more easily observed in its outskirts, an offset AGN due to a merger, or light echoes of ionization from a previous AGN. The latter idea serves as motivation for the research presented in the first paper (see Chapter 2), which combines multiple selection techniques, provided that we start with a careful optical classification.

1.5 The local radio universe

In the context of ground-based observations, unlike other electromagnetic spectrum bands, our atmosphere is transparent to several decades of radio frequencies (see Figure TBA). Radio emission spans several orders of magnitude, from 10 MHz to 1 THz (30 m to 0.3 mm). Our planet's atmosphere sets a natural lower limit by reflecting frequencies below ∼10 MHz. Emissions at radio frequencies are of essential interest due to their ability to be less affected by interstellar dust or gas compared to shorter wavelength emission (Condon & Ransom 2016). This is because radio wavelengths are much larger than typical dust grain sizes in the ISM, making dust scattering negligible. In our Galaxy, the major contributors to radio emission include supernova remnants, some stellar objects, star-forming regions, and the galactic center. On the other side, extragalactic objects dominate the radio sky above and below the Galactic plane.

Radio emission can originate from two main physical processes: free-free radiation and synchrotron radiation. The former is usually referred to as thermal radio emission, while the latter is referred to as non-thermal. This distinction mainly arises due to radiation originating either directly from stellar processes (thermal) or indirectly. As a result, we can leverage these processes to create powerful diagnostics. Below, we describe these two processes (the summary below is based on Condon & Ransom 2016), which can be followed together with the thermal radiation spectrum from dust in Figure 1.10.

- Free-free emission: comes from the interaction of a charged particle and the electric field of another charged particle. It is often referred to as Bremsstrahlung because the interacting particle decelerates, converting its kinetic energy into radiation. Free-free radiation is often also referred to as thermal radiation, because it primarily originates from plasma in local thermodynamic equilibrium (LTE), where particles have a Maxwellian velocity distribution. Free-free emis-

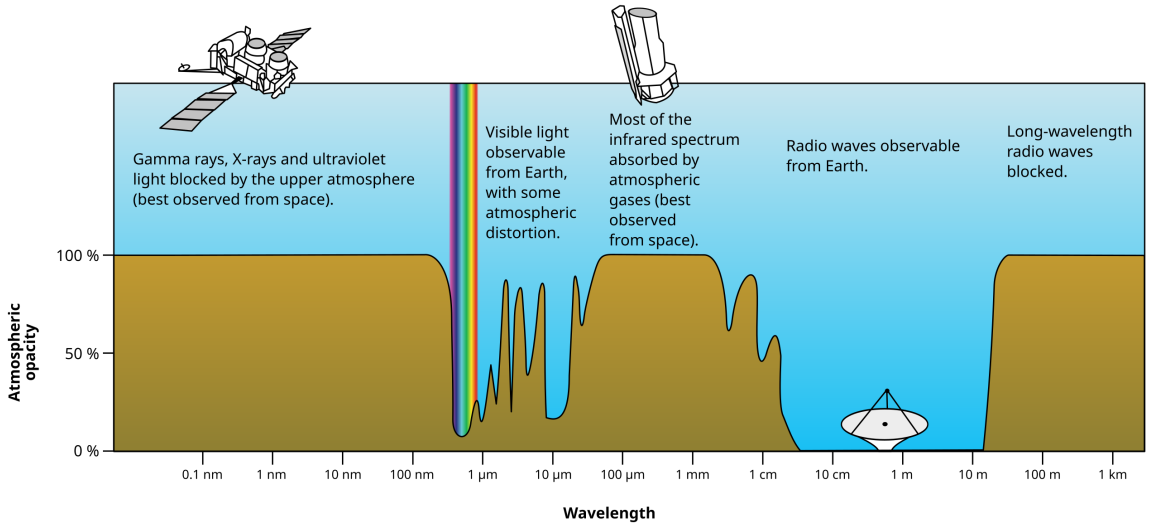

Figure 1.9. Opacity of the Earth's atmosphere. A representation of how opaque our atmosphere is at each electromagnetic radiation. Note that radio is advantageous in terms of ground-based telescopes. Credits from NASA.

sion is strongest at frequencies between 1 and 100 GHz, overlapping with the far-infrared regime.

- Synchrotron radiation: originates from relativistic electrons moving through a magnetic field. The Lorentz force is perpendicular to both the velocity of the charged particle and the magnetic field. This causes the particle to follow a curved trajectory. It follows the form of a power law, which can extend from 0.1 to 10 GHz. It is often referred to as non-thermal emission.

Charged particles are responsible for both types of emission, but electrons are especially significant in contributing to them. This is because the power radiated by a particle, both in synchrotron and free-free, depends on the particle's acceleration, which inversely depends on the mass. Electrons are about 2000 times lighter than protons.

Outside the Milky Way, the primary sources of radio emission are other galaxies with usually active star formation and AGN, the latter of which may be characterized by powerful jets. Diffuse synchrotron emission can also arise in the circumgalactic environments of galaxy clusters and groups (van Weeren et al. 2019). Interestingly, a population of galaxies exists with faint, extended radio structures that seem to host faint or aged radio emission. They can present lobes or jet-like structures without a central core. These objects might represent remnants from AGN echoes (Morganti 2021), a key view from the AGN life cycle.

1.5.1 Star-forming galaxies

The emission from regions with recent star formation is dominated by massive ($M > 8M\odot$), short-lived stars. With high amounts of UV radiation, they ionize their sur-

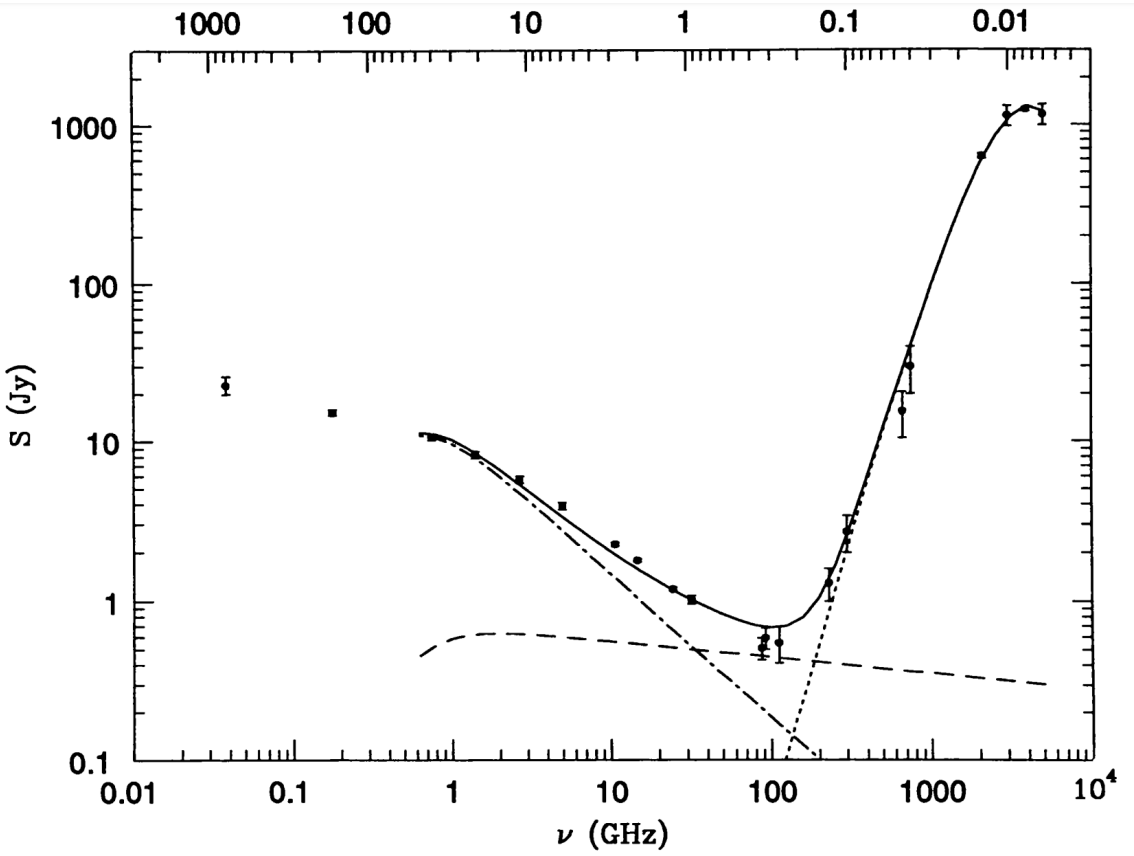

Figure 1.10. Taken from Condon (1992). **The observed radio/FIR spectrum of M82** (Carlstrom & Kronberg 1991; Klein et al. 1988) is the sum (solid line) of synchrotron (dot-dash line), free-free (dashed line), and dust (dotted line) components. The H II regions in this bright starburst galaxy start to become opaque below $\nu \sim 1$ GHz, reducing both the free-free and synchrotron flux densities. The free-free component is largest only in the poorly observed frequency range 30200 GHz. Thermal reradiation from $T \sim 45$ K dust with opacity proportional to $\nu^{1.5}$ swamps the radio emission at higher frequencies. Lower abscissa: frequency (GHz). Upper abscissa: wavelength (cm). Ordinate: flux density (Jy).

rounding gas, giving rise to what we know as H II regions. While strong recombination lines (such as Balmer emission lines) are typically observed in these regions in the optical, in radio, thermal emission processes are the primary contributors to the continuum. This emission is often referred to as free-free (as described above) emission and serves as a common tracer to characterize star-forming regions.

Free-free and synchrotron emission happen simultaneously in active regions of star formation. Therefore, both can be used as tracers of the star formation rate in galaxies. As both trace processes of the exact origin are similar in timescales, this establishes a known correlation known as the far-infrared-radio correlation (FIRC). This empirical relation indicates that the radio continuum luminosity of star-forming galaxies closely correlates with their far-infrared emission, providing a powerful diagnostic for estimating star-formation rates. This correlation is remarkably tight across a wide range of redshifts and star formation rates.

Yet, deviations from the FIRC can be observed, particularly in galaxies hosting an AGN. Here, additional radio emission from the central engine can elevate the radio luminosity beyond what is expected from star formation alone.

1.5.2 Active galaxies

The radio frequencies of AGN are dominated by emission from synchrotron radiation. Unlike in star-forming galaxies, the population of relativistic electrons in AGN originates from particles accelerated through processes linked to accretion into the SMBH (see a detailed explanation in Chapter 5 from Condon & Ransom 2016). This can give rise to compact regions characterized by strong radio emission. In powerful AGN (e.g., Cyg A; see Figure 1 in Ogle et al. 2025), these cores are often accompanied by highly collimated jets that extend up to hundreds of kiloparsecs, sometimes capable of influencing the circumgalactic or intergalactic medium. Some galaxies exhibit extended lobes or jet fragments but lack an active radio core. The absence of core emission implies that accretion onto the SMBH has ceased or significantly dropped, leaving behind fossil radio emission (Morganti 2021). These relics provide evidence of a duty cycle component in the evolution of AGN and galaxies.

Notably, not all AGNs exhibit strong radio emission. Many so-called radio-quiet sources display weak or undetectable AGN-related radio features (Padovani 2016). Although these AGN may still contribute to outflows or winds, their radio emission is often difficult to disentangle from star formation contributions (Panessa et al. 2019). Moreover, outflows can serve as a source of synchrotron emission (e.g., Ishibashi & Courvoisier 2011; Zakamska et al. 2016b), as they can accelerate particles in shocks (Dopita & Sutherland 1995). These energized electrons produce diffuse synchrotron radio emission distinct from classic jets (see an example in Xia et al. 2025, ; recently accepted paper). Although this shock-driven radio emission offers valuable insights into the impact of AGNs, separating it from star formation-related radio signals often requires detailed, high-resolution multiwavelength observations.

1.6 AGNs Through Multiple Lenses

The different AGN structures, obscuration effects, and the AGN variability component (see Section 1.3.2) all contribute to the fact that there is no universal tracer for identifying AGN. Indeed, decades of studies of AGN galaxies have taught us that each selection technique comes with its flaws. For example, optical selection techniques, which are perhaps one of the most used and studied ones, can easily miss strongly obscured AGN (among other limitations). Below, we describe selection techniques, specifically focusing on some of those used in this thesis. We note that our summary of selection techniques is primarily focused on methods applied in large-scale surveys.

1.6.1 Optical diagnostics

We gave special attention to optical emission line ratio diagnostics in Section 1.4 to highlight our work. We refer to this section for a comprehensive overview of the use of BPT diagnostics, which can be used to classify AGN. In this section, we discuss another common optical AGN tracer: broad Balmer lines, a typical signature from the BLR (as described in Section 1.3.2). This tracer gives strong evidence of the presence of an AGN. Furthermore, emission lines from the BLR provide a tool for estimating the mass of the SMBH using the single-epoch mass estimate (Feng et al. 2014).

1.6.2 Radio selection techniques

In section 1.5, we have briefly summarized a perspective of the local radio universe. As mentioned, synchrotron emission is a significant component to consider when searching for AGN. Early radio AGN selection techniques were solely based on the detection of jets and lobes in galaxies. With the advent of large radio surveys and increased depth, this approach has undergone significant changes. Given that, in general, the radio sky is dominated by star-forming galaxies and AGN, a straightforward technique is to use methods to distinguish them.

Using the Faint Images of the Radio Sky at Twenty Centimeters (FIRST; Becker et al. 1995) and the NRAO VLA Sky Survey (Condon et al. 1998) were pioneers in large-scale radio classification. Best et al. (2005) used FIRST and NVSS, in conjunction with optical classification, to identify radio-loud AGN candidates. Later refined in Best & Heckman (2012), this selection technique combines BPT diagnostics, a comparison of radio luminosity to Hα luminosity (to identify radio excesses with star formation), and a comparison of stellar population ages to radio. All the latter diagnostics can separate star-forming galaxies from AGN.

Such classification can miss the radio-quiet AGN population. However, a commonly used and more flexible technique involves using a known SFR rate tracer in conjunction with an independent technique to compare it to the radio luminosity, as both would be expected to be correlated (see 1.5). An excess in the radio when compared to the SFR can be interpreted as the presence of an AGN (Kauffmann et al. 2008). The latter is a method that we actively employ in Paper I, and similar studies have also implemented it (Suresh & Blanton 2024). We note, however, that compact cores that do not show radio excess can still have an AGN in their unresolved emission (Morabito et al. 2025).

1.6.3 Mid Infrared diagnostics

Many AGN remain hidden to optical surveys due to dust obscuration, a central feature of the AGN unified model (see Section 1.3.2). Radiation absorbed by the dusty torus surrounding the AGN is re-emitted in the infrared, making it distinguishable from star-forming galaxies. The infrared displays a broad spectral band. In this section,

we focus on the mid-Infrared (MIR) region. It not only provides a way around this limitation, but it is also the technique with which we were able to obtain the most significant number of galaxies. WISE has imaged the whole sky several times in four mid-infrared bands: 3.4 μm, 4.6 μm, 12 μm, and 22 μm. For this purpose, we specifically use the Wide-field Infrared Survey Explorer (WISE; Wright 2006). MIR AGN selection techniques broadly rely on color-color diagrams (see Assef et al. 2018).

Other selection techniques

Here, we outline a few additional selection techniques, focusing primarily on those used throughout our papers as complements. We do not widely use them in our work because they are either not available (having not yet been observed in any survey) or are redundant for our purposes.

- AGN variability (see Hagen et al. 2024): Given that most high-energy AGN processes happen in extremely compact regions, a change in their behavior can result in variations of luminosity or line widths. Another, and perhaps more extreme category of this behavior is the Changing Look AGN (e.g., Ricci & Trakhtenbrot 2023).

- X-rays: the dominant contributor to the X-ray extragalactic sky is AGN. Nevertheless, in general, to distinguish between different X-ray-dominated sources, flux ratios between X-ray and optical emission have been used (e.g., Brusa et al. 2003).

1.7 Thesis overview

The Universe whispers clues about how galaxies evolve. While observations suggest that galaxy evolution is critically shaped by how SMBHs grow, simulations fail to produce key observables of today's Universe. The latter points toward a feedback mechanism resulting from the SMBH growth. However, finding clear and statistical samples where this effect can be constrained is an active field of research. A growing perspective is that part of the effect of AGN feedback is not immediate; instead, its influence could accumulate through repeated episodes. It is well accepted that AGN activity happens many times in a galaxy's life, but the details of how this happens remain an open question.

Paper I, Paper II, and Paper III aim to address or gain insight into the problem described in the preceding paragraph. Broadly, they drive a strategic approach with the following ingredients: multiple AGN selection techniques, spatially resolved spectroscopy, an automated routine to find ionized outflows, and a careful comparison algorithm to produce control samples (see also Section 1.1.1).

Initial stages of our work are part of Albán & Wylezalek 2023 (summarized in Section 1.4). While this work exploits and optimizes optical diagnostics, it sets the

path of Paper I. The first goal of Paper I is to combine optical with multiple AGN selection techniques, while the second part focuses on the search for outflows. A relevant conclusion from this paper is that selection techniques appear to identify not only different physics but also AGN at various stages of their duty cycle. Our results, which appear to be driven by the radio properties of the AGN, motivate us to conduct follow-up research.

Therefore, continuing in this line, Paper I branches into two main topics. First, given that part of the analysis focuses on characterizing the behavior of AGN that were only picked up by one selection technique, a parallel work, described in Paper II, was done to study the population of AGN that have simultaneous detection (especially in radio and optical). The second path focuses on the AGN duty cycle component based on what we have learned about radio. To do so, we search for AGN-like or outflow signatures in galaxies that evade being AGN in every selection technique. In other words, Paper III searches for fossil outflows: evidence of past AGN activity in galaxies that appear non-active today.

Chapter

2

Mapping AGN winds: A connection between radio-mode AGNs and the AGN feedback cycle

Authors: M. Albán[1], D. Wylezalek[1], J. M. Comerford[2], J. E. Greene[3] and R. A. Riffel[4,5]

[1]Zentrum für Astronomie der Universität Heidelberg, Astronomisches Rechen-Institut, Mönchhofstr, 12-14 69120 Heidelberg, Germany

[2]University of Colorado Boulder, 2000 Colorado Avenue, Boulder, CO 80309, USA

[3]Department of Astrophysical Sciences, Princeton University, 4 Ivy Lane, Princeton, NJ 08544, USA

[4]Departamento de Física, Centro de Ciências Naturais e Exatas, Universidade Federal de Santa Maria, 97105-900, Santa Maria, RS, Brazil

[5]Laboratorio Interinstitucional de e-Astronomia - LIneA, Rua Gal. José Cristino 77, Rio de Janeiro, RJ - 20921-400, Brazil

Published in A&A, 691, A124 (2024)

Marco Albán is the main author of this paper. Marco Albán produced all the figures and wrote all the text. This paper originated from a project proposed by Prof. Dr. Dominika Wylezalek and was shaped by Marco Albán. Dominika Wylezalek provided significant and continuous feedback throughout the project, and also suggested rewording to enhance the narrative text. Rogemar A. Riffel, Jenny Greene, and Julie Comerford offered essential scientific input, particularly during the final stages of the publication process. Their detailed comments and suggestions significantly improved the clarity, structure, and depth of the paper, reinforcing its conclusions. The collaboration and guidance of each co-author led to the successful completion of this work.

ABSTRACT

We present a kinematic analysis based on the large integral field spectroscopy (IFS) dataset of SDSS-IV MaNGA (Sloan Digital Sky Survey / Mapping Nearby Galaxies at Apache Point Observatory; $\sim$ 10.000 galaxies). We have compiled a diverse sample of 594 unique active galactic nuclei (AGNs), identified through a variety of independent selection techniques, encompassing radio (1.4 GHz) observations, optical emission-line diagnostics (BPT), broad Balmer emission lines, mid-infrared colors, and hard X-ray emission. We investigated how ionized gas kinematics behave in these different AGN populations through stacked radial profiles of the [OIII] 5007 emission-line width across each AGN population. We contrasted AGN populations against each other (and non-AGN galaxies) by matching samples by stellar mass, [OIII] 5007 luminosity, morphology, and redshift. We find similar kinematics between AGNs selected by BPT diagnostics compared to broad-line-selected AGNs. We also identify a population of non-AGNs with similar radial profiles as AGNs, indicative of the presence of remnant outflows (or fossil outflows) of past AGN activity. We find that purely radio-selected AGNs display enhanced ionized gas line widths across all radii. This suggests that our radio-selection technique is sensitive to a population in which AGN-driven kinematic perturbations have been active for longer durations (potentially due to recurrent activity) than in purely optically selected AGNs. This connection between radio activity and extended ionized gas outflow signatures is consistent with recent evidence that suggests radio emission (expected to be diffuse) originated due to shocks from outflows. We conclude that different selection techniques can trace different AGN populations not only in terms of energetics but also in terms of AGN evolutionary stages. Our results are important in the context of the AGN duty cycle and highlight integral field unit data's potential to deepen our knowledge of AGNs and galaxy evolution.

Key words. Catalogs – galaxies: active

2.1 Introduction

Active galactic nuclei (AGNs) have become a common element in galaxy evolution studies (Heckman & Best 2014) and a fundamental engine for supermassive black hole (SMBH) growth (Alexander & Hickox 2012). Observational studies have suggested the connection between SMBHs and their host galaxies, finding significant empirical correlations between them (Kormendy & Ho 2013). Specifically, the mass of the SMBH has been seen to correlate with fundamental galaxy properties such as the bulge luminosity (Ferrarese & Merritt 2000) and the bulge velocity dispersion (Marconi & Hunt 2003). Further evidence has shown that the star formation rate history in galaxies peaks at $z \sim 2$, exactly where the black hole accretion history (related to AGN activity) is at its height (Aird et al. 2015; Madau & Dickinson 2014). This suggests an interaction (and coevolution) between the AGN and the interstellar medium (ISM) of

its host galaxy (Fabian 2012; Morganti 2017b), known as AGN feedback. Indeed, the released energy required for such a massive black hole to have grown is comparable to or greater than the binding energy of the host galaxy itself (Silk & Rees 1998), placing AGNs in the spotlight as relevant for understanding galaxy evolution (see also Hopkins et al. 2006).

A common property of galaxies hosting an AGN is the presence of strong winds or outflows (e.g., Cheung et al. 2016; Harrison et al. 2014; Mullaney et al. 2013; Wylezalek et al. 2020) in the ionized gas. Such outflows can be deployed in the form of collimated jets (Worrall & Birkinshaw 2006) or as radiatively driven winds (Netzer 2006) where gas can be ejected and transferred into the host galaxy (see King & Pounds 2015, for a review). This ubiquitous characteristic is a popular mechanism to explain how AGN feedback works and has been a key parameter introduced to solve theoretical problems faced in cosmological simulations (Naab & Ostriker 2017; Somerville & Davé 2015). For example, one notable application is helping to explain the regulation of star formation in massive galaxies (see also Harrison 2017). These phenomena (winds or outflows) have been observed in multiple gas phases (e.g., Aalto et al. 2012; Baron et al. 2021; Fiore et al. 2017; Herrera-Camus et al. 2020; Riffel et al. 2023), from extremely broad X-ray outflow features (reaching fractions of the speed of light; Tombesi et al. 2012) to cold-molecular gas winds (e.g., Cicone et al. 2014).

Even when focusing on one specific phase, outflow signatures can turn out to be very complex (e.g., Zakamska et al. 2016a). In the ionized gas (the main subject of this paper), for example, such outflows display nongravitational winds with a velocity dispersion (full width at half maximum (FWHM) > 500 km s^{-1}) that cannot be explained by the intrinsic rotation of the host galaxy or its dynamical equilibrium (Karouzos et al. 2016). Outflows usually appear in the spectra as secondary spectral components that accompany the main spectral lines (e.g., Heckman et al. 1981; Mullaney et al. 2013). Therefore, the shape of these spectral lines can acquire complex features that a single Gaussian profile cannot model. Instead, multicomponent fitting procedures have been widely used to characterize outflow signatures (e.g., Förster Schreiber et al. 2014). A widely used tracer to study these signatures is the [O III]λ5007 emission line. This forbidden emission line is restricted to low-density environments (such as the narrow-line region) and can be produced as a result of shocks or photoionization (Osterbrock 1989).

Much of what has been learned from AGNs has been through the study of their ionized gas kinematics. For example, in a large sample of optically selected type II AGNs, Woo et al. (2016) found that the velocity dispersion of the outflow as well as the fraction of emission-line ([O III]) shapes exhibiting multiple components both tend to escalate with an increase in [O III] luminosity ($L_{[\mathrm{O\ III}]}$). This is relevant because the $L_{[\mathrm{O\ III}]}$ has been shown to be a good indicator of an AGN's bolometric luminosity (L_{bol}; Heckman et al. 2004; LaMassa et al. 2010), which is an important parameter to understand the involved energy injection of the AGN's SMBH (Heckman & Best 2014) to the host galaxy. For example, Fiore et al. (2017) found that the wind mass

outflow rate correlates with L_{bol}.

Ionized outflows have been routinely found in AGNs selected from infrared (e.g., DiPompeo et al. 2018), X-ray (e.g., Rojas et al. 2019) and optical surveys (e.g., Wylezalek et al. 2020), to mention a few examples. However, none of the multiple AGN selection techniques today offer an ultimately clean AGN population (Padovani 2017) by itself. Attempts to create more complete AGN samples have shown that different selection techniques can find AGN candidates that other single selection techniques would miss (e.g., Alberts et al. 2020). Statistical analysis of AGNs selected based on techniques that are limited to a certain wavelength window can suffer from important biases such as obscuration or data coverage. This is not a simple task and different selection techniques (using various wavelengths) find different AGN populations, even with contrasting host-galaxy properties (e.g., Comerford et al. 2020; Hickox et al. 2009; Ji et al. 2022).

Consequently, the estimated outflow properties, and therefore AGN feedback studies, can be compromised by the way the AGN population is selected. For example, Mullaney et al. (2013) found that the most extreme [O III] kinematics arise from AGNs with moderate radio luminosities (10^{23} W Hz^{-1} > $L_{1.4\ \mathrm{GHz}}$ > 10^{25} W Hz^{-1}), finding evidence of compact radio cores being responsible for driving the most broadened profiles (see also Jarvis et al. 2021, 2019; Molyneux, S. J. et al. 2019). Baron & Netzer (2019) found that AGNs that present outflows (using the [O III] emission line) exhibit an excess in the mid-infrared spectral energy distribution component, suggesting that outflows are carrying dust. Different selection techniques can also be sensitive to different AGN powering mechanisms or stages of the current AGN duty cycle. The latter has been suggested by directly comparing optically selected AGN candidates with mid-infrared radio-detected AGN candidates (see Kauffmann 2018), with the former being found to dominate black hole growth in lower-mass systems.

An additional complication is that ionized outflows can extend from sub-kiloparsec (e.g. Singha et al. 2022) to kiloparsec scales (e.g., Liu et al. 2010; Sun et al. 2017). Due to the limitations of the instruments, most of the studies mentioned above base their results on single-fiber observations. Integral field spectroscopy (IFS) is a valuable technique to study the spatial distribution of outflows in more detail (e.g., Luo et al. 2021; Singha et al. 2022; Wylezalek et al. 2018). One of the latest pioneering IFS surveys is the MaNGA (Mapping Nearby Galaxies at Apache Point Observatory) survey (Bundy et al. 2015), providing 10 010 unique galaxies with spatially resolved spectra. Hence, our primary objective is to investigate how outflow properties vary, not only spatially but also based on the selection technique employed. The responsiveness of our selection methods to outflow characteristics can potentially shed light on their driving mechanisms and a connection to the AGN duty cycle.

This paper is organized as follows. In Sect. 2.2, we describe our data and some available catalogs for them that are relevant to this study to assemble a multiwavelength AGN catalog. The methods employed to study our sample are described in Sect. 2.3, with a description of the host galaxy properties of our sample. The results

are explained in Sect. 2.4, and we present a discussion in Sect. 2.5. Lastly, we summarize our conclusions in Sect. 2.6. The cosmological assumptions used in this study are H_0 =72 km s^{-1} Mpc^{-1}, Ω_M=0.3, and Ω_Λ = 0.7.

2.2 Sample and catalogs

2.2.1 The MaNGA Survey

In this study, we have used the $\sim$ 10,000 galaxies ($0.01 < z < 0.15$) observed in the SDSS-IV/MaNGA survey (Sloan Digital Sky Survey / Mapping Nearby Galaxies at Apache Point Observatory). MaNGA is an integral field unit (IFU) survey, providing 2D mapping of optical spectra at 3622–10354 Å at a resolution of R$\sim$2000. Its field of view ranges from 12″to 32″in diameter. Data reduction has been performed by MaNGA's Data Reduction Pipeline (DRP, Law et al. 2015). Complete spectral fitting is provided by MaNGA's data analysis pipeline (DAP, Westfall et al. 2019b). The DAP fits models for multiple spectral components (e.g., stellar continuum, emission lines) to the entire spectra. Throughout this paper, we have used the spectra (reduced by the DRP) after subtracting their stellar continuum (i.e., emission-line-only spectra provided by the DAP; see details in Sect. 2.3).

Additionally, Sánchez et al. (2022) presents a comprehensive catalog reporting multiple characteristics and integrated host galaxy properties based on a full spectral analysis with the `pyPipe3D` pipeline (Lacerda et al. 2022). Most of the galaxy properties used in our study are taken from this catalog (e.g., stellar mass and star formation rates). Other galaxy properties, such as emission-line ratios and Hα equivalent widths (EW(Hα)), are taken from (Albán & Wylezalek 2023). In this paper, we furthermore compute additional parameters, as is described in Sect. 2.3 (e.g., $L_{[O\ III]}$).

2.2.2 Active galactic nucleus catalogs

This paper aims to assess the behavior of spatially resolved ionized gas kinematics in AGN samples selected through various selection methods.[1] We have used the following set of MaNGA-AGN catalogs, which we shall further describe in subsequent subsections:

- An optical emission-line-based catalog from Albán & Wylezalek (2023) (using the 2 kpc aperture).
- A broad-line-based AGN catalog from Fu et al. (2023).
- A mid-infrared-selected AGN catalog from Comerford et al. (2024).

[1]Throughout this paper, we refer to "AGN population" as a group of AGNs chosen by a specific observational technique rather than speaking about a particular type, mode, or class (except we state the opposite).

- A hard X-ray-selected AGN catalog from Comerford et al. (2024).
- A catalog of radio-selected AGNs that we construct in this paper (see Sect. 2.2.2).

The full MaNGA sample contains a small number of repeated observations, most of which can be identified through their MaNGA-IDs (although there are exceptions; see more in Appendix A.1). We exclude duplicate sources in our final statistics, tables, and figures. In the following sections, we describe the individual AGN catalogs and the respective selection criteria in more detail. The sky coverage of the different surveys used for the classifications described below overlaps with MaNGA.

DR17 optical AGN catalog in flexible apertures from Albán & Wylezalek

Albán & Wylezalek (2023) present galaxy classifications based on optical emission-line diagnostics (Baldwin et al. 1981; Veilleux & Osterbrock 1987) measured within apertures of varying size for the entire MaNGA survey. Galaxies are classified into star-forming (SF), composite, Seyfert, LINER (low-ionization emission-line region, Halpern & Steiner 1983), or ambiguous galaxies (e.g., if a galaxy received two different classifications based on different line ratio diagnostics). The final AGN sample is then defined based on the galaxies in the Seyfert and LINER classes, with an additional cut on Hα equivalent width >3 Å[2] This additional cut minimized the contamination of faint "fake" AGNs (Cid Fernandes et al. 2010).

In this paper, we have used the 399 AGN candidates from the catalog based on a 2 kpc aperture.[3] The aperture was chosen to keep a balance between MaNGA's spatial resolution limit ($\sim$ 1.37 kpc, Wake et al. 2017) and the physical extent of gas ionized by an AGN (known as the narrow-line region (NLR), Bennert et al. 2006; Netzer 2015).

Broad-line AGN catalog

Some active galaxies present broad Balmer emission lines (known as type I AGNs; e.g., Oh et al. 2015). This is attributed to Doppler broadening due to high-velocity ionized gas surrounding the SMBH (Peterson 2006). Comerford et al. (2020) have presented a crossmatch between the MaNGA survey and Oh et al. (2015)'s type I classification that is based on SDSS DR7 data single-fiber spectroscopic observations with a size of 3". More recently, Fu et al. (2023) has carried out an analysis to identify broad-line AGNs and double-peaked emission-line signatures for the total MaNGA sample using the DR17 data release. MaNGA not only uses smaller fibers (2") but also provides additional spatial information.

[2]The equivalent width of each galaxy was obtained using the same aperture size used to measure the emission-line ratios during the classification. Equivalent widths and emission-line ratios are also included in the Albán & Wylezalek (2023) catalog.

[3]Note that the catalog from Albán & Wylezalek (2023) originally reports 419 targets using a 2 kpc aperture. However, we excluded galaxies due to duplication or critical flags (see Appendix A.1).

For each galaxy, Fu et al. (2023) used DAP flux residuals to compare them to the original flux in specific spectral regions (with a size of 20 Å) corresponding to the location of Hα and [O III] emission lines to assess the quality of the DAP's fitting procedure. They arranged the sample in 20 S/N bins (G-band S/N from the DAP) and selected galaxies with residuals $> 1\sigma$ of the residual distribution at each S/N bin (see details on Fu et al. 2023). They then performed a spectral fitting on this sample of 1652 galaxies, allowing multiple components to be fit to emission lines.

They ultimately selected broad-line AGNs as galaxies where the emission-line width (σ) of the broad component is at least 600 km s^{-1} larger than the emission-line width of the narrow component and present a catalog of 139 broad-line AGN (type I) candidates. We have found a few duplicate galaxies in this catalog's observations (see Appendix A.1), which reduces the sample to 135 targets. The work by Fu et al. (2023) almost doubles the number of broad-line-selected galaxies presented Comerford et al. (2020); on the other hand, 21 galaxies presented in Comerford et al. (2020) are not found in Fu et al. (2023). Discrepancies in the latter context can be related to the difference in FWHM($H\alpha$) constraints and possibly effects from changing-look AGNs (see Ricci & Trakhtenbrot 2023, for a review).

Mid-infrared and X-ray AGN catalogs of Comerford et al.

Comerford et al. (2024) have crossmatched MaNGA galaxies with known AGN candidates from multiwavelength surveys (as in Comerford et al. 2020). In this study, we have used the following catalogs:

- Mid-infrared AGN catalog based on observations with the Wide-field Infrared Survey Explorer (Wright et al. 2010, WISE): 123 AGNs.
- X-ray-selected catalog based on observations with the Burst Alert Telescope (Barthelmy et al. 2005, BAT): 29 AGNs.

Comerford et al. (2024) also provide a radio-AGN catalog and a broad-line (type I) AGN catalog, which we hae chosen not to use due to our science goals (see Sects. 2.2.2 and 2.2.2, respectively). Due to repeated observations or critical flags (from the MaNGA DRP; see the details in Appendix A.1), we excluded seven galaxies from the mid-infrared-selected catalog (three were repeated) and one from the X-ray-selected one (one has a critical flag).

Selection of radio AGNs

In this section, we present a catalog of AGN candidates solely based on radio data and independent of the radio-loud or radio-quiet classification often used in the literature. They were chosen independently of whether or not they have a jet (see the details in some comprehensive reviews; e.g., Heckman & Best 2014; Padovani 2016; Panessa et al. 2019). For example, Best & Heckman (2012) used a selection technique combining

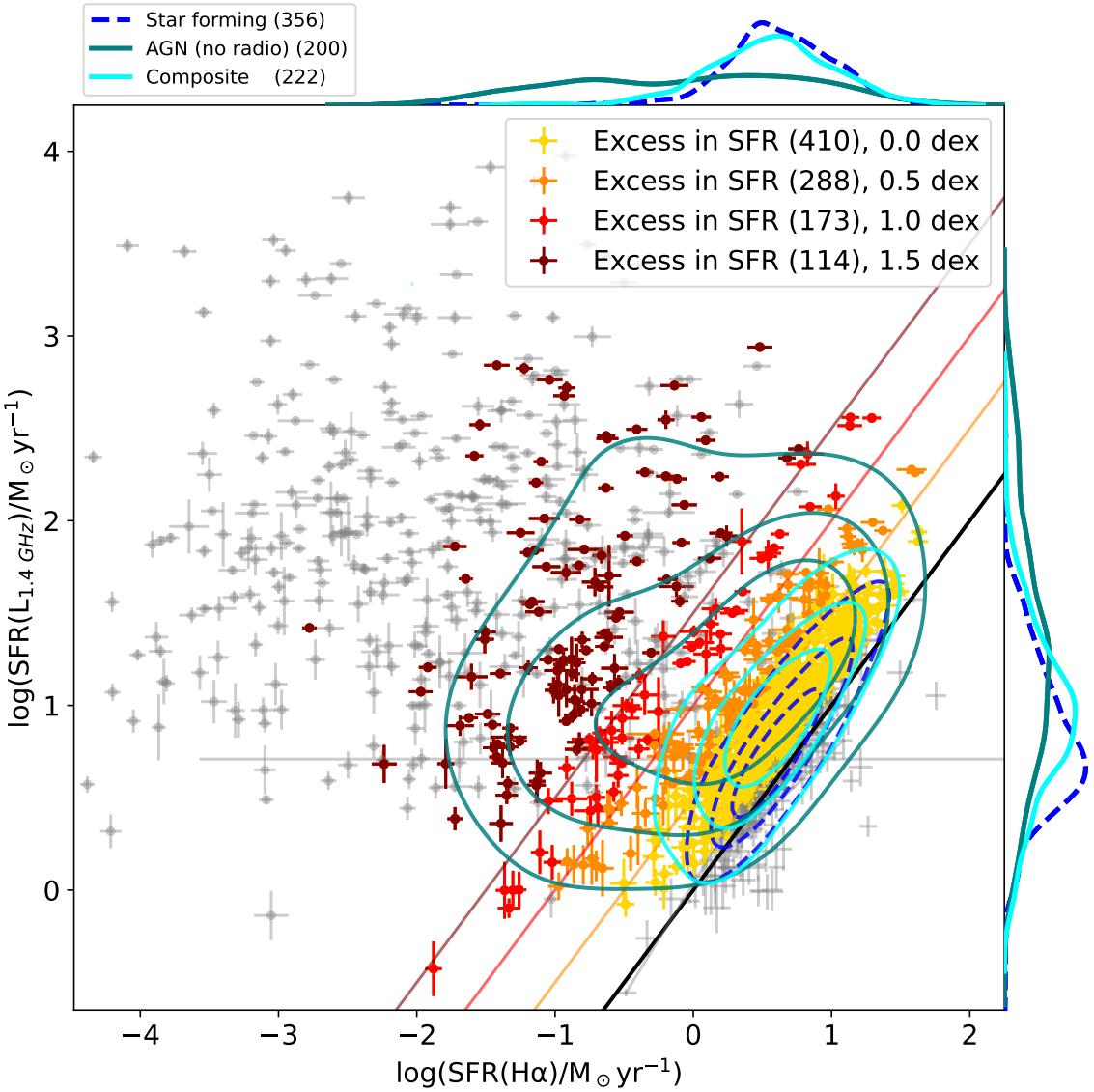

Figure 2.1. Definition of the radio-selected AGN candidates. We plot on the y axis the expected SFR that one would measure, assuming that all the radio luminosity can be attributed to star formation processes (SFR($L_{\rm rad}$; see Sect. 2.2.2). Similarly, on the x axis, the SFR is expected from Hα luminosity (SFR(Hα)). The black line corresponds to the location where SFR($L_{\rm rad}$) = SFR(Hα). The other colored lines (orange, red, and blue) correspond to our SFR excess definition in SFR(Hα) steps of 0.5, 1.0, and 1.5 dex ($\log(x_i)$). We defined each sample of AGN-selected candidates by selecting the targets whose values (and error bars) are above the corresponding line (following SFR($L_{\rm rad}$)/SFR(Hα) = x_i) and we have colored them according to the colored lines (except for $x_i = 0.0$ dex, which corresponds to the yellow ones). We also show targets that did not satisfy any SFR-excess criteria (gray without marker) or did not pass the S/N criteria (gray with marker) for our kinematic analysis (see Sect. 2.3.2). The contours (dashed blue, light blue, and teal) represent the density where specific galaxy populations gather (SF, composite, non-radio-selected AGNs). The top and right-hand plots show the individual parameter distribution of these three galaxy populations.

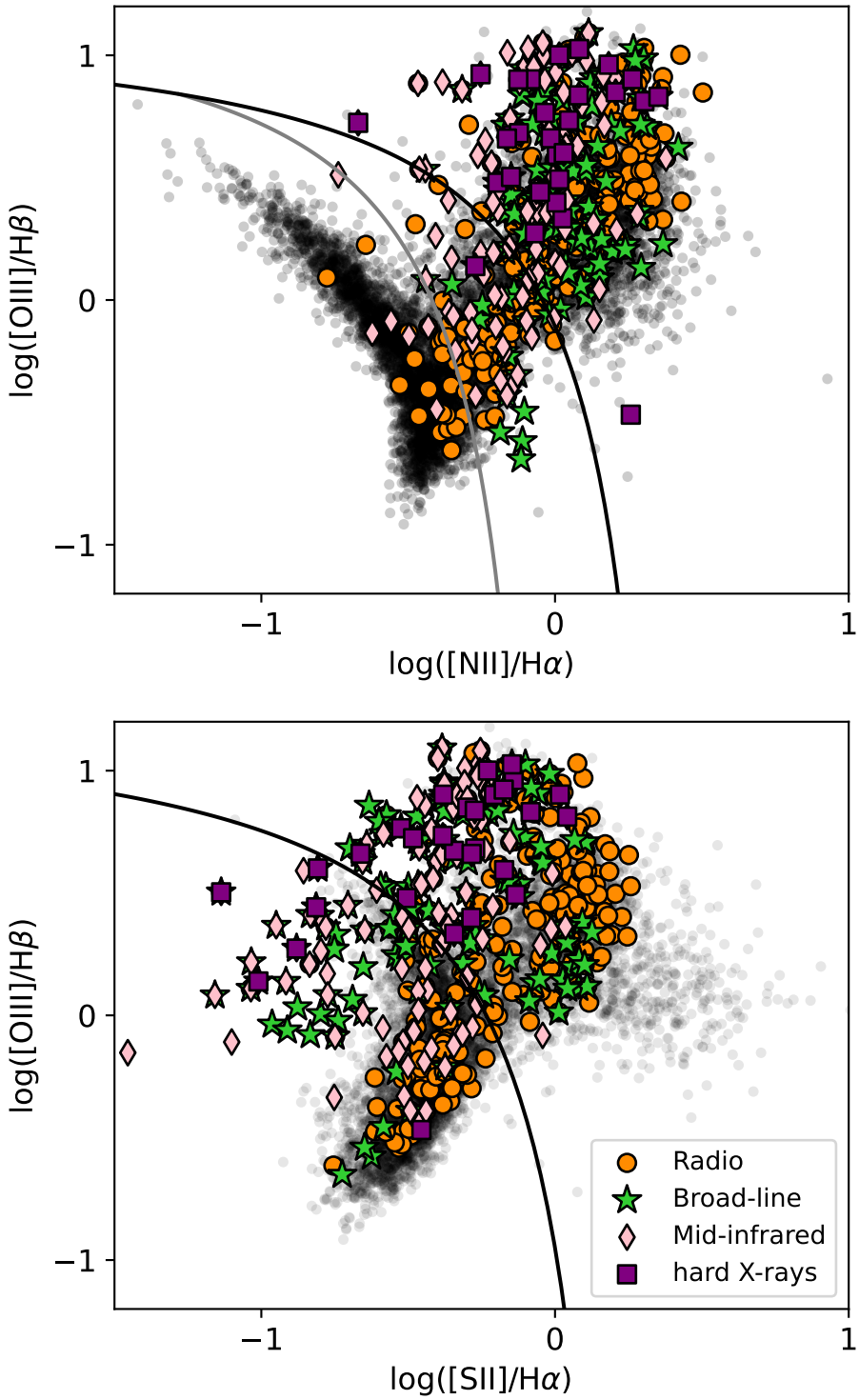

Figure 2.2. Optical diagnostic diagrams for MaNGA galaxies. The black circles in the scatterplot show the emission-line ratio values for all MaNGA galaxies. In colored shapes, we feature the different AGN-selected candidates (see the legend). We took the flux ratio values from the ones measured around their central 2 kpc region (Albán & Wylezalek 2023). In the top panel, the gray line corresponds to the demarcation line from Kauffmann et al. (2003), and the black line (both in the top and bottom plots) corresponds to the ones from Kewley et al. (2001b).

both optical and radio signatures, and this is the catalog that Comerford et al. (2024) presents as the radio-selected MaNGA AGN population (see Sect. 2.2.2). However, this classification prioritizes sources with $f_{1.4\ \mathrm{GHz}} > 5$ mJy as its emphasis lies on the radio-loud population of AGNs (see Padovani et al. 2017; Urry & Padovani 1995, for a review). Instead, we used a different approach and first crossmatched MaNGA SDSS-IV galaxies with data from the NRAO Very Large Array Sky Survey (Condon et al. 1998, NVSS) and the Faint Images of the Radio Sky at Twenty centimeters (Becker et al. 1995, FIRST) radio surveys, adopting a less strict flux cut of > 1 mJy. We note that this threshold is close to the sensitivity of the surveys, and there is likely a population of AGNs emitting even below this limit (e.g., White et al. 2015).

Previous studies have shown that finding genuine associations between targets of two different surveys comes with a trade-off between completeness and reliability (e.g., Best et al. 2005; Ivezić et al. 2002). Choosing a larger offset for searching counterparts can lead to high completeness but increases the number of false associations. To ensure precise spatial alignment between the optical and radio sources, we searched for the closest galaxy within a 1.5 arcsecond aperture for the FIRST survey, which ensures 85% completeness and 97% reliability (see Ivezić et al. 2002), and we used a 5.0 arcsecond aperture for the NVSS survey. For comparison, Best et al. (2005) estimates 90% completeness and 6% contamination from random targets using a 10.0 arcsecond aperture. This choice of apertures aims to maximize completeness and reliability. We find 936 and 1035 crossmatches for the FIRST and NVSS survey, respectively. In total, 1383 unique targets were found, with 588 coincident targets between FIRST and NVSS.

Our aim is to develop a radio-selected sample that is as independent as possible of known optical diagnostics (e.g., BPT diagrams) or other selection criteria. Two significant contributors to the extragalactic radio sky are star formation processes and nuclear activity in galaxies (Padovani 2016). The host galaxies of AGNs have been shown to span several decades in radio luminosity, and are often very faint, raising the question of whether their radio emission is dominated by star formation processes (Panessa et al. 2019) rather than the AGN event. Zakamska et al. (2016b) studied whether the radio signatures (1.4 GHz flux density) of confirmed AGNs can be explained purely by star formation processes when comparing them with a variety of star formation rate tracers. Independently of the used SFR tracer, they conclude that the AGNs had a systematic excess in radio luminosity not consistent with star formation, which might be attributed to the activity in the nucleus. Similarly, Kauffmann et al. (2008) used the Hα luminosity and compared it with the 1.4 GHz flux densities of a sample of SDSS galaxies (crossmatched with radio surveys; FIRST and NVSS) and found that SF galaxies form a tight correlation between both parameters and that their AGN candidates systematically exceed this tight relation toward higher 1.4 GHz flux densities.

Based on the findings described above, we constructed a radio-selected AGN sample similar to the "$L_{H\alpha}$ versus L_{rad}" method used in Best & Heckman (2012). Specifi-

Table 2.1. Coincident targets between the different AGN-selection techniques in the full MaNGA sample.

Selection technique	Optical	Mid-infrared	hard X-rays	Broad-line	Radio
Optical	399	-	-	-	-
Mid-infrared	65	123	-	-	-
hard X-rays	23	24	29	-	-
Broad-line	85	48	14	135	-
Radio	135	55	17	64	642

Here, we have already excluded targets that were repeated observations or targets that had a critical flag (see Appendix A.1).

Table 2.2. Coincident targets between the different AGN-selection techniques in a sample of MaNGA targets limited by S/N.

Selection technique	Optical	Mid-infrared	hard X-rays	Broad-line	Radio
Optical	373	-	-	-	-
Mid-infrared	64	119	-	-	-
hard X-rays	22	23	27	-	-
Broad-line	83	48	14	131	-
Radio	128	55	16	61	288

Here, we only use targets that satisfy the quality criteria described in Sect. 2.3.2.

cally, we identified AGN activity based on the excess in the SFR estimated from the radio luminosity compared to the Hα-based SFR reported in the PIPE3D value-added catalog of Sánchez et al. (2022); that is, values that are above the expected 1-to-1 relation. We used the extension named log_SFR_SF, meaning that only the spaxels that were consistent with star formation regions were used to measure the SFR. Additional ways to minimize or correct for the contribution of the AGN during the SFR measurement have been shown in De Mellos in prep. We note that different methods to estimate the SFR from optical spectra (e.g., the SSP-method, Sánchez et al. (2022)) do not change our results significantly (as has also been seen in Zakamska et al. 2016b).

In Fig. 2.1, we show the relation between the Hα-based SFR and the radio-based SFR for the radio-detected MaNGA galaxies described above, assuming that all radio emission is related to SF processes. We also show the density contours of different galaxy subclasses based on optical diagnostics presented in Albán & Wylezalek (2023) and described in Sect. 2.2.2. Pure SF galaxies agglomerate close to the 1-to-1 line (dashed blue contours), in agreement with the findings presented in Kauffmann et al. (2008). Composite galaxies (see Sect. 2.2.2) occupy values consistent with a radio excess (solid cyan contours). Indeed, the emission in composite galaxies is expected to be a mix of star formation and AGN processes. We also show the location of AGN candidates that have been selected by any of the described selection techniques (apart from a radio selection) — that is, using mid-infrared, hard X-rays (see Sect. 2.2.2), broad lines (see Sect. 2.2.2), and optical diagnostics (see Sect. 2.2.2) — and label

this sample as "AGN (no radio)" in the figure (solid teal-colored line). We show that this AGN population gathers preferentially in the excess region of the plot, consistent with the findings of Zakamska et al. (2016b) and Kauffmann et al. (2008). On the top and right-hand borders of the plot, we show the distribution of the individual SFR values using a smooth histogram.

Using offsets from the 1-to-1 line, following $\mathrm{SFR}(L_{\mathrm{rad}})/\mathrm{SFR}(\mathrm{H}\alpha) = x_i$, we have colored with yellow, orange, red, and maroon the galaxy populations with excesses from $log(x_i) = 0.0$ to $log(x_i) = 1.5$ dex. The gray-colored targets in the plot represent the galaxies that we excluded from our analysis due to one or two of two reasons: they were not above the 1-to-1 relation, or their signal-to-noise (S/N) from the [OIII] 5007 emission line was too low-quality to be accepted for our kinematic analysis (see Sect. 2.3.2).

We defined our radio-AGN sample using the galaxies whose L_{rad} plus associated flux uncertainties were at least 0.5 dex above the 1-to-1 SFR relation. We find 642 galaxies that satisfy this criterion, while 28 of those are either duplicate or critical targets (see Appendix A.1). We note that only 5% of the SF classified galaxies are above the 0.5 dex line. Employing larger cutoffs risks excluding low-luminosity AGNs. Notably, 25% of targets identified as AGNs by alternative methods — in other words, excluding radio observations — were found below the 0.5 dex line. Taking into account additional quality criteria necessary for our emission-line analysis (see Sect. 2.3.2), we worked with a sample of 288 radio-AGNs, which we shall refer to as the radio-selected AGN sample for the remainder of this paper.

Furthermore, while we were writing this paper, Suresh & Blanton (2024) studied a sample of radio AGNs (selected from MaNGA in a very similar way to in this paper) and their Eddington ratios to estimate their radio activity. They found that the Eddington ratio distribution within their AGN sample exhibits a significant dependency on stellar mass, whereas it shows no correlation with the specific star formation rate (sSFR) of the host galaxies. This led them to conclude that, at a fixed stellar mass, SFRs of host galaxies do not influence the radio-AGN selection.

Overlap and discrepancy between the AGN catalogs

In Table 2.1, we compile the number of galaxies identified as AGNs using the various selection methods discussed above, noting that some galaxies were selected as AGNs by multiple techniques. In total, we identify a sample of 970 galaxies that have been classified as an AGN by at least one method.

Since the work of this paper focuses on the ionized kinematics traced by the [O III] 5007 emission line in AGNs, we require additional S/N cuts on emission-line fluxes (e.g., $S/N < 7$; see the details in 2.3.2), which reduces the sample we continue to work with. Table 2.2 lists 594 individual AGN candidates (621 if repetitions or critical targets are not taken into account; see Appendix A.1) that were used in our kinematic analysis, indicating that most AGN selections remain largely unaffected by

our S/N criteria, except for the radio-selected sample. We further discuss this in Sect. 2.3.3.

It is largely known that no selection technique is free from limitations. For example, optical selection techniques are mostly biased toward unobscured AGNs. This spectral window is significantly impacted by absorption and scattering due to the presence of dust and gas that can obscure the central regions of an AGN (where most of its energetic input occurs). Some contaminants to optical selection techniques can be associated with galaxies dominated by post-asymptotic giant branch stars (e.g., Singh et al. 2013b). Furthermore, dilution from the host galaxy can also play a role in missing AGN emission. Given that opacity due to dust is less effective at longer wavelengths, mid-infrared selection techniques are less affected by dust attenuation. Most of its critical contaminants dominate at larger redshifts; with MaNGA we work with sources at $z < 0.5$. Finally, radio selection techniques are also less affected by obscuration. However, low-luminosity AGNs can be difficult to distinguish from SF processes. Padovani et al. (2017) provides a broad and comprehensive overview of this topic.

In Fig. 2.2, we display the emission-line ratio diagrams highlighting our AGN samples, except for the optically selected sample. The AGNs do not show any preferred location on the diagrams (or a specific side of the demarcation lines; see Kauffmann et al. 2003; Kewley et al. 2001b). Using AGNs that were classified differently than optical techniques, only 4% of the SF galaxies are AGNs; this rises to 14% in the case of composite galaxies, and 7% for ambiguous ones. This is an excellent example of the well-known problem that using only one single criterion is insufficient to obtain a complete picture of the AGN population.

We note that the hard X-ray-selected AGN candidates are the smallest sample. This is not surprising, as the BAT's integration time is kept short to fulfill its scientific goals (Barthelmy et al. 2005). It is also the sample with the largest overlap with the other AGN samples; all X-ray-selected AGNs are also selected as AGNs in at least one other selection technique reported in this paper. Indeed, X-ray emission appears to be universal in AGNs and the emission is not significantly contaminated by its host galaxy (see a detailed discussion in Padovani et al. 2017). Hence, the optical, infrared, broad-line, and radio selection techniques make up the four biggest AGN subsamples in our study, with the largest number of independently selected candidates. Additionally, we have defined a sample of non-AGN galaxies that will be used in the discussion section. Our non-AGN sample contains all MaNGA galaxies that were not selected as AGNs by any method used in this paper.

2.3 Analysis

Hereinafter, when referring to kinematics, we specifically refer to the ionized gas (traced by the [O III] 5007 emission line).

2.3.1 Fitting procedure

Spectra from regions with kinematics dominated by winds can display complex emission-line profiles (e.g., Liu et al. 2013). This is not taken into account by the DAP emission-line fitting routine. Therefore, we developed a fitting procedure to account for up to two Gaussian components for each emission line. Our fitting method is based on a least-squares Python program using the documentation from nonlinear least squares minimization (LMFIT, Newville et al. 2016) and it follows standard fitting procedure techniques (e.g., Liu et al. 2013; Wylezalek et al. 2020). In summary, for all spectra in each MaNGA galaxy, our procedure operates in the rest-frame stellar-subtracted region where the [O III] 5007 emission line is (see the details in Appendix A.2). From the maps of the best-fit parameters, we created a nonparametric emission-line width W_{80} map. The W_{80} parameter is the most essential value we extracted from our fitting procedure and is the most relevant for the discussion throughout this paper. Whenever we refer to it, we refer to the W_{80} value obtained from [O III] 5007.

To study the spatial distribution of this parameter, we constructed radial profiles for all galaxies from elliptical annuli in steps of 0.25 effective radius (R_{eff}). To obtain the parameters for the elliptical apertures for each galaxy, we used the b/a axis ratio and position angle (PA) from PIPE3D's value-added catalog from Sánchez et al. (2022), as well as the effective radius. These parameters were adopted from the NASA-Sloan Atlas catalog (Blanton et al. 2011). They use the Petrosian system (see Blanton et al. 2001; Petrosian 1976) applied to the SDSS r-band imaging of galaxies using elliptical apertures. Here, R_{eff} is defined as the major axis containing 50% of the flux inside 2 Petrosian radii, and b/a, and PA were obtained from the elliptical aperture (see the details in Wake et al. 2017). To perform a weighted average on each annulus, we captured the fraction of each pixel enclosed by an annulus so that we avoided average properties over a set of discrete pixels and recovered a smooth distribution. Specifically, we followed the pixel-weighted average procedure used in Albán & Wylezalek (2023) but using ellipses.

In a sample of ∼160 000 normal SDSS (SF BPT selected) galaxies ($z < 0.7$, with $8 < log(M_*/M_\odot) < 11.5$ and $-3 < log(SFR/M_\odot\ yr^{-1}) < 2$), Cicone et al. (2016) find that the gas velocity dispersion (σ) hardly exceeds 150 km s^{-1}. The latter corresponds to a W_{80} of $\sim$ 380 km s^{-1} ($W_{80} = 2.56\sigma$). Furthermore, Gatto et al. (2024) conclude a lower cut, of $\sim$ 315 km s^{-1}, when studying the W_{80} in a control sample of non-AGNs (matched to optically selected AGNs in stellar mass, morphology, inclination, and redshift). Therefore, W_{80} values greater than this threshold suggest the presence of nongravitational motion of gas, such as outflows.

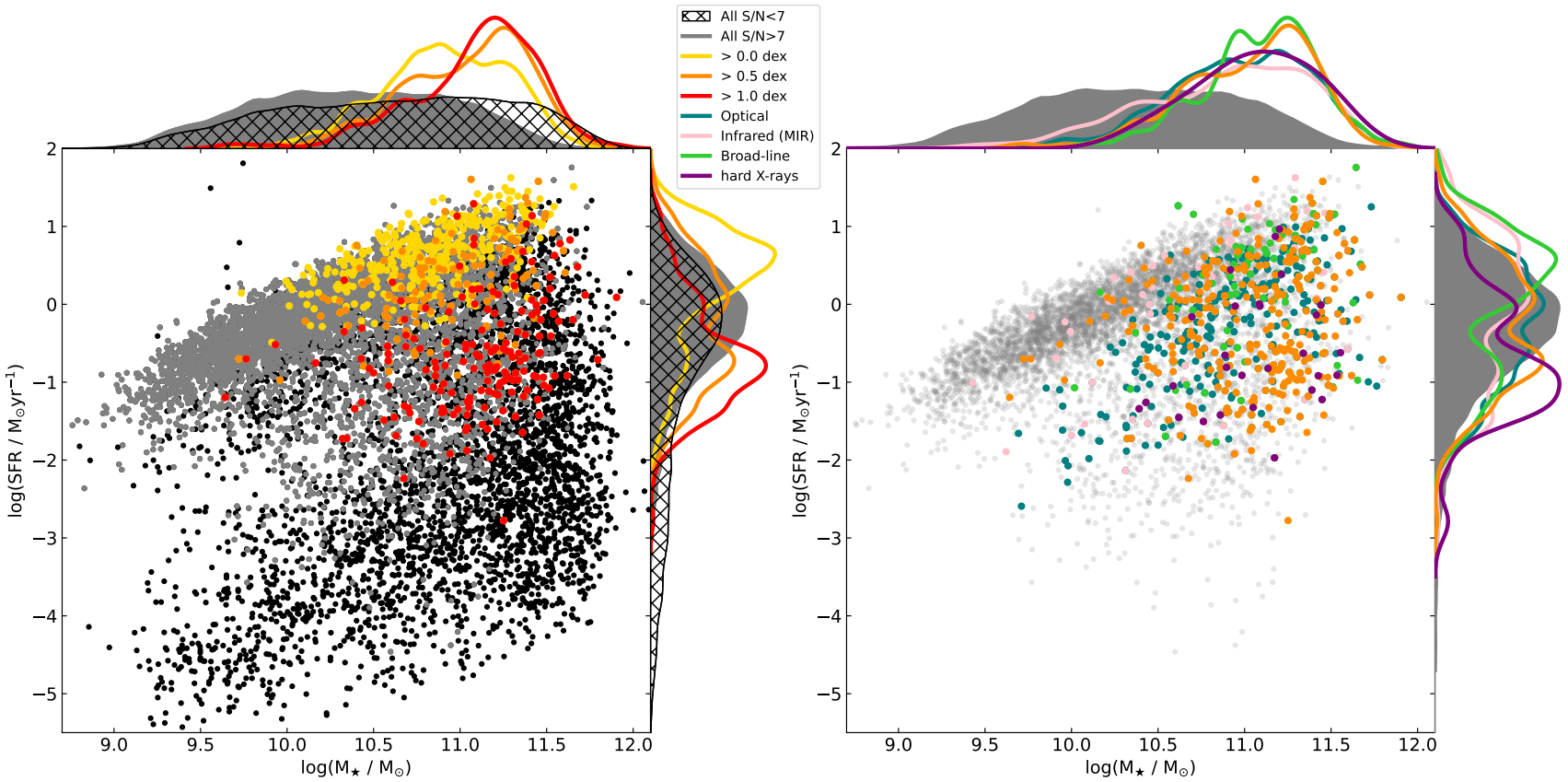

Figure 2.3. Stellar mass versus star formation rates of MaNGA host galaxies. The left panel shows the impact of our quality criteria (see Sect. 2.3.2), excluding galaxies with higher stellar mass and lower star formation rates (represented by the black dots in the scatter plot and hatched black distribution in the top and right-hand diagrams). In red, orange, and yellow, we show the distribution of the AGN candidates selected by radio (using 0.0, 0.5, and 1.0 dex of excess; see Sect. 2.2.2) that satisfy the S/N quality criteria. To understand the properties of the excluded radio-selected hosts, we encourage the reader to look at Fig. 2.1. It can be seen that a long tail of deficient SFR hosts are excluded ($-2 > \log(\mathrm{SFR}(\mathrm{H}\alpha)) > -4$). On the right, we show only the galaxies chosen after the quality criteria and their corresponding AGN classifications. We have provided labels for each color in a panel between both plots.

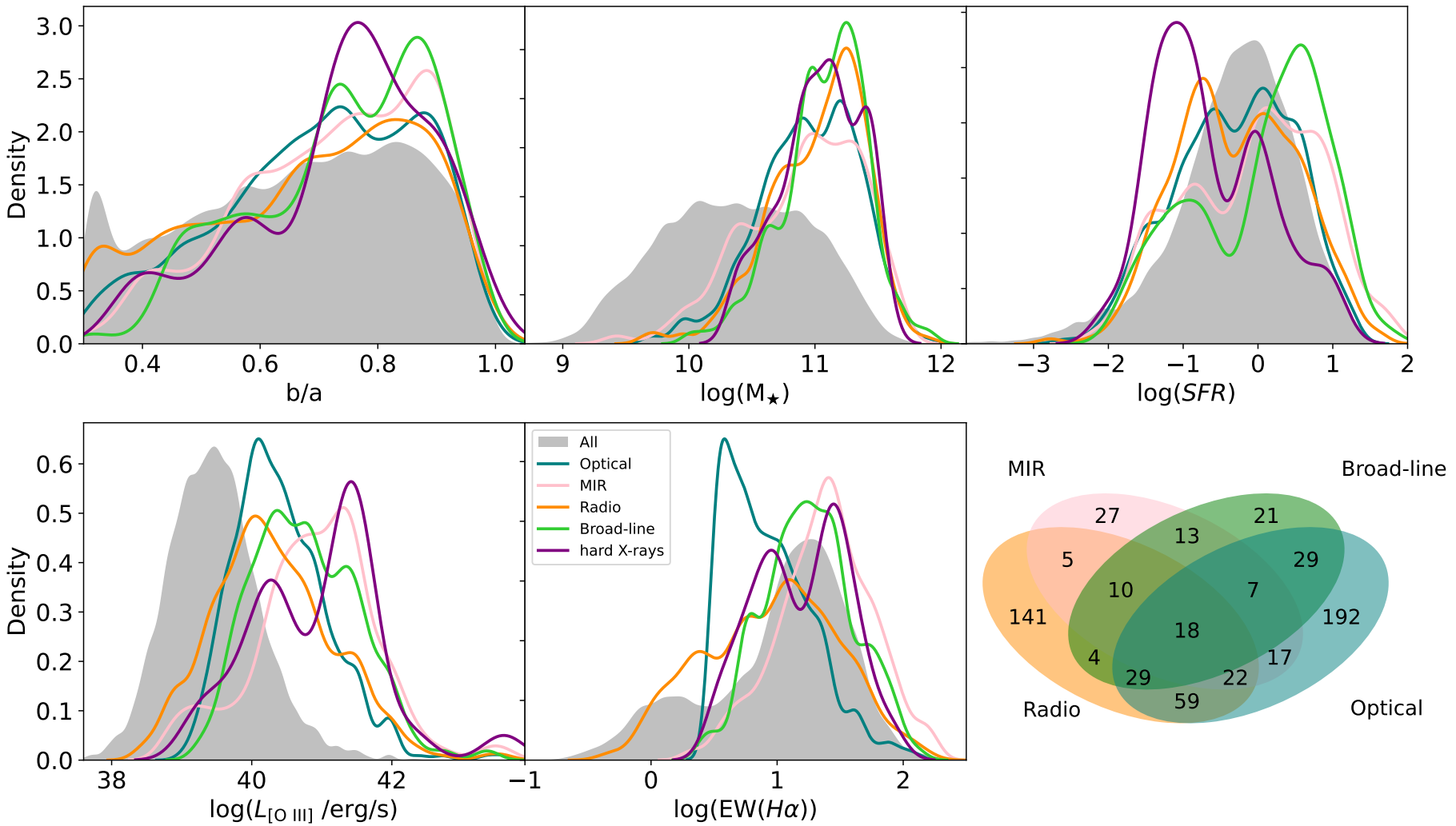

Figure 2.4. Smooth histograms of multiple host galaxy properties. Top (left to right): b/a axis ratio, $\log(M_\star)$, and log(SFR) from Pipe3D. Bottom (left and middle plot): $\log(L_{[\mathrm{O\ III}]})$ and $\log(\mathrm{EW}(\mathrm{H}_\alpha))$, both extracted from an aperture of 1 R_{eff}, and (to the right) a complementary illustration for Table 2.2 employing Venn diagrams. In order to maintain visual clarity, the hard X-ray-selected AGN sample was intentionally omitted from the diagrams. The gray-shaded histogram shows the distribution of all MaNGA that pass our S/N criteria (see Sect. 2.3.2).

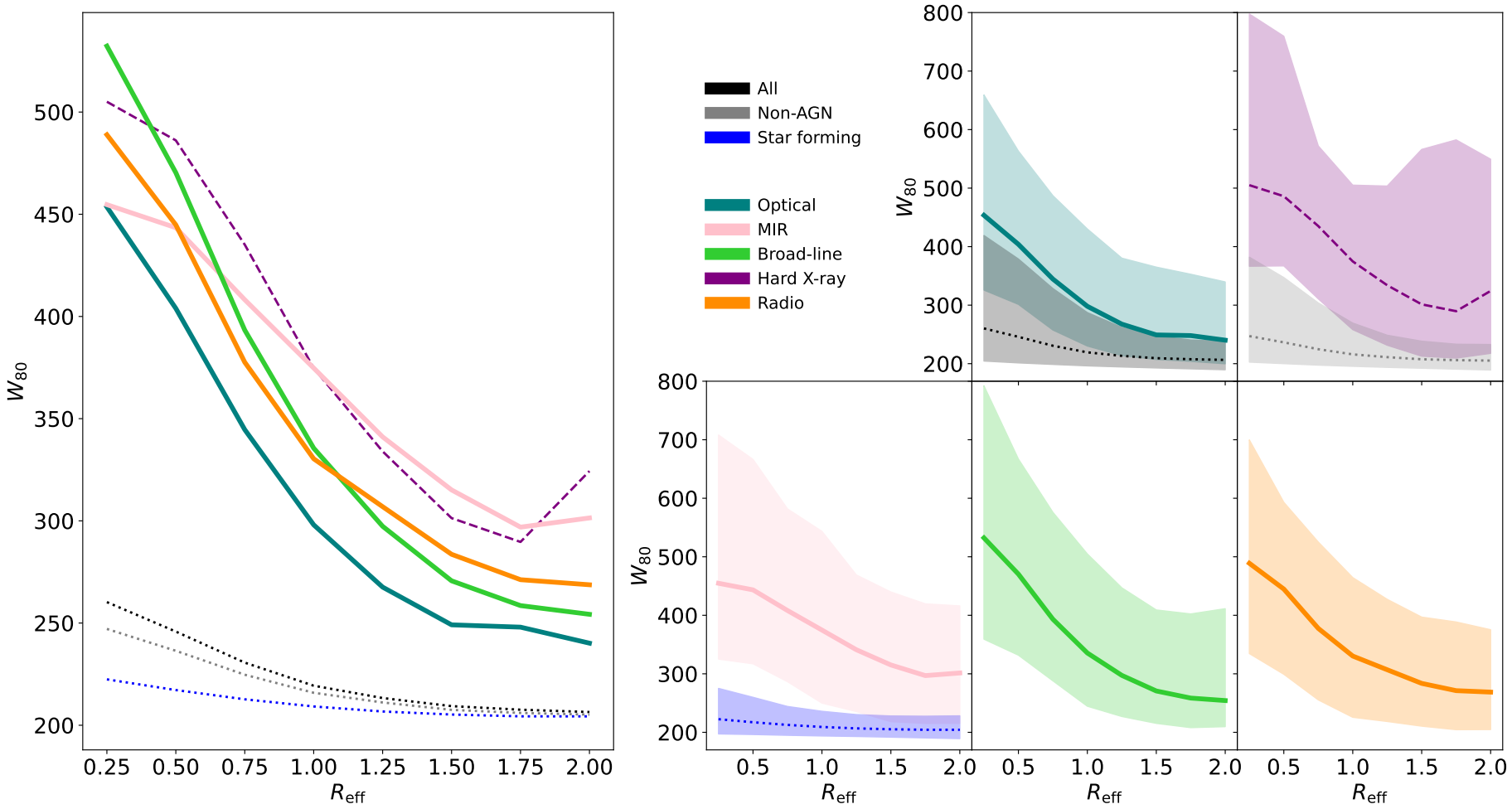

Figure 2.5. W_{80} stacked radial profiles for various galaxy groups. In the upper central panel, the colors represent these groups: black, gray, and blue for all MaNGA galaxies, non-AGNs, and SF galaxies (selected by BPT), while the remaining colors denote AGN-selected candidates. Each line in the plots represents the median value at each $R_{\rm eff}$ ring, with shaded areas indicating the 14th to 86th percentiles. The leftmost plot displays unshaded profiles for easier comparison. Different line styles are used for visual clarity.

2.3.2 Galaxies selected for the kinematic analysis based on signal-to-noise quality criteria

One crucial factor to consider is the impact of the S/N on measuring the line width W_{80}. As S/N decreases, the W_{80} measurements tend to get underestimated (see Liu et al. 2013), especially if there is indeed a (faint) broad component present in the line profile (Zakamska & Greene 2014). To ensure the accuracy of our analysis and avoid incorrect W_{80} measurements, we excluded all spaxels with an $A/N < 7$ (amplitude over noise) before we performed the spectral line fitting. Given the tight relation between S/N and A/N seen in Belfiore et al. (2019), we refer to A/N as simply S/N. To ensure that each individual galaxy retains enough high S/N spaxels, we furthermore applied the following criteria:

- More than 10 spaxels with $S/N > 7$.
- There are at least two annuli (for the radial profile derivation) where the area covered by the spaxels with an $S/N > 7$ is at least 10% of each annulus's total area.

The thresholds for the S/N and pixel fractions were chosen to minimize the number of excluded galaxies, while retaining a suitable quality for the analysis. These quality cuts introduce a bias (driven by the S/N) that rejects galaxies that are more likely to be low in terms of SF, and some high-mass galaxies, respectively (e.g., Albán & Wylezalek 2023; Brinchmann et al. 2004). Our final sample contains 5696 targets (see the left plot in Fig. 2.3). Table 2.1 and Table 2.2 show the crossmatches between the different AGN populations and how the subsample sizes decrease after applying the S/N and quality cuts. Radio-selected AGN candidates are significantly impacted by the quality criteria (see Fig. 2.1). In contrast, the other AGN samples remain relatively unaffected.

According to the optical classification from Albán & Wylezalek (2023), more than 90% of the radio-selected AGNs that were excluded from the final sample due to the quality criteria are LINERs ($\sim$ 30%, with EW(Hα < 3)) or "lineless" ($\sim$ 60%, galaxies that could not be classified by optical analysis, with $S/N < 3$; see the details in Albán & Wylezalek 2023), and around 5% are classified as ambiguous.

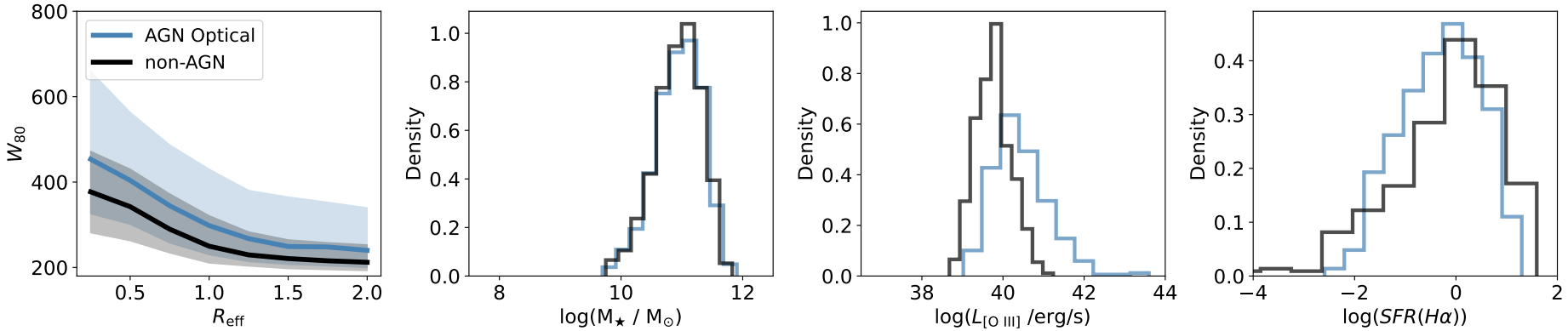

Figure 2.6. Comparison of stacked W_{80} profiles and host galaxy properties between non-AGNs and optical AGNs. In each plot, blue corresponds to the behavior of a specific parameter for optically selected AGNs and black for non-AGNs. We show the W_{80} stacked radial profile, the $\log(M_\star)$ distribution, the $\log(L_{[\rm O\ III]})$ distribution, and the $\log(\rm SFR(H\alpha))$ distribution. For this comparison, only $\log(M_\star)$, redshift, and morphology were controlled.

2.3.3 Typical properties of AGN-selected host galaxies

Focusing on the final sample of galaxies that fulfill the S/N and quality criteria, Fig. 2.4 shows host galaxy properties for our AGN populations, including a Venn[4] diagram (following to Table 2.2). Comparing Table 2.1 with Table 2.2 (samples before and after the quality cuts) reveals that the AGN samples do not experience a significant cut, with the exception of radio-selected AGNs, where a notable fraction of massive galaxies with low SFR and low EW(Hα) got excluded (see 2.3.2). However, the distribution of b/a and $L_{[O\ III]}$ for radio-selected AGNs remains less affected by the S/N cut.

Most AGNs are found in host galaxies with high stellar masses ($M_\star$; see the top-middle plot of Fig. 2.4), regardless of the AGN selection technique. This is a ubiquitous trend that has been found in various AGN samples from different studies (see e.g. Barrows et al. 2021; Best et al. 2005; Kauffmann et al. 2003; Powell et al. 2018). Our different AGN subsamples all have similar stellar mass distributions. This is an important fact to notice, given that more massive galaxies are expected to have larger emission-line widths (e.g., Cappellari 2016; Chae 2011; Zahid et al. 2016, see also Appendix A.3).

Figure 2.4 reveals that the different AGN samples probe different distributions of their host SFR, $L_{[O\ III]}$, and EW(Hα), showcasing the biases of each selection technique. The SFR differences between the samples are reflected in Fig. 2.3, where our AGN candidates tend to gather below the star formation main sequence (SFMS). The AGN studies for samples in the local Universe have found similar results, where AGNs are found in the so-called transition zone or the green valley (e.g., Leslie et al. 2016; Salim 2014; Schawinski et al. 2007). At slightly higher redshifts ($0.25 < z < 0.8$), Hickox et al. (2009) find that mid-infrared selected AGNs have bluer colors and are found preferentially in the blue cloud, while radio-selected AGNs are more likely to gather in the red sequence, suggesting that the latter are relevant for understanding the evolutionary transition of host galaxies from actively SF states to more quiescent ones.

Wylezalek et al. (2018) find that AGN-selected MaNGA (DR14) targets have mostly low to intermediate luminosities ($L_{[O\ III]} \sim 10^{40}$ erg s^{-1}) for an optically selected AGN sample. We observe here the same behavior for our optically selected AGNs in MaNGA-DR17. However, for AGNs selected via infrared, hard X-rays, or broad Balmer lines, we typically observe higher $L_{[O\ III]}$, with distributions peaking at $\sim L_{[O\ III]} \sim 10^{41.6}$ erg s^{-1}. On the other hand, radio-selected AGN candidates show some lower $L_{[O\ III]}$ values. Interestingly, $L_{[O\ III]}$ is known to correlate with the AGN's bolometric luminosity (Heckman et al. 2004; LaMassa et al. 2010; Pennell et al. 2017), which in turn is correlated with AGN-driven wind velocities (e.g., Fiore et al. 2017).

Of the 288 radio-selected AGNs used in this analysis, 52 were optically classified as LINERs with AGNs (see Sect. 2.2.2) and 55 were not classified as AGNs as they

[4]We create our Venn diagrams from an adapted version of this public repository: https://github.com/tctianchi/pyvenn.

did not meet the minimum Hα equivalent width of 3 Å. The 52 LINER galaxies have a median EW(Hα) of $\sim$ 1.75 Å. Other authors have used less strict EW(Hα) constraints (Sánchez et al. 2018, e.g., 1.5 Å) to include fainter AGNs in optically selected samples. However, this might introduce some LINER-like galaxies that have no AGN but that are dominated by a population of post-AGB stars (Singh et al. 2013b) that can mimic AGN-like ionization in a typical optical classification. This emphasizes the importance of a multiwavelength AGN selection technique for a more complete population census. Quite remarkably, AGNs that were selected by mid-infrared, broad-lines, or X-ray observations clearly show EW(Hα) $>$ 3.0 Å (only three galaxies have EW(Hα) $<$ 3.0 Å $\sim$ 2.0 Å), while radio-selected AGNs show lower EW(Hα) $\sim$ 2.0Å. We recall that optically selected AGNs were required to have EW(Hα) $>$ 3.0 Å (Albán & Wylezalek 2023). Therefore, we investigated whether the differences in the W_{80} radial profiles (see Sect. 2.3.4) can be attributed to any differences in host-galaxy properties.

2.3.4 Radial profiles of ionized gas kinematics

Several studies have investigated the overall AGN kinematic properties across many different AGN samples (e.g., Baron & Netzer 2019; Mullaney et al. 2013; Rojas et al. 2019; Zakamska & Greene 2014, among others). However, most of these studies have used single-fiber data and have therefore been limited in assessing spatial dependencies. Consequently, comprehensive studies with large spatially resolved spectral samples are crucial to assessing the impact of selection techniques. We investigated the radial profiles of ionized gas kinematics in the various AGN samples we have defined above. To do so, we first stacked the W_{80} profiles (see Sect. 2.3.1) of galaxies within each individual subsample and used the median value at each annulus.

The resulting profiles are shown in Fig. 2.5. The shaded regions around the profiles represent the 14_{th} and 86_{th} percentiles of the W_{80} distribution at each specific annulus. The median W_{80} profiles reveal distinct behaviors between the AGN samples. Visual inspection indicates variations not only in the magnitude but also in the slopes of these profiles. Notably, regardless of the AGN selection technique, there is a systematic behavior of an enhanced W_{80} profile in the AGN population compared to the overall MaNGA sample. This characteristic continues out to 2 effective radii. Similarly, if we focus only on galaxies that were not selected as AGNs by any of our selection techniques (the non-AGNs; see Sect. 2.2.2), we find the same trend. Moreover, SF-classified galaxies exhibit less pronounced profiles, with minimal enhancements near the center. The subsequent section will explore potential explanations for these observations.

2.4 Results

Figure 2.5 (see the left panel) reveals that the median W_{80} radial profiles of AGN-selected populations are significantly different. In Sect. 2.3.3, we show that the host

galaxies of the different AGN samples are similar with respect to some properties (e.g., stellar mass, or b/a axis ratio) but significantly different with respect to other properties (e.g., $L_{[\mathrm{O\ III}]}$, or SFR(Hα)). We note that samples with higher $M_\star$ will systematically select galaxies with higher $L_{[\mathrm{O\ III}]}$ and vice versa (see also Appendix A.3). At the same time, samples with higher $M_\star$ and $L_{[\mathrm{O\ III}]}$ will systematically select galaxies with higher W_{80} (see the discussion in Sect. 2.3.3). Therefore, in this section, we investigate if and how the differences in the kinematics persist or change when we carefully match the AGN samples so that they have the same host galaxy properties.

We created control samples based on an $M_\star$ and $L_{[\mathrm{O\ III}]}$ parameter space. Given that the number of galaxies per each $M_\star$ and $L_{[\mathrm{O\ III}]}$ bin becomes limited, controlling for redshift and morphology becomes challenging. Therefore, we selected the galaxy that is closest in redshift and in morphology. The morphology was used as a number (obtained from Sánchez et al. 2022). We also note that the radial profiles take the R_{eff} of each galaxy into account by using it as a step for the average W_{80} at each annulus (see Sect. 2.3.4).

2.4.1 AGNs versus non-AGNs

In a recent study, Gatto et al. (2024) used a catalog of optically selected AGNs (selected through emission-line diagnostics) and created a control sample matching properties to the AGN hosts similarly to in this paper, except for the $L_{[\mathrm{O\ III}]}$. When looking at all spaxels, they find that AGNs have greater W_{80} values than the control galaxies, attributing the ionized gas kinematic disturbances to the presence of the AGN. We obtain similar results to Gatto et al. (2024) (see Fig. 1) when using only optically selected AGNs and a similar control sample. In Fig. 2.6, we present the results as radial profiles for this comparison,[5] finding that optically selected AGNs have larger velocity widths than non-AGNs of similar masses. We find similar results when selecting AGNs through other techniques (see below).

[5]We used our non-AGN sample, i.e., also removing AGNs selected by a multiwavelength selection, as is discussed in Sect. 2.2.2.

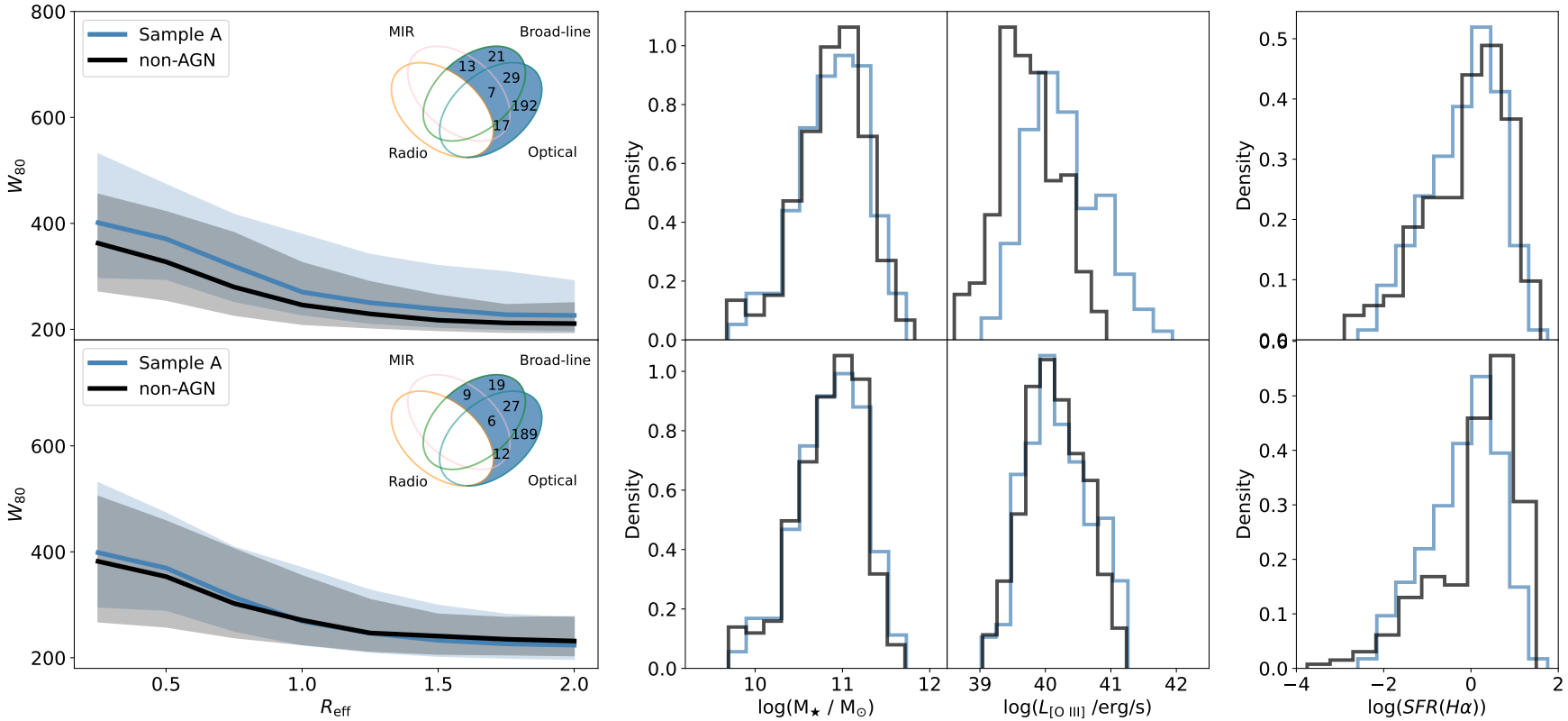

Figure 2.7. Comparison of stacked W_{80} profiles and host galaxy properties between non-AGNs and sample A. In each plot, blue corresponds to the behavior of a specific parameter for sample A (see Sect. 2.4.1) and black for non-AGNs. For each column of plots, from left to right, we show the W_{80} stacked radial profile, the $\log(M_\star)$ distribution, the $\log(L_{[\rm O\ III]})$ distribution, and the $\log(\rm SFR(H\alpha))$ distribution. The plots in the bottom row show how both samples behave after they are matched to have the same $\log(M_\star)$ and $\log(L_{[\rm O\ III]})$. The plots in the top row show how both samples behave if the matching is done only for $\log(M_\star)$. The Venn diagrams shown in each W_{80} plot represent sample A. The discrepancy in the Venn diagram numbers in sample A arises from the incorporation of $L_{[\rm O\ III]}$ into the control.

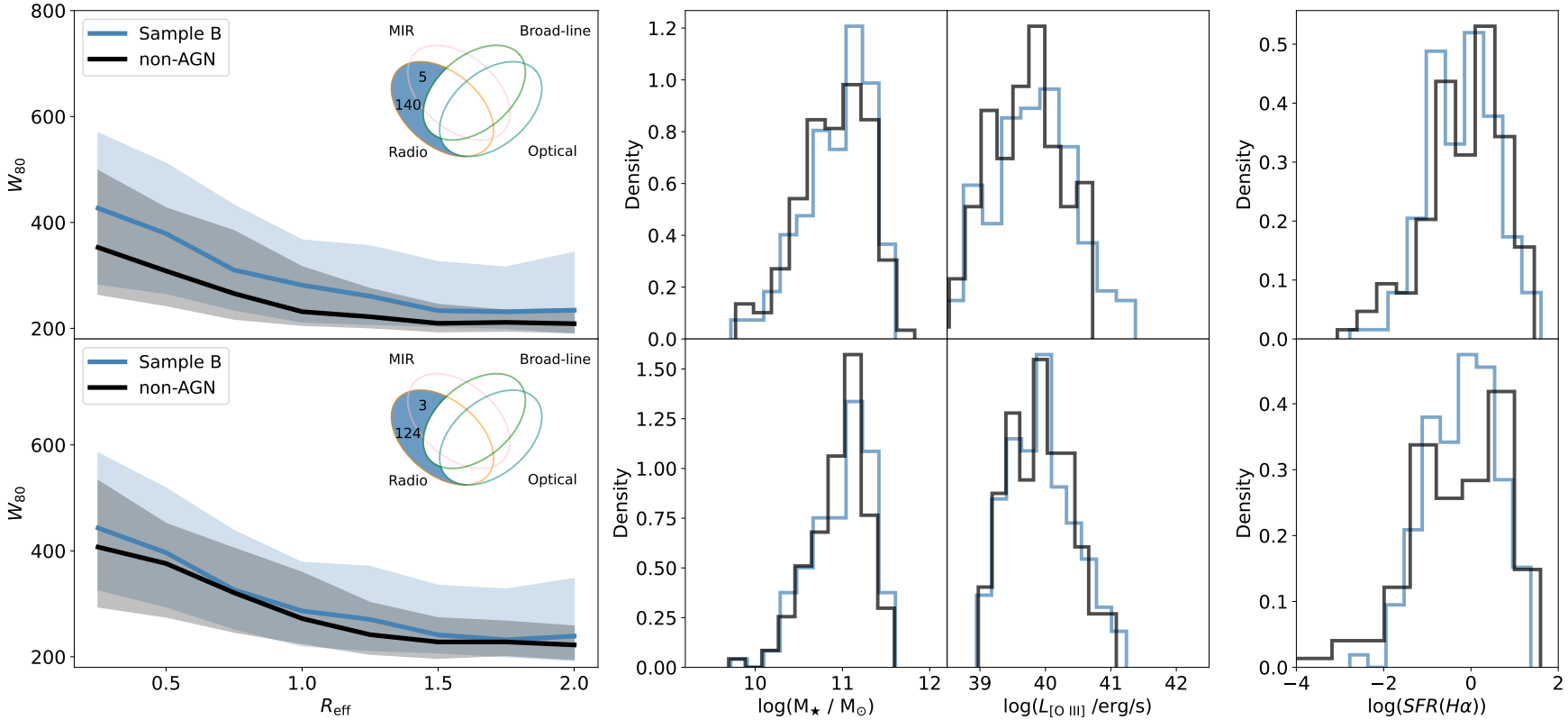

Figure 2.8. Comparison of stacked W_{80} profiles and host galaxy properties between non-AGNs and sample B. Same as Fig. 2.7 but comparing non-AGNs (black) to sample B (blue).

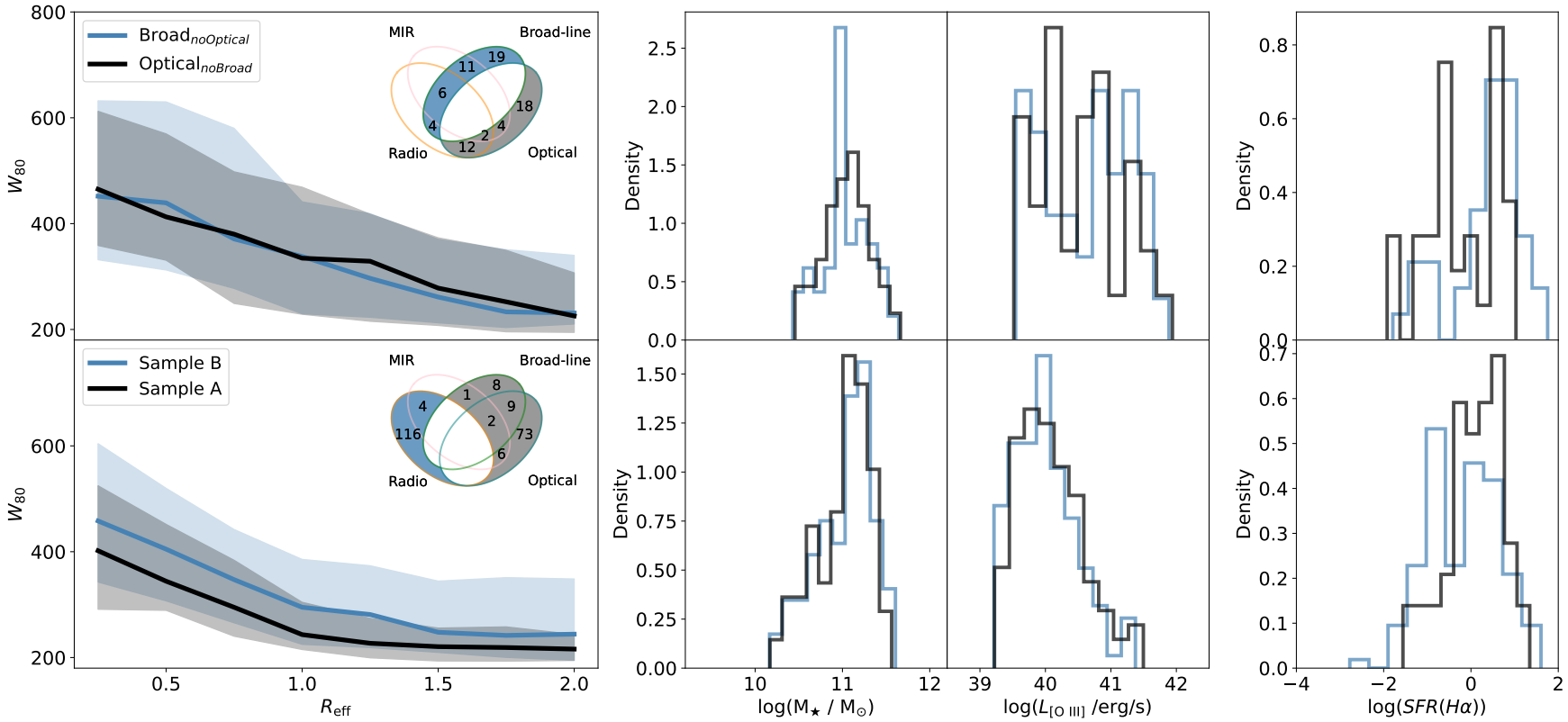

Figure 2.9. Comparison of stacked W_{80} profiles and host galaxy properties between different AGN samples. The plots in the top and bottom rows show how both samples behave after they are matched to have the same $\log(M_\star)$ and $\log(L_{[\rm O\ III]})$. The Venn diagrams shown in each W_{80} plot represent the AGN sample in the label. Top: Blue for optically selected (without broad-line-selected) and gray for the opposite. Bottom: Blue for sample B and gray for sample A. For each column of plots, from left to right, we show the W_{80} stacked radial profile, the $\log(M_\star)$ distribution, the $\log(L_{[\rm O\ III]})$ distribution, and the $\log(\rm SFR(H\alpha))$ distribution.

Gatto et al. (2024) find that both AGNs and control galaxies have $L_{[\mathrm{O\ III}]}$ values that correlate positively with their average W_{80}. We see that their control sample has a median $L_{[\mathrm{O\ III}]}$ that is ∼1 dex lower than the ones from an AGN. Therefore, in our analysis, we ask whether the kinematic differences are still present between non-AGNs and AGNs if $L_{[\mathrm{O\ III}]}$ is taken into account during the control (this removes the most luminous AGNs). Under these conditions, we observe that AGNs and controls are more alike in terms of their W_{80} values (see the discussion in Sect. 2.5).

With this approach, we aim to assess the question of whether the current nuclear activity is responsible for the enhanced radial profiles in the AGN populations, and if so, to what extent these perturbations are spreading. We also seek to investigate how the kinematics may be dependent on the AGN selection technique. Therefore, we look at the W_{80} radial profiles comparing non-AGNs (see Figs. 2.7 and 2.8) with the following samples:

- Sample A: Targets selected via optical or broad lines, excluding the ones selected via radio.
- Sample B: Targets selected via radio but not via optical or broad lines.

We do not observe a significant difference (in terms of ionized gas kinematics) between optically selected and broad-line-selected AGNs (see the details in Sect. 2.4.2). This is the main reason why we merged them when defining sample A and sample B for the purpose of comparing them with radio-selected AGNs.

We present a comparison between non-AGNs and AGNs, using as a control sample of non-AGNs first matched only in stellar mass, morphology, and redshift, and later including $L_{[\mathrm{O\ III}]}$ in the parameter match (as was mentioned at the beginning of this section). Figure 2.7 shows two rows of plots. The top row shows the W_{80} radial profiles as well as histograms of host galaxy properties of sample A and non-AGNs without including $L_{[\mathrm{O\ III}]}$ during the match. The bottom row shows the comparison considering $L_{[\mathrm{O\ III}]}$ during the match. We note that the latter matching procedure leads to the removal of the most extreme AGNs in sample A exhibiting the highest $L_{[\mathrm{O\ III}]}$. The shaded areas in the radial profiles show the 14th and 86th percentiles as in Fig. 2.4, while the histograms report the $M_\star$ and $L_{[\mathrm{O\ III}]}$ (both parameters used during the match) and the SFR($H\alpha$) (same SFR used in Fig. 2.1), which was not used for the match.

The upper left plot shows that sample A has greater W_{80} values at all annuli than non-AGNs when only the $M_\star$ is considered during the match. We can see that $L_{[\mathrm{O\ III}]}$ is systematically lower for non-AGNs. As was mentioned above, Gatto et al. (2024) find that their non-AGN control sample has [O III] line widths that correlate with [O III] luminosity. If we include the $L_{[\mathrm{O\ III}]}$ (bottom left plot of Fig. 2.7), the median W_{80} value at all annuli of sample A and the non-AGN sample behaves similarly. While there might be a small difference at small radii $R_{\mathrm{eff}} < 0.5$, at large radii, there is no difference between both samples. This suggests that the stacked W_{80} radial

profiles of optically selected AGNs together with broad-line-selected AGNs can be easily reproduced by non-AGN hosts with the same distribution of mass, $M_\star$, and $L_{[\mathrm{O\ III}]}$.

In contrast to sample A, sample B (see Fig. 2.8) shows higher W_{80} values compared to non-AGNs. Remarkably, the most significant difference between non-AGNs and sample B is seen at the largest annuli, where high W_{80} values are achieved by sample B. Excluding optically (and broad-line) selected samples from our radio-selected AGNs systematically removes AGNs with low W_{80} at larger annuli. For sample A, it appears that excluding radio-selected AGNs from optically (or broad-line) selected samples consistently removes the W_{80} kinematic excess at larger annuli.

2.4.2 AGNs versus AGNs

In Fig. 2.4, we find that our broad-line-selected AGNs tend to have larger $L_{[\mathrm{O\ III}]}$ than optically selected AGN galaxies. Therefore, in the top panel of Fig. 2.9, we match the two samples within $39.4 < \log(L_{[\mathrm{O\ III}]}) < 42.1$ and $10.4 < \log(M_\star) < 11.7$ (limits within which the parameter distribution can be matched) and compare the two samples: optically selected AGNs excluding broad-line-selected AGNs and vice versa. We find that the median W_{80} radial profile of broad-line-only AGNs is similar to the optically selected AGNs (excluding broad-line AGNs) when both samples are matched in host galaxy properties, with a small excess in the center for the broad-line-selected AGNs (see Fig. 2.9). Gatto et al. (2024) arrive at similar conclusions for their broad-line and optically selected AGNs, reporting no difference when comparing their W_{80} distributions. The results remain unchanged if we also control for inclination (b/a), ruling out possible orientation effects. Therefore, we combined these samples when setting up sample A and sample B (in Sect. 2.4.1).

We now proceed with comparing sample A with sample B directly. As before, we also match the samples in $M_\star$ and $L_{[\mathrm{O\ III}]}$, redshift and morphology. When excluding radio-selected sources from the optically selected AGN catalog (sample A), we do not claim that the remaining optically selected AGNs have no AGN-related radio emission, but we rather aim to investigate kinematic properties of a sample that would not have been detected as AGNs through radio techniques and vice versa.

In the bottom left panel of Fig. 2.9, we present the W_{80} radial profiles of sample A and sample B. Sample A is forced to match sample B within $39.2 < \log(L_{[\mathrm{O\ III}]}) < 41.5$ and $10.1 < \log(M_\star) < 11.7$. Sample B (represented in blue) shows elevated W_{80} values across all annuli, notably at large R_{eff}, aligning with the findings in Sect. 2.4.1. This comparison suggests that while optical and broad-line selection methods can identify AGN hosts with perturbed kinematics extending to large galactocentric distances, the absence (or exclusion) of radio-selected AGNs (as in sample A, shown in gray) results in a population characterized by systematically reduced kinematic disturbances at these distances. Conversely, when optically and broad-line-selected AGNs are removed from a radio-selected sample (as in sample B), the remaining

AGN hosts predominantly exhibit significant kinematic perturbations, especially at extended $R_{\rm eff}$ scales. This suggests that AGN radio-selection techniques are sensitive to finding AGN hosts with disturbed kinematics over larger galactocentric distances.

A key takeaway message is that the selection technique is sensitive to the kinematics found in AGN galaxies and might also be sensitive to the evolutionary stage of the AGN (see the Discussion section). We point out that employing alternative cutoff lines in our radio selection technique (e.g., 1.5 dex; see Sect. 2.2.2 and Fig. 2.1) produces similar outcomes. As is illustrated in Fig. 2.4, a larger cutoff would also result in a cut in the stellar mass. However, this would also substantially reduce the number of targets. Our results concerning radio AGNs are very similar if we consider a different SFR estimator (as is mentioned in Sect. 2.2.2) when selecting our radio sample.

2.4.3 Star-forming galaxies versus AGNs

We performed a similar comparison between AGNs and (see Sect. 2.2.2) SF galaxies (as classified by BPT diagnostics). We find that SF galaxies have a lower median W_{80} radial profile compared to any of the AGN-selected samples (AGNs were excluded from the SF galaxy sample, although only 15 AGNs overlap with it). Furthermore, SF galaxies indeed have higher SFRs than our selected AGNs and even higher SFRs when controlling for $M_\star$ and $L_{[\rm O\ III]}$ to a specific AGN selected population (they also have younger D4000 ages and higher Hα equivalent widths). This suggests that SF galaxies (at least, BPT-classified ones) in MaNGA do not seem to be responsible for driving significant ionized gas outflow signatures, even when they have significantly higher SFRs.

Lastly, in Sect. 2.3.2, we described how we only used galaxies with at least two available annuli where at least 10% of their spaxels have S/N > 7. This quality criteria results in some galaxies having no W_{80} values in some of their annuli. To control for a possible impact of this decision, we have studied the same comparisons described in this section with two samples: one where we use all the galaxies and all their spaxels that have a S/N > 3 (low S/N), and the other one where we only use galaxies that have at least six available annuli where at least 10% of their spaxels have S/N > 7 (a high S/N constraint). Using the latter samples, we confirm that the behavior described in this section is still present for all the comparisons.

2.5 Discussion

2.5.1 AGN selection and their integrated host galaxy properties

In this paper, we find that different AGN selection techniques select AGN samples that hardly overlap in more than 50% of their targets. Similar results have been found in Oh et al. (2022) at $z < 0.2$ when comparing X-ray-selected AGNs to optically

selected ones. Additionally, for higher redshifts ($0.25 < z < 0.8$), in a sample of mid-infrared, radio, and X-ray-selected AGNs, Hickox et al. (2009) find that AGN candidates hardly overlap (their radio selection is at $L_{1.4\ GHz} > 10^{23.8}$ W Hz^{-1}). These findings pose a clear challenge for AGN studies, since AGNs found by the different selection techniques do not always trace the same host galaxy properties and/or AGN accretion state (Hickox & Alexander 2018b).

We find that our radio-selected AGNs are typically found below the SFMS. Similar results have been found, specifically for MaNGA (Comerford et al. 2020; Mulcahey et al. 2022) and other low-redshift studies (e.g. Smolčić 2009). Accordingly, Sánchez et al. (2022) find that optically selected AGNs lie below the SFMS in the Green Valley. Additionally, Schawinski et al. (2007) find that SF galaxies, composite, and AGNs (all optically selected) seem to follow an evolutionary sequence in the star formation and stellar mass plane, with SF galaxies having bluer colors and AGNs found more in the transition zone. Our composite-selected targets are also found between SF and AGN-selected galaxies in the $M_\star$ versus SFR plane. Hickox et al. (2009) obtained similar results and were also in agreement with our mid-infrared selected targets, which they concluded are more likely to be found in slightly more SF hosts. They propose an evolutionary interpretation whereby, as star formation decreases, AGN accretion changes from optical or infrared-bright to optically faint radio sources. These findings suggest that AGN selection techniques are sensitive not only to the physical processes powering them but also to the stage of their duty cycle. We discuss this further in Sect. 2.5.3.

2.5.2 Spatially resolved ionized gas kinematics

We first investigated the radial properties of the [OIII] ionized gas kinematics of unmatched AGNs and non-AGN samples, showcasing a diverse range of ionized gas kinematics (this was done before controlling for host galaxy properties; see Fig. 2.5). Non-AGN and SF galaxies exhibit less disturbed kinematics compared to all AGN samples (lower W_{80} radial profiles).

When comparing AGN samples matched in $M_\star$ and $L_{[O\ III]}$, intrinsic distinct kinematic behaviors emerge. Specifically, the exclusion of radio-selected AGNs from an optical and broad-line-selected AGN sample (sample A) results in lower W_{80} values at greater galactocentric distances, suggesting that much of the kinematic disturbances within an optically selected sample are linked to the radio emission in AGNs (see more discussion on the connection of outflows and radio emission in the next section).

The analysis of sample A also reveals that there is a population of non-AGN galaxies that can easily produce AGN-like W_{80} profiles when controlling for host galaxy properties (see bottom left panel of Fig. 2.7). Simulations suggest that kiloparsec-scale AGN-driven outflows can outlast the AGN activity phase, extending from a few to several orders of magnitude longer in duration (a few Myr, King et al. 2011; Zubovas 2018). For example, Zubovas et al. (2022) predict that fossil outflows (outflows taking

place after the AGN switches off) could actually be more common than finding an outflow and an AGN in a galaxy simultaneously. Consequently, MaNGA non-AGN galaxies may include some galaxies showing fossil outflows. The possible presence of fossil outflows in MaNGA galaxies will be discussed in a future paper.

2.5.3 Radio-selected AGNs as tracers of the final phases of AGN evolution

We find that AGNs identified through radio techniques alone (sample B) show notably stronger kinematics at larger R_{eff} than any other AGN sample. The presence of AGN-related radio emission in AGNs may therefore seem to trace AGNs with more spatially extended outflows.

One explanation for this behavior may be that sources with AGN-related radio emission trace host galaxies that have been experiencing AGN activity (or activities; see below) for a longer time. However, kinematic perturbances up to kiloparsec scales would typically imply an active (AGN) phase longer than the duration of a typical AGN duty cycle. For example, King et al. (2011) used analytical models to study the outflow propagation during an AGN event. They showed that an outflow with an initial velocity of a couple of hundred km s^{-1} in an AGN episode lasting about ∼1 Myr can last up to ten times longer than the AGN itself, reaching several kiloparsecs.

Alternatively, radio-selected AGNs may be sensitive to AGNs that have gone through multiple cycles of AGN activity. Indeed, some galaxies show evidence of past and recurring AGN events (e.g., Rao et al. 2023; Schawinski et al. 2015; Shulevski et al. 2015). Recent studies have used low-frequency (MHz) radio spectra combined with high-frequency (GHz) spectra to trace back emissions from previous activities (e.g., Jurlin et al. 2020). A younger AGN phase is characterized by a peaked spectrum in the center, while a remnant from past events displays a more spread-diffuse emission. Therefore, if a combination of the latter is observed in one target, it can suggest the target is a strong candidate for a restarted AGN phase. In this context, Kukreti et al. (2023) find that around 6% of the targets in their sample (at 10^{23}W Hz^{-1} > L1.4 GHz > 10^{26}W Hz^{-1}, $0.02 < z < 0.23$) are peaked sources classified as compact in GHz frequencies but have extended emission at MHz frequencies, suggesting that they are restarted AGN candidates.

Also, the simulations from Zubovas & Maskeliūnas (2023) show that fossil outflows in gas-poor systems tend to last longer than in gas-rich hosts. Radio-selected AGNs, indeed, are preferentially found in gas-poor galaxies.

With respect to an AGN's impact on its host galaxy, a recent review by Harrison & Ramos Almeida (2024) discusses that simulations predict that feedback that leads to galaxy quenching does not come from a single AGN event but is rather a cumulative effect of multiple AGN episodes (see also Piotrowska et al. 2022). Thus, given the findings in our analysis, AGNs selected through radio observations may preferentially trace galaxies that have experienced episodic AGN events (Morganti 2017a). Sample

B indeed contains host galaxies with older stellar populations (compared to sample A), traced by average D4000 measurements from the PiPE3D catalog.

In a sample of radio-selected AGNs from MaNGA MPL-8, Comerford et al. (2020) find that radio-mode AGN-hosting galaxies reside preferentially in elliptical galaxies that have more negative stellar age gradients with galactocentric distance. The authors suggest that radio-mode AGNs may represent a final phase in the evolution of an AGN. In addition, Hickox et al. (2009) proposed a scenario in which radio AGNs are key to the late stages of galaxy evolution, with them being in general more passive and having lower Eddington ratios than their infrared and optical counterparts. In fact, radio-selected AGNs typically have larger black hole masses (Best et al. 2005; Hickox et al. 2009). Interestingly, the latter parameter is found to be a strong predictor for galaxy quenching (Piotrowska et al. 2022). These results are in line with the work presented here on the spatially resolved ionized gas kinematics in radio-selected AGNs, which suggests that radio selection methods may be used to identify AGNs at a more advanced stage of their activity (and feedback) cycle. Lastly, we note that most of the removed radio-selected AGNs (see Sects. 2.3.2 and 2.3.3) are massive galaxies with low SFRs (see Fig. 2.1), located near the red sequence, suggesting an even later evolutionary phase.

2.5.4 The connection between radio-emission and outflow activity in AGNs

Our results discussed above raise the question of what mechanisms are responsible for the observed radio emissions. The possible origins of radio emission in low-luminosity radio AGNs is reviewed in Panessa et al. (2019). The review discusses several mechanisms such as jets, winds, accretion disk corona, and star formation. In the context of our work, winds are discussed as a mechanism in which a shock is driven by the wind (e.g., Riffel et al. 2021) and produce radio emission due to the acceleration of relativistic electrons on sub-kiloparsec scales. Similarly, in a small sample of AGNs ($z < 0.07$), Mizumoto et al. (2024) found that NLR-scale shocks (traced by [Fe II]/[P II]; see Oliva et al. 2001) are likely triggered by ionized outflows (traced by [S III] in Mizumoto et al.).

Notably, in a sample of galaxies at $z < 0.8$, Zakamska & Greene (2014) show that the radio luminosity in formally radio-quiet AGNs correlates with the [O III] velocity width, which is consistent with our findings. Zakamska & Greene (2014) propose two scenarios: one in which radio emission is produced by accelerated particles as a result of shock fronts due to outflows (extended and diffuse radio emission), and another one in which an unresolved radio jet (unresolved in FIRST/NVSS data) is launching an outflow (expected to be compact). We argue that both scenarios could simultaneously be present in one system (e.g., if the galaxy had more than one recent AGN event). High-spatial-resolution radio observations would be needed to distinguish between them.

Calistro Rivera et al. (2023) arrive at similar conclusions by analyzing the CIV and [O III] velocities (in a sample of ∼100 AGNs). They discover minimal or no correlation between the CIV velocities and radio luminosity, in contrast to a connection between the [OIII] velocity width and radio luminosity. Given that CIV emission originate from within the broad-line region (sub-parsec scales), and [O III] emission traces ionized gas on galactic or kiloparsec scales, Calistro Rivera et al. (2023) conclude that the interplay between winds and radio luminosity predominantly occurs on these circumnuclear scales. Similarly, Liao et al. (2024) not only shows that [O III] velocity widths of AGNs (in their sample: $z < 1.0$, and a median $\log(L_{[O\ III]}) \sim 42.1$) correlate with radio emission but also that the conversion efficiencies align with those needed to account for the observed radio luminosities in galaxies exhibiting large [O III] velocity widths. Their results also support the idea that AGN-driven outflows contribute to the radio emission in AGNs.

While the results discussed above suggest a connection between the radio emission and the ionized gas kinematics in AGNs, we note that they were done predominantly using single fiber spectra and investigating higher-redshift galaxies ($z \lesssim 0.8$), averaging the gas kinematics over larger areas. Our work adds to the picture using a spatially resolved kinematic analysis and while we cannot exclude the presence of jetted radio-AGNs in our radio-selected sample, our results also suggest that there is a strong connection between radio activity and ionized gas outflows in AGNs.

2.5.5 Star-forming galaxies

We find that SF galaxies show less enhanced kinematic profiles when compared to AGN candidates, even when controlling for $M_\star$, $L_{[O\ III]}$, morphology, and redshift. A detailed comparison between sample A and SF galaxies highlights that sample A demonstrates significantly higher W_{80} values within its central regions. In contrast, such differences fade at larger effective radii (R_{eff}), where the kinematic behaviors of both populations (sample A and the matched star formation sample) align closely. Moreover, the matched SF galaxy sample exhibits higher star formation rates than sample A (and higher than the SF sample before matching). In a larger sample (> 50000) of local ($0.05 < z < 0.1$) SF galaxies, Yu et al. (2022) study the ionized gas kinematics of these galaxies, finding that they can indeed present outflow signatures. But the authors also show that the SF sample hardly ever reaches $\sigma > 150$ km s^{-1}; that is, $W_{80} > 375$ km s^{-1}. This is consistent with our findings. Therefore, we infer that the enhanced W_{80} values in our AGN-selected population are likely driven by AGNs and do not expect SF processes to play a significant role.

However, the most massive ($M_\star > 10^{11} M_\odot$) SF galaxies in our sample reveal remarkably high W_{80} values (although not as high as those of AGNs). Sabater et al. (2019) found that 100% of the galaxies with masses above this limit ($10^{11} M_\odot$) host radio AGNs even though sometimes with radio luminosities ($L_{150\ MHz} > 10^{21.5}$ W Hz^{-1}, or $L_{1.4\ GHz} \gtrsim 10^{21}$ W Hz^{-1}; most of our galaxies are above this limit). Indeed, $> 50\%$

of massive SF galaxies in our sample have radio detections, while only $\sim 10\%$ of lower-mass SF galaxies ($< 10^{11} M_{\odot}$) have radio detections. This suggests that some of our massive SF galaxy populations may be AGNs as well.

2.6 Summary and conclusions

We have assembled a multiwavelength AGN-selected sample for the SDSS-IV MaNGA-DR17, comprising 594 unique AGNs identified through optical, hard X-ray, radio, infrared, and broad-line selection techniques. We seek to explore the extent to which ionized gas kinematics, quantified by W_{80} of [O III]λ5007, is influenced by the diversity in AGN selection methods, thereby offering insights into feedback processes and the duty cycle of AGN activity. To do so, we fit up to two Gaussian components to the [O III]λ5007 emission-line region in all spaxels ($S/N > 7$; see Sect. 2.3.2) of each galaxy and derived the W_{80} velocity widths (see Sect. 2.4). We then mapped the spatial distribution of this parameter for each galaxy. Furthermore, we created W_{80} radial profiles and stacked them according to each defined AGN subsample. Our findings are summarized as follows:

- We find that different AGN selection techniques do not completely overlap with each other. Overlap ranges from $\sim$34% (e.g., between radio and optical selection) up to $\sim$80% (the latter percentage only achieved by the X-ray selection, although it is the smallest sample).

- The different AGN populations are found in galaxies with different host galaxy properties. The most significant differences are found in the distribution of $L_{[O\ III]}$, EW($H\alpha$), D4000, and the W_{80} radial profiles.

- Regarding AGNs versus non-AGNs: Regardless of the selection technique, all AGN populations show more perturbed ionized gas kinematics (traced by W_{80}) at all annuli when compared to non-AGNs of similar $M_{\star}$ of the host, redshift, and morphology. These kinematic differences become less pronounced when $L_{[O\ III]}$ is taken into account in the non-AGN control sample. Remarkably, the differences between AGNs and non-AGNs disappear when we compare pure optical (BPT and broad-line, but excluding radio-detect AGNs: sample A) AGNs to non-AGNs (see Sect. 2.4.1). We suggest that some non-AGNs may host fossil outflows (i.e., relic outflows of a past AGN phase), which may outnumber outflows in currently active AGNs (Zubovas et al. 2022).

- Regarding AGNs versus AGNs: Our different AGN samples display not only hosts with different properties but also hosts with differences in the stacked radial profiles of their kinematic signatures. Interestingly, when controlling for host galaxy properties, we find that removing radio-selected AGNs from optically selected candidates leaves a sample (sample A) of galaxies that lack

significantly high W_{80} at high R_{eff}, suggesting that many of the kinematic disturbances within an optically selected sample are linked to the radio emission in AGNs. In addition, radio-selected AGNs show more enhanced ionized gas kinematics at all radii and their hosts show evidence of older stellar populations. Our results support a scenario in which radio selection methods may be used to identify AGNs at a more advanced stage of their activity (and feedback) cycle.

- AGNs versus SF galaxies: SF galaxies in our sample do not show significant kinematic signatures in the ionized gas compared to AGNs (regardless of the selection technique; see Sect. 2.2). We highlight that when controlling for $L_{[O\ III]}$ and $M_\star$ when comparing AGNs to non-AGNs, SF galaxies tend to have significantly larger SFR(Hα)) than AGNs. We conclude that in our sample the main driver of the enhanced kinematic signatures in AGNs cannot be accounted for by star formation processes alone.

Our study shows that a given AGN selection technique can impact what sorts of ionized kinematic signatures are found in their host galaxies. Our results have been tested in low-redshift ($z < 0.1$) galaxies with low to intermediate luminosities. The impact of AGN selection techniques could be more significant at higher redshift. Moreover, our results highlight the importance and utility of spatially resolved spectroscopy.

Chapter

3

Feedback from low-to-moderate-luminosity radio-active galactic nuclei with MaNGA

Authors: Pranav Kukreti, Dominika Wylezalek, Marco Albán and Bruno Dall'Agnol de Oliveira

Astronomisches Rechen-Institut, Zentrum für Astronomie der Universität Heidelberg, Münchhofstr. 12-14, 69120 Heidelberg, Germany

Published in A&A, 698, A99 (2025)

Dr. Pranav Kukreti is the main author of this paper, and his work is reproduced here under his permission. This paper is a project elaborated by Pranav Kukreti, and he produced all the text and figures. The text has been adapted to English spelling, and figures have been adapted to the format of this thesis. Marco Albán contributed significantly to this article in many aspects: (1) providing data used in this paper, particularly maps of the fitting results on the [O III] emission-line region for all the galaxies (which contained [O III] W_{80}, noise maps, S/N, etc) and assisting on how to use them, (2) sharing the codes to (a) combine the maps according to the best fitting result, and (b) to produce radial profiles of each map (3) provide active discussion that helped shaping the context of the article. The latter contributions were essential to producing the figures used in this work. Dominika Wylezalek majorly assisted during the development of this work and Bruno Dall'Agnol de Oliveira provided helpful discussion and comments throughout its development.

ABSTRACT

Context. Spatially resolved spectral studies of galaxies hosting a radio-active galactic nucleus (radio-AGN) have shown that these systems can impact ionized gas on galactic scales. However, it is still unclear whether jet and radiation-driven feedback occurs simultaneously. The relative contribution of these two mechanisms in driving feedback in the AGN residing in the Local Universe is also poorly understood.
Aims. We selected a large and representative sample of 806 radio-AGN from the MaNGA survey, which provides integral field unit (IFU) optical spectra for nearby galaxies. We define radio-AGN as sources having excess emission above the level that is expected from star formation. We aim to study the feedback driven by radio-AGN on the galaxy's ionized gas, its location, and its relation to AGN properties. We also aim to disentangle the role of jets and radiation in these systems.
Methods. We used a sample of nearby radio-AGN from $L_{1.4\mathrm{GHz}} \approx 10^{21} - 10^{25}\,\mathrm{W\,Hz^{-1}}$to trace the kinematics of the warm ionized gas phase using their [O III] emission line. We measured the [O III] line width and compared it to the stellar velocity dispersion to determine the presence and location of the disturbed gas. We investigated the dependence of radial profiles of these properties on the presence of jets and radiation, along with their radio luminosities.
Results. We mainly found disturbed [O III] kinematics and proportion of disturbed sources up to a radial distance of $0.25\,R_{\mathrm{eff}}$, when both radio- and optical-AGN are present in a source, and when the radio luminosity is greater than $10^{23}\,\mathrm{W\,Hz^{-1}}$. When it is either only radio- or optical-AGN present, the impact on [O III] is milder. Irrespective of luminosity and the presence of an AGN, we find no evidence for feedback from radio-AGN on [O III] kinematics at radial distances larger than $0.25\,R_{\mathrm{eff}}$.
Conclusions. The presence of more kinematically disturbed warm ionized gas in the central region of radio-AGN host galaxies is related to both jets and radiation in these sources. We propose that in moderate-radio-luminosity AGN ($L_{1.4\mathrm{GHz}} \approx 10^{23} - 10^{25}\,\mathrm{W\,Hz^{-1}}$), the gas clouds pushed to high velocities by the jets (radiation) are driven to even higher velocities by the impact of radiation (jets) when both radio- and optical-AGN are present. At lower luminosities ($L_{1.4\mathrm{GHz}} \approx 10^{21} - 10^{23}\,\mathrm{W\,Hz^{-1}}$), the correlation between the disturbed ionized gas and enhanced radio emission could either be due to wind-driven shocks powering the radio emission or low-power jets disturbing the gas. Finally, beyond $0.25R_{\mathrm{eff}}$, the lack of any disturbed [O III] suggests a weak coupling between the jets and the ionized gas in these sources.
Key words. evolution - galaxies: interactions - galaxies: jets - ISM: jets and outflows - galaxies: evolution - galaxies: active

3.1 Introduction

Feedback from active galactic nuclei (AGN) is a critical component of models of galaxy evolution. A fraction of the energy released during an AGN phase can couple with

the gas of the host galaxy, preventing it from forming stars. This kind of negative feedback is used to explain the cessation of star formation in massive galaxies that would otherwise be too large and too massive (e.g. Di Matteo et al. 2005; Fabian 2012; Silk & Rees 1998). The radiative and mechanical energy required for this feedback can be carried by accretion-driven winds, radiation pressure, collimated jets of plasma, and other effects (see Harrison & Ramos Almeida 2024; King & Pounds 2015 for a review).

On intergalactic scales, the released energy can prevent the cooling and eventual accretion of gas from the hot halos surrounding galaxies, which fuels star formation (McNamara & Nulsen 2007, 2012). On galactic scales, AGN-driven feedback can shock the gas clouds, making them turbulent and sometimes even pushing them to high velocities (outflows). This prevents the gas clouds from collapsing to form stars. These processes occur on different physical scales and timescales, therefore, an understanding of how AGN interact with their host galaxies is crucial. Over the past few years, many studies have found evidence for negative feedback on galactic scales, attributed to both radiatively efficient and inefficient AGN (e.g. Morganti 2021; Murthy et al. 2019; Speranza et al. 2021; Venturi et al. 2021).

Statistical studies of large samples have found a positive correlation between the presence of an AGN and its energy output, as well as the presence of kinematically disturbed gas (e.g. Kukreti & Morganti 2024; Mullaney et al. 2013; Santoro et al. 2020; Woo et al. 2017), albeit with spatially unresolved spectra. Although it is useful to understand the population as a whole, these unresolved spectra cannot provide information about the location of the disturbed gas or the affected stellar population in the galaxy. This spatial information is needed to understand the scales of AGN-driven feedback occurring in galaxies.

Spatially resolved spectra from an integral field unit (IFU) can provide information about the gas and stellar emission at different locations in the host galaxy. This has led to the discovery of a number of trends between the spatial distribution of the disturbed gas and the energy released by the AGN. For example, a positive correlation between the size of the kinematically disturbed ionized gas region and the radiative luminosity has been found for AGN with radiatively efficient accretion (Seyferts, Quasars; e.g. Gatto et al. 2024; Kang & Woo 2018; Kim et al. 2023). For similar sources, positive correlations have also been found between the width of the emission line profiles tracing the disturbed gas and the radiative luminosity (e.g. Deconto-Machado et al. 2022; Wylezalek et al. 2020). This illustrates the role of radiation in driving feedback in AGN host galaxies. However, such systematic spatially resolved studies in radiatively inefficient AGN where jets are prominent have rarely been conducted. It is important to study feedback in sources where both the jets and radiation from the AGN are present, so that we can understand the role and relative contributions of these two mechanisms.

Studying feedback in radio-AGN hosts can help us gain key insights in this direction. In this paper, we define radio-AGN as sources with excess radio emission above

the level expected from star formation. However, we note that the definition is not uniform across the literature. Although the excess radio emission in radio-AGN is often due to collimated plasma jets launched during the active phase, in some low-luminosity sources, it can also originate from shock interactions between AGN-driven winds and the interstellar medium (ISM; Zakamska et al. 2016b), relating the radio emission to the radiative output of the AGN. A large fraction of radio-AGN have radiatively inefficient accretion, but a significant proportion also show radiatively efficient accretion. This makes them ideal for improving our understanding of the role of the mechanical and radiative energy output of an AGN.

Many studies have found observational evidence for jet-driven feedback on the ionized gas in these galaxies using IFU data. However, these studies have mostly been focused on single objects or small samples (e.g. Cresci et al. 2023; Girdhar et al. 2022; Jarvis et al. 2021, 2019; Nesvadba et al. 2021; Riffel et al. 2023; Ruffa et al. 2022; Speranza et al. 2021; Ulivi et al. 2024; Venturi et al. 2021). Studies of large samples of radio-AGN with spatially resolved spectra have been challenging to perform due to the lack of IFU data for a large sample of galaxies. This can now be achieved with the Mapping Nearby Galaxies at APO (MaNGA) survey (SDSS-IV), which is the largest IFU survey till date, covering a sample of $\sim$10,000 galaxies over a redshift range of $0.01 < z < 0.15$. This survey provides spatially resolved spectra from 3600−10300Å, which covers emission lines such as [O III] , Hβ, Hα, [NII], and others that can serve as good indicators of AGN interaction and ionization. Recently, Albán et al. (2024) identified AGN in MaNGA using multi-wavelength data and they studied the warm ionized gas kinematics using the [O III] line. They found evidence for enhanced ionized gas kinematics over galactic scales for radio-AGN compared to optical-AGN, suggesting that radio-AGN might be tracing AGN at an advanced stage of the activity and feedback cycle.

We use the MaNGA survey data to study feedback from radio-AGN on the host galaxy's warm ionized gas ($T \sim 10^4$ K), using the [O III] $\lambda\lambda$4958,5007Å doublet as a tracer. We use two radio surveys: the LOFAR Two-metre Sky Survey at 144 MHz (LoTSS; Shimwell et al. 2022, 2017) and the Faint Images of the Radio Sky at Twenty-cm survey at 1400 MHz (FIRST; Becker et al. 1995) to identify the largest sample of radio-AGN from MaNGA. We trace the ionized gas using the [O III] emission line and determine the physical scales on which the radio-AGN impacts it. Our main aim is to disentangle the role of jets and radiation in driving feedback on warm ionized gas and determine the impact of these two mechanisms when they are present in the same source. The large size of these three surveys, combined with the high sensitivity of LoTSS to faint radio emission, allows us to cover a large range of radio luminosities from $L_{1.4\mathrm{GHz}} \approx 10^{21} - 10^{25}$ W Hz^{-1}. This makes the sample a good representative of the radio-AGN population in the Local Universe and ideal for investigating and understanding their potential feedback mechanisms.

This paper is structured as follows. Section 3.2 describes the sample construction and selection of radio-AGN. Section 3.3 describes the modeling of the stellar contin-

uum and emission line profiles of the sources. We present the results for different source groups in Sect. 3.4, discuss them in Sect. 3.5 and summarize our results in Sect. 3.6. Throughout the paper, we use the ΛCDM cosmological model, with $H_0 = 70$ km s^{-1} Mpc^{-1}, $\Omega_M = 0.3$, and $\Omega_{vac} = 0.7$.

3.2 Sample construction

This section outlines the approach used to select the radio-AGN, optical-AGN, and control sample of non-AGN. The MaNGA survey provides a wavelength coverage over $3600 - 10300$ Å with a spectral resolution of $R \sim 2000$, corresponding to a spectral line-spread function width of about $70\,\mathrm{km\,s^{-1}}$ (1σ). The IFU field of view diameter varies from $12''$ to $32''$. For more details on the survey, we refer to Bundy et al. (2015). The data reduction was performed using the MaNGA Data Reduction Pipeline (DRP), described in Law et al. (2016); Law et al. (2021). Next, the spectral fitting was done using the MaNGA data-analysis pipeline (DAP) described in Westfall et al. (2019a), which fits the stellar continuum and emission lines to the entire spectrum. Since this paper is focussed on the [O III] gas kinematics, we used the emission line-only spectra from the DAP, obtained after subtracting the stellar continuum from the reduced observed spectra. Sánchez et al. (2022) constructed a catalog of the host galaxy properties from a spectral analysis using the `pyPipe3D` pipeline (Lacerda et al. 2022). We used the stellar mass, effective radius, and ellipticity properties from their value-added catalog.

Furthermore, we removed duplicate observations from the catalog. Albán et al. (2024) carried out a careful inspection of the MaNGA data and identified new duplicate observations, then combined them with the already known duplicates from Sánchez et al. (2022) and the survey website[1]. They also removed sources flagged `CRITICAL` in the `MANGA_DRP3QUAL` column of the DRP table. Finally, this gave us a sample of 9,777 sources.

Selecting a large sample of radio-AGN from MaNGA is important to obtain statistically reliable results. LoTSS has high sensitivity and source density, whereas FIRST has a larger area overlap with MaNGA. LoTSS and FIRST have 56% and 97% sky area overlap with MaNGA, respectively. Therefore, we used both surveys to maximize the number of radio cross-matches. We cross-matched the MaNGA sample with the LoTSS DR2 ($6''$angular resolution) and FIRST ($5.4''$angular resolution) catalog using Topcat (Taylor 2005), with a $6''$ radius, which is equal to LoTSS and close to FIRST resolution. We cross-matched the sample down to flux densities of 0.3 mJy in LoTSS and 0.5 mJy in FIRST, to ensure that the detections have a $S/N > 3$. This limit is chosen to maximize the number of cross-matches with MaNGA, while keeping only reliable detections. At a search radius of $6''$, we determined a contamination level from false-positive matches of $\sim 2.5\%$ for LoTSS cross-matches and 0.7% for FIRST

[1] `https://www.sdss4.org/dr17/manga/manga-caveats/`

cross-matches (Galvin et al. 2020). We found cross-matches for 2493 sources in LoTSS and 1155 sources in FIRST. LoTSS is sensitive to extended emission around sources and therefore provides a reliable measurement of the total flux density at 144 MHz. However, FIRST has poor sensitivity to extended emission, meaning it could underestimate the total flux density at 1.4 GHz. For more reliable estimates of the total flux density at 1.4 GHz, we used the combined radio catalog from Mingo et al. (2016), which cross-matched the FIRST and NRAO VLA Sky Survey (NVSS; Condon et al. 1998). They used the flux densities from the lower resolution ($\sim 45''$) NVSS survey, which recovers the total flux better than FIRST. Finally, we used the 144 MHz and 1.4 GHz total flux densities to estimate the k-corrected total radio luminosities, $L_{144\mathrm{MHz}}$ and $L_{1.4\mathrm{GHz}}$.

The diagnostics we used to select radio-AGN were constructed and optimized using the value-added spectroscopic catalogs produced by the group from the Max Planck Institute for Astrophysics, and The Johns Hopkins University (MPA-JHU; Brinchmann et al. 2004). These include galaxy parameters measured using single fiber spectra from SDSS DR8. Since we used these diagnostics for radio-AGN selection, we used the MPA-JHU catalog measurements for our galaxies, which include the $D_{\mathrm{n}}(4000)$, [O III] , Hβ, [NII], and Hα fluxes. Using a matching radius of $6''$, we found cross-matches for 9072 sources in our sample. Since this cross-match missed some MaNGA sources, we also used the Sánchez et al. (2022) value-added catalog, which provides these measurements using a $2.5''$ aperture (similar in size to the SDSS fiber). Although we did not use the Sánchez et al. (2022) catalog measurements for all the sources, we note that using the $2.5''$ aperture values for the entire sample only leads to a small fraction of sources being classified differently, but does not change our results.

In one of the diagnostics discussed in Sect. 3.2.1, we used mid-infrared (MIR) colors to separate star-forming and passive sources. For this, we used Wide-field Infrared Survey Explorer (WISE) data from the allWISE IPAC release (November 2013; Cutri et al. 2021). This provides magnitudes in three bands: W1 at 3.4μm, W2 at 4.6μm, and W3 at 12μm, with an angular resolution of $6.1 - 6.5''$. To obtain reliable detections, we only selected sources with `cc_flag=000`, as suggested in the online user manual. We used a signal-to-noise ratio (S/N) threshold of 5 for W1 and W2 and 3 for W3 (due to its poorer sensitivity). With these criteria, we obtained a WISE cross-match for 7616 sources.

Finally, we aimed to construct radial profiles of [O III] line widths to study the spatial changes in [O III] kinematics. Galaxy morphology is an important property that can affect the gravitational motion of the gas and, thus, the spatial distribution of the [O III] line widths as well. This distribution can change depending on the relative strength of the bulge or disk component. To control for this, we added morphological classifications of the MaNGA galaxies from the Deep Learning DR17 Morphology catalog (Domínguez Sánchez et al. 2022; Fischer et al. 2019). We used the `T-Type` parameter for this purpose. Broadly, galaxies with `T-Type` < 0 are ellipticals, `T-Type` ~ 0 are S0s, and `T-Type` > 0 are late types. We controlled the `T-Type` distribution

of the different groups studied in Sect. 3.4 to ensure that the effect of morphology is not driving the trends that we have observed.

3.2.1 Selecting radio-AGN

In the Local Universe, star-forming galaxies (SFGs) dominate a radio-selected sample up to $L_{1.4\mathrm{GHz}} \approx 10^{23}$ W Hz^{-1}(Best et al. 2005; Sadler et al. 2002). Most MaNGA sources with a radio cross-match have a luminosity lower than this value. Therefore, we first need to select a clean sample of radio-AGN, namely, sources where radio emission exceeds that expected from star formation and can be attributed to the AGN in the galaxy. To this end, we use a combination of four diagnostics created by Best & Heckman (2012); Best et al. (2005) and further developed by Sabater et al. (2019). We point to these references for a detailed discussion of these methods. We first selected radio-AGN from the LoTSS cross-matched sample using diagnostics shown in Fig. 3.1 and then from the FIRST cross-matched sample using the diagnostics shown in Fig. B.1.

The first diagnostic is the '$D_{\mathrm{n}}(4000)$ versus $L_{\mathrm{radio}}/M_{\star}$' method. Here, $D_{\mathrm{n}}(4000)$ is the spectral break at 4000 Å, which is an indicator of the mean stellar age, while $L_{\mathrm{radio}}/M_{\star}$ is the ratio of radio luminosity and stellar mass. These quantities depend on the star formation rate of a galaxy and can be used to locate SFGs on a plane. Best et al. (2005) showed that SFGs broadly occupy the same region on a plot of these two quantities for a large variety of star formation histories. But in the case of radio-AGN, excess radio emission from the AGN would increase the $L_{\mathrm{radio}}/M_{\star}$ value, separating them from the SFGs. Based on this idea, Best et al. (2005) and Kauffmann et al. (2008) obtained a track to separate SFGs from radio-AGN. Sabater et al. (2019) selected radio-AGN from LoTSS-DR1 and added another track that follows the original track till $D_{\mathrm{n}}(4000) = 1.7$, then continues horizontally. They helped maximize agreement with the more sophisticated selection of SFGs by Gürkan et al. (2018) for the H-ATLAS sample and select low-luminosity radio-AGN that have high $D_{\mathrm{n}}(4000)$ values. Since MaNGA sources typically have low radio luminosities, we also used the track of Sabater et al. (2019)[2]. For L_{radio}, we used the 144 MHz and 1.4 GHz luminosity, respectively, for LoTSS and FIRST cross-matched sources. For FIRST cross-matched sources, we scaled the diagnostic tracks to 1.4 GHz, assuming an optically thin spectrum modeled as $S \propto \nu^{\alpha}$, with a spectral index of $\alpha = -0.7$. Varying α between -0.5 and -1 does the change the classification of a few sources, but does not affect our results. In the '$D_{\mathrm{n}}(4000)$ versus $L_{\mathrm{radio}}/M_{\star}$' plot in Fig. 3.1 and B.1, sources above the solid line are classified as radio-AGN, sources below the dashed line are classified as SFGs and sources between the two lines are classified as intermediate.

The second diagnostic is the $L_{\mathrm{H}\alpha}$ versus L_{radio} plot. The star formation rate of massive stars can determine both Hα and radio luminosities of galaxies. Therefore, sources with excess radio emission contribution from an AGN can be separated

[2]Both tracks were provided by Philip Best (private communication)

on a plot of these two properties. We again use the relations from Sabater et al. (2019) for the 144 MHz luminosity of LoTSS cross-matched sources: $\log(L_{\mathrm{H}\alpha}/\mathrm{L}_{\odot}) = \log(L_{144\mathrm{MHz}}/\,\mathrm{W\,Hz^{-1}}) - 16.1$ and $\log(L_{\mathrm{H}\alpha}/\mathrm{L}_{\odot}) = \log(L_{144\mathrm{MHz}}/\,\mathrm{W\,Hz^{-1}}) - 16.9$. These relations were derived to again maximize the agreement with the results of Gürkan et al. (2018) for the H-ATLAS sample to avoid any misclassification of low-luminosity sources. In the plots shown in Fig. 3.1 and B.1, sources with less $L_{\mathrm{H}\alpha}$ than the lower line are classified as radio-AGN, sources between the two lines as intermediate and above the upper line are classified as star-forming. We used Hα non-detections in cases where they provided useful upper limits on $L_{\mathrm{H}\alpha}$. For FIRST cross-matched sources, we scaled the relations mentioned above to 1.4 GHz and performed the same classification.

The third diagnostic used is the BPT diagram, where we use the [NII]/Hα and [OIII]/Hβ emission line ratios to separate sources ionized by AGN or star-formation. We used the division from Kauffmann et al. (2003) and the maximum starburst relation form Kewley et al. (2006). Sources with larger ratios than the maximum starburst curve were classified as AGN, between the two curves as intermediate and below the lower curve as star-forming. Although this does not use any radio property, it can still give information about the presence of AGN or star formation in the source. Again, we used non-detections in cases where they provided useful upper limits.

The final diagnostic is the WISE color-color diagram, between the $W1 - W2$ and $W2 - W3$ colors. Radio-AGN host galaxies are typically ellipticals, with low levels of star formation. These can be separated from star-forming galaxies based on their $W2 - W3$ color (Yan et al. 2013). Sabater et al. (2019) modified the division of Herpich et al. (2016) based on comparison with the results of Gürkan et al. (2018) for the H-ATLAS field as mentioned before. We used their division of $W2 - W3$ (AB) = 0.8.

We classified the LoTSS and FIRST cross-matched sources independently. This was done to maximize the number of radio-AGN selected from the sample. In each diagnostic (except the WISE diagram), a source can be labelled as radio-AGN, intermediate, star-forming, or unclassified. This gives a total of 192 possible combinations. These combinations are used to give a final classification, following the approach of Sabater et al. (2019) and Best & Heckman (2012). This approach gives the most weight in classification to the '$D_{\mathrm{n}}(4000)$ versus $L_{\mathrm{radio}}/M_{\star}$' and '$L_{\mathrm{H}\alpha}$ versus L_{radio}' diagnostic. Sources classified by either of these plots as an AGN are classified as a radio-AGN in the final classification. The BPT and WISE color-color diagnostics have the least weight (as they have no radio information) and are used only when the first two diagnostics give inconclusive classifications. Their main purpose at this stage is to check whether a source is hosting SF or not. For example, if both of the first two radio diagnostics classify a source as 'intermediate', we used the BPT and WISE color-color plot to check if the source lies in the SF region to determine whether the radio emission can be explained by SF. It is worth noting that the main aim of this selection technique is to select a clean sample of radio-AGN and is not necessarily

Table 3.1. Diagnostic combinations for LoTSS sources

$D_{\rm n}(4000)$ vs $L_{144\rm MHz}/M_\star$	BPT	$L_{\rm H\alpha}$ vs $L_{144\rm MHz}$	WISE col-col	Number	Final class
AGN	AGN	AGN	AGN	14	AGN
AGN	Uncl.	AGN	AGN	13	AGN
AGN	Uncl.	AGN	Uncl.	10	AGN
AGN	Uncl.	Uncl.	AGN	20	AGN
AGN	Uncl.	Uncl.	Uncl.	11	AGN
Int.	AGN	AGN	SF	13	AGN
Int.	AGN	Int	AGN	116	AGN
Int.	AGN	Int.	SF	28	SF
Int.	AGN	Int.	Uncl.	12	AGN
Int.	AGN	SF	AGN	170	SF
Int.	Int.	Int.	AGN	31	AGN
Int.	Int.	Int	SF	28	SF
Int.	Int.	SF	AGN	64	SF
Int.	Uncl.	Int.	AGN	29	AGN
Int.	Uncl.	SF	AGN	21	SF
Int.	Uncl.	Uncl.	AGN	80	AGN
Int.	Uncl.	Uncl.	Uncl.	15	AGN
SF	AGN	SF	AGN	40	SF
SF	AGN	Int.	AGN	12	AGN
SF	AGN	Int.	SF	17	SF
SF	Int.	SF	Uncl.	18	SF
SF	AGN	SF	SF	43	SF
SF	Int.	Int.	SF	65	SF
SF	Int.	SF	AGN	55	SF
SF	Int.	SF	SF	142	SF
SF	SF	Int.	SF	124	SF
SF	SF	SF	AGN	43	SF
SF	SF	SF	SF	829	SF
SF	SF	SF	Uncl.	54	SF
SF	Uncl.	Int	SF	17	SF
Uncl.	Uncl.	Uncl.	Uncl.	27	Uncl.

Combinations for classification of a source using the diagnostic diagrams discussed in Sect. 3.2.1, and the final classification assigned. Only groups with more than 40 sources are shown here. The same table for FIRST detected sources is shown in Table B.1.

Table 3.2. Classification of LoTSS cross-matched sources

Diagnostic	AGN	Int.	SF	Uncl.
	(No. of overall radio-AGN)			
$D_n(4000)$ vs $L_{144MHz}/M_\star$	102	705	1675	11
	(102)	(378)	(19)	-
$L_{H\alpha}$ vs L_{144MHz}	148	623	1583	139
	(134)	(216)	(24)	(125)
BPT	593	484	1122	294
	(220)	(52)	(6)	(221)
WISE col-col	839	-	1433	221
	(374)	-	(27)	(98)

Number of sources classified by each diagnostic discussed in Sect. 3.2.1. The different classes are: AGN, intermediate (Int.), star-forming (SF), and unclassified (Uncl.). The numbers in brackets are sources from each group classified as radio-AGN after combining the four diagnostics.

complete, as it might miss some radio-AGN that reside in SF galaxies.

The different combinations of the diagnostics, the number of sources in each group and the final classification are shown in Table 3.1 for LoTSS sources and Table B.1 for FIRST sources. The number of sources classified in each diagnostic and the final number of radio-AGN from LoTSS and FIRST cross-matches, are shown in Tables 3.2 and B.2, respectively. Finally, we select 499 LoTSS and 512 FIRST sources as radio-AGN, which leads to a combined sample of 806 radio-AGN identified either with LoTSS or FIRST. Of these, 205 are common in both LoTSS and FIRST samples, 294 are unique in LoTSS, and 307 are unique in the FIRST radio-AGN sample. For radio-AGN with only a LoTSS detection, we estimated the k-corrected 1.4 GHz luminosity by extrapolating the flux from 144 MHz using a power law of the form $F_\nu \propto \nu^\alpha$, with a spectral index $\alpha = -0.7$. This allows us to assess them together with radio-AGN that have FIRST detections. The distribution of this radio-AGN sample on the $L_{1.4GHz}$ versus $L_{[O\,III]}$ plot is shown in Fig. 3.2.

Our radio-AGN sample mostly covers a $L_{1.4GHz}$ range of $\approx 10^{21}-10^{24}$ W Hz^{-1}, with the majority of sources below 10^{23} W Hz^{-1}, which can be classified as low-luminosity radio-AGN. Over the past years, studies of feedback in radio-AGN host galaxies with IFU data have mostly focused on moderate to high luminosity ($\gtrsim 10^{25}$ W Hz^{-1}) radio-AGN, as discussed in the Introduction. However, with the combination of large IFU surveys like MaNGA and sensitive radio surveys like LoTSS, it is now possible to perform such studies for low-to-moderate luminosity radio-AGN, which make up the majority of the radio-AGN population in the Local Universe (Best et al. 2005; Sabater et al. 2019; Sadler et al. 2002). Therefore, our study of mostly low-luminosity radio-AGN can help us understand the role of this population in driving feedback. The

low-luminosity nature of our sample is highlighted in Fig. 3.2, where we also show the sample from Kukreti & Morganti (2024) for comparison. Radio-AGN in this sample were selected using the same diagnostics to study feedback on [O III] up to $z = 0.8$ using single fiber SDSS spectra.

Although the radio emission in radio-loud AGN is attributed to jets of relativistic plasma, the origin is less clear for radio-quiet AGN. One interesting explanation for radio emission in these sources is the shock scenario. This includes radiatively accelerated winds driving shocks into the host galaxy medium, which accelerate particles that then produce synchrotron emission (Faucher-Giguère & Quataert 2012; Zakamska & Greene 2014; Zakamska et al. 2016b; Zubovas & King 2012). This scenario can explain the origin of radio-emission in low-to-moderate radio-luminosity sources, similar to the ones in our sample. In Fig. 3.2, we also show the expected shock-generated radio luminosities from the fiducial models of Nims et al. (2015). This model estimates the expected radio luminosity for a certain AGN bolometric luminosity. However, there are significant uncertainties in the coupling efficiencies between the AGN bolometric luminosity, wind kinetic luminosity, and energy of the accelerated electrons. The conversions determining the bolometric luminosity from the observed [O III] luminosity are also uncertain. We show the Nims et al. (2015) model for two different conversions of [O III] to bolometric luminosity, from Heckman et al. (2004) and Stasińska et al. (2025), covering a range of coupling efficiencies. We find that ∼40% of the sources with radio+optical AGN (Sect. 3.2.3) lie beyond the radio luminosity limit of this model and very likely have radio emission dominated by jets. In the rest, the radio emission could also be due to shocks. We discuss this further in Sect. 3.5.

3.2.2 Other MaNGA radio-AGN catalogs

Multiple studies in the literature have selected radio-AGN samples from the MaNGA catalog and we compare those samples to our own in this work. Comerford et al. (2024) cross-matched the MaNGA catalog with the radio-AGN catalog of Best & Heckman (2012), which was itself selected using the SDSS DR7 source catalog with the FIRST and NVSS surveys. They found 221 of these radio-AGN in the MaNGA catalog. We cross-matched the Best & Heckman (2012) catalog with our 9,777 MaNGA sources using a 6″match radius and found 214 radio-AGN instead. The discrepancy could be due to the different number of MaNGA sources used to start with. Out of these 214 sources, 199 were selected as radio-AGN by our selection criteria with FIRST data. Of the remaining 15 sources, 13 do not have a cross-match in FIRST in our sample, likely due to a difference in the cross-matching criteria from Best & Heckman (2012); the remaining 2 sources have a FIRST crossmatch but are not classified as radio-AGN in our sample. Although our selection criteria are based on Best & Heckman (2012), we used the modified selection criteria by Sabater et al. (2019), which attempt to include more low-luminosity radio-AGN misclassified as SF before. We also select sources below the 5 mJy threshold used by Best & Heckman (2012), which would

explain the larger number of radio-AGN we identified compared to Comerford et al. (2024). Broadly, almost all the radio-AGN in the Comerford et al. (2024) sample are included in ours.

A sample of 307 radio-AGN has also been selected from MaNGA by Mulcahey et al. (2022) using the same diagnostics as we use and LoTSS DR2 data. Compared to the radio-AGN selected using LoTSS data in our sample, we find an overlap of 189 sources. The sources that do not overlap are among the low-luminosity ($L_{144\mathrm{MHz}} \approx 10^{21} - 10^{23}$ W Hz^{-1}) sources in our sample. We found that the radio luminosities in that study have been overestimated, which could affect the classification and explain this discrepancy. However, this does not affect the results of that study [3].

Recently, Albán et al. (2024) also selected a sample of 288 radio-AGN from the MaNGA catalog with a [O III] $S/N > 7$, by comparing the star formation rates (SFRs) estimated from 1.4 GHz (FIRST+NVSS) and Hα luminosities (obtained from Sánchez et al. (2022) catalog). On a plot of the two SFRs, they selected sources with a radio SFR more than 0.5 dex away from the 1:1 relation. Out of their 288 sources, 97 are also classified as radio-AGN in our sample using FIRST, and 159 are classified as SF/radio-quiet. This discrepancy is due to the significantly different selection methods and the different FIRST detection threshold they use of 1 mJy. Indeed, most of the disagreeing sources in the two samples lie close to the 0.5 dex division line on the SFR plot of Albán et al. (2024). Thirty sources in their sample do not have a FIRST crossmatch in our sample. This discrepancy is because they also cross-match with the NVSS catalog, which gives them more sources with a radio detection at 1.4 GHz. We compare and discuss the Albán et al. (2024) catalog in more detail in Sect. 3.5, since these authors also measured the radial profiles of the [O III] line width. Recently, Suresh & Blanton (2024) also selected a sample of radio-AGN using a similar approach of comparing radio and Hα based SFRs, but used a 1 dex threshold from the 1:1 line.

[3] private communication.

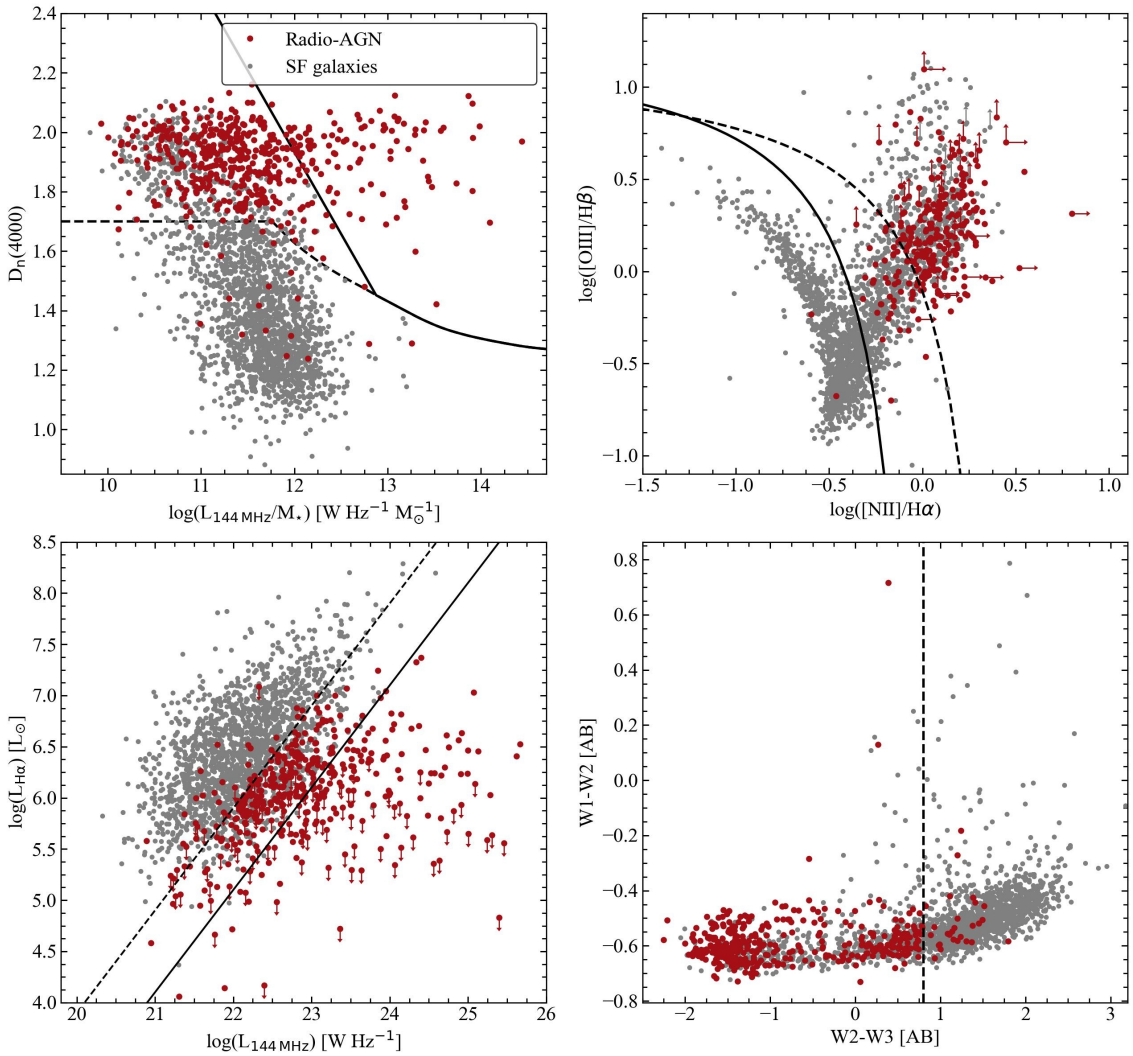

Figure 3.1. Diagnostic plots for selecting radio-AGN using LoTSS data. Red points mark the sources classified as radio-AGN after combining all four diagnostics, and grey points show the star-forming/radio-quiet AGN: (a) $D_n(4000)$ vs $L_{1.4GHz}/M_\star$ plot. The solid and dashed curves mark the radio-AGN, intermediate and SF/RQAGN division from Best & Heckman (2012) and Sabater et al. (2019); (b) $L_{H\alpha}$ versus $L_{1.4GHz}$ plot, with the separation lines from Sabater et al. (2019); (c) BPT diagram where the solid curve shows the semi-empirical relation from Kauffmann et al. (2003), and the dashed curve shows the maximum starburst curve from Kewley et al. (2006); (d) WISE color-color plot for sources with the division line from Sabater et al. (2019).

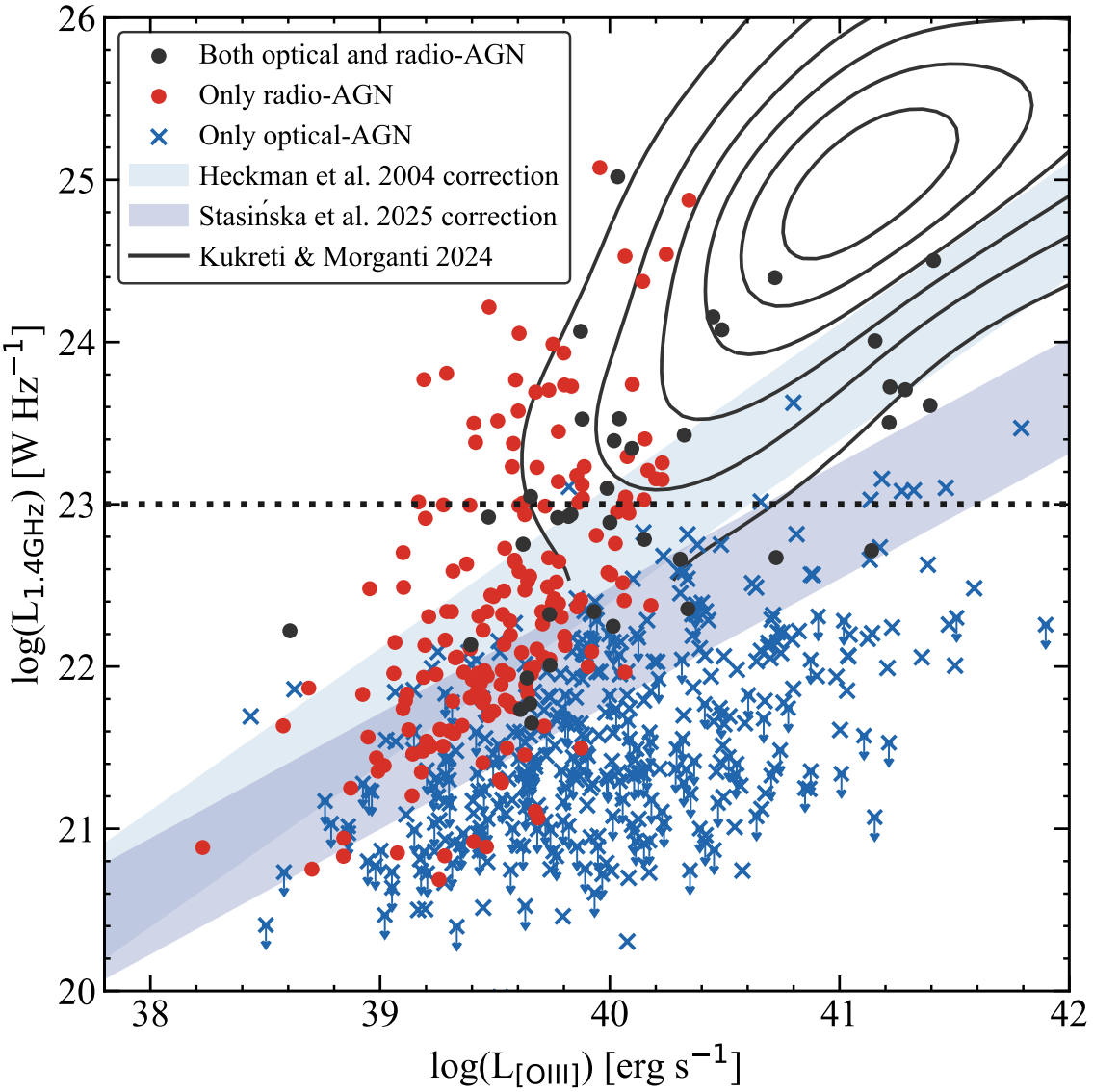

Figure 3.2. 1.4 GHz and [O III] luminosities of the sources with an [O III] detection. Sources with radio+optical AGN, radio-AGN, and optical-AGN are shown. For optical-AGN without a radio detection, the arrows show the upper limits on $L_{1.4\mathrm{GHz}}$. The shaded regions show the expected radio luminosity from the shocks scenario using the Nims et al. (2015) model, where the lower and upper edges show the limits for 5% and 25% coupling efficiency between AGN luminosity and wind kinetic luminosity, respectively. Different regions show the [O III] to bolometric luminosity conversion factors from Heckman et al. (2004) and Stasińska et al. (2025). The horizontal dotted lines show the luminosity divisions used in Sect. 3.4. To highlight the low-to-moderate luminosity nature of the sources in our study, we also show the parameter space occupied by the radio-AGN sample from Kukreti & Morganti (2024) in black contours, which examines the relation between radio properties and feedback on [O III] out to $z = 0.8$.

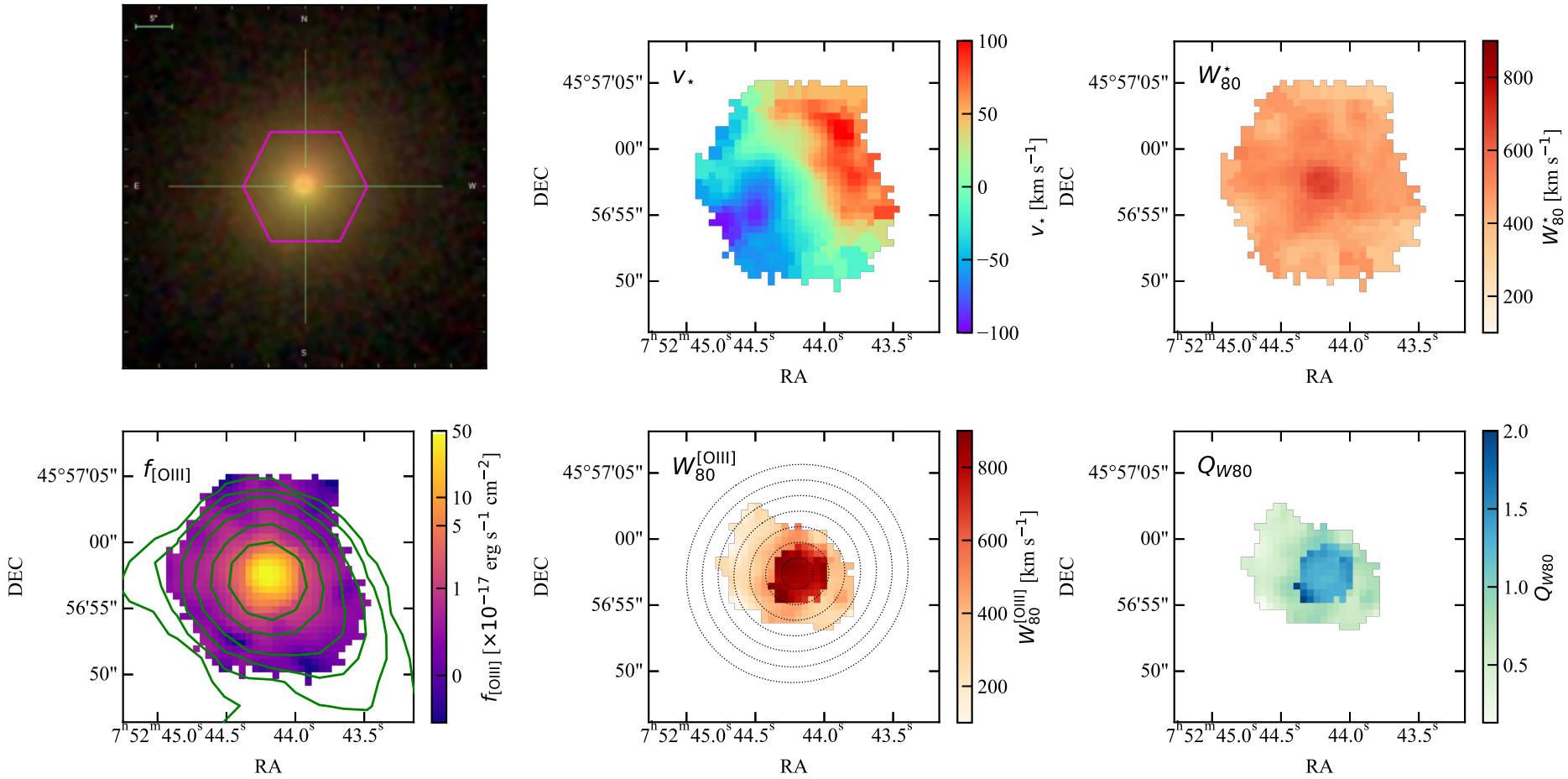

Figure 3.3. Maps of a radio-AGN from the sample (plateifu = 8714-3704). The top left image shows the SDSS optical color image of the host galaxy, with the MaNGA FoV marked with magenta. The other panels show the stellar and [O III] emission line properties. Only spaxels with a [O III] detection of $S/N > 5$ are shown and used throughout the paper for analysis. The green contours show the radio emission from FIRST at 1.4 GHz in the bottom left panel. The elliptical annuli regions used for constructing radial profiles are shown in the bottom middle panel. The same plot for a non-AGN source is shown in Fig. B.2 to illustrate the differences in their gas kinematics.

3.2.3 Optical-AGN sample

Since we are aiming to understand the complementary roles of jets and radiation in driving feedback, we also constructed a sample of optical-AGN using the BPT classification in Sect. 3.2.1. We first identified all sources with an AGN classification in the BPT diagram. We then selected only those sources with an Hα equivalent width greater than 3Å. This was done to ensure that the ionization is due to an AGN in these sources, as Cid Fernandes et al. (2011, 2010) showed that sources with weaker Hα emission that lie in the AGN (LINER) region of the BPT diagram, can have ionization from hot low mass evolved stars, instead of an AGN. This gives us a sample of 482 optical-AGN, out of which 73 are also classified as radio-AGN. We therefore have 409 sources that are optical-AGN. We note that an optical-AGN sample using MaNGA data was also selected by Albán & Wylezalek (2023) using different aperture sizes. We find that 369 of our optical-AGN sources are also classified as AGN in their study. However, 113 of our sources are not classified as an AGN in their selection. These sources have low S/N line detections and [O III] luminosities. Therefore, this difference is likely a result of the different data used for selection. They use a 2 kpc aperture in the central region to classify sources, whereas we use the data from the MPA-JHU catalog, which is based on single fiber SDSS data. Since the single fiber data provides integrated fluxes over larger areas ($\sim 2-8$ kpc) at these redshifts, it can recover lower flux emission with higher S/N than IFU data.

Finally, we also split the radio-AGN sample into those with and without an optical-AGN, using the same criteria as above. This helps us disentangle the role of jets and radiation in Sect. 3.4. Out of the 806 radio-AGN selected above, 73 are also optical-AGN. For the rest of the paper, we refer to sources with both radio and optical-AGN as radio+optical AGN. Sources with either only a radio or optical-AGN are simply referred to as radio or optical-AGN.

The selection methods used above can miss radio+optical AGN that have low radio luminosities, but are optically bright. The extra contribution from AGN to the Hα luminosity, on top of any star-formation, might shift the sources vertically upwards on the $L_{\mathrm{H}\alpha}$ versus L_{radio} plot, into the SF region. Therefore, our selection techniques would not be able to identify the radio-AGN in these sources. This has been observed before for quasars with low radio luminosities by Jarvis et al. (2021), and would require high-resolution (sub-arcsecond) radio imaging to confirm the presence (or absence) of a radio-AGN. We note that such missed sources could contaminate our optical-AGN sample. However, the selection techniques used here still enabled us to select a clean sample of radio and radio+optical AGN.

The presence of broad emission lines from the type 1 AGN in the sample can affect the derived measurements of the host galaxy properties. We tested for any systematic bias introduced by the presence of broad-line AGN in the $D_{\mathrm{n}}(4000)$, stellar velocity dispersion and stellar mass measurements by comparing the broad-line optical (and radio+optical) AGN with the narrow-line AGN. We used the broad-line galaxy catalog

of MaNGA from Fu et al. (2023), which contains 135 galaxies. In comparing the broad-line and narrow-line AGN, we found no systematic bias in the measurements mentioned above. Thus, we conclude that this potential bias does not contaminate our radio-AGN sample selection.

3.2.4 Non-AGN control sample

To test whether any disturbed [O III] is associated with the presence of a radio-AGN, we also selected a control sample of non-AGN galaxies for comparison. These sources do not necessarily have radio detection. First we only selected sources classified as SF on the BPT diagram. We removed all the sources classified as radio-AGN in Sect. 3.2.1. Then, we removed the AGN selected using MIR data from WISE (123) and X-ray data from BAT (29), compiled by Comerford et al. (2024). Lastly, we also removed any broad-line galaxies (135) present in the catalog of Fu et al. (2023), since these are mostly AGN as well. After visual inspection of the optical images and the [O III] maps shown in Fig. 3.3 and B.2, we also removed any mergers where the [O III] kinematics was affected by the interactions. We then restricted the sample to $M_\star > 10^{11}\,\mathrm{M}_\odot$ and $\sigma_\star > 150\ \mathrm{km\,s^{-1}}$, to match the distributions of our radio-AGN sample. This gave us a total of 63 non-AGN sources. We estimated that the radio non-detections in the non-AGN sample have a radio luminosity value below $L_{1.4\mathrm{GHz}} = 3 \times 10^{22}\,\mathrm{W\,Hz^{-1}}$. An example of a non-AGN source is shown in Fig. B.2.

3.3 [O III] spectra modeling and analysis

We went on to characterize the [O III] spectra of the MaNGA galaxies. The presence of disturbed gas kinematics is often evident in the broad low amplitude components of the emission line. This requires careful modeling of the [O III] line profile. Although the DAP catalog provides measurements for emission lines, they used only a single component when modeling the line profiles, which is insufficient for our purpose. Therefore, we used the best-fit models from Albán et al. (2024), who fit the [O III] spectrum of each spaxel with up to two Gaussian components. They used the least-squares algorithm to fit the components to both lines in the [O III] doublet simultaneously. We refer to Sect. 3 of their paper for more details on the fitting procedure.

After determining the best-fit model, we estimated the W_{80} widths of the [O III] profiles. This line width encloses 80% of the total flux and is defined as the difference between the velocities that enclose 10% and 90% of the cumulative flux; namely, $W_{80} = v_{90} - v_{10}$. Using W_{80} allows us to include emission from broad components that are likely tracing kinematically disturbed gas, while also avoiding being overly sensitive to the low S/N emission. It also enables comparison between profiles fit with different numbers of components. For a single Gaussian component, W_{80} is related to the velocity dispersion σ as $W_{80} = 2.563 \times \sigma$, but the relation is not straightforward for multiple components. Using the approach outlined in Sun et al. (2017), we correct the

W_{80} values using the instrumental spectral resolution of $\approx 70\,\mathrm{km\,s^{-1}}$and subtract the equivalent W_{80} value in quadrature from the [O III] value. An example of a corrected $W_{80}^{[\mathrm{O\,III}]}$ map for a source in our radio-AGN sample is shown in Fig. 3.3.

Next, to inspect the spatial changes in the line widths of , we constructed radial profiles of W_{80} using the procedure described in Albán & Wylezalek (2023); Albán et al. (2024). These profiles are constructed using elliptical annuli apertures of widths equal to $0.25 \times R_{\mathrm{eff}}$, where R_{eff} is the galaxy's effective radius. Using annuli widths in units of R_{eff} makes it possible to compare the radial profiles of galaxies with different sizes. The ratio of the major and minor axis and the position angle of the elliptical aperture are set using 'b/a' ratio and position angle values from the value-added catalog of Sánchez et al. (2022). Figure 3.3 shows a source from the sample with the elliptical annuli used. We then estimated each annuli's pixel-weighted average W_{80}, using the routine described in Albán et al. (2024). Furthermore, we only used galaxies with (a) at least 10 spaxels with a peak $S/N > 5$ detection and (b) at least two annuli with 10% area covered by spaxels with a peak $S/N > 5$. Although this drastically reduces the number of radio-AGN used later in our study, we used these criteria to obtain reliable radial profiles. The S/N threshold of 5 is chosen to maximize the number of sources while avoiding contamination from low S/N spectra. Changing the S/N threshold to 3 or 10 changes the number of sources with [O III] radial profiles, but it does not alter our conclusions. Out of the 806 radio-AGN selected using LoTSS and FIRST, there are 378 sources with [O III] W_{80} radial profiles. We removed four sources from this sample that show signs of mergers in their optical images and where the [O III] kinematics was affected by these interactions. Finally, we have a sample of 374 radio-AGN. From the control sample discussed above, we have 28 sources with [O III] radial profiles that we use for comparison with the AGN groups in Sect. 3.4.

The line width of [O III] profiles can provide insights into the impact of AGN feedback. However, the observed width of the profiles is determined by both gravitational kinematics due to the motion of gas in the galaxy and non-gravitational kinematics due to AGN and star formation-driven feedback. It is therefore crucial to assess the contribution of both to understand the extent to which [O III] gas is disturbed. We control for this first by constraining the sample to a certain stellar mass and stellar velocity dispersion limit, as described in the next section. Furthermore, in spatially resolved maps, [O III] profiles at the central region of the galaxy can also be broad due to the blending of narrow-line profiles attributed to rotation (also depending on the inclination angle of the galaxy). This makes it hard to judge the impact of AGN solely with [O III] profile widths. We attempt to overcome this by normalising the [O III] W_{80} with stellar W_{80} values. This should (mostly) correct for the effects mentioned above since there is a broad correlation between [O III] and stellar velocity dispersions ($\sigma_\star$) observed in AGN host galaxies (e.g. Boroson 2002; Nelson & Whittle 1996; Sexton et al. 2020), and has been used before to trace AGN feedback (e.g. Ayubinia et al. 2023; Woo et al. 2016). The stellar velocity dispersions would also be affected by the gravitational potential of the galaxy and the blending effect mentioned above.

Therefore, any relative differences in the [O III] / stellar W_{80} ratios could be due to non-gravitational kinematics, tracing AGN or star formation-driven feedback. We construct these ratio maps as described below.

We first construct maps of $\sigma_\star$, using the `STELLAR_SIGMA` extension in the `MAPS` files from the MaNGA DAP data products. We correct the stellar velocity dispersions using the `STELLAR_SIGMACORR` extension included in the `MAPS` files, and as described in the online user manual. We then convert $\sigma_\star$ to a W_{80} value, using a single Gaussian component conversion. Finally, we make the [O III] to stellar W_{80} ratio maps (only for pixels with $S/N > 5$ [O III] detection) defined as $Q_{W80} \equiv \frac{[\mathrm{O\,III}]\ W_{80}}{\mathrm{Stellar}\ W_{80}}$, and extract its radial profiles using the same approach outlined above. Examples of Q_{W80} maps are shown in Fig. 3.3 for a radio-AGN source and Fig. B.2 for a non-AGN source. An enhancement in the Q_{W80}values in the central region can be seen in the radio-AGN source. These radial profiles are discussed further in Sect. 3.4.

3.4 Results

In this section, we present the results for the [O III] kinematics of our radio-AGN sample and compare them to optical-AGN and the control sample of non-AGN sources selected above. We only use the sources with an [O III] detection for our analysis. For the most part, we will use the radial profiles of W_{80} and Q_{W80}, to gauge the changes in these properties with distance from the galaxy center and disentangle the role of radio and [O III] luminosities. At the end of this section, we will also test for any relation between these properties and the radio-AGN alignment. The radio-AGN host galaxies are typically more massive ($M_\star > 10^{11} M_\odot$) than optical-AGN and non-AGN galaxies. They also have larger average stellar velocity dispersions. We have therefore attempted to control for average $\sigma_\star$ (within an aperture of size R_{eff}), $M_\star$ and `T-Type` of the different source groups as much as possible while keeping a sufficient number of sources in each group. Since the optical-AGN galaxies also have larger [O III] luminosities than radio-AGN galaxies and it can affect the [O III] radial profiles significantly, we also controlled for [O III] luminosities of the groups. Controlling for these properties and using normalized $W_{80}^{[\mathrm{O\,III}]}$ (i.e. Q_{W80}) on a pixel-by-pixel basis accounts for any significant differences in the [O III] kinematics due to gravitational motion. However, this also reduces the number of sources in each group. The final number of sources in each group used for our analysis in this section are summarized in Table 3.3.

3.4.1 Radial [O III] profiles of AGN groups

First, we compare the $W_{80}^{[\mathrm{O\,III}]}$ and Q_{W80} radial profiles of the different AGN groups, selected in Sect. 3.2, and shown in Fig. 3.4. These radial profiles are assessed using violin plots, which help describe the distribution of the values at every radial point. The bottom panels of the figure show the p-values for a two-sample KS test between

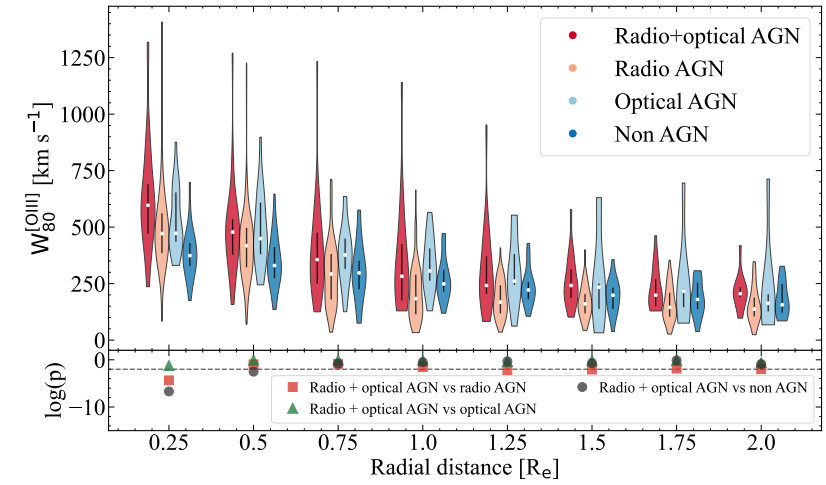

(a) Radial profiles of $W_{80}^{[\mathrm{O\,III}]}$

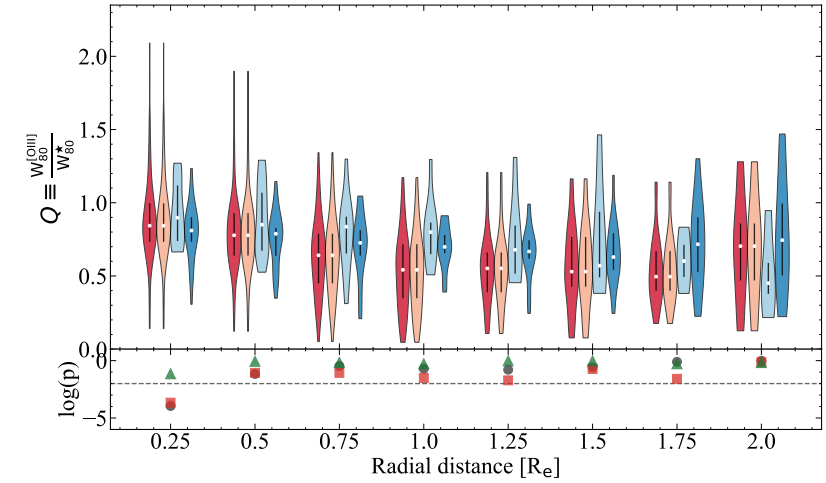

(b) Radial profiles of Q_{W80}

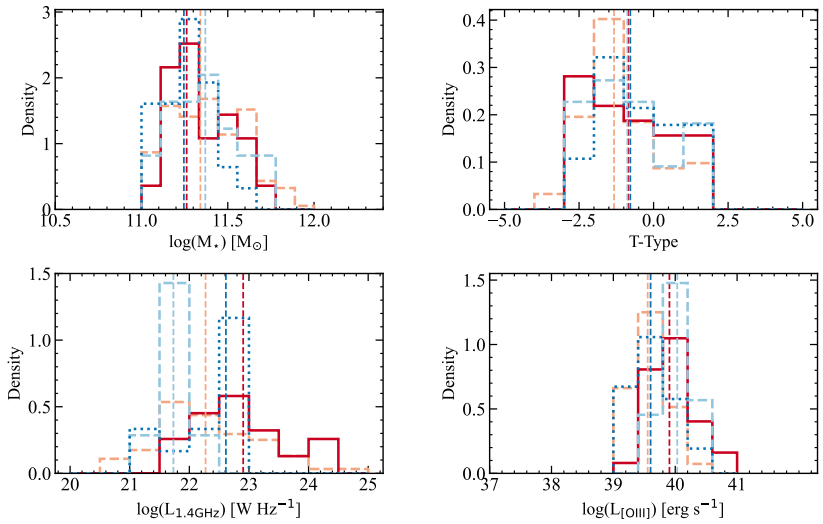

(c) Host galaxy properties

Figure 3.4. Comparison of the four groups with: an optical and radio-AGN, radio-AGN, optical-AGN, and non-AGN. Radial profiles of $W_{80}^{[\mathrm{O\,III}]}$ (a) and Q_{W80} (b) values, in steps of 0.25 R_{eff}. The violin plots show the distributions for every group at every radial point, with the white circle showing the median values and the black lines showing the range from the 25th to 75th percentile of the distributions. The bottom panel shows the p-values for a two-sample KS test at every radial point, with the two sample combinations marked in the legend. The horizontal dashed line marks the 99% confidence level p-value. (c) Host galaxy properties of the source groups, showing the stellar mass, host galaxy T-type, radio luminosity, and [O III] luminosity. Vertical lines show the median values. The colors represent the same sources as in the top panels. All source luminosities are only for radio and [O III] detections.

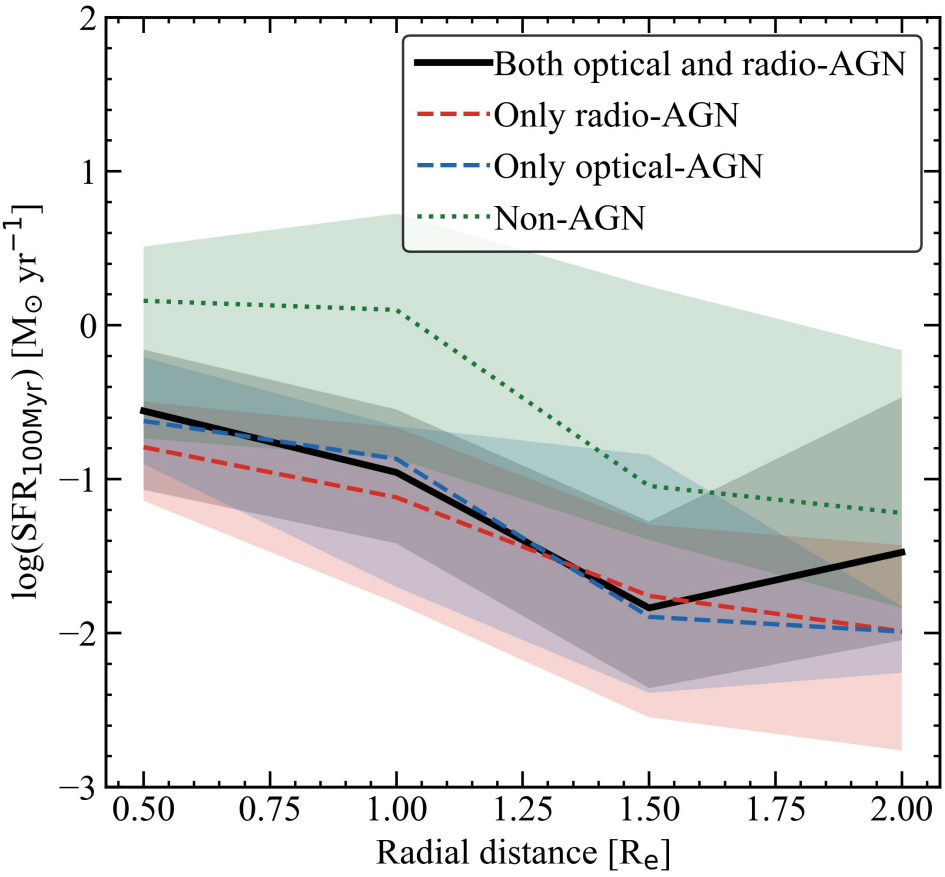

Figure 3.5. Radial profiles of recent (100 Myr) SFRs of the different source groups, discussed in Sects. 3.4.1 and 3.4.2. The lines show the median SFRs and the shaded regions mark the 25th and 75th percentile values of the SFR distributions. SFRs for the non-AGN group are larger at every radial point than the AGN groups.

these groups. Broadly, both $W_{80}^{[\mathrm{O\,III}]}$ and Q_{W80}values show a decreasing trend with radial distance up to $r = 1R_{\mathrm{eff}}$, with a flatter trend beyond this distance. Interestingly, we find that sources with radio+optical AGN have larger $W_{80}^{[\mathrm{O\,III}]}$ than the group with either only radio or optical-AGN and non-AGN, up to $r = 1.25\ R_{\mathrm{eff}}$. However, the p values show this difference is significant at >99% significance only up to $r = 0.5\ R_{\mathrm{eff}}$, when comparing to non-AGN group. However, normalizing this for $W_{80}^{\star}$, we find that the Q_{W80}values are the largest for radio+optical AGN sources only up to $r = 0.25\ R_{\mathrm{eff}}$, at >99% significance. Using the Q_{W80} values decreases the radial distance up to which we see a significant difference. However, we prefer to use the Q_{W80} values to judge the presence of disturbed gas since it accounts for gravitational motion and rotational line blending to some extent. This suggests that the differences in $W_{80}^{[\mathrm{O\,III}]}$ seen at $r = 1.25R_{\mathrm{eff}}$ were due to differences in the stellar velocity dispersion profiles and not necessarily a sign of disturbed gas. At larger radial distances, the different group profiles seem to agree with each other, judging by the p-values.

It is worth noting that the Q_{W80} values at $r = 0.25\ R_{\mathrm{eff}}$ are largest for sources with

radio+optical AGN, followed by optical- and radio-AGN (which have roughly similar medians) and then non-AGN. These results show that when radio+optical AGN are present, the ionized gas in the central region could be most disturbed. Although there are significant number of Q_{W80} values below 1, the relatively larger values show that the [O III] line is broader in these sources than would be expected from gravitational motion only. Since the sample covers about three orders of magnitude in both $L_{1.4\mathrm{GHz}}$ and $L_{[\mathrm{O\,III}]}$, it is possible that any luminosity-dependent differences are being washed out. Therefore, we performed the same analysis for sources above and below $L_{1.4\mathrm{GHz}} = 10^{23}\,\mathrm{W\,Hz^{-1}}$in the next section to isolate any radio luminosity dependence.

The distributions of radio+optical AGN sources have a tail of large $W_{80}^{[\mathrm{O\,III}]}$ ($\gtrsim 1000\,\mathrm{km\,s^{-1}}$) and $Q_{W80}(\gtrsim 2)$ values out to $r = 1.25R_{\mathrm{eff}}$. Such broad line widths likely denote disturbed ionized gas. However, since the radio-AGN in our sample are low-to-moderate radio-luminosity systems, it is not entirely clear why these tails are mostly seen in radio+optical AGN. In moderate radio luminosity systems, a jet-ISM interaction could drive fast outflows, which would explain the tail of this distribution. However, if the tail is mostly from low radio luminosity systems, it could also be an effect of the strong outflows shocking the surrounding gas and causing the radio emission. We discuss this further in Sects. 3.4.2 and 3.5. Despite the tail of the distributions, we only find significant differences in the central small-scale region.

Beam smearing can affect the measured sizes of the kinematically disturbed [O III] region and has been shown to overestimate the size in MaNGA data by Deconto-Machado et al. (2022). This could, in part, also explain the tail of the distributions that we observe out to large distances and discuss above. However, we only detect a significant difference on small scales ($r = 0.25R_{\mathrm{eff}}$) compared to the MaNGA PSF (FWHM $\sim$2.5″). Therefore, we do not expect beam smearing to affect our results significantly.

As mentioned before, non-gravitational gas kinematics can also be attributed to feedback from star formation, which can disturb the ionized gas and drive outflows (Heckman et al. 2015). It is, therefore, important to ensure that any localized star formation is not driving any difference we observe in the [O III] kinematics is important. To compare the star formation rates (SFRs) of the groups, we used the radial profiles of SFRs measured by Riffel et al. (2023). These profiles were extracted using a similar approach but with annuli widths of $0.5\,R_{\mathrm{eff}}$. Although their step size is twice ours, these profiles can still provide useful comparisons of the radial distribution of SFRs. In Fig. 3.5, we compare the radial profiles of star-formation rates (SFRs) for our radio-AGN and non-AGN control samples. We find that the SFR radial profiles are in agreement for all AGN groups, whereas the non-AGN group has the largest values. Therefore, star formation does not drive the differences in the [O III] kinematics found between the AGN groups. Here, we present only the SFRs averaged over the last 100 Myr, but we find the same results using SFRs averaged over the last 200 Myr.

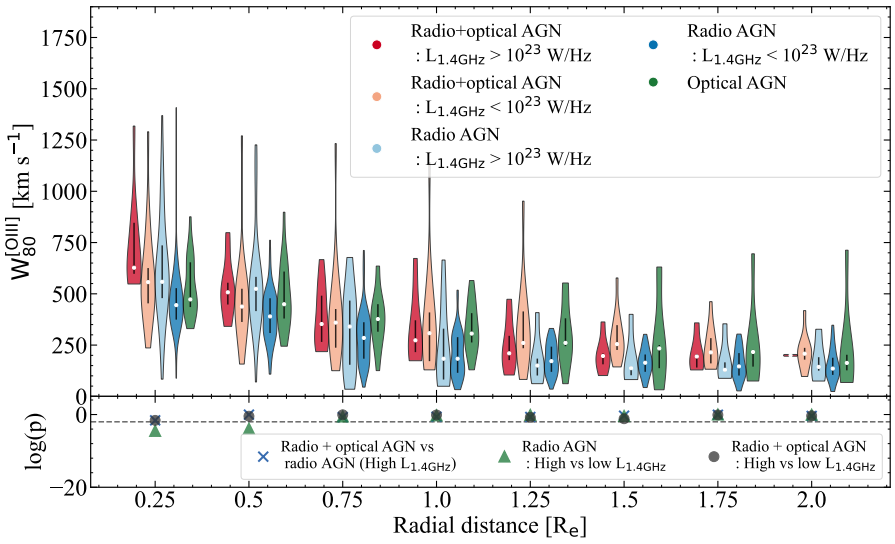

(a) Radial profiles of $W_{80}^{[\mathrm{O\,III}]}$ for $L_{1.4\mathrm{GHz}} > 10^{23}\,\mathrm{W\,Hz^{-1}}$ radio-AGN.

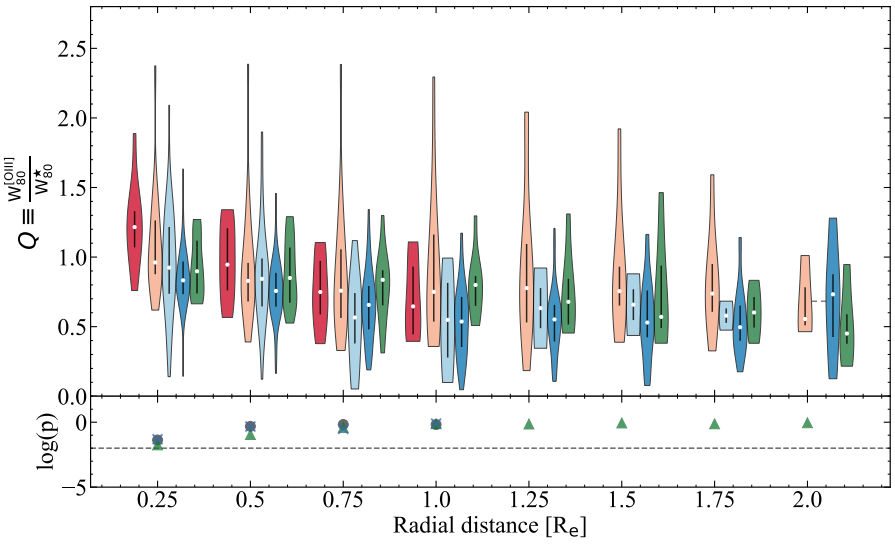

(b) Radial profiles of Q_{W80} for $L_{1.4\mathrm{GHz}} > 10^{23}\,\mathrm{W\,Hz^{-1}}$ radio-AGN.

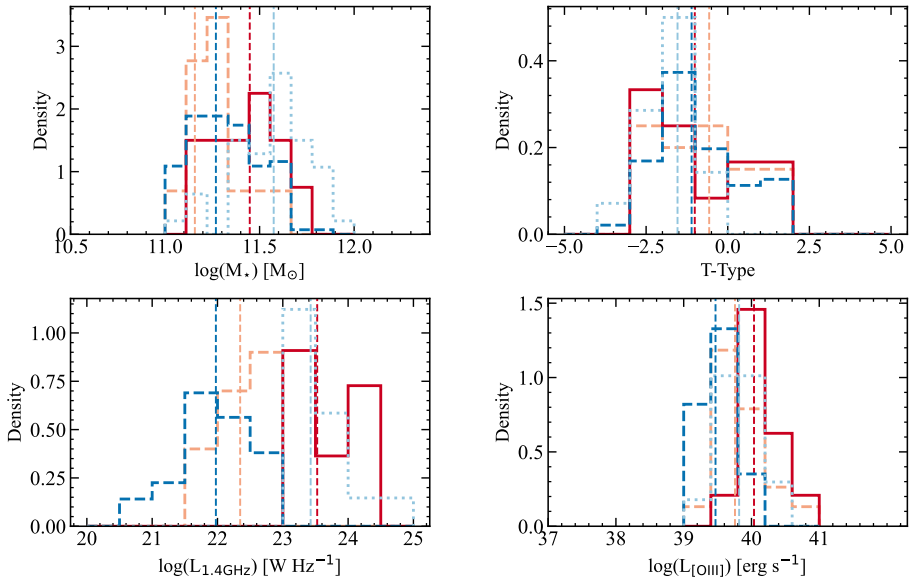

(c) Host galaxy properties for the groups

Figure 3.6. Same radial profiles in (a) and (b) as in Fig. 3.4 but for high and low $L_{1.4\mathrm{GHz}}$ radio+optical AGN and radio-AGN sources. The colors in panel (c) represent the same sources as in the top panels.

Table 3.3. Source groups.

Group	All	$L_{1.4\mathrm{GHz}}$ $10^{21}-10^{23}$	$L_{1.4\mathrm{GHz}}$ $10^{23}-10^{25}$
Radio+optical AGN	32	20	12
Radio-AGN	184	142	42
Optical-AGN	22	-	-
Non-AGN	28	-	-

Number of sources in different source groups discussed in Sect. 3.4, after matching the groups in host galaxy properties. These only include sources with an [O III] detection in the MaNGA data.

3.4.2 Dependence on radio luminosity

The total mechanical energy output of a radio-AGN is correlated to $L_{1.4\mathrm{GHz}}$ (e.g. Cavagnolo et al. 2010; McNamara & Nulsen 2012). Therefore, investigating the dependence of [O III] kinematics on radio luminosity can help understand the relation between feedback and the total mechanical energy emitted. Using the spatially resolved maps we can determine if the scales on which [O III] is disturbed change with $L_{1.4\mathrm{GHz}}$. Since the radio-AGN sample also has some optical-AGN, we handle the radio-AGN sources with and without an optical-AGN separately, as done above. We then split the sample into groups of radio luminosity at $L_{1.4\mathrm{GHz}} = 10^{23}\,\mathrm{W\,Hz^{-1}}$. Low $L_{1.4\mathrm{GHz}}$ sources cover a luminosity range of $10^{21}-10^{23}\,\mathrm{W\,Hz^{-1}}$and high $L_{1.4\mathrm{GHz}}$ sources from $10^{23}-10^{25}\,\mathrm{W\,Hz^{-1}}$, although most sources in the high $L_{1.4\mathrm{GHz}}$ groups are between $10^{23}-10^{24}\,\mathrm{W\,Hz^{-1}}$. In the group of radio+optical AGN, this gives 20 low $L_{1.4\mathrm{GHz}}$ sources and 12 high $L_{1.4\mathrm{GHz}}$ sources. In the group of radio-AGN, this gives 142 low $L_{1.4\mathrm{GHz}}$ sources and 42 high $L_{1.4\mathrm{GHz}}$ sources (summarized in Table 3.3).

The radial profiles of these four groups are shown in Fig. 3.6. We find that the median values of $W_{80}^{[\mathrm{O\,III}]}$ and Q_{W80} are largest for radio+optical AGN with high $L_{1.4\mathrm{GHz}}$, within $r = 0.25R_{\mathrm{eff}}$[4]. However, this difference is only marginally significant when compared to radio+optical AGN with low $L_{1.4\mathrm{GHz}}$. Similarly, radio-AGN with high $L_{1.4\mathrm{GHz}}$ show larger $W_{80}^{[\mathrm{O\,III}]}$ and Q_{W80} up to $r = 0.5R_{\mathrm{eff}}$, but it is only marginally significant till $r = 0.25R_{\mathrm{eff}}$. Judging by the p values of the distributions beyond $r = 0.5R_{\mathrm{eff}}$, we find that distributions for all groups agree with each other. This shows that the presence of a moderately powerful radio+optical AGN disturbs the [O III] gas most, although the spatial extent at which gas is disturbed does not increase at higher $L_{1.4\mathrm{GHz}}$.

Looking at the Q_{W80} radial profiles of the radio+optical AGN with low $L_{1.4\mathrm{GHz}}$ in Fig. 3.6b, it is interesting to note that they have a tail of high Q_{W80}values out to large

[4]The Q_{W80} radial profiles of this group have very few (< 5) points beyond $r = 1\,R_{\mathrm{eff}}$, therefore the distributions are not reliable and are not shown here

radial distances ($r = 1.75R_{\rm eff}$). However, this tail is not visible in the radio+optical AGN with high $L_{1.4\rm GHz}$. We described this tail in the previous section. Given that its most prominent in low $L_{1.4\rm GHz}$ radio+optical AGN, a likely explanation for this could be that the radio emission observed in these sources is due to shocks driven by the radiation from the optical-AGN; therefore, it would be an effect coming from the disturbed ionized gas and not the cause. This shock interpretation is discussed more in Sect. 3.5.

3.5 Discussion

In this paper, we study the impact of low-to-moderate-luminosity radio- and optical-AGN on the [O III] gas in the Local Universe up to $z \approx 0.15$. We selected a sample of 806 nearby radio-AGN from the MaNGA catalog, using a combination of LoTSS and FIRST surveys, out of which 378 have an [O III] detection. We then controlled for host galaxy properties and finally used a sample of 32 radio+optical AGN, 184 radio-AGN, 22 optical AGN, and 28 non AGN sources for our analysis. Constructing such groups allowed us to systematically study the feedback from radio and optical AGN selected from the same survey. Using spatially resolved maps of [O III] spectra, we constructed radial profiles of $W_{80}^{[\rm O\,III]}$ and Q_{W80}, to study the impact on the warm ionized gas. Our sample covers a radio luminosity range of $L_{1.4\rm GHz} \approx 10^{21} - 10^{24}$ W Hz^{-1}, including systems that are traditionally called radio-loud and radio-quiet AGN.

3.5.1 Impact of radio-AGN on [O III]

Comparing the $W_{80}^{[\rm O\,III]}$ and Q_{W80} radial profiles of different AGN groups from our sample allows us to determine the presence of disturbed [O III] and its relation to the radio- and optical-AGN. Comparing the Q_{W80} profiles of all sources in Fig. 3.4, we find a statistically significant difference at $r = 0.25\,R_{\rm eff}$, between sources that have radio+optical AGN and sources that have only either a radio- or an optical-AGN. We also find that when radio+optical AGN are present, more than half the sources have $Q_{W80} > 1$ at $r = 0.25\,R_{\rm eff}$. This shows that [O III] is more disturbed than when radio+optical AGN are present, compared to when only either one is present. The radial distance of $r = 0.25R_{\rm eff}$, corresponds to a physical radial distance range of $\sim 0.5 - 5.9$ kpc for our sample and 1.9 kpc at the median redshift. We propose that the warm ionized gas in nearby AGN host galaxies is disturbed on compact scales. Similar results for the compact nature of disturbed ionized gas have been found before (for example Holden & Tadhunter 2025; Tadhunter et al. 2018).

Beyond this point, we find that the Q_{W80} radial profiles of all AGN groups are largely similar, except the high values that create the tails seen in the distributions of radio+optical AGN. Although similar trends can be seen in the $W_{80}^{[\rm O\,III]}$ radial profiles of the different groups, the differences between them are suppressed when normalizing them with $W_{80}^{\star}$. This shows that the differences in the [O III] kinematics can also be

attributed to locally different gravitational motions and a difference in $W_{80}^{[\mathrm{O\,III}]}$ does not necessarily imply more or less disturbed [O III] kinematics. This highlights the advantage and necessity of using Q_{W80}values for comparing different sources.

In the radio+optical AGN group, both jets and shocks can be responsible for the observed radio emission, as discussed in Sect. 3.2.1. In the case of jets, the presence of more disturbed [O III] in radio+optical AGN would point to a co-active role of jets and radiation, such that when both are present, the impact on warm ionized gas kinematics is the strongest. In the case of radiative wind-driven shocks, this would mean that the disturbed [O III] is essentially tracing sources with strong shocks, which cause the radio emission. Therefore, the radio-emission would not be the cause but the effect of the feedback on the host galaxy.

Differentiating between the two cases would ideally require high-resolution radio imaging and radio spectral analysis. Lacking this information for the sample, splitting the radio+optical AGN sample into high and low $L_{1.4\mathrm{GHz}}$ sources sheds some light on this. We find that the trend we discussed above, with more than half of these sources having $Q_{W80} > 1$ at $r = 0.25\,R_{\mathrm{eff}}$, is driven by the high luminosity sample, as can be seen in Fig. 3.6. These systems are more likely to have their radio emission dominated by jets, as can be seen by their positions with respect to the models in Fig. 3.2. Therefore, we propose that in these systems, the radio emission is dominated by jets and the signatures of disturbed ionized gas observed on small scales are likely due to jet-ISM interaction.

However, the prominent tail of large $W_{80}^{[\mathrm{O\,III}]}$ and Q_{W80} values in the low $L_{1.4\mathrm{GHz}}$ sources likely point towards a shock origin of radio emission in these systems (although beam smearing also contributes to this, as mentioned before). Indeed, these systems also fall on or below the (Nims et al. 2015) models shown in Fig. 3.2. Therefore, it is possible that at these low radio luminosities, the high [O III] line widths are a selection effect, as selecting radio-AGN essentially means searching for sources with strong shocks. Overall, this highlights the role of both sources of radio emission in understanding feedback in low-to-moderate radio-luminosity systems.

Our results reinforce the positive correlation between disturbed [O III] kinematics and the presence of radio emission in AGN host galaxies, which has also been observed before with SDSS single fiber spectra that cover the central 3″of the galaxies (e.g. Kukreti & Morganti 2024; Kukreti et al. 2023; Molyneux, S. J. et al. 2019; Mullaney et al. 2013; Woo et al. 2016). Recently, using a sample of ∼5 700 radio-AGN and SDSS spectra, Kukreti & Morganti (2024) found a positive correlation between the [O III] line-widths and $L_{1.4\mathrm{GHz}}$, with more disturbed gas sources with $L_{1.4\mathrm{GHz}} > 10^{23}$ W Hz^{-1}. Using a large sample of ≈ 24 000 type 1 and 2 AGN, Mullaney et al. (2013) also found that the width of [O III] profiles was larger for AGN with a radio detection, peaking between $10^{23} - 10^{25}$ W Hz^{-1}. However, the sources in this study were not selected to be radio-AGN, and the shock origin of radio-emission could be quite significant contributor in this sample. Although the single fiber spectra used in these studies only cover the innermost region of our galaxies as mentioned above, our results are

still in agreement with these studies over that region. The $0.25\,R_{\rm eff}$ point up to which we detect disturbed [O III] covers the same size of central region as the SDSS single fiber studies at these redshifts. However, the spatially resolved MaNGA IFU data allows us to investigate the impact on larger scales, where we find no significant differences in the impact of various low-to-moderate-luminosity AGN groups.

3.5.2 The simultaneous impact of jets and radiation

Separating sources with a radio+optical AGN from those with either only a radio-AGN or only an optical-AGN allows us to perform a comparative analysis of the role of jets and radiation in low-to-moderate-luminosity AGN. This is illustrated in Fig. 3.6, which shows the $W_{80}^{[\rm O\,III]}$ and Q_{W80} radial profiles for different $L_{1.4\rm GHz}$ of radio-AGN sources, with and without an optical-AGN. When radio+optical AGN are present in a source, we find that [O III] is more likely to be disturbed on small scales (when the radio-AGN has $L_{1.4\rm GHz} > 10^{23}$ W Hz^{-1}) than when it is less luminous.

Even though optical-AGN of similar [O III] luminosities are present in both $L_{1.4\rm GHz}$ groups, the presence of more powerful jets correlates with relatively more disturbed [O III] , judging by the difference in Q_{W80} values. These jets are likely the source of radio emission in the high $L_{1.4\rm GHz}$ sources, as mentioned above. This group of radio+optical AGN has more disturbed [O III] sources at $0.25R_{\rm eff}$ than their low $L_{1.4\rm GHz}$ counterparts and the optical-AGN group. This shows that when moderately powerful radio-AGN and optical-AGN are present in a source simultaneously, the gas is most likely to be disturbed. Therefore, jets and radiation in these systems seem to be acting in a manner where the both enhance the impact of each other on the surrounding ionized gas kinematics. When radiation pressure from the AGN is present along with the jets, the AGN is more effective in disturbing the [O III] kinematics than it would be if it only had jets (and vice versa). Comparing only points with $Q_{W80}> 1$, we see that the impact is strongest for the group with radio+optical AGN and radio-AGN with high $L_{1.4\rm GHz}$. We recall here that sources with $L_{1.4\rm GHz} > 10^{23}$ W Hz^{-1}are still moderate-luminosity sources, with typical luminosities between $10^{23} - 10^{24}$ W Hz^{-1}.

Our results show that the strongest impact of jets in radio+optical AGN systems is limited to the central region of the galaxies. Comparing the radio sizes and optical host galaxy sizes sheds some more light on this trend. The ratio between the radio sizes of our sources, which we have taken from the LoTSS value-added catalog of Hardcastle et al. (2023), and the effective radii of the host galaxies has a median value of 0.5. This means that the radio emission from the AGN is typically on much smaller scales than the host galaxy size. This explains why the impact we see on [O III] in the $L_{1.4\rm GHz} > 10^{23}$ W Hz^{-1}radio-AGN groups, is limited to the central region.

Combining this finding with the results discussed above, we propose a scenario in which jet and radiation-driven feedback are simultaneously active in moderate-luminosity radio-AGN host galaxies. The ionized gas appears to be impacted by both, as can be seen in the highly disturbed radial profiles of sources that have both types of

AGN. This shows that feedback on ionized gas in AGN selected based on their having radio jets is not necessarily only driven by the jets. The presence of radiation from the AGN makes it more likely for the gas to be kinematically disturbed in radio-AGN host galaxies, compared to the case where only jets are present. Furthermore, comparing the radio-AGN groups with and without an optical-AGN suggests that gas clouds, perhaps pushed to high velocities by the jets, are driven to even higher velocities by the impact of radiation, and vice versa.

3.5.3 Feedback in low-to-moderate-luminosity radio-AGN

Feedback on [O III] in radio-AGN host galaxies was also studied by Albán et al. (2024), and we used the same routine to extract the radial W_{80} profiles for our study. In their analysis, Albán et al. (2024) found that radio-AGN exhibit larger W_{80} values at large $R_{\rm eff}$ in comparison to broad-line and optical AGN, even when the samples are matched in host galaxy properties. We find that [O III] is most disturbed, in terms of the gas velocity and proportion of sources disturbed, in the central region when radio+optical AGN are present. The impact is relatively milder when either only radio- or optical-AGN are present. This is qualitatively in agreement with the results of Albán et al. (2024); however, the differences we find in the impact on [O III] are limited to a radial distance of $0.25R_{\rm eff}$. The differences in the [O III] line widths reported by Albán et al. (2024) beyond this distance could be due to the low-luminosity radio+optical AGN that we have in our sample.

It is also worth noting that these differences could be due to the differences in the selection techniques and the host galaxies of the radio-AGN selected. The radio-AGN we selected are predominantly hosted by passive early-type galaxies, whereas theirs are equally distributed among early and late-type galaxies. Since early-type galaxies are dispersion-dominated and passive in terms of star formation, their Q_{W80} and SFR are lower than late-type galaxies. This explains the differences observed in the two samples at larger radii. Indeed, setting controls for early-type (or late-type) galaxies brings the radial profiles in agreement with each other.

Our results propose a scenario in which the impact of low-to-moderate-luminosity radio-AGN is strongest on the ionized gas in the central $0.25\,R_{\rm eff}$ region of galaxies in the Local Universe. The lifetime of a radio-AGN phase of $\sim 10 - 100$ Myr is significantly smaller than the galaxy's lifetime of a few Gyr (see Morganti 2017a for a review). Therefore, a single phase of activity is unlikely to impact star-formation significantly over the galaxy's lifetime. Indeed, many radio-AGN with multiple epochs of activity have been detected (e.g. Brienza et al. 2020; Kukreti et al. 2022; Sridhar et al. 2020), pushing the need to understand the cumulative impact of multiple AGN phases on the galaxy. If every phase of activity had the strongest impact on the gas in the central regions, we would expect to see less star formation in these regions compared to non-AGN host galaxies. Evidence for such inside-out quenching has been found in MaNGA galaxies, albeit in AGN selected using emission line ratios (e.g. Bertemes

et al. 2022; Bluck et al. 2020; Lammers et al. 2023). AGN feedback over multiple phases of activity could have suppressed the star formation in the central regions of these galaxies. Although we are studying the warm ionized phase, which is not the fuel for star formation, our results provide evidence supporting this scenario. Further studies of feedback in restarted radio-AGN on molecular gas phases (fuel for star formation) would be required to test these scenarios. We plan to conduct such studies in the future.

3.6 Summary

We selected a sample of radio-AGN using LoTSS and FIRST surveys and combined them with MaNGA to obtain spatially resolved spectra for a subsample over a redshift range of $z = 0.01 - 0.15$. The radio-AGN were selected on the basis of their greater radio emission compared to what is otherwise expected from star formation and are low-to-moderate radio and [O III] luminosity sources. We assessed the impact of radio and optical-AGN on the [O III] kinematics in these sources, to disentangle the role of jets and radiation in driving feedback. Our main finding is that when radio+optical AGN are present, sources are significantly more likely to have disturbed [O III] up to a radial distance of $0.25\,R_{\rm eff}$, than when there is either only a radio- or optical-AGN present. This shows that when both jets and radiation are present in a system, AGN have the strongest impact on the surrounding warm ionized gas. This relation is dependent on radio luminosity and so, high radio luminosity sources are more likely to have more disturbed gas in the central region. We note that in low radio-luminosity radio+optical AGN, the observed radio emission could be due to wind-driven shocks instead of jets. However, this does not affect our results, which are mainly driven by higher radio-luminosity AGN. Finally, we find that any differences in the impact on [O III] are only visible up to a radial distance of $0.25\,R_{\rm eff}$. We find no evidence of a broader, large-scale impact of moderate-luminosity jets on the warm ionized gas in these galaxies.

Chapter 4

On the origin of radio emission in star-forming galaxies: connection to restarted or relic AGN activity

Authors: Marco Albán[1], Dominika Wylezalek[1], Pranav Kukreti[1], R. A. Riffel[2], R. Riffel[3]

[1]Zentrum für Astronomie der Universität Heidelberg, Astronomisches Rechen-Institut, Mönchhofstr, 12-14 69120 Heidelberg, Germany

[2]Departamento de Física, Centro de Ciências Naturais e Exatas, Universidade Federal de Santa Maria, 97105-900, Santa Maria, RS, Brazil

[3]Departamento de Astronomia, Instituto de Física, Universidade Federal do Rio Grande do Sul, CP 15051, 91501-970 Porto Alegre, RS, Brazil

Submitted to A&A, currently in the reviewing process.

Marco Albán is the main author of this paper. Marco Albán produced all the figures and wrote all the text. A significant portion of this work benefited from international collaboration, made possible by Dominika Wylezalek, Rogerio Riffel, and Rogemar A. Riffel. Dominika Wylezalek majorly contributed to shaping the direction of this work, providing critical comments and suggesting significant improvements. Rogerio Riffel and Rogemar A. Riffel not only contributed to a deep discussion about the question of the paper, but also provided help with the usage and interpretation of MEGACUBES, a tool whose data products are widely used in this work. Pranav Kukreti made significant contributions to this work, particularly in the physics and interpretation of radio emission. All authors actively contributed throughout the review process.

ABSTRACT

Increasing evidence shows that active galactic nuclei (AGN) with radio detections have more perturbed ionized gas kinematics and higher outflow detection rates, suggesting a link between radio emission and these processes. In galaxies with weak or ambiguous AGN signatures, some studies attribute the radio emission to star formation, while others propose AGN-driven winds or weak, unresolved jets as the dominant mechanism. To investigate this connection, we take a step back and analyze a sample of star-forming (SF) galaxies with no clear current AGN signatures. Using low-frequency (LOFAR, 144 MHz) and high-frequency (FIRST, 1.4 GHz) radio surveys, combined with spatially resolved spectroscopy from the SDSS-IV MaNGA survey, we compare SF galaxies with 144 MHz detections that either do or do not have GHz detections. Despite being matched in stellar mass, redshift, and radio (MHz) luminosity, GHz-detected SF galaxies systematically differ from their non-GHz-detected counterparts. The former display enhanced ionized gas emission-line widths, higher central outflow fractions, redder colors, increased central obscuration, and offset emission-line ratios that shift towards (or closer to) the AGN regime (in the [N II] BPT diagram). Furthermore, the non-GHz galaxies are likely undetected due to their extended radio morphologies, while the GHz-detected ones are significantly more radio compact. Most of the properties from the GHz-detected (compared to non-detected) remarkably resemble the behavior found in many studies of radio-detected AGN. This suggests that the underlying physical mechanisms shaping GHz-detected SF galaxies' properties are fundamentally similar. This raises intriguing questions about whether some compact SF galaxies represent a precursor phase of AGN evolution or a form of low-power AGN activity. The radio compact characteristic sizes of GHz-detected SF galaxies also suggest a connection between AGN and old starburst galaxies.

4.1 Introduction

Several studies have pointed out that the growth of supermassive black holes (SMBHs) can have an impact on their host galaxies as both evolve through cosmic times (e.g., Fabian 2012; Heckman & Best 2014; Kormendy & Ho 2013). This growth is fueled by gas accretion from secular processes in galaxies (Alexander & Hickox 2012), or angular momentum loss via mergers (Hopkins & Hernquist 2009; Hopkins et al. 2006). Such accretion is today understood to happen either through a singular, highly significant accretion event or via multiple accretion episodes (Harrison et al. 2023) throughout the galaxy's history. These phases are characterized as active galactic nuclei (AGNs), and their presence can manifest throughout multiple wavelengths (e.g., Alberts et al. 2020; Lyu et al. 2022; Padovani 2017). It is known that different techniques to select AGN (in general, multiwavelength-based) can find galaxies with different AGN populations and host galaxy properties (e.g., Hickox et al. 2009), potentially indicating not only different powering mechanisms but also AGN in different evolutionary stages. Addi-

tionally, obscuration effects influence AGN selection across different wavelengths, as dust and gas can obscure UV, optical, and even X-ray emission (Hickox & Alexander 2018a).

Radio observations provide an essential window into AGN activity, given that they operate in a low-optical-depth regime. However, the evidence is hampered by the fact that radio emission in galaxies can come from various complex processes (Condon 1992; Panessa et al. 2019). Star-forming (SF) galaxies (with no current AGN activity) have a radio continuum dominated by a combination of free-free emission and synchrotron radiation (Condon & Ransom 2016). Below 30 GHz, most of this emission comes from synchrotron radiation, and above 30 GHz, the contribution of free-free emission from H II regions becomes important. Indeed, at 1 GHz, free-free emission is responsible for about 10% of the radio continuum (Condon & Ransom 2016).

In the local Universe, for example, SF galaxies typically dominate at $L_{1.4\,GHz} < 10^{23}$ W Hz^{-1} (Condon et al. 2002), and their current radio emission is a good tracer of their star-formation rate (SFR). Most of the synchrotron here comes from relativistic electrons, and candidates for accelerating these particles are Type II supernova remnants. These explosions come from short-lived stars more massive than $\sim 8\ M_{\odot}$, making the radio continuum a good tracer of recent star formation on SF galaxies. On the other hand, galaxies hosting AGNs usually show excess radio emission from what we would expect from pure stellar processes (Zakamska & Greene 2014). A relevant component contributing to radio emission in AGN has been attributed to jet (resolved or unresolved) structures (Padovani 2017). Controversially, some of the usually so-called radio-quiet AGN display radio emissions that can also be explained by star-formation processes (see Padovani 2016). However, alternative processes that can give rise to radio emission in AGN have been proposed in the literature. For example, radio emission can originate due to shocks driven by outflows (e.g., Zakamska et al. 2016b). Albán et al. (2024) suggests that the latter could explain why radio-AGN selection techniques can find more perturbed gas compared to a purely optical AGN selection. They show that radio-selected AGN have larger ionized gas velocity widths when compared to optically selected AGN.

Indeed, Torres-Papaqui et al. (2024) found that SDSS optically selected AGN ($z < 0.4$) with radio detections display systematically ionized gas emission line widths than non-radio-detected AGN. This has been explored in Escott et al. (2025), even finding that the outflow detection rate is increased on radio-detected ($z < 0.8$) AGN (see also Nandi et al. 2025). Spanning more moderate redshifts ($z < 2.5$), studies on red quasars (when compared to blue-selected ones) have shown that they are more likely to be detected through radio observations, having the enhanced kinematics, and more significant obscuration levels (e.g., Calistro Rivera et al. 2023; Fawcett et al. 2023, 2020). Despite including different redshifts or AGN types, these studies show a clear pattern of the role of radio emission in AGN. While some of these studies have suggested that such differences in the radio properties might be related to outflow-driven shocks, star formation, or low-power jets (e.g., Escott et al. 2025; Nandi et al.

2025; Torres-Papaqui et al. 2024), other studies attribute the differences to an AGN evolutionary phase effect, depending on the studied sample (e.g., Albán et al. 2024; Fawcett et al. 2023; Hickox et al. 2009; Jin et al. 2024). Interestingly, comparably significant distinctions between radio-detected and non-radio-detected sources are also observed among non-AGN galaxies (see below).

Ivezić et al. (2002) discussed that SDSS galaxies with detected radio emission have differing colors, and therefore, also differing morphologies when compared to the overall SDSS galaxies. However, they discuss that such differences significantly reduce when looking at fixed redshift and absolute magnitudes, suggesting that a selection bias drives the differing properties due to the sensitivity of the survey. In contrast, studies focusing specifically on star-forming (SF) galaxies have found evidence for an intrinsic sub-population among radio-detected SF galaxies. For example, Hopkins et al. (2003b) showed that SF galaxies have redder colors and higher obscuration levels (traced by optical colors and Balmer decrements (BD), respectively), which cannot be explained solely by selection effects or sample contamination. The latter results in SF galaxies having differing colors and morphologies. For example, lower BD are observed on bluer galaxies (Stasińska & Sodré 2001) and analogously, BD have been shown to increase from late to early type galaxies (Stasińska et al. 2004). Hopkins et al. (2003b) attribute the differences to a combination of optical sample undersampling redder galaxies, or radio detections undersampling the blue ones, both possibilities being attributed to intrinsic physical differences and the differences in the timescales of such processes. Further evidence was presented in Afonso et al. (2003), showing that such obscuration in SF radio-detected galaxies happens at a given SFR compared to optically selected SF galaxies. More recently, Ahmed et al. (2024) confirm that star-forming galaxies with radio detections have systematically higher obscuration levels (traced by BDs), ruling out radio sensitivity limits as the primary cause. These findings suggest that intrinsic physical differences drive the observed trends rather than selection biases alone.

In summary, it has been shown that both AGN and non-AGN seem to display a sub-population when radio is detected. Motivated by these systematic findings, we attempt to understand the origin of this behavior in a series of papers taking advantage of spatially resolved spectroscopy. In this first paper, we take a step back and analyze this effect on galaxies where no clear AGN is present. If we assume that the radio emission in SF galaxies arises from star-forming processes and not from nuclear activity (AGN), a radio-detected SF galaxy sample (which lies on the SF main sequence) compared to a non-detected one with similar morphologies and SFR properties should not display substantial differences in other properties of their host galaxies. Therefore, we present a comparative analysis in this sample to explore the properties of SF galaxies with and without radio detections at GHz frequencies. Our SF galaxy classification is based on central BPT diagnostics following the criteria of Albán & Wylezalek (2023). Our study combines rich multi-wavelength surveys, spatially resolved spectroscopy and stellar population synthesis models. In this way,

we can attack the question of whether simple differences related to star formation processes can explain the excess in the kinematics (or other properties) when radio emission is present. The findings can provide hints into the connection between radio emission in active and inactive galaxies and potentially give clues on the episodic nature of AGN.

The paper is organized as follows. The data and catalogs used for this study are shown in Section 4.2. In Section 4.3, we define samples of radio-detected and undetected star-forming galaxies, carefully removing non-detection biases. And in Section 4.4, we show our analysis and results. Discussion and conclusions can be found in the last two sections (Section 4.5 and 4.6). Throughout this paper, we have assumed a flat ΛCDM cosmology with $H_0 = 72$ km s^{-1} Mpc^{-1}, $\Omega_M = 0.3$, and $\Omega_\Lambda = 0.7$.

4.2 Data and catalogs

4.2.1 MaNGA

Combining multi-wavelength data and integral field spectroscopic (IFS) surveys has proven to be insightful. This section details the sources of these datasets used in our study. For IFS, we use the MaNGA SDSS-IV (DR17; Abdurro'uf et al. 2022). The survey has observed 10010 unique galaxies ($0.01 < z < 0.15$) covering wavelengths between 3622 to 10354 Å with a spectral resolution of R$\sim$2000. The field-of-view depends on the integral field unit array and varies from 12" to 32" in diameter, achieving a median physical resolution of around 1.37 kpc. MaNGA provides already-reduced spectral cubes obtained by the Data Reduction Pipeline (DRP Law et al. 2015), as well as derived spectroscopic quantities obtained from the Data Analysis Pipeline (DAP; Westfall et al. 2019a). We further combine the latter with many MaNGA-focused value-added catalogs from the literature to broaden our parameter space for understanding the properties of our host galaxies.

Derived values from the MaNGA DRP and DAP

We use spectral cubes from the DRP to obtain the [O III] 5007 ionized gas kinematics from the per-spaxel spectroscopy. Details of the latter can be found in Albán et al. (2024), where we compute the W_{80} maps and effective radius (R_{eff}) normalized radial profiles (at annuli steps of 0.25 R_{eff}). For emission-line profiles where one or more Gaussians were fitted, the W_{80} measures the width enclosing 80% of the total flux to account for potential non-gravitational motions. For a single Gaussian profile, $W_{80} \approx 2.56\sigma$. We will mainly discuss about the W_{80} from [O III] 5007, unless specified otherwise. We use the W_{80} values with a $S/N > 3$, and note that our results for W_{80} hold if the S/N cut is set to 7 or 10. We keep this S/N threshold to be consistent with the one applied to the emission lines (see below).

We use the Dn4000[1] from the DAP maps and compute their radial profiles the same way as in the W_{80}. The D4000 break has been widely understood as a tracer of the mean age of stellar populations. Both D4000 and W_{80} have been corrected for instrumental broadening following MaNGA's documentation guidelines. We get the emission-line ratio DAP-maps ([O III]/Hβ, [N II]/Hα, [S II]/Hα, [O I]/Hα); note that when referring to [S II], we are adding both emission lines from [S II] (at 6717 Å and 6731 Å). We create maps based on the closest distance to the extreme starburst line (Kewley et al. 2001a) from the scatter plot of the [N II] BPT diagram (see Kewley et al. 2006). From all these maps, we also create radial profiles. The properties mentioned above are used (either as resolved maps or integrated annulus) after masking for a signal-to-noise ratio (S/N) larger than 3 at each emission line. Constraining this cut to galaxies with a $S/N > 10$ does not change our results significantly. In this context, we note that star-forming galaxies are seen to be less affected in comparison to other BPT-classified groups (see Brinchmann et al. 2004).

Global, morphological and environmental quantities

Global parameters of each galaxy were taken from the value-added catalog from Sánchez et al. (2022), which are a product of the PIPE3D software (see Lacerda et al. 2022; Sánchez et al. 2016) applied on the MaNGA survey. The latter includes adopted redshift measurements from the NASA-Sloan Atlas (NSA; Blanton et al. 2011) catalog[2]. Below, we list the parameters using the same key defined in the catalog. The individual definitions following the link in the footnote[3] and more details can be found in references therein. From this catalog, we use the log_Mass, log_SFR_Ha, T90, D4000_Re_fit1, D4000_alpha_fit, Re_kpc, ellip, PA. Namely, stellar mass, star formation rate from Hα, look-back time at which a galaxy formed 90% of its current mass, the D4000 stellar index at 1 effective radius and the slope of its gradient (alpha_fit), and the last parameters are used to normalize the step of the radial profiles and follow the inclination and ellipticity of the galaxy (as described in Albán et al. 2024).

Morphological parameters for each galaxy are taken mainly from Vázquez-Mata et al. (2022) and Vázquez-Mata in prep., an exhaustive visual classification focused on MaNGA galaxies. They perform a visual inspection using the image post-processing and image residuals (r-band) combining the ones from SDSS and the Dark Energy Spectroscopy Instrument (DESI, Dey et al. 2019). With its deeper imaging compared to SDSS, DESI enables a more refined classification, particularly improving the identification of morphological features in edge-on galaxies. From the catalog, we extract

[1] In this paper, we use Dn4000, which is similar to the standard D4000 but with a narrower measurement band (see https://www.sdss4.org/dr17/manga/manga-analysis-pipeline/). For simplicity, we will refer to it as D4000.

[2] http://www.nsatlas.org

[3] Pipe3D catalog for SDSS-DR17: https://data.sdss.org/datamodel/files/MANGA_PIPE3D/MANGADRP_VER/PIPE3D_VER/SDSS17Pipe3D.html

the values of T-Types, which assign a number to the Hubble classification; UNSURE, which flags galaxies with diffuse or compact morphologies where classification was ambiguous; and BARS, which characterizes the identification of a bar. Concerning the Hubble morphological types, T-types < 0 are usually associated with elliptical galaxies, T-types ~ 0 correspond to S0s, and T-types > 0 usually refer to spiral Hubble morphologies (Conselice 2006).

Additionally, we use the Galaxy Environment for MaNGA Value Added Catalog (GEMA-VAC[4]) which will be described in Argudo-Fernández et al. (in prep). The catalog provides large-scale environment characterizations within 1 Mpc using a line-of-sight velocity difference of 500 km s^{-1} (see Argudo-Fernández et al. 2015). We use the projected distances (in kpc) to the 1st and 5th nearest neighbors for each MaNGA galaxy.

Resolved quantities

Stellar population fits for MaNGA have been performed by adapting the STARLIGHT code (Cid Fernandes et al. 2005) to work with cube data using the URUTAU code (Dullius Mallmann & Riffel 2023). Known as MEGACUBES, these data products are derived as outlined in Section 3 of Riffel et al. (2023) and references therein (e.g., Riffel et al. 2021). The data products include per-spaxel values of SFRs, stellar population vectors, stellar extinction, and stellar population age weighted by luminosity. Subsequently, MEGACUBES offers radial profiles from fitted parameters of these maps[5]. We list here the parameters that are used for analysis in our study:

- Mage/L: mean age weighted by stellar luminosity.
- A_V Stellar extinction: V-band parameterized extinction obtained from modeling the stellar continuum.
- Star formation rate here is defined as the mass processed into stars over an age interval.
- Stellar mass: the stellar population mass.

We note that the radial profiles from the MEGACUBES are obtained in steps of 0.5 R_{eff}, while our radial profiles for the D4000 and W_{80} use steps of 0.25 R_{eff}. However, this should not have a significant effect on the comparisons. The radial profiles from MEGACUBES also accommodate the galaxy's b/a axis-ratio and position angle. The mean or integrated values at each annulus are obtained after masking values where the continuum's S/N is lower than 10. Lastly, in figures, we present the radial profiles of galaxy subsamples by showing the median profile within each annulus as a solid line, with shaded regions indicating the 25th and 75th percentiles.

[4]GEMA-VAC: https://data.sdss.org/datamodel/files/MANGA_GEMA/GEMA_VER/GEMA.html

[5]The radial profiles and per-spaxel parameters can be downloaded or interactively seen in the following link: https://manga.linea.org.br/

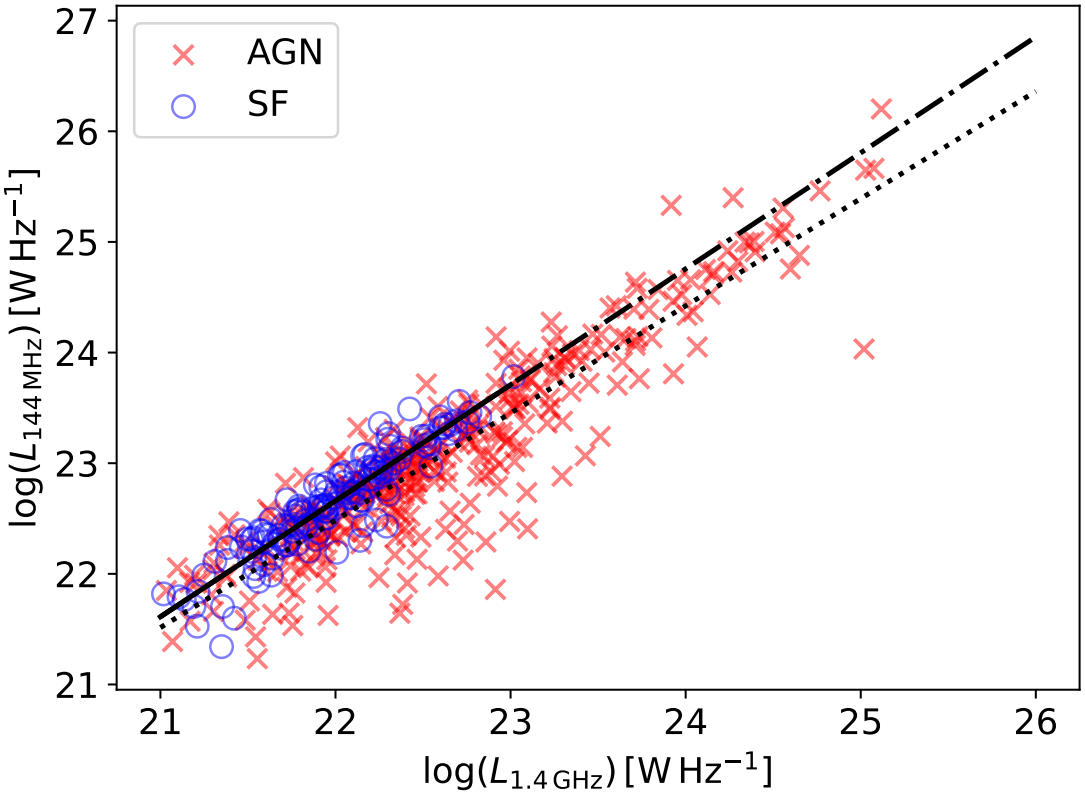

Figure 4.1. Comparison of the radio continuum luminosities between MHz and GHz frequencies. Blue circles represent SF galaxies and red X-symbols represent AGN candidates chosen from multi-wavelength selection techniques (all the ones mentioned in Section 4.2.3). The black solid line is a 1D-polynomial fitted to SF galaxies, and it is followed by a dashed-dotted line that extrapolates it to $L_{1.4GHz} > 23$ [W Hz^{-1}]. The dotted line is the same fit for AGN candidates.

The 1.4 GHz vs. 144 MHz relation in SF galaxies

4.2.2 Crossmatching MaNGA with different surveys

We crossmatch multi-wavelength data from different surveys with MaNGA. All the surveys mentioned here have full coverage of MaNGA galaxies, except for the radio low-frequency data (see below).

The radio counterparts of MaNGA galaxies

To gain insights into the origin of the radio continuum of our targets, we combine low and high-frequency radio surveys. We use the Low-Frequency Array (LOFAR, van Haarlem et al. 2013) two-metre Sky Survey (LoTSS, Shimwell et al. 2022, 2017) to obtain the continuum counterparts at 144 MHz and the Faint Images of the Radio Sky at Twenty centimeters (FIRST, Becker et al. 1995) for 1.4 GHz observations. These radio surveys have a comparable resolution, with 6.0” for LoTSS and 5.4” for FIRST.

While the sky coverage overlap between FIRST and MaNGA is almost a 100%, for LOFAR (DR2), the current data release covers around ∼60% of MaNGA.

Several studies have found that radio-detected galaxies form a subpopulation relative to non-detected ones. This has been shown for AGN (e.g., Escott et al. 2025; Fawcett et al. 2020; Nandi et al. 2025; Torres-Papaqui et al. 2024), and for star-forming galaxies (e.g., Afonso et al. 2003; Ahmed et al. 2024; Hopkins et al. 2003a). Given that this behavior has been primarily tested with single-fiber spectroscopic data, we are interested in exploring it by exploiting MaNGA's spatially resolved spectroscopy. In this paper, we start with a sample of SF galaxies to compare sources with and without radio detections. We define non-detections based on the absence of GHz continuum emission in the FIRST survey. While we define detections by the presence of GHz, all our galaxies (detected in GHz or not) have MHz detections. This allows us to reliably control radio emission distribution when comparing samples with each other. The crossmatch method in Kukreti et al. (2025) follows standard radio crossmatching techniques commonly used in the literature (e.g., Best & Heckman 2012). The current selection technique ensures that crossmatched galaxies have robust detections ($S/N > 3$) well above the survey's sensitivity limit. The crossmatch is performed within a 6.0" radius, and for FIRST, a flux density threshold of 0.5 mJy is applied. Therefore, we emphasize that a GHz non-detection does not mean that the source is radio silent at this frequency.

We crossmatch these surveys to MaNGA from (Kukreti et al. 2025) to obtain the luminosities at both frequencies (GHz and MHz) and deconvolved size estimates for the MHz continuum based on the semi-major fitted 2D Gaussian for the cross-matched counterpart, normalized by the galaxy's effective radius. A detailed discussion on the difficulties and artifacts about the size measurements of radio sources can be found in Shimwell et al. (2022), where they suggest a criterion to distinguish resolved and unresolved sources. We use the latter to characterize the fraction of unresolved galaxies in our samples.

In the context of SF or non-active galaxies, radio emission is a reliable estimator of recent star formation as it is, in principle, extinction-free (Condon 1992). Below ∼30 GHz, most of the radio continuum is dominated by synchrotron emission. Consequently, their radio continuum in different windows is ubiquitously shown to be correlated with their star formation rate (SFR; see Kennicutt & Evans 2012, for a review). For example, high frequency surveys such as FIRST (at 1.4 GHz) have been extensively used and shown to correlate with the SFR (measured by many indicators; e.g., Davies et al. 2017; Kennicutt et al. 2009). Similarly, Gürkan et al. (2018) have shown the same for lower-frequency surveys such as LoTSS (able to probe at ∼144 MHz). Therefore, it is well expected that both bands offer an extinction-free SFR indicator for SF galaxies. Naturally, the emission at low- and high-frequency is expected to be correlated in SF galaxies. Indeed, we show this in Figure 4.1 (see below).

To select SF galaxies, we use the catalog from Albán & Wylezalek (2023), which, in

summary, are BPT-selected (at an aperture of 2 kpc; see the details in the reference). In Figure 4.1, we show that such correlation holds with a small scatter for these SF galaxies (highlighted in blue circles). However, the red crosses show a significant scatter for AGN candidates (selected by different techniques; see Section 4.2.3). We fit 1-D polynomials for SF galaxies and AGN candidates separately (we extrapolate the one from SF galaxies in the plot). This shows that AGN candidates are generally offset from this correlation, suggesting that their radio emission is not solely attributable to SF processes, and likely includes contributions from AGN activity (see Padovani 2016). By leveraging this tight relationship for SF galaxies, we can effectively mitigate possible biases between GHz detections and non-detections by comparing samples within matched MHz luminosity bins. This is incorporated when constructing our control sample (see the details in 4.3).

Mid infrared filters

We cross-match MaNGA galaxies with the Wide-field Infrared Survey Explorer (WISE, Wright et al. 2010). WISE is a mid-infrared all-sky survey that observes through filters in four different bands: W1 ($3.4\mu m$), W2 ($4.6\mu m$), W3 ($12\mu m$), W4 ($22\mu m$). We use the coordinates from MaNGA sources to find crossmatching targets from the AllWise data release using a 6" aperture. Mid-infrared luminosities, as obtained by the WISE bands, have been shown to correlate with SFRs for SF galaxies (e.g., Wen et al. 2013). In our analysis, we use W1, W2, and W3 with $S/N > 3$. Nevertheless, all the galaxies that we use (see Section 4.3) have a S/N above this threshold, noting that their spatial resolution is comparable to that of LOFAR and FIRST.

4.2.3 MaNGA AGN catalogs used in this work

In this section, we list some of the existing MaNGA AGN catalogs we know about up to date. We list each selection technique and direct the reader to the respective references for further details. Catalogs not mentioned may be redundant to the scope of this paper, given the catalogs already listed below. We use the following catalogs:

- Mid-infrared colors: Comerford et al. (2024).
- Broad Balmer lines: Fu et al. (2023) and Negus et al. (2024).
- Mid-infrared variability: Pai et al. (2024).
- X-rays: Molina et al. (2023) and Comerford et al. (2024).
- Radio (MHz): Kukreti et al. (2025).
- Optically (BPT): Albán & Wylezalek (2023).
- Radio (GHz): Albán et al. (2024).

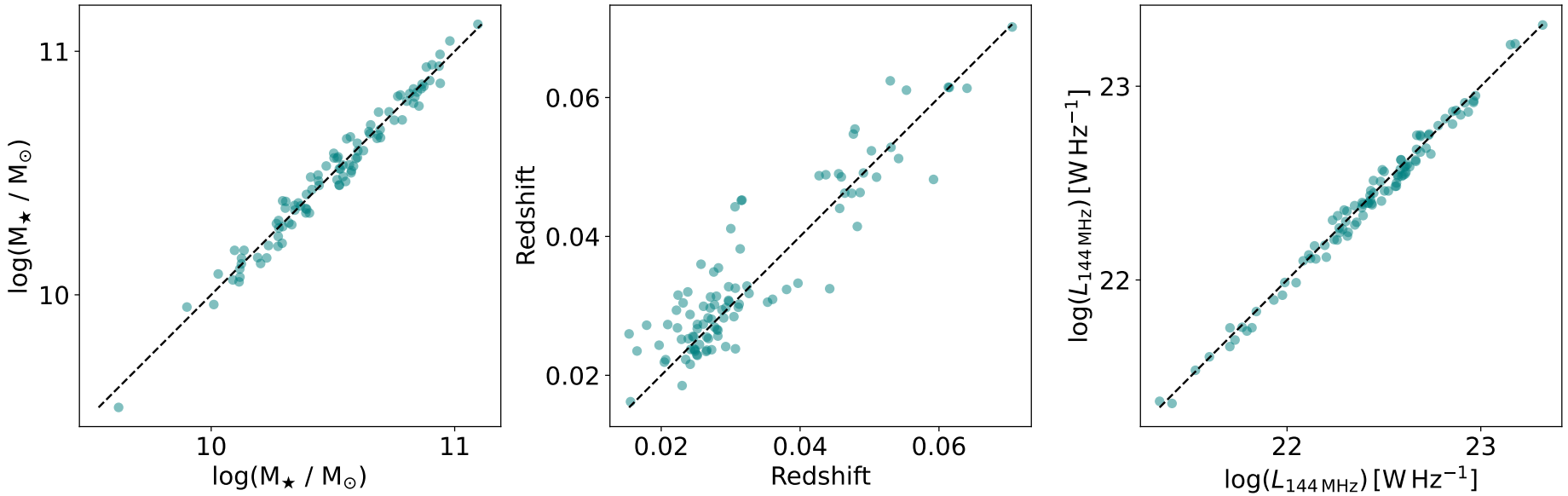

Figure 4.2. Parameter space used to match pairs of SF galaxies with and without GHz detections. We compared the properties of each pair, with GHz-SF on the x-axis and nGHz-SF on the y-axis, where both axes represent the same parameter. The dashed line in each plot represents the 1-to-1 correspondence where the parameter pairs are equal.

Approximately 18% of MaNGA galaxies are classified as AGN in one way or another. While a detailed exploration of their combined relevance might deserve a separate study, it lies outside the scope of the current work. Here, we simply note that only about 30 of our SF galaxies are present in any of the above-mentioned AGN catalogs, with roughly half showing radio-GHz detections. Including or excluding these targets does not significantly affect any results discussed in this paper. We emphasize this to clarify that our conclusions are not subject to the presence of current AGN activity unless a population of heavily obscured AGN (see discussion) at low redshifts has managed to evade several AGN multi-wavelength selection techniques.

4.3 Characteristics of our sample and their controls

We aim to explore the origin of radio emission in galaxies by selecting a sample of main-sequence SF galaxies where no clear current AGN is present. We start with a sample of purely SF galaxies (see Section 4.2.1) with 144 MHz detections in LOFAR. This sample is divided into two groups, based on whether a FIRST (GHz) counterpart was detected or not. While the distinctions reported in Section 4.2.1 were initially established using GHz detections alone, we include LOFAR due to its greater sensitivity relative to FIRST (Best et al. 2023). This addition accounts for the fact that star-forming galaxies are expected to produce radio emissions, ensuring that non-detections at GHz frequencies are not solely due to sensitivity limitations.

Radio detections, or, in other words, the crossmatch between radio and MaNGA (see Section 4.2.2, and also Kukreti et al. 2025) is defined following general selection techniques used in the literature (see also, Best et al. 2005). We define GHz detected SF galaxies as GHz-SFs, with 139 sources, and non-GHz detected SF galaxies as nGHz-SFs, with 813 sources (note that these numbers are after selecting sources with a LoTSS detection). To understand whether the detection of radio emission (specifically GHz) impacts other galaxy properties, we create a control sample over a fixed parameter space. For each GHz-SF, we select one nGHz-SF if possible, controlling simultaneously for three parameters: $L_{144\ \mathrm{MHz}}$, stellar mass (from the VACs), and redshift.

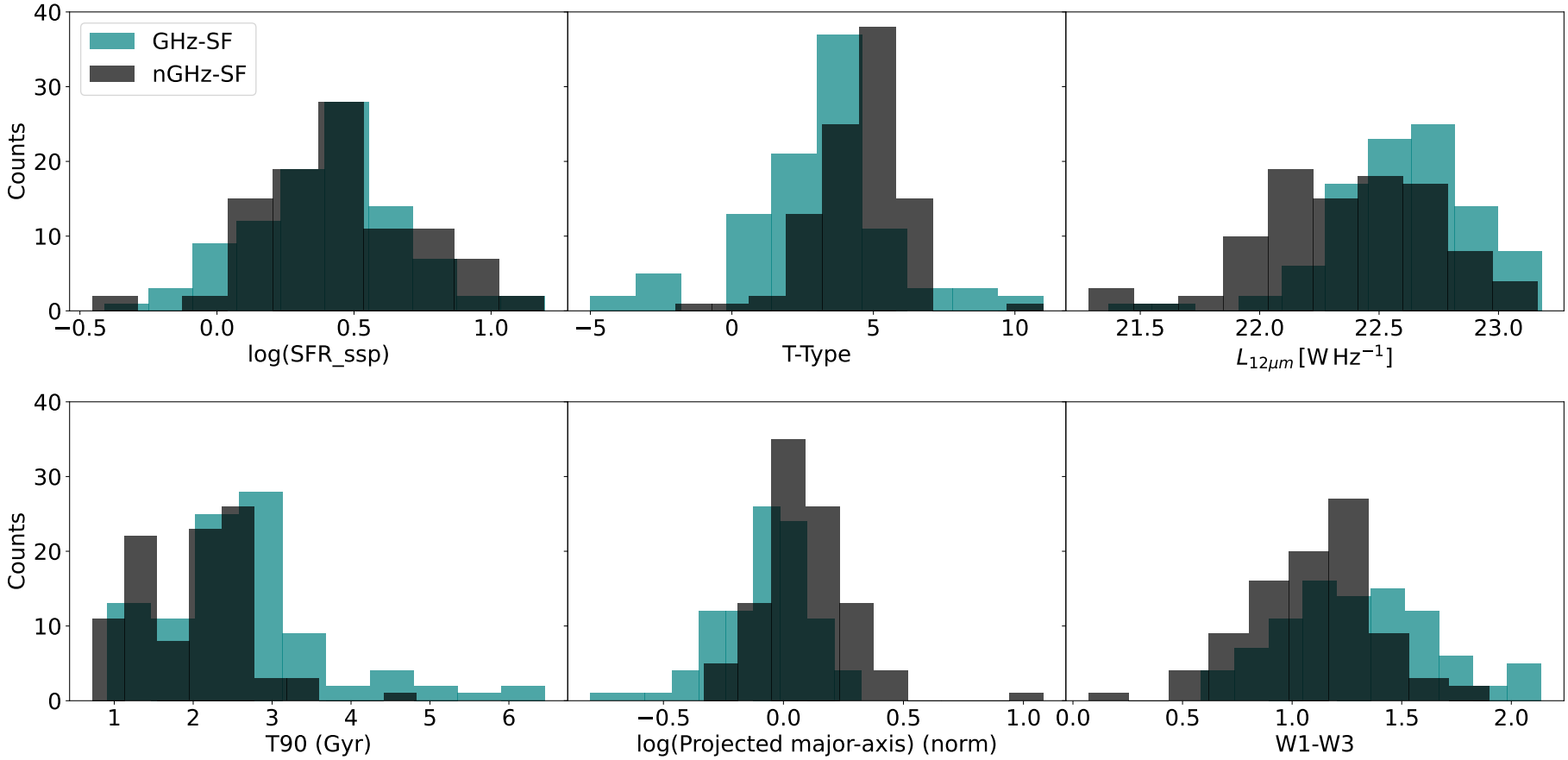

Figure 4.3. Uncontrolled global or integrated properties of SF galaxies with and without GHz detections.

Matching in stellar mass and redshift ensures that more massive and nearby galaxies, which are intrinsically easier to detect, are appropriately paired. More importantly, $L_{144\ MHz}$ does not only attempt to pair galaxies by similar extinction-free SFRs but also intends to control for the GHz global luminosity that we cannot detect. The latter is based on the tight relation seen between radio emission and the SFR in galaxies (see Section 4.2.1). We could similarly do this using SFR estimated from Hα, given the correlation between $L_{1.4\ GHz}$ and SFR(Hα) in star-forming galaxies. However, as we will show later, the SFR (from Hα or the stellar populations) gets self-controlled with $L_{144\ MHz}$ (see Figure 4.3). This leaves us with a sample of 97 galaxy pairs, removing some GHz-SFs due to a lack of suitable controls in nGHz-SFs. These removed GHz-SF galaxies do not affect the overall results of our study. Including them within a more flexible control sample selection would still yield comparable distributions of control properties between nGHz-SFs and GHz-SFs, albeit at the cost of compromising the pairing of one-to-one galaxy comparisons. Therefore, we adopt a stricter control sample criteria to ensure that variations in behavior are not driven by significant disparities in control parameters (even when the overall distributions would appear similar). During the discussions, we will mainly refer to these (GHz-SFs and nGHz-SFs) galaxies.

4.4 Analysis

The strategy of our control sample ensures that GHz-SFs and nGHz-SFs have the same SFR and stellar masses. This section shows how uncontrolled parameters behave in each group when the only difference is whether a galaxy has a GHz detection.

4.4.1 Comparison of integrated or global properties

In Figure 4.3, we display a set of parameters not used during the control algorithm. Our sample of GHz-SF and nGHz-SFs galaxies has not been matched directly to have the same SFR; however, as we see in this Figure, our samples have very similar values (we show here the SFRs derived from stellar population modeling of the VACs). Similar results are found when looking at the SFR derived from Hα from the VACs (as well as the SFRs derived from Riffel et al. 2021). The latter can be naturally explained noting that, for star-forming galaxies, there is a correlation between SFR and $L_{144\ MHz}$, and SFR and $L_{1.4\ GHz}$ (see discussion in Section 4.2.1). Furthermore, our galaxies lie on the star-forming main sequence (SFMS), where stellar mass and SFR are tightly correlated. As a result, they occupy a similar locus in the SFMS. We show, therefore, that the global SFR is a parameter that is self-controlled by our control sample and suggests that differences in properties in these galaxies should be independent of SFR.

We use the T-types to infer a morphological classification of these galaxies. Slightly lower T-type values are found on GHz-SFs despite being in similar positions on the

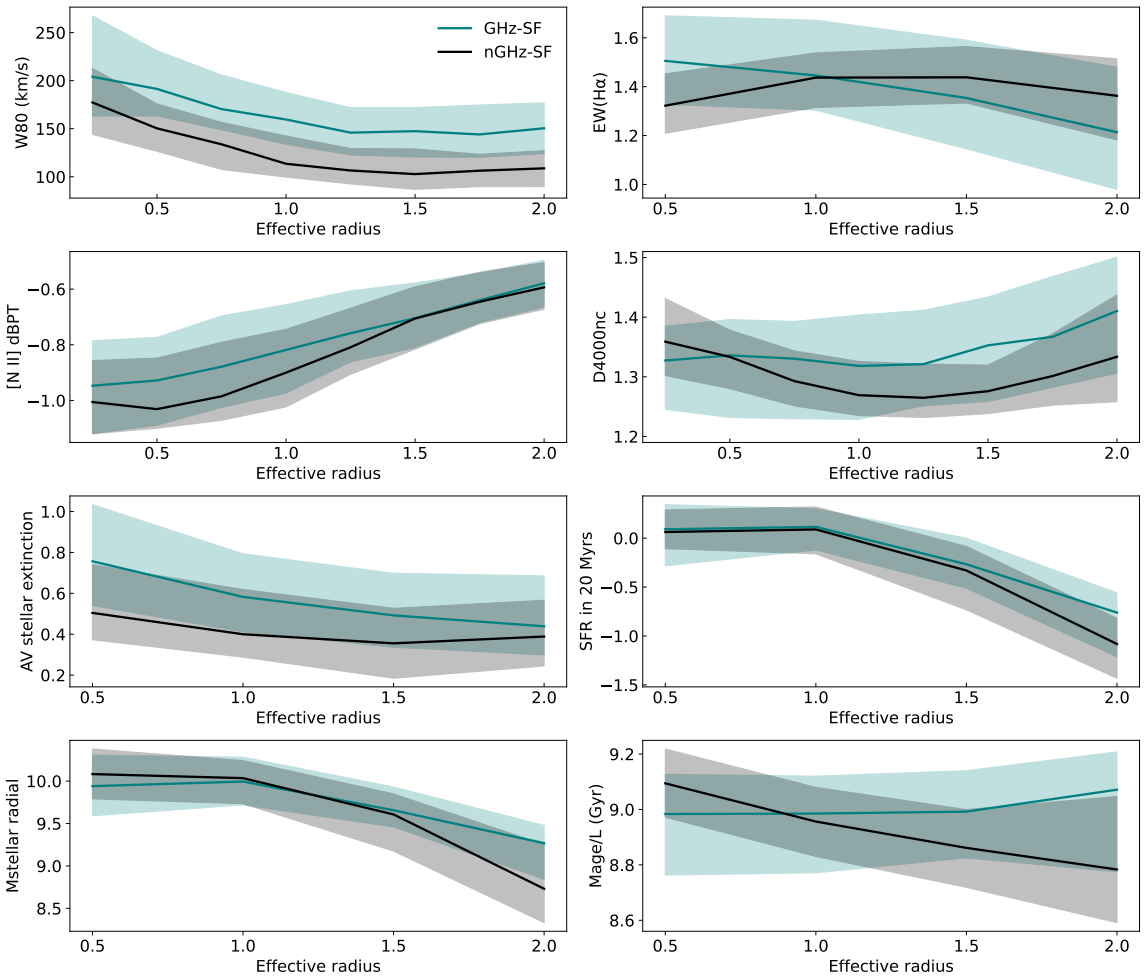

Figure 4.4. Comparison of empirically resolved properties between GHz-SFs and nGHz-SFs. The solid lines represent the median value at each annulus and the shaded region represents the 25th and 75th percentiles.

main sequence compared to nGHz-SFs (with a mean value of 4.5 in nGHz-SFs and 3.0 in GHz-SFs). This is confirmed by the T-Types and the *best_n_type* from the VACs, which directly classifies the galaxy according to its Hubble type. Lower T-types are usually associated with redder colors (Conselice 2006), which can explain the larger luminosity in WISE filters and the redder WISE colors when compared to nGHz-SFs (however, we still observe this at fixed morphologies).

Earlier spiral types have been associated with the so-called red spirals. Indeed, using $(g-r) > 0.63 - 0.02(Mr + 20)$ as a threshold for the latter (see Masters et al. 2010), shows that ∼31% of our GHz-SFs can be classified as red spirals, while only ∼9% of nGHz-SFs satisfy the condition (if we remove edge-on galaxies, with $log(a/b) < 0.2$, to minimize the effect of dust reddening, this would change those numbers to 12% and 4% respectively; see Appendix C.2). One of the suggestions is that these galaxies are a more evolved version of the usual blue spirals. However, removing the galaxies that satisfy the red spiral threshold does not modify the general differences between GHz-SFs and nGHz-SFs. If red spirals represent an older version of blue spirals, GHz-

SFs (even when removing the red spirals) may represent an intermediate population bridging the two. To get insights into the latter in more detail, we show the T90 measurements from the VACs, which measure the look-back time at which a galaxy assembled 90% of its mass. Figure 4.3 shows that, indeed, GHz-SFs are more likely to have assembled their mass earlier than nGHz-SFs.

Redder colors in GHz-SFs can also indicate higher levels of obscuration and the presence of dust. In SF galaxies, mid-infrared luminosities have been seen to correlate with SFR. Given that our galaxies have the same SFR, this immediately means that a SFR excess is measured from SFR(L_{W4}) or SFR(L_{W3}) for GHz-SFs. Offsets from the latter correlation have been attributed to the presence of an AGN. However, the overwhelming AGN selection techniques we have gathered (see Section 4.2.3) do not show evidence of any current activity in these galaxies. The excess in infrared colors can also be explained in terms of excess in the kinematics. Baron & Netzer (2019) has shown that optically-selected AGN with an outflow detection (which, in our context, translates into finding higher W_{80}) have redder colors than those without outflows. The authors interpret the latter as follows, in the sense that outflows, common in AGNs, can carry dust which is heated by the AGN emission, reemitting in the infrared. We argue that such an effect could still be present when the optical signature from the AGN has turned off, given that our GHz-SFs resemble this kinematic excess and the corresponding redder colors. Therefore, redder colors in GHz-SFs can be related to pre-heated dust carried by an outflow ejected from a previous AGN event.

We have analyzed further morphological and environmental characteristics. For example, differences in the observed properties between GHz-SFs and nGHz-SFs do not depend on the environment or whether there's a bar. Using the distance to the 5th nearest neighbor, less than 2% of galaxies (in GHz-SFs and nGHz-SFs) have more than 5 companions in the surroundings of 200 kpc. If we observe broader scales, no substantial differences arise. Similarly, no differences are seen if looking at the distance to their 1st nearest neighbor. We, therefore, do not expect to have environmental effects impacting our results. As for the radio morphologies (central-bottom panel in Figure 4.3), the semi-major axis, normalized by the galaxy's effective radius, shows that GHz-SFs are more compact. We note that the unnormalized semi-major axis sizes (in arcseconds) from the GHz-SFs are also smaller than the ones from nGHz-SFs $\sim$ 96% of the cases. In this context, using a criterion for distinguishing between resolved and unresolved sources (following the methods from Shimwell et al. 2022, ; see Section 3), we find that $\sim$75% of GHz-SFs are unresolved. In contrast, only $\sim$19% nGHz-SFs are unresolved. This is true at fixed optically derived properties (see Section C.2).

It can be argued that supernova remnants can also carry outflows and perhaps mimic the observed contrasting properties. However, we find no evidence of an excess of SNRs when using SNR diagnostics in our samples. This is somewhat expected given that the SFR of our targets is similar. We emphasize that in the sample of our current study, we have no AGN active in our targets. An alternative explanation is that given

that redder colors can, in turn, translate into stronger star-formation events. However, the latter needs to be true at fixed extinction-free SFR($L_{144\,MHz}$). We emphasize that the parameters discussed here are model-independent and use a purely empirical comparison between the samples. Below, we discuss resolved properties to get insights into this observed behavior.

4.4.2 Resolved ionized gas kinematics

The excess in the emission line width is discussed first, as it was the initial parameter we found to differ in the presence of detected radio emission, and it is particularly explored in recent literature. Across all radial bins, GHz-SFs display systematically higher W_{80} values than nGHz-SFs. Despite having similar global and resolved SFRs, the broader emission-line profiles suggest that the process responsible for the broadening may be connected to the compact radio emission morphology. Interestingly, although we are working with SF galaxies, studies on AGN samples have suggested that shocks generated along the outflows can accelerate particles, giving origin to radio emission (e.g., Zakamska et al. 2016b).

In a sample of radio-detected-AGN and non-radio-detected-AGN, Escott et al. (2025) find that the former are more likely to present outflows and larger W_{80} values. Our targets show no signs of current nuclear activity yet display kinematic excesses resembling the behavior of the AGN from Escott et al. (2025). We further confirm that the kinematic differences persist in spatially resolved spectra. Escott et al. discuss that radio emission is unlikely to originate from high-powered radio jets in their sample. They suggest that other likely origins can be related to low-powered radio jets, AGN outflow-driven shocks, or star formation. Given that our sample has virtually the same SFRs, as shown by many tracers (even resolved), we suggest that star formation processes are unlikely to explain the kinematic differences (although contrasting SF histories might be an alternative explanation; see the discussion in Section 4.5). Similar results have been found in Nandi et al. (2025) for radio-detected AGN. The interpretation of our results becomes challenging given that there is also no clear evidence for a current AGN present today in any of our galaxies. Below, we expand our study to other resolved quantities to gain insights into the possible processes causing this behavior.

4.4.3 Modeled and empirical resolved properties

We split the resolved properties into empirical in the first 2 rows (e.g., the D4000 stellar index) and modeled in the last two rows (e.g., stellar extinction) of Figure 4.4. Empirically, we can observe that when compared to nGHz-SFs, the sample of GHz-SFs (aside from differences in the velocity widths) has a larger EW(Hα) in the central regions but lower in the outskirts, off-nuclear emission-line ratios closer to the extreme starburst line of the [N II] BPT-diagram, and lower D4000 in the inner regions

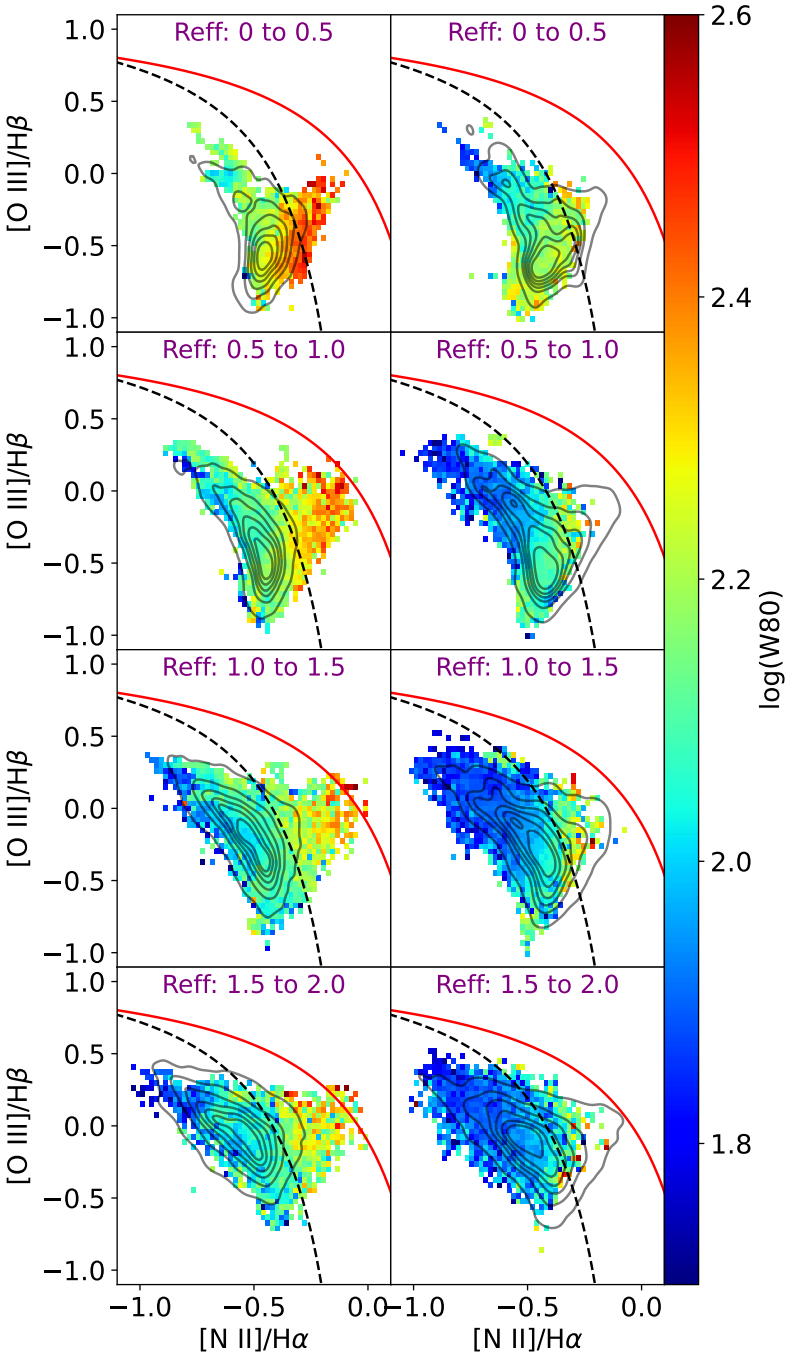

Figure 4.5. Resolved emission line ratios binned by their W_{80}. The first column of plots shows the positions of the spaxels (from the DAP, see Section 4.2.1) binned by W_{80} for GHz-SFs. The second column shows the same for nGHz-SFs. The distribution of the emission-line ratio spaxels of either GHz-SF or nGHz-SFs is shown in the opposite columns using black contours (see 4.4.4). For example, in the left column, W_{80} is binned for GHz-SF, but the contours show the spaxel distribution of nGHz-SF. In all plots, the Kewley et al. (2001a) and Kauffmann et al. (2003) lines for transition objects and extreme starbursts are shown in the red solid and black dashed lines, respectively. Bins where fewer than three scatter points were present have been excluded.

but larger at the outskirts. We emphasize that most radial distribution changes are likely lost or diluted in single-fiber spectroscopic studies, highlighting the importance of spatially resolved samples.

Continuing the comparison between the global stellar mass and star formation rates, we show that the same is true for their resolved behavior (see the last two rows of Figure 4.4). In the figure, we have used the SFR averaged over the last 20 Myrs, and similar results are found when we look at the SFR over the last 100 Myrs. We note that some discrepancies can appear at $R_{eff} > 1.5$, however, MaNGA covers in general up to 1.5 R_{eff} (in Section C.2, we discuss that our results are not dramatically changed by controlling for optical sizes). The relation between SFR and stellar mass for SFMS galaxies has also been shown to hold in resolved data (Sánchez 2020). Indeed, our GHz-SFs and nGHz-SFs display the same resolved specific SFR (sSFR).

The A_V stellar extinction is more elevated in the central regions, and the luminosity-weighted age follows a similar pattern as described by D4000. Indeed, the D4000_Re_fit (from the VACs), which shows the slope from a 1D-polynomial from the D4000 radial profile, shows that the D4000 has positive slopes for GHz-SFs and more negative for nGHz-SFs. Both D4000 (tracing stellar population ages) and M_{age}/L show that GHz-SFs are slightly younger in the central regions and older in the outskirts when compared to nGHz-SFs. If we explain this behavior only in terms of star-formation processes, this shows that GHz-SFs have slightly younger central stellar populations at fixed SFR and stellar mass compared to nGHz-SFs. Judging by the increased stellar extinction and Balmer decrements in the central regions, an obscured SF event can be in place in a group of GHz-SFs that was supposed to have older stellar populations, inverting their D4000 gradients. However, the latter is unlikely, as we have similar SFRs in both samples.

In Figure 4.6, we illustrate key properties of a GHz-SF in the two rightmost columns and its nGHz-SFs twin in the two leftmost columns. From top to bottom, the left column in each pair shows the SDSS optical image, LOFAR 144 MHz continuum image, and FIRST 1.4 GHz continuum image. Analogously, the right column presents the W_{80}, stellar population age, and stellar extinction (from our measurements and values from the MEGACUBES; see Section 4.2.1). A quick comparison of the right columns reveals that the resolved trends observed as radial profiles in Figures 4.4 are also evident at the spaxel level. Namely, GHz-SFs are more centrally obscured and seem to have slightly younger stellar populations. Despite having similar MHz radio luminosities, nGHz-SFs likely remain undetected at GHz frequencies due to their more extended radio morphologies, also seen statistically in the bottom-left panel of Figure 4.3. In fact, nGHz-SFs will insist on being more extended than GHz-SFs even in a restricted control sample (see Figure C.3 and Section C.2). Notably, FIRST's detection limit (1 mJy) falls below the contrast scale used for GHz-SFs in both figures. This is likely related to the effect described in Becker et al. (1995), where sources at fixed integrated flux densities have a critical size limit above which are likely undetected.

4.4.4 Emission-line diagnostics

In Figure 4.5, we show the resolved distribution of the emission-line diagnostics of the [N II] BPT diagram. We use the emission line ratios from the DAP (see Section 4.2.1). Each panel in the figure shows spaxels from either the GHz-SF sample (left column) or the nGHz-SF sample (right column), separated by radial annuli in steps of 0.5 R_{eff} (per row). The spaxels are plotted according to their emission-line ratios and are color-coded by the average W_{80} in that bin. To facilitate comparison, the distribution of spaxel densities for one sample is overlaid as black contours in the opposite column. For example, in the left column (GHz-SF), spaxels are shown in color according to their W_{80} values. In the corresponding right column (nGHz-SF), black contours indicate the density distribution of those same GHz-SF spaxels.

The GHz-SFs are more likely to present values in the transition zone and closer to the extreme starburst line. The latter is more evident when looking at regions offset from the center. This suggests that GHz-SF may have had a previous active nucleus, which left AGN-like emission. Variations in the [N II]/Hα have been routinely related to changes in the metallicity (estimated from the stellar populations, weighted by luminosity). We argue that at fixed spatially resolved metallicity, [N II]/Hα is still in excess. We note that the kinematic differences and emission-line ratio excesses peak in off-nuclear regions. We argue that this can be related to light echoes of previous AGN (e.g., Wylezalek et al. 2020).

Overall, when no clear AGN is present, the presence of radio emission (in the GHz continuum) or its compact radio morphology seems to favor slightly earlier T-Type morphologies, which in turn have redder infrared colors. Lastly, many systematics have been addressed in the literature regarding the effects of the b/a axis ratio when studying galaxy properties. In Appendix C.2, we show a restrictive sample where this is accounted for. We show that most of the trends discussed persist.

4.5 Discussion

Our analysis of star-forming galaxies distinguishes two groups: those with GHz detections (GHz-SFs) and those without (nGHz-SFs). Both have been matched in stellar mass, redshift, and $L_{144\mathrm{MHz}}$ (also as a proxy for extinction-free SFR). At the same time, both groups display similar signatures associated with star formation (global and resolved) and occupy similar space in the main sequence. However, GHz-SFs show distinct properties, including enhanced ionized gas velocity dispersion and off-nuclear emission line ratios, suggesting an additional process at play. Moreover, GHz-SFs are more radio compact (from MHz) than nGHz-SFs. The latter can be true even if matching galaxies for their visual extension or concentration (see Appendix C.2).

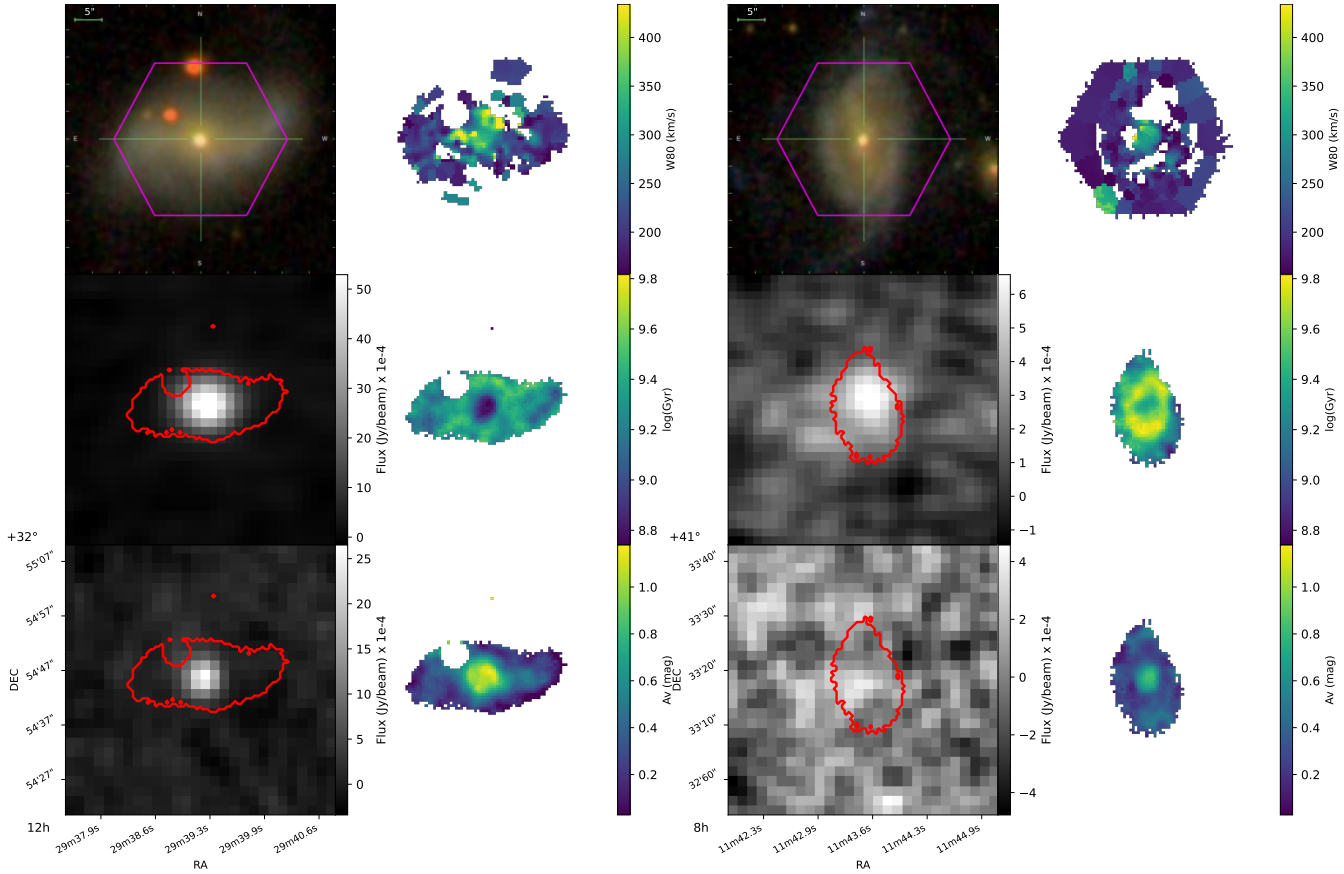

Figure 4.6. Continuum and spatially resolved properties from a pair of galaxies of the main sample. We show four columns of plots, where the two left columns correspond to GHz-SF and the right ones to nGHz-SF. The GHz-SF and nGHz-SF shown here are twins (control sample pairs) in the parameter space defined in Section 4.3. The left column in each shows the SDSS optical image at the top, the LOFAR sky cut in the same region as shown in SDSS is seen in the middle, and the FIRST counterpart at the bottom. The right columns show MaNGA's spatially resolved properties. At the top, the W80, at the middle, the age-weighted luminosity, and at the bottom, the Visual extinction. The red regions in the radio continuum images display the region of MaNGA's coverage.

Our results indicate a strong connection between the presence and compactness of radio emission and the host galaxy properties. In this section, we also show that the fraction of outflows is enhanced in the central regions from GHz-SFs. Given that no differences in SFR are evident, we suggest that GHz-SFs are consistent with radio emission originating in weak shocks (and we can't discard unresolved weak jets), which persist more effectively in gas that has experienced more significant kinematic perturbation, as seen in our evidence. Nevertheless, if shocks were to be the only source responsible for this difference, our results suggest that star formation (or at least, the recent one) is not the primary factor producing them. Here, we explore and discuss the possible mechanisms behind this behavior.

4.5.1 Connection to AGN

We have shown that GHz-SFs have emission-line ratios closer to the extreme starburst line from Kewley et al. (2001a) in the [N II] BPT diagram. Figure 4.5 shows that this is particularly evident when looking at off-nuclear regions with values exceeding the Kauffmann et al. (2003) line. The emission line ratios from GHz-SFs inside this transition zone also have larger W_{80} values. Nevertheless, enhanced W_{80} values also occur below the Kauffmann et al. (2003) demarcation line compared to nGHz-SF; a behavior seen at all annuli. Kewley et al. (2013) have shown that galaxies, even with slow shocks ($\sim$ 100 km s^{-1} to 200 km s^{-1}), can mimic the emission line ratios seen in the transition zone. Therefore, the observed off-nuclear AGN-like emission in GHz-SFs may not uniquely point to AGN photoionization. Supernova-driven outflows and minor galaxy interaction shocks could contribute to the enhancement of the observed line ratios. However, given the comparable SFRs and environmental properties between GHz-SFs and nGHz-SFs, such a scenario is unlikely to serve as a sole explanation. A detailed disentanglement of shock contributions (AGN-related or not) is beyond the scope of our analysis.

Interestingly, literature has suggested that light echoes of previous AGN can explain AGN-like emissions from off-nuclear regions (e.g., Lintott et al. 2009; Wylezalek et al. 2020; Xu & Wang 2023). After an activity period has ended, the galaxy's center now lacks its AGN powering mechanism, and off-nuclear regions can still be ionized by the previous activity, slowly diluting in time (Zubovas & Maskeliūnas 2023). In this context, a past AGN's outflow (or its cumulative effect) can also have perturbed the gas, enhancing the galaxy's emission-line widths. Over the past decade, several studies have suggested that AGN activity in galaxies can be recurrent, with phases of activity turning on and off over time (e.g., Rao et al. 2023; Sebastian et al. 2019; Wolnik et al. 2024). Therefore, not only a single epoch but a cumulative AGN event effect can play a significant role in the evolution of their host galaxies (Harrison & Ramos Almeida 2024). Based on the off-nuclear AGN-like emission in GHz-SFs and the above-mentioned evidence, we suggest that an explanation for these observations is that galaxies in the GHz-SFs sample are more likely to have had one AGN event

(or more) in the recent past than nGHz-SFs. If so, we do not expect that the galaxy has had a jetted AGN episode.

Furthermore, GHz-SFs have enhanced $L_{12\mu m}$ when compared to nGHz-SFs (we show this in Figure 4.3). Given that our targets have the same radio luminosity (at 144 MHz), the ratio between the radio luminosity and mid-infrared luminosities is lower for GHz-SFs. The latter resembles the behavior of the red quasars from Klindt et al. (2019), which also have a larger radio detection fraction. Mid-infrared luminosities can also be used to estimate global SFRs in galaxies. For example, in a sample of star-forming galaxies in Lee et al. (2013), the luminosity at 22 μm and 12 μm is correlated with SFR from Hα. We have compared the SFR from Hα and from $L_{144\mathrm{MHz}}$ with $L_{12\mu m}$. We observe that GHz-SFs offset from such expected relation, having larger SFRs estimated from infrared filters. Offsets from expected SFR estimators have been commonly associated with starburst galaxies or AGN. Similarly, redder WISE colors are found in GHz-SFs. The redder WISE colors may explain why GHz-SFs have slightly earlier T-types. Note that, as discussed in Section 4.4, outflows from AGN in different studies have been seen to carry dust.

Redder infrared colors in GHz-SFs resemble the behavior seen in AGN from Baron & Netzer (2019), where they show that larger velocity widths are observed when AGNs have redder colors, and suggest that outflows from AGNs are carrying dust. Curiously, the properties of our GHz-SFs resemble some of the characteristics of the so-called red quasars (although we do not directly claim a direct correspondence in their physical origin, but perhaps similar). Fawcett et al. (2023) has shown that quasars selected by their red colors have higher chances of being radio-detected when compared to their blue counterparts. The latter has been interpreted as red quasars being an initial phase of the AGN cycle. More strikingly, their results reveal that the radio detection fraction increases in sources with high extinction. The third-left plot of Figure 4.4 reveals that GHz-SFs resemble the same behavior.

We note that the kinematic enhancements in GHz-SFs strikingly mirror the behavior of AGN when they are radio-detected (e.g., Escott et al. 2025; Torres-Papaqui et al. 2024), also independent of their star formation. Escott et al. (2025) find that AGN with radio detections have higher chances of presenting outflow signatures. We perform a similar exercise for our star-forming galaxies. In Figure 4.7, we report the median radial profiles for GHz-SFs and nGHz-SFs based on the fraction of spaxels (in annuli steps of 0.5 R_{eff}) where a second component is needed. We show that our population of GHz-SFs has a slightly greater chance of fitting an additional Gaussian component than nGHz-SFs when looking at the central regions, suggestive of an increased outflow rate. The decision of whether a second component is needed when fitting the emission line profile is described in Albán et al. (2024) and is more detailed in their Appendix. This excess in non-active galaxies independent of the SFR is consistent with the idea that past AGN episodes (or cumulative weak AGN events) may leave behind "fossil" outflows that persist and drive turbulence long after the central engine has turned off (from 2 to 3 times longer than the AGN event, or even

10 times in extreme cases; Zubovas & Maskeliūnas 2023). In this context, galaxies experiencing recent AGN episodes would be more likely to have experienced shock events and, therefore, nGHz-SFs either have yet to undergo an AGN event or have suffered a weaker event, leaving only extended MHz, given that emission at higher frequencies cools earlier than lower frequencies (e.g., Jiang et al. 2010). In simulations, it has been found that the cooling timescale of a shocked wind can last several Myrs (Zubovas & Maskeliūnas 2023), although for a single shock event, the GHz emission may fade during the AGN phase, before the shock fully dissipates (Jiang et al. 2010).

The similarity in the environments of GHz-SF and nGHz-SF galaxies, characterized by the proximity of the closest neighbors, suggests that environmental factors are unlikely to explain the observed differences. Even if the restricted sample (Section C.2) shows a slight close neighbor excess in GHz-SFs, it still demonstrates that it can't be the dominant factor. Therefore, we suggest that this can be explained by GHz-SFs potentially being composed of galaxies that have experienced more (or more recent) AGN events in the past. If the latter is accurate, we do not claim that a previous AGN was present in all GHz-SFs, but GHz-SFs are more likely to have experienced an AGN (or more than one) than nGHz-SFs. Ultimately, our GHz-SFs are systematically more compact in their 144 MHz radio morphology. In a sample of optically selected AGN with radio GHz emission, Mullaney et al. (2013) found that [O III]λ5007 profiles appear more disturbed when 1.4 GHz radio emission originates from a compact core (see also Miranda Marques et al. 2025; Molyneux, S. J. et al. 2019), supporting a link between radio compactness and kinematic disturbances and they suggest this connection to be a result of young or weak radio jets. We can't rule out that a very young AGN is present in GHz-SFs. Studies with increased resolution have shown that a significant population of AGN might be hidden in such compact cores (e.g., Morabito et al. 2025). Part of our GHz-SFs could not only be previous AGN, but also restarting.

In summary, many observed properties in GHz-SFs resemble behaviors from radio-detected AGN, suggesting that similar physical processes are at play.

4.5.2 Star formation processes

We have shown that the fundamental differences between GHz-SFs and nGHz-SFs remain at fixed SFRs. Given that SNRs are one of the candidates for accelerating particles into synchrotron emission, one possibility is that a recent star-formation event has systematically left a larger population of SNRs in the radio-detected population, provided that nGHz-SFs appear to have different star formation histories (e.g., see the T90s in Figure 4.3). A commonly used approach to distinguish between typical HII regions and SNRs often relies on [S II]/Hα > 0.4 as a threshold for SNRs (e.g., Dodorico et al. 1980; Matonick & Fesen 1997). The latter is based on pioneering work from Mathewson & Clarke (1973), where it was observed that the strength of [S II] relative to Hα in SNRs is larger than in H II regions. These SNRs are thought to have

stronger shock fronts compared to H II regions, behind which a sufficiently high-density cool region allows collisionally excited ionization states, such as [S II]. These studies often rely on either Galactic sources or very nearby galaxies, usually depending on high-resolution data (e.g., Cid Fernandes et al. 2021; Li et al. 2024), which is not available for our sample. However, given that we have IFU data available, if a higher fraction of SNRs is present in GHz-SF galaxies, some excess in the [S II]/Hα ratio can be expected. For example, Li et al. (2024) has shown that SNRs in resolved spectroscopy on nearby galaxies can display excess in the emission line ratios, even if SNRs are blended with HII regions. In our study, the [S II]/Hα radial profiles of both GHz-SFs and nGHz-SFs look almost identical, with GHz-SFs even having slightly smaller values. Nevertheless, only a few sources have values that cross the threshold of [S II]/H$\alpha > 0.4$ in any of the samples, with 6 galaxies in nGHZ-SF and 1 in GHz-SF.

Other more elaborated diagnostics for SNRs, based on photoionization and shock excitation models, rely on comparing [S II]/Hα to [O I]/Hα or employing the [O I] BPT diagnostic (Kopsacheili et al. 2020). However, we have done these comparisons, and none of these diagnostics show an excess in favor of a population of SNRs in GHz-SFs.

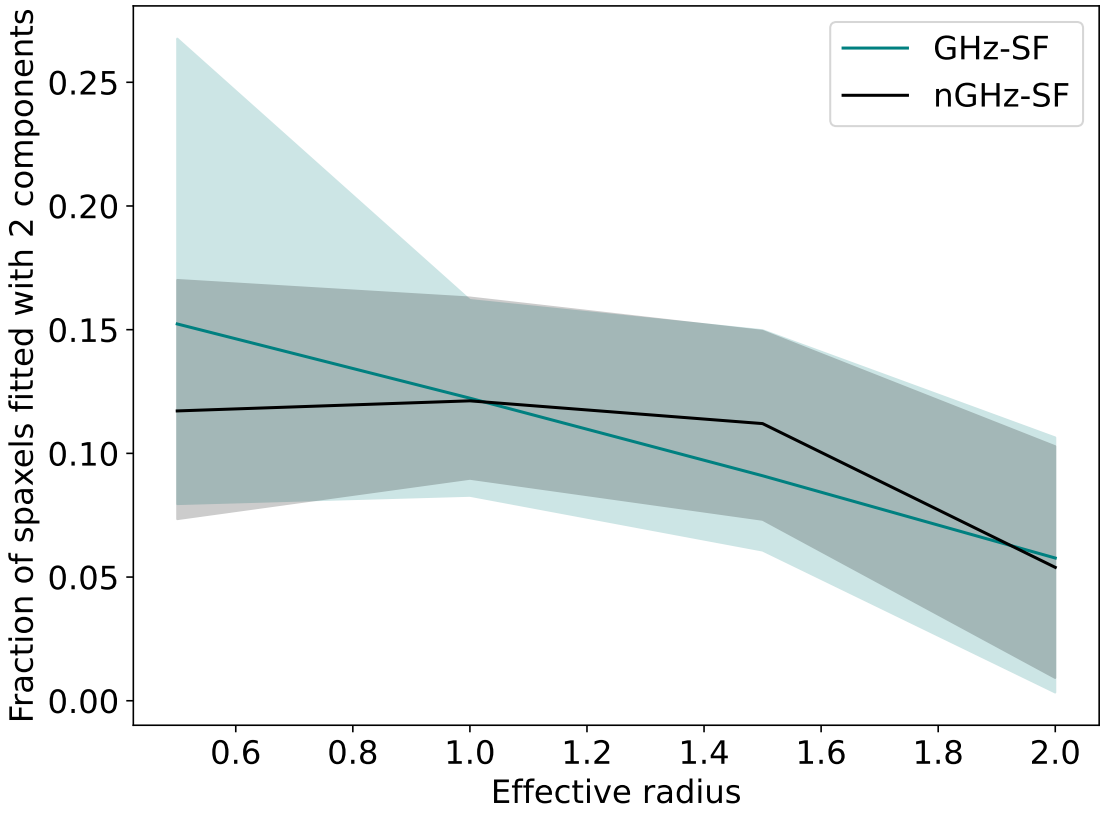

Figure 4.7. Radial outflow fraction. The plot shows the median fraction of pixels that, at each annulus, were fitted with more than 2 Gaussian components, suggesting an outflow.

Table 4.1. Summary of the behavior comparison between GHz-SFs and nGHz-SFs. The first column describes the parameter in comparison, and the second column explains the behavior of GHz-SFs when compared to nGHz-SFs. For example, the gas velocity dispersion of GHz-SFs is in excess at all annuli when compared to nGHz-SFs. The last two columns specify whether the parameter is a resolved property or a global/integrated one. The first block shows empirical properties, while the second shows the modeled ones.

Empirical properties	**Behavior of GHz-SFs compared to nGHz-SFs**	**Resolved**	**Global**
Star formation rates	Identical or very similar	✓	✓
[O III] velocity dispersion	Excess at all annuli	✓	
Outflow detection rate	Central and off-nuclear excess	✓	
[N II] BPT	Central and off-nuclear excess	✓	
D4000 stellar index	Inverted, slightly younger in the center	✓	
Redshift or distance to the target	Similar		✓
Galaxy morphology	Earlier T-Types		✓
Wise colors (W1-W3, W2-W3)	Redder colors		✓
144 MHz morphology	More compact semi-major axis size (norm)		✓
5th nearest neighbor	Similar, but slightly closer neighbors		✓
Modeled properties			
Stellar masses	Identical or very similar	✓	✓
Star formation rates	Identical or very similar	✓	✓
Stellar population ages	Inverted, slightly younger in the center	✓	
Central metallicity	Higher in the central regions	✓	
Stellar extinction	Excess at all annuli	✓	
Look-back time of 90% mass assembly	Earlier, faster		✓

However, the sizes of SNRs can be several orders of magnitude smaller than MaNGA's resolution. Li et al. (2024) show that blended SNR can mimic HII-emission-like regions. Therefore, this effect may still be present but not observable in our sample.

More flexible diagnostics for SNRs have been tested after correcting blended SNR emission line fluxes to get their intrinsic emission line ratios (Cid Fernandes et al. 2021). It is important to note that, as Cid Fernandes et al. (2021) shows, the SNR contribution/impact to the global properties of galaxies is negligible in terms of when measuring SFR (estimated from Hα) or when testing emission-line ratios. For example, Cid Fernandes et al. (2021) finds that only 0.7% of the Hα from their studied galaxy contributes to the overall SFR. Similarly, a detailed study in a larger sample shows that, on average, 5% of the Hα flux can come from SNRs (Vučetić et al. 2015). Conversely, this is not a concern in our study and only shows that we would overestimate their SFR if SNRs were indeed in excess in GHz-SFs. Such an overestimation would bias GHz-SFs to have slightly larger SFRs while keeping lower line widths. If this overestimation were the case, our differences in the kinematics would be even more significant. It is unlikely that a population of SNRs can leave mid-infrared emission imprints in the global properties of our host galaxies. Studies of SNRs in mid-infrared colors show that, even if detected, they are still too faint. For example, Lee (2005) and more references therein show that in the mid-infrared, only around 16% of 100 confirmed galactic SNRs were detected at around $\sim 4.5 - 5.8 \mu m$. This is expected as the integrated Hα luminosity from SNRs is also far from dominant in the global emission in their hosts.

Alternatively, as indicated in the restricted sample, if star formation (SF) were the dominant factor underlying the differences between GHz-SFs and nGHz-SFs, it would imply distinct ongoing SF histories for the two populations. We can get some insights on the latter by looking at the T90s in Figure 4.3, which suggest that GHz-SFs have evolved faster. Similarly, the radio compact morphologies of GHz-SFs may lead to a fraction of GHz-SFs being older starbursts, presumably in their initial path to quiescence (this has been seen at $0.5 < z < 3.0$; Gómez-Guijarro et al. 2019). This, in turn, can be discussed in terms of the AGN-starburst connection (Alexander & Hickox 2012; Ishibashi & Fabian 2016), and has been explored in limited samples. Indeed, an important component in galaxy evolution, potentially driving star formation to quiescence, has been discussed by the role of Post-starburst galaxies (see the comprehensive review from French 2021). For example, post-starburst galaxies have been seen to present AGN light echoes (in MaNGA galaxies French et al. 2023), consistent with a delayed AGN effect on the galaxy.

Despite being out of the scope of our study, we have briefly compared our sample (GHz-SFs and nGHz-SFs) with samples of post-starburst (PSB) galaxies for MaNGA. Cheng et al. (2024) classifies poststarburst galaxies in different categories: irregular, central, and ring-like poststarbursts. A simple look at the GHz or non-GHz detected poststarbursts (that also have MHz in the LOFAR DR2), shows that around 20% are

GHz detected and 80% are not. For our specific sample and control, we find that 14% and 19% of GHz-SFs and nGHz-SFs have a poststarburst classification from Cheng et al. (2024). Irregular post starbursts have most of the counts (95%; only one target here is ring-like PSB) in nGHz-SFs, while 50% are irregular and the other 50% are ring-like, in GHz-SFs. Cheng et al. (2024) discusses that ring PSBs in their sample show positive D4000s and negative EW($H\alpha$). Curiously, GHz-SFs are likely to have the latter behavior, and also more GHz-SFs have ring-like PSB (compared to nGHz-SFs), although this represents a very small fraction of all GHz-SFs. Our results are not changed if we remove all PSBs from MaNGA and repeat the analysis.

4.6 Conclusions

Radio-detected galaxies have been found to differ when compared to their non-detected counterparts. These differences span from modest to moderate changes, such as colors, morphological types, and obscuration levels in the case of SF galaxies, to complex differences such as strongly differing obscuration and gas velocity dispersions in AGN. This effect has been observed or replicated for AGN and SF galaxies at multiple radio frequencies (e.g., $\sim$ 144 MHz to 1.4 GHz; Ahmed et al. 2024; Escott et al. 2025; Hopkins et al. 2003a; Nandi et al. 2025; Torres-Papaqui et al. 2024). To gain insights on the origin of these findings, we study non-detections based on GHz frequencies and virtually follow them up with available and more sensitive low-frequency data. We primarily use SF galaxies to first understand whether the differences can arise without the presence of a currently active AGN.

We have compared star-forming galaxies with (GHz-SF) and without (nGHz-SF) radio-GHz detections at fixed stellar masses, 144 MHz luminosities, and redshifts. From a multi-wavelength perspective, none of these galaxies present evidence of having a currently active AGN. Despite showing the same SFRs (estimated by several tracers), both samples systematically differ in global and resolved properties. In Table 4.5.2, we summarize the comparisons we have discussed. Below, we provide an overview of our main results:

i) Radio detection in galaxies, whether they are AGN or not, impacts their properties. We have tested this at 1.4 GHz detections. Analogous findings are seen in other studies at lower or equal frequencies.

ii) As summarized in Table 4.5.2, when compared to nGHz-SFs at fixed stellar masses and SFRs, our GHz-SFs are more centrally obscured; they have larger ionized gas velocity dispersions accompanied by larger outflow detection rates. Redder colors and earlier galaxy morphologies. Inverted stellar age gradients while appearing slightly younger in the center, and they have assembled their current stellar mass faster.

iii) Broadly speaking, the behavior in GHz-SFs mentioned resembles the behavior from radio-detected AGN of many recent studies. Specifically, larger velocity widths, more obscuration, redder, higher outflow detection rates, and more compact morphologies are seen in GHz-SFs.

iv) GHz-SFs have off-nuclear emission line ratios closer to AGN-like signatures. Together with being more radio compact, it appears that GHz-SFs might have suffered an AGN in the recent past, or have an old starburst, probably also related to the connection between starbursts and AGN.

v) SF processes (or at least recent ones) seem unlikely to be the dominant process in explaining all the contrasting behavior.

vi) Environmental processes and bars present in the morphologies do not seem to have an impact on these differences.

Concerning what is found in the literature, we confirm that for SF galaxies, radio detections come preferentially from galaxies that are more obscured by visual extinction. Broadly suggesting them to be a sub-population of SF galaxies themselves (as seen in Hopkins et al. 2003b). Similar findings have been found for AGN sources. Interestingly, AGN also have larger values in their velocity widths and are more likely to show outflow detections when radio emission is detected (and/or has compact morphologies), discarding star-formation processes as the main responsible driver. The similarity of the behavior in AGN hosts and SF galaxies when radio is present suggests that historic AGN events could partly explain the different behavior seen in GHz-SFs. If this were not the case, the contrasting properties when radio is detected would need to be typical behavior of galaxies regardless of AGN activity.

We speculate that part of the reason why GHz-SFs are different from nGHz-SFs is that the GHz-SFs have a population of galaxies that have experienced more recent AGN events in their hosts. If the latter is the case, the enhanced kinematics in GHz-SFs contain evidence of the impact of fossil outflows (e.g., Zubovas & Maskeliūnas 2023). We show that for a galaxy sample where each target must have a radio detection, a preferred parameter space in a low-redshift sample is already set. Notably, some of the behavior seen in our results can be washed out using single-fiber spectroscopic data, emphasizing the utility and motivation to exploit IFU data. Both points mentioned above should be held in mind when studying high redshift targets. In a future study, we will repeat this exercise, BPT-transition objects, quenched galaxies, and AGN.

Chapter 5

Summary and Conclusions

Although feedback from supermassive black holes is now widely accepted as a necessary ingredient in galaxy evolution models, its observational signatures remain diverse and sometimes ambiguous. Not only do selection effects hinder us from achieving a complete picture, but the variety of galaxies and environments in which AGN occur also makes finding their signature more challenging. At the top of this cake, the timescales governing AGN and galaxy-wide secular processes are not only non-simultaneous, but they can differ by a few orders of magnitude, operating on fundamentally different scales.

This thesis embraces that view and builds on the premise that AGN are events in the evolution of galaxies. That means accounting for selection effects, probing activity across wavelengths, and critically, incorporating the role of the AGN duty cycle, at least first order. From this perspective, the imprint of AGN feedback may persist long after the observable AGN phase has ended. Therefore, many of our interpretations have a door open in the context of the AGN duty cycle. This approach has been recognized recently as a significant consensus within the scientific community (Alexander et al. 2025, a highly relevant review), where there is no reason to believe that the impact of AGN feedback in galaxies is always observable while the AGN is currently active. In this context, the three studies presented here combine a multi-wavelength selection strategy, leverage spatially resolved spectroscopy, and maintain rigorous control over host galaxy properties to disentangle selection-driven biases from genuine physical effects.

In Paper I, we addressed the core issue of selection bias, showing that different techniques can identify distinct AGN populations. We demonstrate that, even in a controlled sample of host-galaxy properties, two independent (radio vs. optical) selection techniques can identify AGN with contrasting ionized gas kinematics. Our study shows that radio-selected AGN are more likely to exhibit broader outflow linewidths, suggesting a connection between radio selection and the presence of outflows. The broader extent of the emission linewidths can be attributed to radio observations, which reveal more evolved AGN within the context of the duty cycle, with their hosts' ionized gas more perturbed due to prolonged or repetitive AGN events.

While Paper I examines the non-overlapping radio and optical AGN populations, Paper II combines the overlapping ones, finding that they present the strongest outflow-like kinematic signatures. These "dual-flagged" AGN demonstrate that feedback may peak when radiative and kinetic processes act together. Importantly, we also note that in low radio-luminosity AGN, where both radio and optical observations agree on the AGN selection, the radio emission could originate from wind-driven shocks. Another important addition in Paper II is the inclusion of LOFAR survey data, which enables the study of lower radio frequencies and a significant increase in the number of sources detected at radio frequencies.

Crucially, Paper I and Paper II both discuss whether the effects of AGN feedback persist after the AGN has ceased to operate. Moreover, both studies emphasize the significance of radio emission in identifying high emission linewidths. Paper III addresses this question by searching for galaxies that exhibit ionized gas kinematics consistent with outflow signatures, yet no longer display nuclear activity. Motivated by our findings that radio emission is often associated with more perturbed kinematics and the possibility that radio emission results from shocks driven by outflows, we ask if the same is true for non-active galaxies. This is done following our carefully controlled sample criterion.

Paper III shows a persistent view, where galaxies, even if not AGN, show greater emission linewidths provided that they present radio emission. This study combines a vast amount of properties, ranging from environmental scales to multiwavelength observations and morphology. When looking at many (resolved) galaxy-wide properties, radio-detected star-forming galaxies differ from their radio-non-detected star-forming counterparts exactly as when comparing radio-detected AGN with non-detected ones (note that we remove AGN from the star-forming galaxy sample). Rather than being a coincidence, we interpret this as indicating that radio-detected galaxies are more likely to have experienced an AGN event in the past than non-radio-detected ones. Wind-driven shocks, as suggested by the excess outflow rate and emission linewidths, indicate that some of these targets may be fossil AGN-driven outflow candidates. This is in line with the idea that the absence of AGN indicators does not necessarily imply the absence of feedback. Paper III thus adds a crucial temporal layer to our understanding of AGN-galaxy coevolution: while feedback may be long-lived, AGN signatures are often short-lived and intermittent.

Together, these three studies converge on a picture of AGN feedback that is multimodal: temporally extended, and highly sensitive to how we define and detect AGN in the first place. The consistent use of integral field spectroscopy across this work enabled us to link nuclear activity with spatially extended gas kinematics and galaxy-scale structure, providing insights that would be inaccessible with unresolved data.

This thesis proposes a more comprehensive understanding of AGN feedback. It is open to accept AGN, not as an event we catch in real-time, but as a long-lasting imprint in the kinematics of galaxies. It invites us to think about past activity in the gas that remains. A significant caveat of our study is that we only probe the

ionized gas for its kinematics and outflow tracer properties. Future work will require more time-domain diagnostics, higher spatial resolution spectroscopy, and deeper multiwavelength coordination. However, the path is now open to insightful exploration. Feedback is not just what AGN do at the moment; it is what they have left behind.

List of publications

First author publications

- **Marco Albán** and Dominika Wylezalek
  Classifying the full SDSS-IV MaNGA Survey using optical diagnostic diagrams: Presentation of AGN catalogs in flexible apertures
  A&A 674, A85 (2023); doi:10.1051/0004-6361/202245437

  *Not fully included in any chapter, but summarized in the Introduction (Section 1.4).

- **Marco Albán**, Dominika Wylezalek, Julie M. Comerford; Jenny E. Greene, and Rogemar A. Riffel
  Mapping AGN winds: A connection between radio-mode AGNs and the AGN feedback cycle
  A&A 691, A124 (2024); doi:10.1051/0004-6361/202451738

  *Included in Chapter 2

- **Marco Albán**, Dominika Wylezalek, Pranav Kukreti, Rogemar A. Riffel, and Rogerio Riffel
  On the origin of radio emission in star-forming galaxies: connection to restarted or relic AGN activity
  Submitted to A&A (in the referee process)

  *Included in Chapter 4

Publications as co-author

- Pranav Kukreti, Dominika Wylezalek, **Marco Albán**, and Bruno Dall'Agnol de Oliveira

  Feedback from low-to-moderate-luminosity radio-active galactic nuclei with MaNGA
  A&A 698, A99 (2025); doi:10.1051/0004-6361/202453307

  *Included in Chapter 3

- Maitê S. Z. de Mellos, Rogemar A. Riffel, Jaderson S. Schimoia, Sandro B. Rembold, Rogerio Riffel, Thaisa Storchi-Bergmann, Dominika Wylezalek, Gabriele S. Ilha, **Marco Albán**, Oli L. Dors, Lara Gatto, Angela C. Krabbe, Nicolas D.

Mallmann, and Marina Trevisan
Determining star formation rates in AGN hosts from strong optical emission lines
MNRAS 535, 123–131 (2024); doi:10.1093/mnras/stae2352

*Not included in any chapter

- Caroline Bertemes, Dominika Wylezalek, **Marco Albán**, Manuel Aravena, William M. Baker, Sara Cazzoli, Claudia Cicone, Sergio Martín, Alice Schimek, Jeff Wagg, and Wuji Wang
  MASCOT: molecular gas depletion times and metallicity gradients - evidence for feedback in quenching active galaxies
  MNRAS 518, 5500–5521 (2023); doi.org/10.1093/mnras/stac3448

  *Not included in any chapter.

Bibliography

Aalto, S., Garcia-Burillo, S., Muller, S., et al. 2012, A&A, 537, A44

Abazajian, K., Adelman-McCarthy, J. K., Agüeros, M. A., et al. 2003, AJ, 126, 2081

Abdalla, E., Abellán, G. F., Aboubrahim, A., et al. 2022, JHEAP, 34, 49

Abdurro'uf, Accetta, K., Aerts, C., et al. 2022, ApJS, 259, 35

Afonso, J., Hopkins, A., Mobasher, B., & Almeida, C. 2003, ApJ, 597, 269

Ahmed, U. T., Hopkins, A. M., Ware, J., et al. 2024, Publ. Astron. Soc. Aust., 41, e021

Aird, J., Coil, A. L., Georgakakis, A., et al. 2015, MNRAS, 451, 1892

Alatalo, K., Lacy, M., Lanz, L., et al. 2015, ApJ, 798, 31

Albán, M. & Wylezalek, D. 2023, A&A, 674, A85

Albán, M., Wylezalek, D., Comerford, J. M., Greene, J. E., & Riffel, R. A. 2024, A&A, 691, A124

Alberts, S., Rujopakarn, W., Rieke, G. H., Jagannathan, P., & Nyland, K. 2020, ApJ, 901, 168

Alexander, D. M. & Hickox, R. C. 2012, New Astron. Rev., 56, 93

Alexander, D. M., Hickox, R. C., Aird, J., et al. 2025, arXiv e-prints, arXiv:2506.19166

Almaini, O., Wild, V., Maltby, D., et al. 2025, MNRAS, 539, 3568

Alonso Herrero, A., García-Burillo, S., Pereira-Santaella, M., et al. 2023, A&A, 675, A88

Andrae, R., Schulze-Hartung, T., & Melchior, P. 2010, Dos and don'ts of reduced chi-squared

Antonucci, R. 1993, ARA&A, 31, 473

Argudo-Fernández, M., Verley, S., Bergond, G., et al. 2015, A&A, 578, A110

Assef, R. J., Stern, D., Noirot, G., et al. 2018, ApJS, 234, 23

Ayubinia, A., Woo, J.-H., Rakshit, S., & Son, D. 2023, ApJ, 954, 27

Bañados, E., Venemans, B. P., Mazzucchelli, C., et al. 2018, Nature, 553, 473

Bae, H.-J., Woo, J.-H., Karouzos, M., et al. 2017, ApJ, 837, 91

Baldwin, J. A., Phillips, M. M., & Terlevich, R. 1981, PASP, 93, 5

Bambi, C. 2020, in Multifrequency Behaviour of High Energy Cosmic Sources - XIII. 3-8 June 2019. Palermo, 28

Baron, D. & Netzer, H. 2019, MNRAS, 482, 3915

Baron, D., Netzer, H., Davies, R. I., & Xavier Prochaska, J. 2020, MNRAS, 494, 5396

Baron, D., Netzer, H., Lutz, D., Prochaska, J. X., & Davies, R. I. 2021, MNRAS, 509, 4457

Baron, D., Netzer, H., Prochaska, J. X., et al. 2018, MNRAS, 480, 3993

Barrows, R. S., Comerford, J. M., Stern, D., & Assef, R. J. 2021, ApJ, 922, 179

Barthelmy, S. D., Barbier, L. M., Cummings, J. R., et al. 2005, Space Science Reviews, 120, 143

Becker, R. H., White, R. L., & Helfand, D. J. 1995, ApJ, 450, 559

Behroozi, P., Wechsler, R. H., Hearin, A. P., & Conroy, C. 2019, MNRAS, 488, 3143

Belfiore, F., Westfall, K. B., Schaefer, A., et al. 2019, AJ, 158, 160

Bennert, N., Jungwiert, B., Komossa, S., Haas, M., & Chini, R. 2006, A&A, 456, 953–966

Bertemes, C., Wylezalek, D., Albán, M., et al. 2022, MNRAS, 518, 5500

Best, P. N. & Heckman, T. M. 2012, MNRAS, 421, 1569

Best, P. N., Kauffmann, G., Heckman, T. M., & Ivezić, Ž. 2005, MNRAS, 362, 9

Best, P. N., Kondapally, R., Williams, W. L., et al. 2023, MNRAS, 523, 1729

Blanton, M. R., Dalcanton, J., Eisenstein, D., et al. 2001, AJ, 121, 2358

Blanton, M. R., Kazin, E., Muna, D., Weaver, B. A., & Price-Whelan, A. 2011, AJ, 142, 31

Bluck, A. F., Maiolino, R., Piotrowska, J. M., et al. 2020, MNRAS, 499, 230

Boroson, T. A. 2002, ApJ, 585, 647

Brienza, M., Morganti, R., Harwood, J., et al. 2020, A&A, 638

Brinchmann, J., Charlot, S., Heckman, T. M., et al. 2004, arXiv [[arXiv]0406220]

Brinchmann, J., Charlot, S., White, S. D. M., et al. 2004, MNRAS, 351, 1151

Brusa, M., Comastri, A., Mignoli, M., et al. 2003, A&A, 409, 65

Buitrago, F., Trujillo, I., Conselice, C. J., & Häußler, B. 2013, MNRAS, 428, 1460

Bull, P., Akrami, Y., Adamek, J., et al. 2016, Physics of the Dark Universe, 12, 56

Bundy, K., Bershady, M. A., Law, D. R., et al. 2015, ApJ, 798, 7

Calistro Rivera, G., Alexander, D. M., Harrison, C. M., et al. 2023, arXiv e-prints, arXiv:2312.10177

Canizares, C. R., Fabbiano, G., & Trinchieri, G. 1987, ApJ, 312, 503

Cappellari, M. 2016, ARA&A, 54, 597

Cappellari, M. & Copin, Y. 2003, MNRAS, 342, 345

Cardelli, J. A., Clayton, G. C., & Mathis, J. S. 1989, ApJ, 345, 245

Carlstrom, J. E. & Kronberg, P. P. 1991, ApJ, 366, 422

Cavagnolo, K. W., McNamara, B. R., Nulsen, P. E. J., et al. 2010, ApJ, 720, 1066

Chae, K.-H. 2011, MNRAS, 413, 887

Cheng, Z., Li, C., Li, N., Yan, R., & Mo, H. 2024, ApJ, 961, 216

Cheung, E., Bundy, K., Cappellari, M., et al. 2016, Nature, 533, 504

Cicone, C., Maiolino, R., & Marconi, A. 2016, A&A, 588, A41

Cicone, C., Maiolino, R., Sturm, E., et al. 2014, A&A, 562, A21

Cid Fernandes, R., Carvalho, M. S., Sánchez, S. F., de Amorim, A., & Ruschel-Dutra, D. 2021, MNRAS, 502, 1386

Cid Fernandes, R., Mateus, A., Sodré, L., Stasińska, G., & Gomes, J. M. 2005, MNRAS, 358, 363

Cid Fernandes, R., Stasinska, G., Mateus, A., & Asari, N. V. 2011, MNRAS, 413, 1687

Cid Fernandes, R., Stasińska, G., Schlickmann, M. S., et al. 2010, MNRAS, 403, 1036–1053

Combes, F. 2017, Frontiers in Astronomy and Space Sciences, 4, 10

Comerford, J. M., Negus, J., Müller-Sánchez, F., et al. 2020, ApJ, 901, 159

Comerford, J. M., Nevin, R., Negus, J., et al. 2024, ApJ, 963, 53

Condon, J. J. 1992, ARA&A, 30, 575

Condon, J. J., Cotton, W. D., & Broderick, J. J. 2002, AJ, 124, 675

Condon, J. J., Cotton, W. D., Greisen, E. W., et al. 1998, AJ, 115, 1693

Condon, J. J. & Ransom, S. M. 2016, Essential Radio Astronomy

Conselice, C. J. 2006, MNRAS, 373, 1389

Cresci, G., Tozzi, G., Perna, M., et al. 2023, A&A, 672, A128

Croton, D. J., Springel, V., White, S. D. M., et al. 2006, MNRAS, 365, 11

Cutri, R. M., Wright, E. L., Conrow, T., et al. 2021, VizieR Online Data Catalog, II/328

Cyburt, R. H., Fields, B. D., Olive, K. A., & Yeh, T.-H. 2016, Reviews of Modern Physics, 88, 015004

Daddi, E., Delvecchio, I., Dimauro, P., et al. 2022, A&A, 661, L7

Das, S., Kharb, P., Morganti, R., & Nandi, S. 2021, MNRAS, 504, 4416

Davies, L. J. M., Huynh, M. T., Hopkins, A. M., et al. 2017, MNRAS, 466, 2312

Davies, R. L., Belli, S., Park, M., et al. 2024, MNRAS, 528, 4976

Deconto-Machado, A., Riffel, R. A., Ilha, G. S., et al. 2022, A&A, 659, 131

Dey, A., Schlegel, D. J., Lang, D., et al. 2019, AJ, 157, 168

Di Matteo, T., Springel, V., & Ilernquist, L. 2005, Nature, 433, 604

DiPompeo, M. A., Hickox, R. C., Carroll, C. M., et al. 2018, ApJ, 856, 76

Dodorico, S., Dopita, M. A., & Benvenuti, P. 1980, A&AS, 40, 67

Domínguez Sánchez, H., Margalef, B., Bernardi, M., & Huertas-Company, M. 2022, MNRAS, 509, 4024

D'Onofrio, M., Marziani, P., & Chiosi, C. 2021, Frontiers in Astronomy and Space Sciences, 8, 157

Dopita, M. A., Kewley, L. J., Heisler, C. A., & Sutherland, R. S. 2000, ApJ, 542, 224

Dopita, M. A. & Sutherland, R. S. 1995, ApJ, 455, 468

Du, P., Wang, J.-M., & Zhang, Z.-X. 2017, ApJ, 840, L6

Dubois, Y., Peirani, S., Pichon, C., et al. 2016, MNRAS, 463, 3948

Dullius Mallmann, N. & Riffel, R. 2023, ndmallmann/urutau: Urutau

Durret, F. & Bergeron, J. 1988, A&AS, 75, 273

Escott, E. L., Morabito, L. K., Scholtz, J., et al. 2025, MNRAS, 536, 1166

Fabian, A. 2012, Annual Review of Astronomy and Astrophysics, 50, 455

Fabian, A. C. 1979, Proceedings of the Royal Society of London Series A, 366, 449

Fabian, A. C. 1994, ARA&A, 32, 277

Falcón-Barroso, J., Sánchez-Blázquez, P., Vazdekis, A., et al. 2011, A&A, 532, A95

Faucher-Giguère, C. A. & Quataert, E. 2012, MNRAS, 425, 605

Fawcett, V. A., Alexander, D. M., Brodzeller, A., et al. 2023, MNRAS, 525, 5575

Fawcett, V. A., Alexander, D. M., Rosario, D. J., et al. 2020, MNRAS, 494, 4802

Feng, H., Shen, Y., & Li, H. 2014, ApJ, 794, 77

Ferrarese, L. & Merritt, D. 2000, ApJ, 539, L9

Feruglio, C., Maiolino, R., Piconcelli, E., et al. 2010, A&A, 518, L155

Fiore, F., Feruglio, C., Shankar, F., et al. 2017, A&A, 601, A143

Fischer, J. L., Domínguez Sánchez, H., & Bernardi, M. 2019, MNRAS, 483, 2057

Fluetsch, A., Maiolino, R., Carniani, S., et al. 2019, MNRAS, 483, 4586

Förster Schreiber, N. M., Genzel, R., Newman, S. F., et al. 2014, ApJ, 787, 38

French, K. D. 2021, PASP, 133, 072001

French, K. D., Earl, N., Novack, A. B., et al. 2023, ApJ, 950, 153

Fu, Y., Cappellari, M., Mao, S., et al. 2023, MNRAS, 524, 5827

Galvin, T. J., Huynh, M. T., Norris, R. P., et al. 2020, MNRAS, 497, 2730

Gatto, L., Storchi-Bergmann, T., Riffel, R. A., et al. 2024, MNRAS, 530, 3059

Girdhar, A., Harrison, C. M., Mainieri, V., et al. 2022, MNRAS, 512, 1608

Gómez-Guijarro, C., Magdis, G. E., Valentino, F., et al. 2019, ApJ, 886, 88

Goto, T., Yamauchi, C., Fujita, Y., et al. 2003, MNRAS, 346, 601

Graham, A. W. 2016, in Astrophysics and Space Science Library, Vol. 418, Galactic Bulges, ed. E. Laurikainen, R. Peletier, & D. Gadotti, 263

Greene, J. E. & Ho, L. C. 2004, The Astrophysical Journal, 610, 722

Greene, J. E., Strader, J., & Ho, L. C. 2020, ARA&A, 58, 257

Gunn, J. E., Siegmund, W. A., Mannery, E. J., et al. 2006, AJ, 131, 2332

Gürkan, G., Hardcastle, M. J., Smith, D. J. B., et al. 2018, MNRAS, 475, 3010

Gültekin, K., Richstone, D. O., Gebhardt, K., et al. 2009, The Astrophysical Journal, 698, 198

Haffner, L. M., Dettmar, R. J., Beckman, J. E., et al. 2009, Reviews of Modern Physics, 81, 969

Hagen, S., Done, C., & Edelson, R. 2024, MNRAS, 530, 4850

Halpern, J. P. & Steiner, J. E. 1983, ApJ, 269, L37

Hardcastle, M. J., Horton, M. A., Williams, W. L., et al. 2023, A&A, 678, A151

Hardcastle, M. J., Williams, W. L., Best, P. N., et al. 2019, A&A, 622, A12

Harrison, C. M. 2017, Nature Astronomy, 1, 0165

Harrison, C. M., Alexander, D. M., Mullaney, J. R., & Swinbank, A. M. 2014, MNRAS, 441, 3306

Harrison, C. M., Girdhar, A., & Ward, S. R. 2023, arXiv e-prints, arXiv:2307.03770

Harrison, C. M. & Ramos Almeida, C. 2024, Galaxies, 12, 17

Heckman, T. M. 1980, A&A, 87, 152

Heckman, T. M., Alexandroff, R. M., Borthakur, S., Overzier, R., & Leitherer, C. 2015, ApJ, 809, 147

Heckman, T. M. & Best, P. N. 2014, ARA&A, 52, 589

Heckman, T. M., Kauffmann, G., Brinchmann, J., et al. 2004, ApJ, 613, 109

Heckman, T. M., Miley, G. K., van Breugel, W. J. M., & Butcher, H. R. 1981, ApJ, 247, 403

Heger, A., Müller, B., & Mandel, I. 2023, arXiv e-prints, arXiv:2304.09350

Herpich, F., Mateus, A., Stasińska, G., Fernandes, R. C., & Asari, N. V. 2016, MNRAS, 462, 1826

Herrera-Camus, R., Janssen, A., Sturm, E., et al. 2020, A&A, 635, A47

Hickox, R. C. & Alexander, D. M. 2018a, ARA&A, 56, 625

Hickox, R. C. & Alexander, D. M. 2018b, ARA&A, 56, 625

Hickox, R. C., Jones, C., Forman, W. R., et al. 2009, ApJ, 696, 891

Ho, L. C. 1999, Advances in Space Research, 23, 813

Holden, L. R. & Tadhunter, C. N. 2025, MNRAS, 536, 1857

Hopkins, A. M., Afonso, J., Georgakakis, A., et al. 2003a, arXiv e-prints, astro

Hopkins, A. M., Miller, C. J., Nichol, R. C., et al. 2003b, ApJ, 599, 971

Hopkins, P. F. & Hernquist, L. 2009, ApJ, 694, 599

Hopkins, P. F., Hernquist, L., Cox, T. J., et al. 2006, ApJS, 163, 1

Husemann, B. & Harrison, C. M. 2018, Nature Astronomy, 2, 196

Ishibashi, W. & Courvoisier, T. J. L. 2011, A&A, 525, A118

Ishibashi, W. & Fabian, A. C. 2016, MNRAS, 463, 1291

Ivezić, Ž., Menou, K., Knapp, G. R., et al. 2002, AJ, 124, 2364

Jarvis, M. E., Harrison, C. M., Mainieri, V., et al. 2021, MNRAS, 503, 1780

Jarvis, M. E., Harrison, C. M., Thomson, A. P., et al. 2019, MNRAS, 485, 2710

Jeon, J., Liu, B., Taylor, A. J., et al. 2025, arXiv e-prints, arXiv:2503.14703

Ji, Z., Giavalisco, M., Kirkpatrick, A., et al. 2022, ApJ, 925, 74

Jiang, Y.-F., Ciotti, L., Ostriker, J. P., & Spitkovsky, A. 2010, ApJ, 711, 125

Jin, G., Kauffmann, G., Best, P. N., Shenoy, S., & Małek, K. 2024, arXiv e-prints, arXiv:2409.01279

Juodžbalis, I., Maiolino, R., Baker, W. M., et al. 2024, Nature, 636, 594

Jurlin, N., Morganti, R., Brienza, M., et al. 2020, A&A, 638, A34

Kang, D. & Woo, J.-H. 2018, ApJ, 864, 124

Karouzos, M., Woo, J.-H., & Bae, H.-J. 2016, The Astrophysical Journal, 819, 148

Kauffmann, G. 2018, MNRAS, 480, 3201

Kauffmann, G., Heckman, T. M., & Best, P. N. 2008, MNRAS, 384, 953

Kauffmann, G., Heckman, T. M., Tremonti, C., et al. 2003, MNRAS, 346, 1055

Kennicutt, R. C. & Evans, N. J. 2012, ARA&A, 50, 531

Kennicutt, Jr., R. C., Hao, C.-N., Calzetti, D., et al. 2009, ApJ, 703, 1672

Kewley, L. J., Dopita, M. A., Leitherer, C., et al. 2013, ApJ, 774, 100

Kewley, L. J., Dopita, M. A., Sutherland, R. S., Heisler, C. A., & Trevena, J. 2001a, ApJ, 556, 121

Kewley, L. J., Dopita, M. A., Sutherland, R. S., Heisler, C. A., & Trevena, J. 2001b, ApJ, 556, 121

Kewley, L. J., Groves, B., Kauffmann, G., & Heckman, T. 2006, MNRAS, 372, 961

Kewley, L. J., Nicholls, D. C., & Sutherland, R. S. 2019, ARA&A, 57, 511

Kim, C., Woo, J.-H., Luo, R., et al. 2023, ApJ, 958, 145

King, A. & Pounds, K. 2015, ARA&A, 53, 115

King, A. R., Zubovas, K., & Power, C. 2011, MNRAS, 415, L6

Klein, U., Wielebinski, R., & Morsi, H. W. 1988, A&A, 190, 41

Klindt, L., Alexander, D. M., Rosario, D. J., Lusso, E., & Fotopoulou, S. 2019, MNRAS, 488, 3109

Kopsacheili, M., Zezas, A., & Leonidaki, I. 2020, MNRAS, 491, 889

Kormendy, J. & Ho, L. C. 2013, ARA&A, 51, 511

Kormendy, J. & Richstone, D. 1995, ARA&A, 33, 581

Kukreti, P. & Morganti, R. 2024, A&A, 690, A140

Kukreti, P., Morganti, R., Shimwell, T. W., et al. 2022, A&A, 658, A6

Kukreti, P., Morganti, R., Tadhunter, C., & Santoro, F. 2023, A&A, 674, A198

Kukreti, P., Wylezalek, D., Alb\'an, M., & DallAgnol de Oliveira, B. 2025, arXiv e-prints, arXiv:2503.20889

Lacerda, E. A. D., Sánchez, S. F., Mejía-Narváez, A., et al. 2022, New Astron., 97, 101895

Lai, T. S. Y., Armus, L., U, V., et al. 2022, ApJ, 941, L36

Laker, M. A., Camacho, C. D., Jones, D., & Moody, J. 2022, Symmetry, 14

LaMassa, S. M., Heckman, T. M., Ptak, A., et al. 2010, ApJ, 720, 786

Lammers, C., Iyer, K. G., Ibarra-Medel, H., et al. 2023, ApJ, 953, 26

Lammers, C., Iyer, K. G., Ibarra-Medel, H., et al. 2023, ApJ, 953, 26

Larson, R. L., Finkelstein, S. L., Kocevski, D. D., et al. 2023, ApJ, 953, L29

Law, D. R., Cherinka, B., Yan, R., et al. 2016, AJ, 152, 83

Law, D. R., Westfall, K. B., Bershady, M. A., et al. 2021, The Astronomical Journal, 161, 52

Law, D. R., Yan, R., Bershady, M. A., et al. 2015, AJ, 150, 19

Le Fèvre, O., Lemaux, B. C., Nakajima, K., et al. 2019, A&A, 625, A51

Lee, H.-G. 2005, Journal of Korean Astronomical Society, 38, 385

Lee, J. C., Hwang, H. S., & Ko, J. 2013, ApJ, 774, 62

Leslie, S. K., Kewley, L. J., Sanders, D. B., & Lee, N. 2016, MNRAS, 455, L82

Li, J., Kreckel, K., Sarbadhicary, S., et al. 2024, A&A, 690, A161

Liao, M., Wang, J., Ren, W., & Zhou, M. 2024, MNRAS, 528, 3696

Lilly, S. J., Carollo, C. M., Pipino, A., Renzini, A., & Peng, Y. 2013, ApJ, 772, 119

Lintott, C. J., Schawinski, K., Keel, W., et al. 2009, MNRAS, 399, 129

Liu, G., Zakamska, N. L., Greene, J. E., Nesvadba, N. P. H., & Liu, X. 2013, MNRAS, 436, 2576

Liu, X., Greene, J. E., Shen, Y., & Strauss, M. A. 2010, ApJ, 715, L30

Luo, R., Woo, J.-H., Karouzos, M., et al. 2021, ApJ, 908, 221

Lynden-Bell, D. 1969, Nature, 223, 690

Lyu, J., Alberts, S., Rieke, G. H., & Rujopakarn, W. 2022, ApJ, 941, 191

Madau, P. & Dickinson, M. 2014, ARA&A, 52, 415

Marconi, A. & Hunt, L. K. 2003, ApJ, 589, L21

Masters, K. L., Mosleh, M., Romer, A. K., et al. 2010, MNRAS, 405, 783

Mathewson, D. S. & Clarke, J. N. 1973, ApJ, 180, 725

Matonick, D. M. & Fesen, R. A. 1997, ApJS, 112, 49

McElroy, R., Croom, S. M., Pracy, M., et al. 2015, MNRAS, 446, 2186

McNamara, B. R. & Nulsen, P. E. 2007, ARA&A, 45, 117

McNamara, B. R. & Nulsen, P. E. 2012, NJoP, 14, 055023

Mingo, B., Watson, M. G., Rosen, S. R., et al. 2016, MNRAS, 462, 2631

Miranda Marques, B. L., Rodríguez-Ardila, A., Fonseca-Faria, M. A., & Panda, S. 2025, ApJ, 978, 16

Mizumoto, M., Sameshima, H., Kobayashi, N., et al. 2024, ApJ, 960, 41

Molina, M., Duffy, L., Eracleous, M., et al. 2023, The Astrophysical Journal Supplement Series, 268, 63

Molyneux, S. J., Harrison, C. M., & Jarvis, M. E. 2019, A&A, 631, A132

Morabito, L. K., Kondapally, R., Best, P. N., et al. 2025, MNRAS, 536, L32

Morganti, R. 2017a, Nature Astronomy, 1, 596

Morganti, R. 2017b, Frontiers in Astronomy and Space Sciences, 4, 42

Morganti, R. 2021, Nuclear Activity in Galaxies Across Cosmic Time, 356, 229

Mulcahey, C. R., Leslie, S. K., Jackson, T. M., et al. 2022, A&A, 665, A144

Mullaney, J. R., Alexander, D. M., Fine, S., et al. 2013, MNRAS, 433, 622

Murthy, S., Morganti, R., Oosterloo, T., et al. 2019, A&A, 629, A58

Naab, T. & Ostriker, J. P. 2017, ARA&A, 55, 59

Nandi, P., Stalin, C. S., & Saikia, D. J. 2025, arXiv e-prints, arXiv:2503.06719

Negus, J., Comerford, J. M., & Sánchez, F. M. 2024, ApJ, 971, 92

Nelson, C. H. & Whittle, M. 1996, ApJ, 465, 96

Nesvadba, N. P. H., Wagner, A. Y., Mukherjee, D., et al. 2021, A&A, 654, 8

Netzer, H. 2006, Active Galactic Nuclei: Basic Physics and Main Components, ed. D. Alloin, R. Johnson, & P. Lira (Berlin, Heidelberg: Springer Berlin Heidelberg), 1–38

Netzer, H. 2015, ARA&A, 53, 365–408

Newville, M., Stensitzki, T., Allen, D. B., et al. 2016, Lmfit: Non-Linear Least-Square Minimization and Curve-Fitting for Python, Astrophysics Source Code Library, record ascl:1606.014

Nims, J., Quataert, E., & Faucher-Giguére, C. A. 2015, MNRAS, 447, 3612

Ogle, P. M., Sebastian, B., Aravindan, A., et al. 2025, ApJ, 983, 98

Oh, K., Koss, M. J., Ueda, Y., et al. 2022, ApJS, 261, 4

Oh, K., Yi, S. K., Schawinski, K., et al. 2015, ApJS, 219, 1

Oliva, E., Marconi, A., Maiolino, R., et al. 2001, A&A, 369, L5

Osterbrock, D. 1989, Astrophysics of Gaseous Nebulae and Active Galactic Nuclei, A Series of books in astronomy (University Science Books)

Padilla, N. D. & Strauss, M. A. 2008, MNRAS, 388, 1321

Padovani, P. 2016, A&A Rev., 24, 13

Padovani, P. 2017, Frontiers in Astronomy and Space Sciences, 4, 35

Padovani, P., Alexander, D. M., Assef, R. J., et al. 2017, A&A Rev., 25, 2

Pai, A., Blanton, M. R., & Moustakas, J. 2024, ApJ, 977, 102

Pan, H.-A., Lin, L., Hsieh, B.-C., et al. 2019, ApJ, 881, 119

Panessa, F., Baldi, R. D., Laor, A., et al. 2019, Nature Astronomy, 3, 387

Pardo, K., Goulding, A. D., Greene, J. E., et al. 2016, The Astrophysical Journal, 831, 203

Pennell, A., Runnoe, J. C., & Brotherton, M. S. 2017, MNRAS, 468, 1433

Peterson, B. M. 2006, in Physics of Active Galactic Nuclei at all Scales, ed. D. Alloin, Vol. 693, 77

Petrosian, V. 1976, ApJ, 210, L53

Piotrowska, J. M., Bluck, A. F. L., Maiolino, R., & Peng, Y. 2022, MNRAS, 512, 1052

Planck Collaboration, Ade, P. A. R., Aghanim, N., et al. 2014, A&A, 571, A16

Powell, M. C., Cappelluti, N., Urry, C. M., et al. 2018, ApJ, 858, 110

Ramos Almeida, C., Martínez González, M. J., Asensio Ramos, A., et al. 2016, MNRAS, 461, 1387

Rao, V. V., Kharb, P., Rubinur, K., et al. 2023, MNRAS, 524, 1615

Rees, M. J. 1984, ARA&A, 22, 471

Ricci, C. & Trakhtenbrot, B. 2023, Nature Astronomy, 7, 1282

Riffel, R., Mallmann, N. D., Ilha, G. S., et al. 2021, MNRAS, 501, 4064

Riffel, R., Mallmann, N. D., Rembold, S. B., et al. 2023, MNRAS, 524, 5640

Riffel, R. A., Riffel, R., Bianchin, M., et al. 2023, MNRAS, 521, 3260

Rojas, A. F., Sani, E., Gavignaud, I., et al. 2019, MNRAS, 491, 5867

Ruffa, I., Prandoni, I., Davis, T. A., et al. 2022, MNRAS, 510, 4485

Sabater, J., Best, P. N., Hardcastle, M. J., et al. 2019, A&A, 622, A17

Sadler, E. M., Jackson, C. A., Cannon, R. D., et al. 2002, MNRAS, 329, 227

Salim, S. 2014, SAJ, 189, 1

Sánchez, S. F. 2020, ARA&A, 58, 99

Sánchez, S. F., Avila-Reese, V., Hernandez-Toledo, H., et al. 2018, Rev. Mex. Astron. Astrofis., 54, 217

Sánchez, S. F., Barrera-Ballesteros, J. K., Lacerda, E., et al. 2022, ApJS, 262, 36

Sánchez, S. F., Kennicutt, R. C., Gil de Paz, A., et al. 2012, A&A, 538, A8

Sánchez, S. F., Pérez, E., Sánchez-Blázquez, P., et al. 2016, Rev. Mex. Astron. Astrofis., 52, 171

Sánchez-Blázquez, P., Peletier, R. F., Jiménez-Vicente, J., et al. 2006, MNRAS, 371, 703

Santoro, F., Tadhunter, C., Baron, D., Morganti, R., & Holt, J. 2020, A&A, 644, A54

Schawinski, K., Koss, M., Berney, S., & Sartori, L. F. 2015, MNRAS, 451, 2517

Schawinski, K., Thomas, D., Sarzi, M., et al. 2007, MNRAS, 382, 1415

Schaye, J., Crain, R. A., Bower, R. G., et al. 2015, MNRAS, 446, 521

Sebastian, B., Kharb, P., O'Dea, C. P., Gallimore, J. F., & Baum, S. A. 2019, MNRAS, 490, L26

Sexton, R. O., Matzko, W., Darden, N., Canalizo, G., & Gorjian, V. 2020, MNRAS, 500, 2871

Shields, G. A. 1990, ARA&A, 28, 525

Shields, G. A. 1999, PASP, 111, 661

Shimwell, T. W., Hardcastle, M. J., Tasse, C., et al. 2022, A&A, 659, A1

Shimwell, T. W., Röttgering, H. J. A., Best, P. N., et al. 2017, A&A, 598, A104

Shulevski, A., Morganti, R., Barthel, P. D., et al. 2015, A&A, 583, A89

Silk, J. & Rees, M. J. 1998, A&A, 331, L1

Singh, R., van de Ven, G., Jahnke, K., et al. 2013a, A&A, 558, A43

Singh, R., van de Ven, G., Jahnke, K., et al. 2013b, A&A, 558, A43

Singha, M., Husemann, B., Urrutia, T., et al. 2022, A&A, 659, A123

Smirnova-Pinchukova, I., Husemann, B., Davis, T. A., et al. 2022, A&A, 659, A125

Smolčić, V. 2009, ApJ, 699, L43

Somerville, R. S. & Davé, R. 2015, ARA&A, 53, 51

Speranza, G., Balmaverde, B., Capetti, A., et al. 2021, A&A, 653

Sridhar, S. S., Morganti, R., Nyland, K., et al. 2020, A&A, 634, A108

Stasińska, G., Mateus, Jr., A., Sodré, Jr., L., & Szczerba, R. 2004, A&A, 420, 475

Stasińska, G. & Sodré, Jr., L. 2001, A&A, 374, 919

Stasińska, G., Vale Asari, N., Cid Fernandes, R., et al. 2008, MNRAS, 391, L29

Stasińska, G., Vale Asari, N., Wójtowicz, A., & Kozieł-Wierzbowska, D. 2025, A&A, 693, A135

Storey, P. J. & Zeippen, C. J. 2000, MNRAS, 312, 813

Strauss, M. A., Weinberg, D. H., Lupton, R. H., et al. 2002, AJ, 124, 1810

Sun, A.-L., Greene, J. E., & Zakamska, N. L. 2017, ApJ, 835, 222

Sun, A.-L., Greene, J. E., & Zakamska, N. L. 2017, ApJ, 835, 222

Suresh, A. & Blanton, M. R. 2024, arXiv e-prints, arXiv:2404.04780

Sánchez, S. F., Avila-Reese, V., Rodríguez-Puebla, A., et al. 2018, MNRAS, 482, 1557

Tadhunter, C., Rodríguez Zaurín, J., Rose, M., et al. 2018, MNRAS, 478, 1558

Taylor, M. 2005, in ASP Conf. Ser. Vol. 347, 29

Tempel, E., Saar, E., Liivamägi, L. J., et al. 2011, A&A, 529, A53

Terrazas, B. A., Bell, E. F., Pillepich, A., et al. 2020, MNRAS, 493, 1888

Thorne, J. E., Robotham, A. S. G., Davies, L. J. M., et al. 2021, MNRAS, 505, 540

Toba, Y., Komugi, S., Nagao, T., et al. 2017, ApJ, 851, 98

Tombesi, F., Cappi, M., Sambruna, R. M., et al. 2012, in ASPCS, Vol. 460, AGN Winds in Charleston, ed. G. Chartas, F. Hamann, & K. M. Leighly, 8

Torres-Papaqui, J. P., Coziol, R., Robleto-Orús, A. C., Cutiva-Alvarez, K. A., & Roco-Avilez, P. 2024, AJ, 168, 37

Tremonti, C. A., Heckman, T. M., Kauffmann, G., et al. 2004, ApJ, 613, 898

Ulivi, L., Venturi, G., Cresci, G., et al. 2024, A&A, 685, 122

Urry, C. M. & Padovani, P. 1995, PASP, 107, 803

van Haarlem, M. P., Wise, M. W., Gunst, A. W., et al. 2013, A&A, 556, A2

van Weeren, R. J., de Gasperin, F., Akamatsu, H., et al. 2019, Space Sci. Rev., 215, 16

Vázquez-Mata, J. A., Hernández-Toledo, H. M., Avila-Reese, V., et al. 2022, MNRAS, 512, 2222

Veilleux, S. & Osterbrock, D. E. 1987, ApJS, 63, 295

Venturi, G., Cresci, G., Marconi, A., et al. 2021, A&A, 648, A17

Vink, J. 2004, in IAU Symposium, Vol. 218, Young Neutron Stars and Their Environments, ed. F. Camilo & B. M. Gaensler, 57

Vogelsberger, M., Genel, S., Springel, V., et al. 2014, Nature, 509, 177

Volonteri, M. 2010, A&A Rev., 18, 279

Vučetić, M. M., Arbutina, B., & Urošević, D. 2015, MNRAS, 446, 943

Wake, D. A., Bundy, K., Diamond-Stanic, A. M., et al. 2017, AJ, 154, 86

Wellons, S., Faucher-Giguère, C.-A., Hopkins, P. F., et al. 2023, MNRAS, 520, 5394

Wen, X.-Q., Wu, H., Zhu, Y.-N., et al. 2013, MNRAS, 438, 97

Westfall, K. B., Cappellari, M., Bershady, M. A., et al. 2019a, AJ, 158, 231

Westfall, K. B., Cappellari, M., Bershady, M. A., et al. 2019b, AJ, 158, 231

Westmoquette, M. S., Exter, K. M., Christensen, L., et al. 2009, arXiv e-prints, arXiv:0905.3054

White, S. V., Jarvis, M. J., Häußler, B., & Maddox, N. 2015, MNRAS, 448, 2665

Wolnik, K., Jurusik, W., & Jamrozy, M. 2024, A&A, 691, A76

Woo, J.-H., Bae, H.-J., Son, D., & Karouzos, M. 2016, ApJ, 817, 108

Woo, J.-H., Son, D., & Bae, H.-J. 2017, ApJ, 839, 120

Worrall, D. & Birkinshaw, M. 2006, Multiwavelength Evidence of the Physical Processes in Radio Jets, ed. D. Alloin, R. Johnson, & P. Lira (Berlin, Heidelberg: Springer Berlin Heidelberg), 39–76

Wright, E. L. 2006, PASP, 118, 1711

Wright, E. L., Eisenhardt, P. R. M., Mainzer, A. K., et al. 2010, AJ, 140, 1868

Wylezalek, D., Flores, A. M., Zakamska, N. L., Greene, J. E., & Riffel, R. A. 2020, MNRAS, 492, 4680–4696

Wylezalek, D. & Morganti, R. 2018, Nature Astronomy, 2, 181

Wylezalek, D., Schnorr Müller, A., Zakamska, N. L., et al. 2017, MNRAS, 467, 2612

Wylezalek, D., Zakamska, N. L., Greene, J. E., et al. 2018, MNRAS, 474, 1499

Xia, H., Yuan, F., Li, Z., & Zhu, B. 2025, arXiv e-prints, arXiv:2507.19716

Xu, X. & Wang, J. 2023, ApJ, 943, 28

Yan, L., Donoso, E., Tsai, C. W., et al. 2013, AJ, 145, 55

Yesuf, H. M., Koo, D. C., Faber, S. M., et al. 2017, ApJ, 841, 83

York, D. G., Adelman, J., Anderson, Jr., J. E., et al. 2000, AJ, 120, 1579

Yu, B. P. B., Angthopo, J., Ferreras, I., & Wu, K. 2022, Publ. Astron. Soc. Aust., 39, e054

Zahid, H. J., Geller, M. J., Fabricant, D. G., & Hwang, H. S. 2016, ApJ, 832, 203

Zakamska, N. L. & Greene, J. E. 2014, MNRAS, 442, 784

Zakamska, N. L., Hamann, F., Pâris, I., et al. 2016a, MNRAS, 459, 3144

Zakamska, N. L., Lampayan, K., Petric, A., et al. 2016b, MNRAS, 455, 4191

Zhang, K., Yan, R., Bundy, K., et al. 2017, MNRAS, 466, 3217

Zubovas, K. 2018, MNRAS, 473, 3525

Zubovas, K., Bialopetravičius, J., & Kazlauskaitė, M. 2022, MNRAS, 515, 1705

Zubovas, K. & King, A. 2012, ApJL, 745, L34

Zubovas, K. & Maskeliūnas, G. 2023, MNRAS, 524, 4819

Appendix

A

Appendix for Chapter 2: Mapping AGN winds: A connec- tion between radio-mode AGNs and the AGN feedback cycle

A.1 Targets in our sample

Due to the amount of data, and catalogs available for MaNGA, this section details our sample. We intend to remove duplicate observations to be specific about which targets we use since we require specific host-galaxy properties from the galaxies.

We start defining the sample with all the targets present on Sánchez et al. (2022) value-added catalog, which starts with a sample of 10 220 galaxies. We use the plate-ifu as the main identifier of our targets, given that MaNGA has a number of repeated observations (some with the same MaNGAID). We follow MaNGA's steps to mask the sample for unique galaxies[1], reducing the sample to 9 995 targets. The sample gets reduced to 9 992 galaxies because three of them had no data stored on the public website of the data reduction pipeline: 11939-1901, 11949-1901, and 8626-9102 (also reported in a list of targets that failed to be analyzed by the DAP[2].

Table A.1. Plate-IFU pairs of repeated observations.

10513-1901 — 9512-6104	7963-12702 — 8651-12702
10513-3702 — 9512-6103	7963-12704 — 8651-12704
10843-12704 — 11866-9101	7963-12705 — 8651-12705
10843-6103 — 11866-1901	7963-3701 — 8651-3701
11016-12705 — 11827-9101	7963-3704 — 8651-3704
11016-1901 — 8309-6101	7963-6101 — 8651-9102
11016-1902 — 8309-1902	7963-6102 — 8651-1902
11016-3702 — 8309-12705	7963-6103 — 8651-6104
11016-6101 — 11827-6103	7963-6104 — 7964-12705
11016-6104 — 11827-6104	7963-9101 — 8651-6102
11017-12703 — 11758-3702	7963-9102 — 8651-6103
11017-1902 — 8319-6104	7964-12701 — 8651-12703

[1] https://www.sdss4.org/dr17/manga/manga-tutorials/drpall/
[2] https://www.sdss4.org/dr17/manga/manga-caveats/

Continuation of Table A.1

11017-9101 — 11758-3701	7964-3702 — 8651-3703
11757-1902 — 11868-12705	8239-6104 — 8567-12702
11823-3703 — 11950-1902	8247-3702 — 8249-3701
11823-6104 — 11950-1901	8249-12705 — 8250-3702
11823-9102 — 11950-3701	8249-6104 — 8250-9101
11827-12701 — 8325-12704	8256-12701 — 8274-12701
11827-3701 — 8325-6103	8256-12702 — 8274-12702
11827-3703 — 9864-3701	8256-1901 — 8274-1901
11827-3704 — 8326-1901	8256-3701 — 8274-3701
11827-9102 — 8326-9101	8256-3702 — 8274-3702
11838-12703 — 11865-1901	8256-9102 — 8274-9102
11838-3703 — 11865-9101	8261-1901 — 8262-1901
11867-12702 — 12511-1902	8309-12702 — 9884-1902
11867-12703 — 12511-3703	8312-12703 — 8550-9102
11867-6101 — 9512-1901	8319-1902 — 8324-1901
11867-6103 — 9512-3702	8319-3704 — 8324-9102
11867-6104 — 9512-3704	8325-12703 — 8326-12701
11867-9101 — 9512-12701	8325-3704 — 8328-1901
11867-9102 — 9512-3701	8326-3701 — 8329-1901
11940-6104 — 12667-3701	8328-3704 — 8329-12702
11946-6101 — 12667-1902	8329-3701 — 8333-12701
11947-3702 — 12675-1902	8329-3703 — 8333-12704
11948-12703 — 12675-3704	8329-3704 — 8333-3702
11949-1902 — 8613-1901	8454-6103 — 8456-6104
11949-3703 — 8613-6103	8459-3701 — 8461-6104
11978-6101 — 9894-3702	8459-3702 — 8461-3704
11978-6104 — 9894-1901	8459-3704 — 8461-12703
12066-1901 — 8652-3702	8484-9101 — 8555-3704
12066-3704 — 8652-12701	8555-12701 — 8600-9102
12667-3704 — 12675-3702	8588-3701 — 8603-12701
7815-12701 — 8618-1902	8596-12701 — 8598-12703
7815-12702 — 7972-12705	8596-12702 — 8598-9102
7815-12705 — 8618-6101	8600-1902 — 8979-3703
7815-1902 — 8618-6103	8600-3702 — 8979-12704
7815-6101 — 7972-3701	8606-6104 — 8614-3702
7815-9101 — 7972-12704	8651-6101 — 9191-3703
7958-1901 — 9185-1901	8950-12702 — 8951-12704
7958-3703 — 9185-3702	8996-12705 — 8997-12701
7960-12702 — 9185-3704	8998-3703 — 8999-9101
7962-3701 — 9085-3701	9031-12701 — 9036-12703

Continuation of Table A.1

7962-6101 — 9085-3703	9031-12705 — 9036-6101
7962-6104 — 9085-3704	9031-3701 — 9036-1901
7963-12701 — 8651-12701	9031-3704 — 9036-3703

Table A.2. Repeated observations with more than two elements.

7963-3702 — 8651-1901 — 9191-3702
8256-12703 — 8274-12703 — 8451-12704
8256-12704 — 8274-12704 — 8451-12701
8256-12705 — 8274-12705 — 8451-12702
8256-1902 — 8274-1902 — 8451-1902
8256-3703 — 8274-3703 — 8451-3703
8256-3704 — 8274-3704 — 8451-3704
8256-6101 — 8274-6101 — 8451-6101
8256-6102 — 8274-6102 — 8451-3702
8256-6103 — 8274-6103 — 8451-6102
8256-6104 — 8274-6104 — 8451-6103
8256-9101 — 8274-9101 — 8451-9101
8479-3703 — 8480-3701 — 8587-3702
8953-3702 — 9051-6103

*the last row is a target repeated five times.

In Sánchez et al. (2022), a table showing duplicate observations is reported, and similarly, a table of duplicates is also reported on the latter website (warning about duplicate galaxies with different MaNGA IDs). We note that some targets present in the MaNGA's duplicate table are not present in Sanchez's table. Therefore, we merge both repeated target tables and select from each pair the plate-ifu of which had more available annuli with higher S/N when measuring their W80. This removes twenty more galaxies, leaving our sample with 9 972. We further double-checked for duplicate observations matching targets by MaNGA-ID and ensuring that the coordinates were consistent with each other and found more repetitions in the sample. We show these duplicate observations in Table A.1, while some observations are repeated more than two times, as shown in Table A.2 (most of the targets in both tables come from cluster ancillary programs discussed in the drpall website mentioned above). As before, we remove these, keeping the one that offers a better quality of W_{80}. With the latter, we end up with 9 853 targets. Finally, we remove targets flagged by the MANGA_DRP3QUAL as CRITICAL by the DRP. This leaves us with a final sample of 9777 galaxies.

The quality criteria used in our analysis remove a number of extra galaxies from the study (see Sect. 2.3.2). We do not analyze separately additional galaxies (e.g., if more than one galaxy was found in a specific plate-ifu, Pan et al. 2019) found in the same IFU, and do not include any special treatment where this happens.

A.2 Fitting procedure details

Our pipeline starts by subtracting the stellar continuum (provided by the DAP Westfall et al. 2019b) from all spectra and moving each to its rest frame. We focus on the 4920-5080 Å region and subtract an additional continuum component from a 1D polynomial using two spectral windows (the first between 4870-4900 Å and the second between 5040-5100 Å). We execute the fitting two times: the first using a single Gaussian for each emission line and the second allowing two Gaussians for each emission line to account for possible asymmetries in the line profiles.

Below, we list the constraints used during the fitting procedure. The model with just one Gaussian profile has three free parameters to be fitted: amplitude, width, and systemic velocity, denoted by A, σ, and μ, respectively. The details are given below:

- The [O III] 4959,5007 Å doublet is fixed to the theoretical flux ratio of 2.98 ($\lambda5007/\lambda4959$; Laker et al. 2022; Storey & Zeippen 2000).
- The velocity dispersion (σ) and systemic velocity (μ) of both [O III] 4959 Å and 5007 Å are tied to the same value, which will be a free parameter on the fitting procedure.
- We limit velocity values to $0 < \sigma < 1000$ km s^{-1}, and $-1000 < \mu < 1000$ km s^{-1}

In the two-Gaussian model, the fitting procedure has six free parameters. The first Gaussian component with A, σ, and μ, and similarly, the second with A_w, σ_w, and μ_w (for the amplitude, width and offset of the "wing" component). We adopt the same considerations as listed above, and we add the following to the second Gaussian component:

- The amplitude, A_w, is a fraction of the main Gaussian amplitude (A), constrained between 0 and 1.
- The velocity dispersion, σ_w, is forced to be higher and up to 1500 km s^{-1} to avoid fitting noise.
- The systemic velocity, μ_w, can be blue or redshifted up to 1000 km s^{-1} from the main Gaussian's offset, μ.

A visual inspection of many of our results motivated us to add an extra condition to prevent the second component from fitting noise. To do this, we impose an additional condition to decide whether to use one or two Gaussians for the emission line. The second Gaussian component (after fitted) should have at least $S/N_{[O\ III]}$>3. If this S/N requirement is not satisfied, the emission line is kept fitted with only one Gaussian.

We store each fitted parameter in maps (for the single- and double-Gaussian fitting procedures), including the reduced-chi-square provided by LMFIT. From the resulting

maps, we construct the $L_{[O\ III]}$ map (the sum of both components' fluxes in the case of the double-Gaussian model) and a nonparametric emission-line width map. To capture the emission-line width of a complex profile (e.g., a mixture of two Gaussian profiles) and reduce being influenced by the criteria of our fitting procedure, nonparametric measurements are routinely adopted (e.g., Wylezalek et al. 2020; Zakamska & Greene 2014). Specifically, we use the width that encloses the 80% of the total flux, known as the nonparametric W_{80} parameter (see the details in Liu et al. 2013). This parameter aims to prevent discarding information from the additional components of a profile composed of multiple components.

Finally, the decision to keep one fitting procedure from both models is based on the best-reduced chi-square (the one closer to 1; Andrae et al. 2010). With the latter, we construct best-model mask maps (see Fig. A.1), which are used to combine the results from the two fitting techniques into one containing the results of the models that fitted the spectral region the best (in the figure, we show this for the [O III]λ5007 W_{80}). The same best-model map creates the combined $L_{[O\ III]}$ map for each galaxy. From these two maps, we extract the following parameters:

- W_{80} radial profiles for each map: average W_{80} at elliptical ring apertures with a step of 0.25 R_{eff} from the center of each target (see below).
- $L_{[O\ III]}$ averaged at a radius of 0.5 R_{eff}.

A.3 Binning parameters

We show how the ionized gas kinematics from the [O III] emission-line (traced by the central W_{80} averaged over an aperture of 0.5 R_{eff}) changes (for different galaxy populations) when observed in different parameter spaces of host galaxy properties. This is shown in Figs. A1.A.3 and A1.A.2. When looking at SF galaxies, in most cases, there is no significant evolution in their W_{80}. Conversely, in the case of AGN-selected galaxies, stronger W_{80} values are found as we move to a specific direction of the parameter spaces. This is visually represented in Fig. A1.A.2, where minimal gradients are observed for SF galaxies, whereas AGN-selected galaxies show not only larger gradients but also a distinct trend toward increased stellar mass ($M_\star$) and $L_{[O\ III]}$ luminosity.

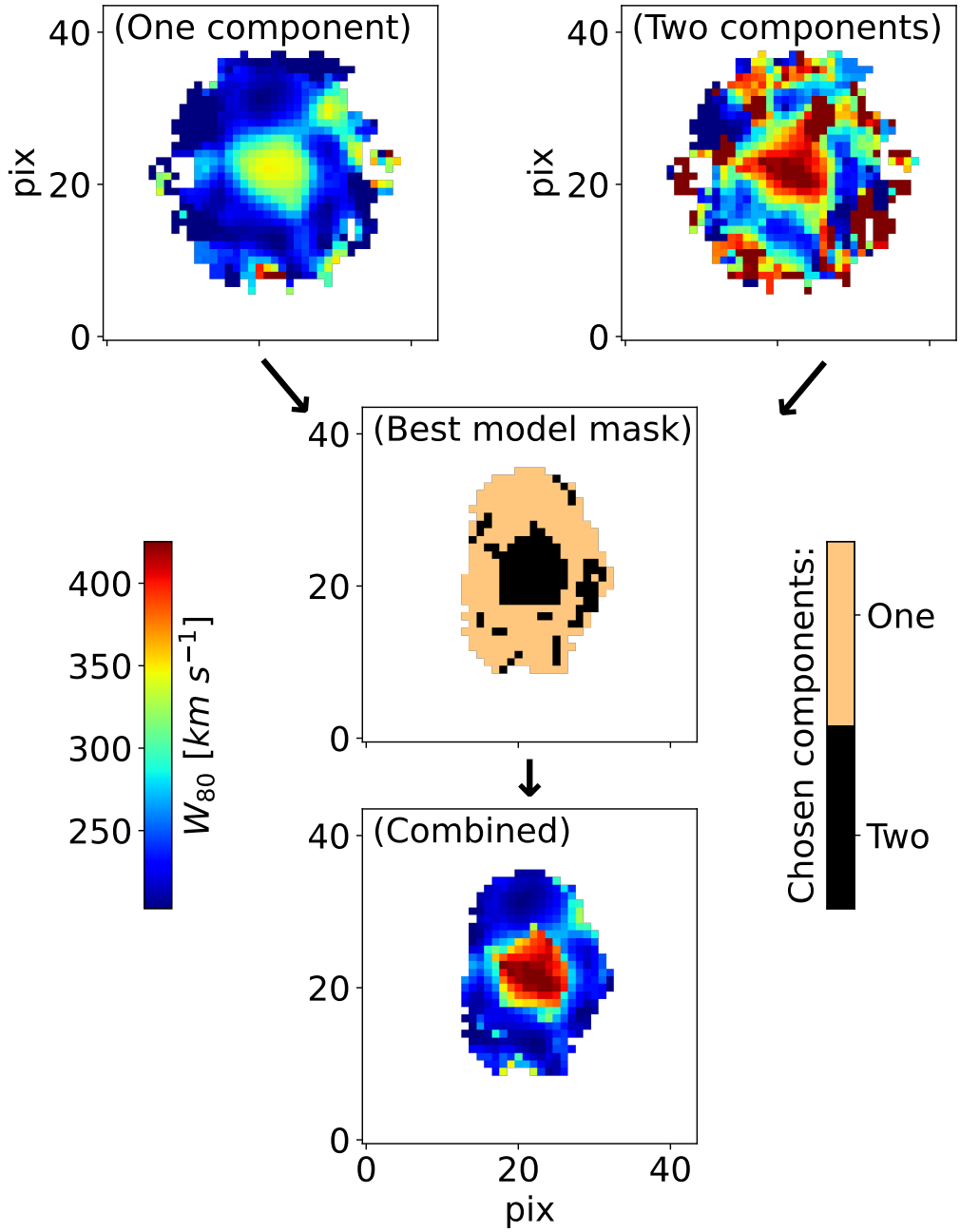

Figure A.1. Output for MaNGA plate-IFU: 8244-3702. Final W_{80} map (bottom plot) combined from the W_{80} map of each model (top plots) based on the best χ^2_{red} mask (middle plot) and an additional S/N cut on the second Gaussian component (see Sect. 2.3.1). All these figures' W_{80} maps have the same contrast colored following the same colorbar (on the middle-left)

.

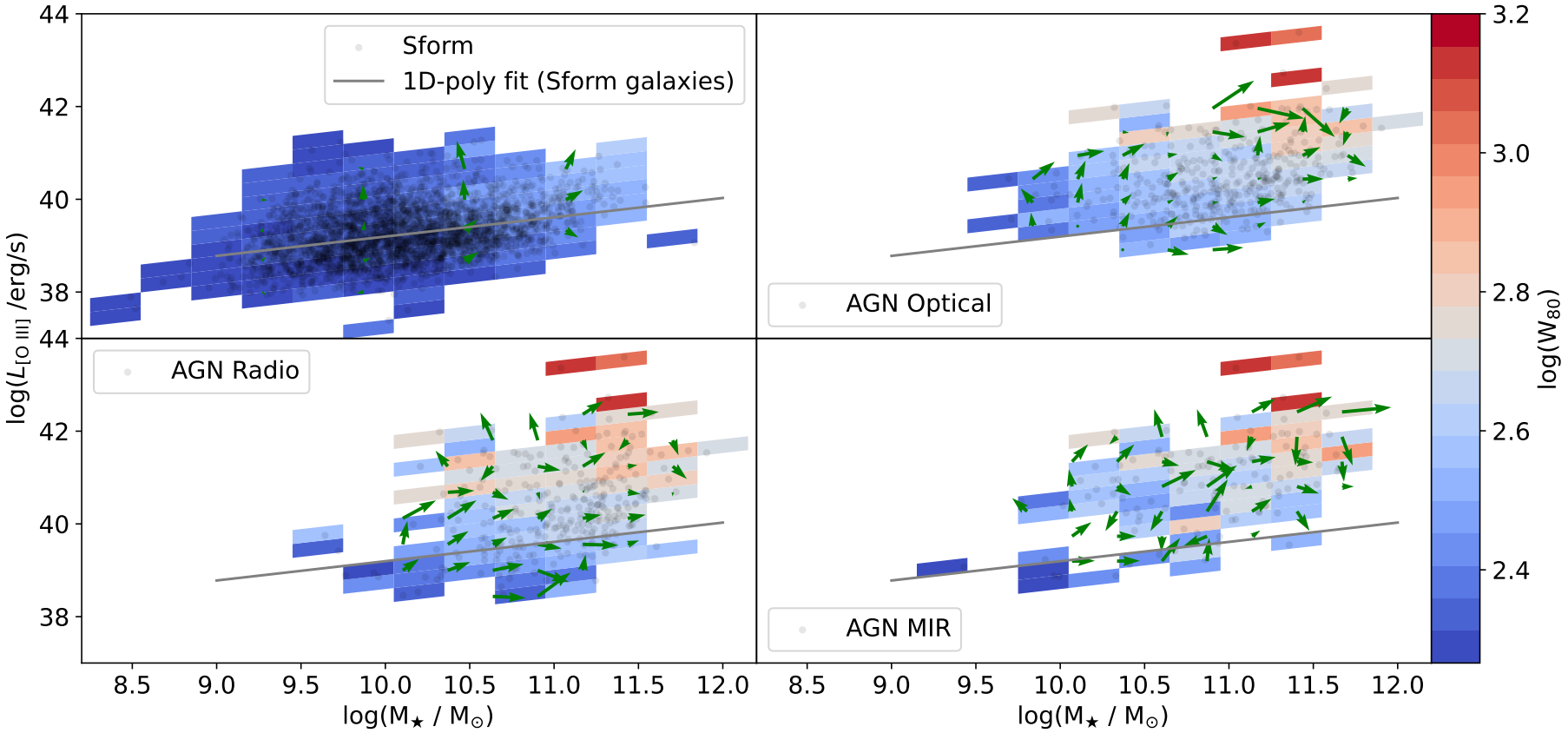

Figure A.2. Average W_{80} binned on a plane of $M_\star$ vs. $L_{[O\ III]}$. The bins have a size of 0.3 dex in each parameter, colored by the strength of the W_{80}. The scatter dots show the distribution of a specific galaxy population and the line shows a 1D polynomial fitted to the location of the SF galaxies. The green arrows in the plots illustrate the gradient change of W_{80} in the parameter space, with the arrowhead indicating the direction and the arrow's size representing the magnitude.

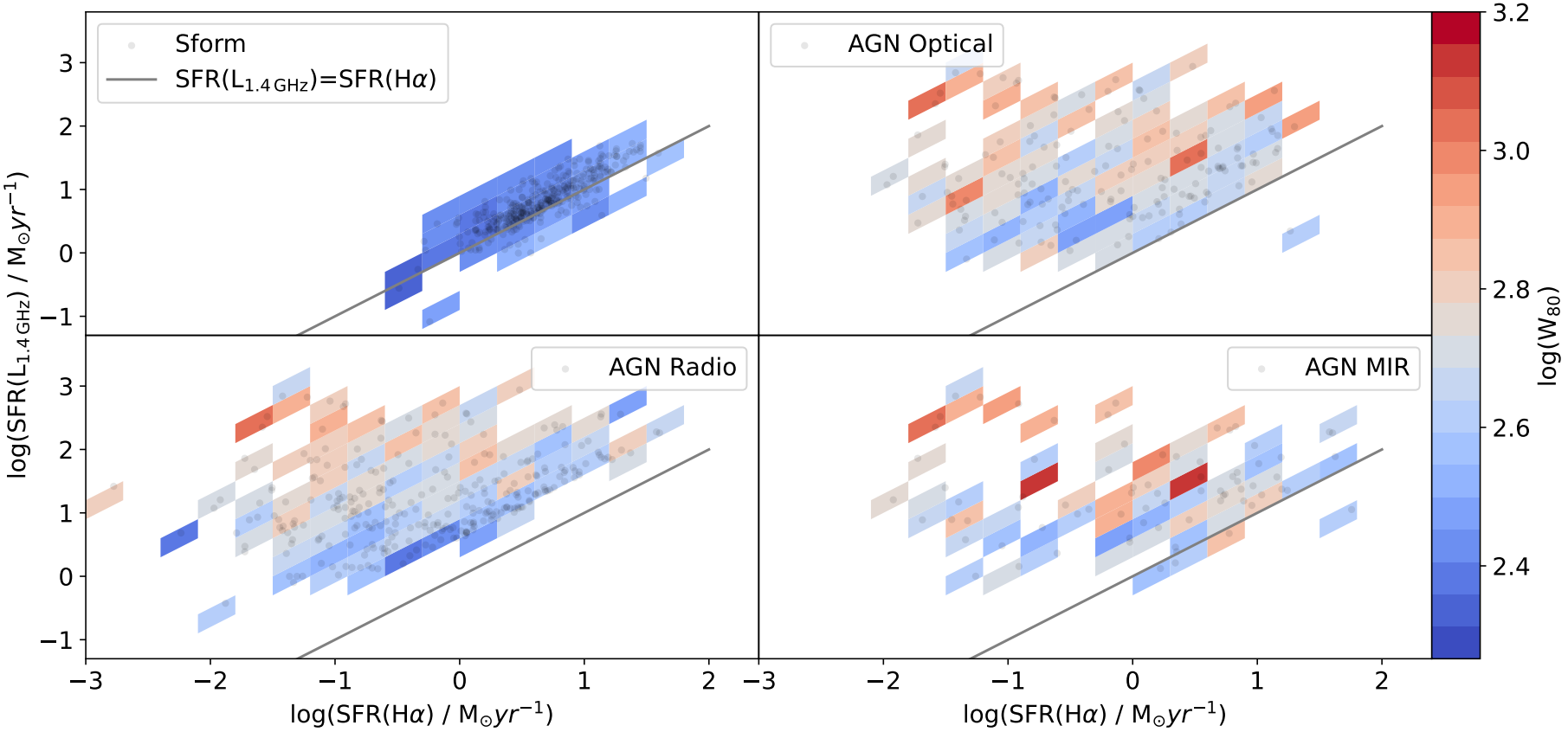

Figure A.3. Average W_{80} binned on a plane of star formation rate measured from L_{rad} and $L_{H\alpha}$. The bins have a size of 0.3 dex in each parameter, colored by the strength of the W_{80}. The scatter dots show the distribution of a specific galaxy population and the line shows the 1-to-1 relation if both SFR tracers are equal.

APPENDIX

B

Appendix for Chapter 3: Feedback from low-to-moderate-luminosity radio-active galactic nuclei with MaNGA

B.1 Selecting radio-AGN from FIRST

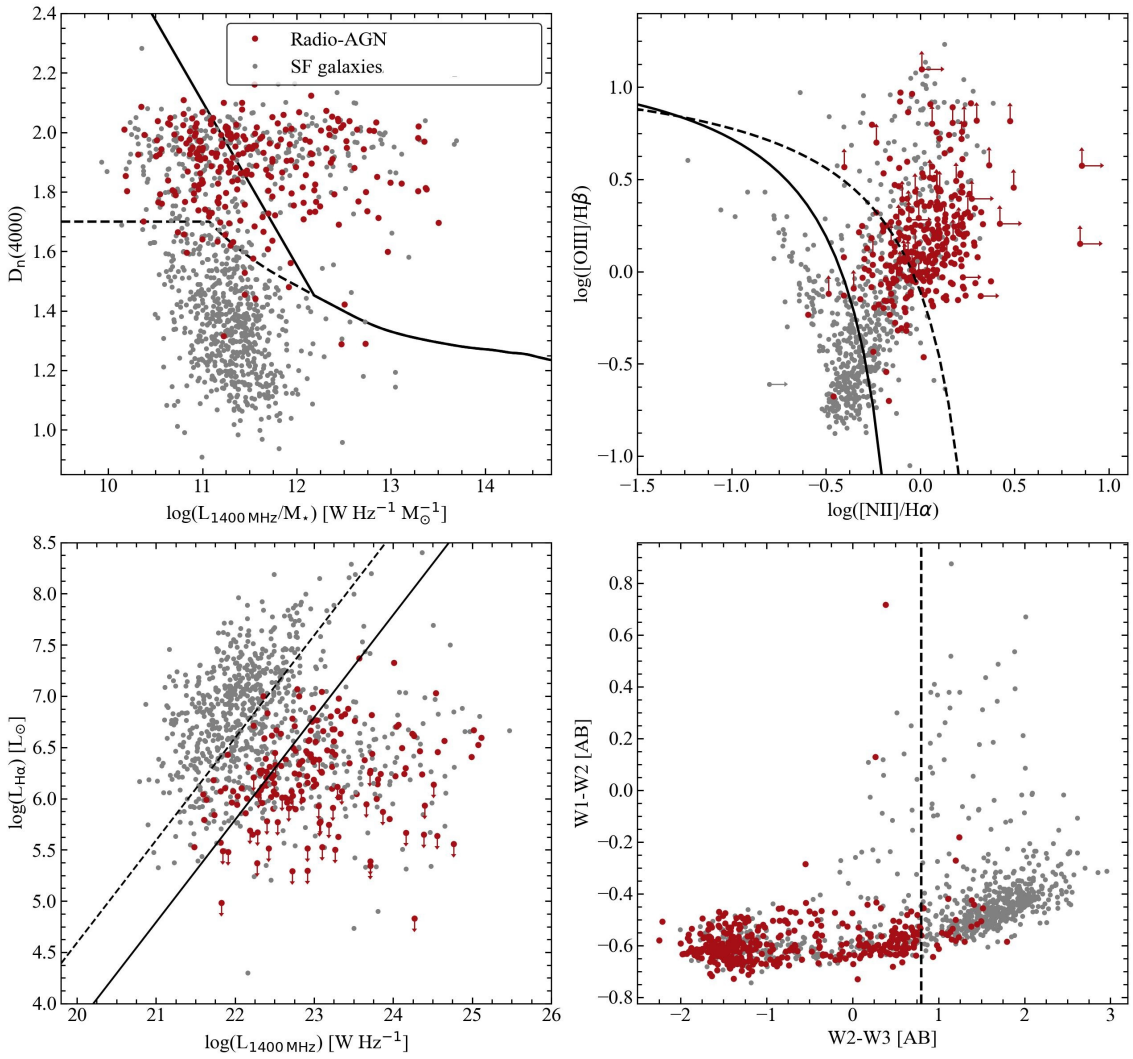

Figure B.1. Same as Fig. 3.1, but selecting radio-AGN using FIRST data.

Table B.1. Diagnostic combinations for FIRST sources.

$D_{\rm n}(4000)$ vs $L_{\rm 1.4GHz}/M_\star$	BPT	$L_{\rm H\alpha}$ vs $L_{\rm 1.4GHz}$	WISE col-col	Number	Final class
AGN	AGN	AGN	AGN	46	AGN
AGN	AGN	AGN	Uncl.	17	AGN
AGN	Int.	AGN	AGN	21	AGN
AGN	Uncl.	AGN	AGN	27	AGN
AGN	Uncl.	AGN	Uncl.	15	AGN
AGN	Uncl.	Uncl.	Uncl.	21	AGN
Int.	AGN	AGN	AGN	15	AGN
Int.	AGN	Int.	SF	16	SF
Int.	AGN	Int.	Uncl.	14	AGN
Int.	AGN	SF	AGN	24	SF
Int.	Int.	AGN	AGN	10	AGN
Int.	Int.	Int.	AGN	19	AGN
Int.	Int.	Int.	SF	14	SF
Int.	Int.	SF	AGN	10	AGN
Int.	Uncl.	AGN	AGN	12	AGN
Int.	Uncl.	Uncl.	AGN	32	AGN
Int.	Uncl.	Uncl.	Uncl.	13	AGN
AGN	Uncl.	Uncl.	AGN	43	AGN
Int.	AGN	Int.	AGN	61	AGN
SF	AGN	Int.	SF	22	SF
SF	AGN	SF	SF	40	SF
SF	Int.	Int.	SF	49	SF
SF	Int.	SF	SF	99	SF
SF	SF	Int.	SF	65	SF
SF	SF	SF	SF	254	SF
SF	SF	SF	Uncl.	15	SF
Uncl.	Uncl.	Uncl.	Uncl.	19	Uncl.

Combinations for classification of a source using the diagnostic diagrams discussed in Sect. 3.2.1, and the final classification assigned. Only groups with more than 40 sources are shown here.

Table B.2. Classification of FIRST cross-matched sources.

Diagnostic	AGN	Int.	SF	Uncl.
	(No. of overall radio-AGN)			
$D_{\rm n}(4000)$ vs $L_{1.4{\rm GHz}}/M_\star$	261	277	611	6
	(260)	(227)	(25)	-
$L_{\rm H\alpha}$ vs $L_{1.4{\rm GHz}}$	288	299	457	111
	(270)	(124)	(11)	(107)
BPT	360	278	324	200
	(233)	(80)	-	(191)
WISE col-col	440	-	554	161
	(374)	-	(17)	(121)

Number of sources classified by each diagnostic discussed in Sect. 3.2.1. The different classes are - AGN, intermediate (Int.), star-forming (SF), and unclassified (Uncl.). The numbers in brackets are sources from each group classified as radio-AGN after combining the four diagnostics.

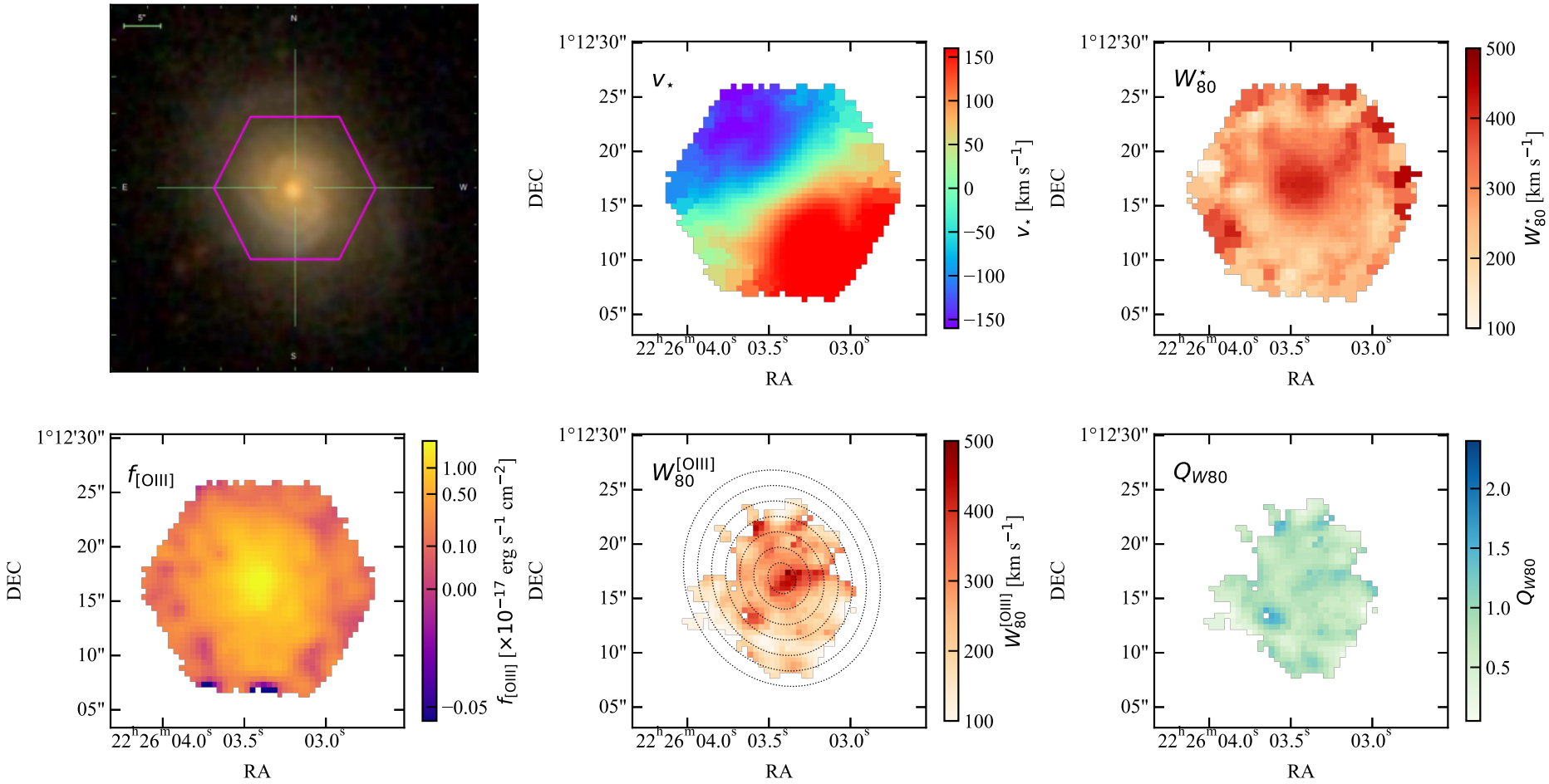

Figure B.2. Same as Fig. 3.3, but for a non-AGN galaxy (plateifu=12068-6104).

Appendix C

Appendix for Chapter 4: On the origin of radio emission in star-forming galaxies: connection to restarted or relic AGN activity

C.1 Statistical significance of parameters

We perform two-sample Kolmogorov-Smirnov tests to obtain the statistical p-values. Low p-values (e.g., $p < 0.05$) reject the null hypothesis that the compared samples are related and indicate that the observed differences are unlikely to have occurred by chance. In Figure C.1, we show the p-values for the integrated/global galaxy properties shown in Figure 4.3, and, additionally, we have added the values for the environmental characteristics and b/a axis ratio. We include the latter two here to show that they also do not exhibit significant differences between GHz-SFs and nGHz-SFs. The p-values at each annulus for the radial profiles are shown in Figure C.2, following the order of the parameters adopted in Figure 4.4. For the case of the outflow fraction (Figure 4.7), the only value with statistical significance (a p-value below 0.05) is in the central annuli.

C.2 A restricted sample

In Section 4.3, we establish that GHz-SFs and nGHz-SFs share the same stellar mass, $L_{144\ MHz}$, and redshifts. Here, we explore whether the effect of b/a can affect our conclusions. This criterion has been used to minimize the effect of dust reddening ($log(a/b) < 0.2$; Masters et al. 2010). This parameter is not included in the primary analysis for two reasons. First, neither GHz-SFs nor nGHz-SFs show significant differences in b/a (see C.1). This can be expected given their slightly differing morphologies (elliptical galaxies are less common at lower b/a, and late-type galaxies tend to exhibit flatter b/a distributions (Buitrago et al. 2013; Padilla & Strauss 2008; Tempel et al. 2011)). Nevertheless, we account for this parameter when measuring the radial profiles, and its effect should be minimal. Second, we aim to maximize the number of targets without compromising the robustness of the control process. Refining the control sample by including b/a significantly reduces statistical power.

Lastly, we want to know whether galaxies that look extremely similar (from the

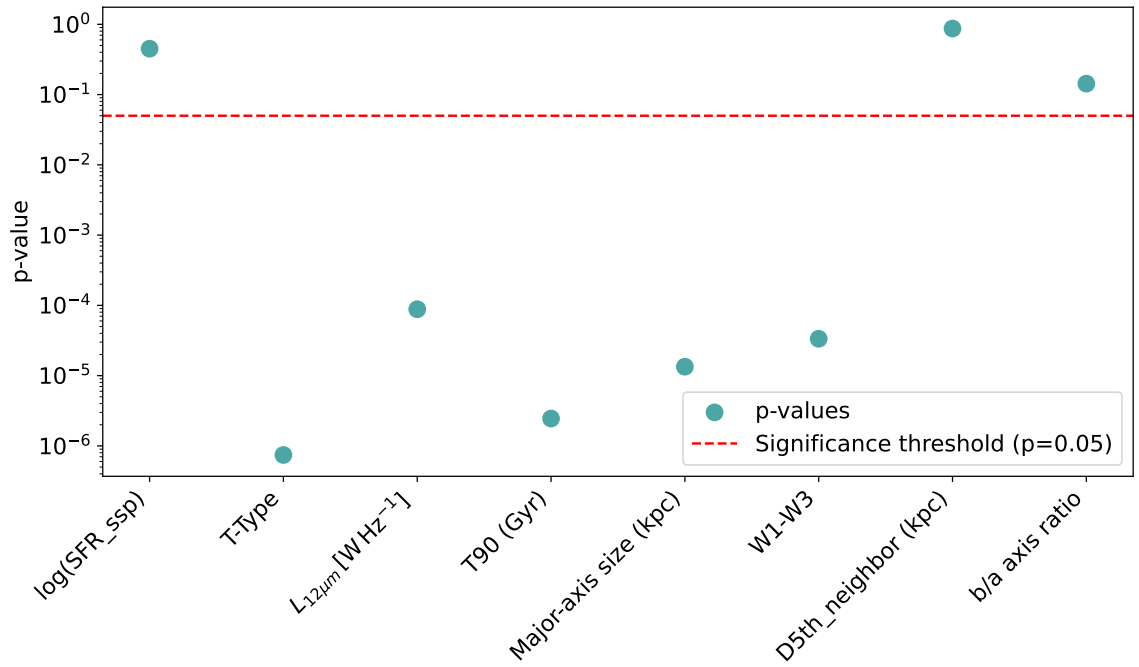

Figure C.1. Kolmogorov-Smirnov test for integrated or global properties. The red-dashed line shows $p = 0.05$.

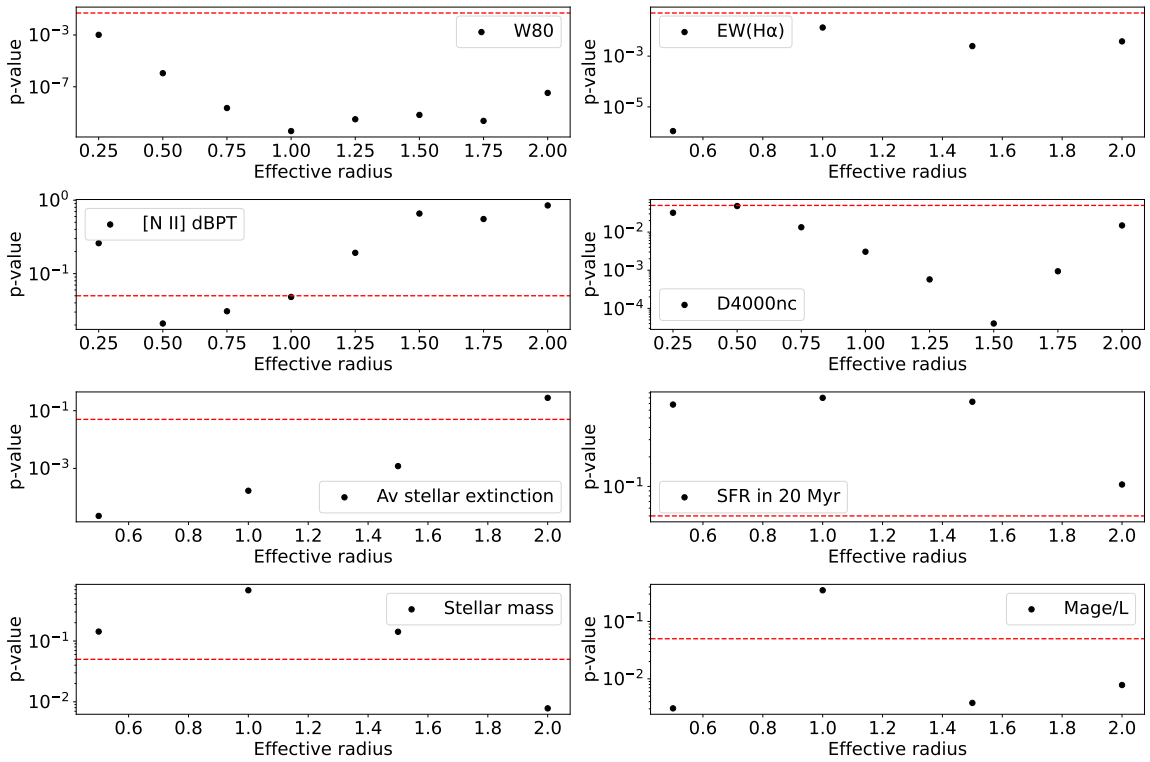

Figure C.2. Kolmogorov-Smirnov test for radial profiles. We show the p-values at each annulus for each parameter of Figure 4.4. The red-dashed lines show $p = 0.05$.

point of an analysis of their rest-frame optical characteristics) can still be different because of their radio properties. The motivation to do this is the fact that GHz-SFs would insist on also being optically compact when including control parameters. Therefore, we chose the R90 from the VACs as the extent of the optical size (defined as the size at which 90% of the total V band integrated flux is achieved) and included this parameter in the control sample. We examine whether key trends persist under this stricter selection and if new insights can be learned. The trade-off between sample size and robustness of this galaxy pairing leaves us with 48 galaxy pairs. We anticipate that the results below are very similar if, instead of R90, a concentration (C) parameter is chosen or other radius estimations such as the Petrosian radius from the MaNGA-DRPALL. In this comparison, the environment also does not seem to play a significant role in the differences discussed.

Much of what we observe from GHz-SFs and nGHz-SFs persists in the restricted sample. The W_{80} radial profile persists in excess at all annuli for GHz-SFs, and the global SFRs are kept self-controlled. Similarly, the stellar extinction and the Balmer decrement, both tracers of obscuration, remain in excess for the restricted GHz-SFs, although not as drastically as in the main sample. Strikingly, T90 values have a more evident excess between both samples. A similar behavior is seen in EW(Hα) and the T-Type morphological value. Reproducing Figure 4.5 with the restricted sample gives similar behavior to the primary sample. A slight increase in the closest neighbors is observed in GHz-SFs. Indeed, later morphologies are expected to occupy less dense environments (Goto et al. 2003). An important change to the observed behaviors is the appearance of higher values in the resolved SFRs for GHz-SFs. The latter, even if there is a slight difference, suggests that GHz-SFs have had different star-formation histories than nGHz-SFs. The results here are observed at fixed stellar mass, $L_{144\,\mathrm{MHz}}$, redshifts, simultaneously avoiding edge-on galaxies and matching for the visual extension (R90). The number of targets in this exercise is reduced to 48 targets, and in turn, we do not conclusively claim that this will always be true at fixed optical extensions. This emphasizes a known issue (Hopkins et al. 2003b), where constraining a sample to only objects with radio detections is subject to the shown behavior. However, this restricted sample comparison broadly recover the property differences from the main sample.

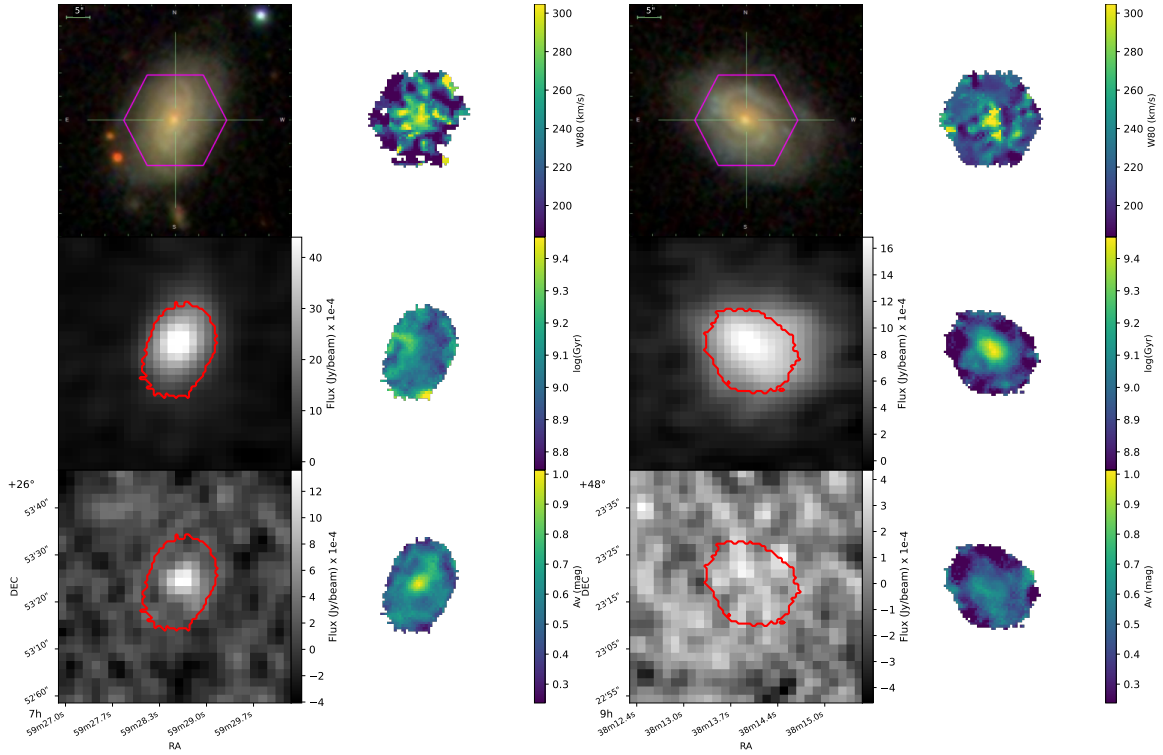

Figure C.3. Continuum and spatially resolved properties from a pair of galaxies of the restricted sample. The caption description follows Figure 4.6.

Acknowledgments

My first words of gratitude are to Prof. Dr. Dominika Wylezalek. A source of inspiration and wisdom builds from witnessing her growth as a leader and her exceptional career from the front row. Dominika has an incredible ability to balance high standards with kind, constructive, and patient feedback. Her enthusiasm during scientific discussions, sharp thinking, and support during countless rehearsals and paper writing are invaluable to me. Dominika's trust in my abilities lifted me from the beginning. I feel incredibly fortunate to have walked this journey through her guidance and supervision. It has taught me attributes that will be useful for my whole life.

I am thankful to be part of the GALENA research group and for their active discussions, constructive criticism, sharing of knowledge, and motivation throughout all our meetings and lunch discussions.

I want to thank Anna Pasquali for her kind support during the early stages of my career as a Master's student. She paid attention to my interests and work, and quickly pointed me in a fantastic direction, introducing me to Dominika.

I want to thank Rogerio Riffel and Rogemar Riffel for their trust, not only for welcoming me as a visitor to their home institute, but also for their active support and motivation throughout our collaboration.

Deep words go to my mother, Verónica Morales, who, without being a scientist, cultivated my early curiosity through books. Late in high school, I discovered what a black hole is by accident while cleaning a small, old bookshelf at our home, a task she had assigned to me. The book reads: "*A Brief History of Time: From the Big Bang to Black Holes*", by Stephen Hawking. Before that, I don't remember even liking to read. I am grateful for her support of this passion and for encouraging me to seek more books. She not only made sure I learned English early but also helped me understand why it mattered. Besides mentioning that most values in my life come from her upbringing, if there's one reason I know how to seek out opportunities, it's thanks to her.

Before choosing my career, I surprisingly did not know that Astronomy was a field one could pursue at the university level. I want to thank my father, Marco Albán (García), who, aware of my devotion and excitement about astronomy, informed himself about the field and later discussed it with me to explore it as a path, even accompanying me to astronomy courses. He always pushed me to reach my full po-

tential. He ensured that I could begin my studies in Heidelberg. I know one of his dreams was to have, besides him, another doctor in the family. He never specified "medical". This is how I become one.

To my brother, Adrian Graber, if there's one reason I can say I am good at computer programming, it's mainly because his extreme talent in informatics has inspired me throughout my life. I particularly thank him for his kind suggestions on some of the programming challenges I've faced in my career.

Franziska Werkman. She has powerful listening abilities. I sincerely appreciate every time you took a minute to listen to whatever cosmic thought I had in mind and wanted to share. I appreciate your efforts to understand what I do and your curiosity. I am so grateful for her belief in what I do and for her unconditional love.

Words of gratitude go to my whole family, the Albáns, Morales, and Grabers, as bright as a galaxy cluster. Despite the distance, the values you've taught me have shaped my approach to facing problems. I would like to particularly thank Michelle Andrade for the long, remote conversations when I was experiencing some kind of struggle.

Pursuing an achievement like this, far from home, is also far from being easy. This paragraph is dedicated to my close friends. Many of them are in my heart as a family. The beginning of my PhD studies was a rollercoaster of feelings. Throughout any trouble, my thoughts found their way back to a sunny place thanks to their company.